



HAL
open science

Synthesis of magnetic and thermosensitive iron oxide based nanoparticles for biomedical applications

Gauvin Hemery

► **To cite this version:**

Gauvin Hemery. Synthesis of magnetic and thermosensitive iron oxide based nanoparticles for biomedical applications. Chemical Physics [physics.chem-ph]. Université de Bordeaux, 2017. English. NNT : 2017BORD0729 . tel-01661602

HAL Id: tel-01661602

<https://theses.hal.science/tel-01661602>

Submitted on 12 Dec 2017

HAL is a multi-disciplinary open access archive for the deposit and dissemination of scientific research documents, whether they are published or not. The documents may come from teaching and research institutions in France or abroad, or from public or private research centers.

L'archive ouverte pluridisciplinaire **HAL**, est destinée au dépôt et à la diffusion de documents scientifiques de niveau recherche, publiés ou non, émanant des établissements d'enseignement et de recherche français ou étrangers, des laboratoires publics ou privés.

THÈSE PRÉSENTÉE
POUR OBTENIR LE GRADE DE
DOCTEUR DE
L'UNIVERSITÉ DE BORDEAUX

ÉCOLE DOCTORALE DES SCIENCES CHIMIQUES
SPÉCIALITÉ: Physico-chimie de la matière condensée

Par Gauvin HEMERY

**Synthesis of magnetic and thermosensitive iron oxide based
nanoparticles for biomedical applications**

**Synthèse de nanoparticules magnétiques et thermosensibles à base d'oxyde de fer
pour des applications biomédicales**

Sous la direction de : Dr. Olivier SANDRE
Co-encadrant : Dr. Elisabeth GARANGER

Soutenance prévue le 10 novembre 2017

Membres du jury :

Mme. AMMAR, Souad

M. SUBRA, Gilles

Mme. BEGIN COLIN, Sylvie

Mme. WILHELM, Claire

M. CHILKOTI Ashutosh

M. LECOMMANDOUX, Sébastien

M. SANDRE, Olivier

Mme. GARANGER, Elisabeth

M. COUILLAUD, Franck

Professeur, Université Paris Diderot

Professeur, Université de Montpellier

Professeur, Université de Strasbourg

Directeur de recherche, Université Paris Diderot

Professeur, Duke University

Professeur, Université de Bordeaux

Directeur de recherche, Université de Bordeaux

Chargé de recherche, Université de Bordeaux

Directeur de recherche, Université de Bordeaux 2

Rapporteur

Rapporteur

Examineur

Examineur

Examineur

Président de Jury

Directeur de thèse

Co-encadrant

Invité

L'avenir n'est jamais que du présent à mettre en ordre.
Tu n'as pas à le prévoir, mais à le permettre.

-Antoine de Saint-Exupéry

TITRE ET RESUME EN FRANÇAIS

Synthèse de nanoparticules magnétiques et thermosensibles à base d'oxyde de fer pour des applications médicales.

Nous avons développé des nanoparticules hybrides composées de cœurs magnétiques et de couronnes thermosensibles. Des cœurs inorganiques d'oxyde de fer (IONPs) ont été synthétisés pour leurs propriétés magnétiques et biocompatibles. Des couronnes organiques de polymères et polypeptides recombinants à base de motifs élastine appelés « elastin-like polypeptides » (ELPs) ont été greffés pour leurs propriétés thermosensibles. Les nanoparticules hybrides cœurs-couronnes inorganiques-organiques ainsi obtenues ont présenté des propriétés à la fois magnétiques et thermosensibles d'intérêt pour des applications médicales. Ces nanoparticules peuvent être utilisées pour le diagnostic en tant qu'agents de contraste pour l'IRM, et pour le traitement de cancer par hyperthermie magnétique. Des essais *in vitro* et *in vivo* sont venus confirmer ces applications potentielles. Ce projet de thèse dédié aux nanotechnologies pour la santé a ainsi intégré de la physique, chimie et biologie. Les résultats les plus représentatifs de ce projet sont présentés ci-dessous.

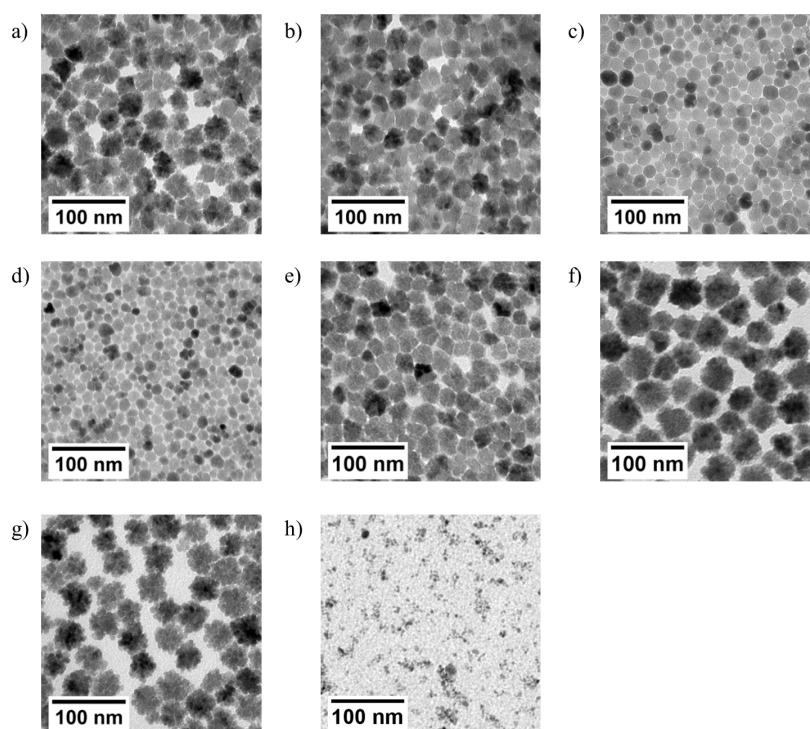


Figure 1 Images TEM de nanoparticules d'oxyde de fer monocœurs et multicœurs. **a)** 36ff (32.3±5.0 nm), **b)** 35ff (29.1±4.4 nm), **c)** 34ff (18.5±3.2 nm), **d)** 32ff (14.5±3.4 nm), **e)** 31ff (27.5±4.2 nm), **f)** 30ff (46.9±8.5 nm), **g)** 15ff (36.9±4.8 nm), et **h)** 17ff (4.3±1.1 nm). Les valeurs entre parenthèses correspondent aux diamètres moyens, associés à leurs déviations standards respectives.

Dans un premier temps, les nanoparticules d'oxyde de fer ont été produites par coprécipitation de chlorures de fer dans une base en milieu aqueux. Cette stratégie de synthèse a permis d'obtenir de larges quantités de matière, de l'ordre du gramme. Cependant, la synthèse par coprécipitation a eu pour désavantage de ne pas contrôler efficacement la morphologie et les propriétés

magnétiques des nano-cristaux obtenus. Pour ces raisons, nous avons sélectionné une nouvelle voie de synthèse dite « polyol » pour produire des nanoparticules d'oxyde de fer. Cette méthode a permis de produire des lots de nano-cristaux avec des morphologies et propriétés magnétiques mieux définies. Des paramètres réactionnels d'importance ont déjà été rapportés dans la littérature, comme la température et la durée de réaction, la vitesse d'élévation de température, la nature des solvants et des précurseurs organométalliques. Pourtant, le rôle crucial de l'eau n'a jamais été rapporté, malgré sa présence nécessaire pour produire des nanoparticules. Nous avons étudié l'influence de la quantité d'eau, et la température à laquelle elle a été injectée dans le système à reflux pour un solvant diéthylène glycol (DEG) ou un mélange de DEG et *N*-méthyl-diéthanolamine (NMDEA). Différentes morphologies ont été obtenues et caractérisées par microscopie électronique à transmission (TEM). Des nanoparticules sphériques (monocœurs) avec des diamètres de 4 nm ont été synthétisées, ainsi que de plus grosses avec des diamètres de 37 nm. Des morphologies particulières faites d'assemblages irréversibles de plus petits grains (multicœurs) ont aussi été synthétisées. Une bibliothèque d'échantillons de divers diamètres et morphologies a ainsi été produite, en jouant sur la nature des solvants, et sur l'ajout de traces d'eau à haute ou basse température. Les propriétés de ces nanoparticules ont été étudiées. La mesure par diffusion dynamique de la lumière (DLS) de nanoparticules dispersées dans l'eau a permis d'évaluer leurs stabilités en milieux aqueux. Leurs magnétisations ont été mesurées, démontrant les propriétés superparamagnétiques, avec des aimantations à saturation équivalentes à celle de l'oxyde de fer maghémite sous forme solide (bulk). Leurs doses d'absorption spécifique (specific absorption rates, SARs) ont été évaluées par mesure calorifique, en mesurant l'élévation de température sous application d'un champ magnétique alternatif. Nous avons obtenu des SARs allant jusque $296 \text{ W}\cdot\text{g}^{-1}$ en utilisant des fréquences et amplitudes de champs applicables dans des conditions médicales (fréquence de 755 kHz, amplitude de $10.2 \text{ kA}\cdot\text{m}^{-1}$). Les échantillons les plus prometteurs ont été étudiés à différentes fréquences et amplitudes à l'aide d'un magnétomètre. Des SARs aussi importantes que $2.000 \text{ W}\cdot\text{g}^{-1}$ (fréquence de 1023 kHz, amplitude de $20 \text{ kA}\cdot\text{m}^{-1}$) ont ainsi été obtenus. Les nanoparticules ont aussi été testées pour des applications en tant qu'agents de contraste pour l'IRM, en mesurant leurs capacités à relaxer les protons de l'eau en utilisant un appareil de relaxation magnétique nucléaire (RMN) de paillasse à 1.41 T. Les échantillons ont présenté des relaxivités transverses r_2 variant de manière quadratique avec le diamètre dans le cas des nanoparticules sphères lisses, en accord avec les modèles « motional averaging regime » et « outer sphere ». Les relaxivités longitudinales r_1 des plus petites nanoparticules associées avec un ratio modéré de r_2/r_1 leurs permettent d'être une bonne alternative aux complexes de gadolinium utilisés en tant qu'agent de contrastes positifs pour l'IRM, avec des effets cytotoxiques moindres attendus pour les patients. Les nanoparticules ainsi synthétisées présentent des intérêts pour des applications en tant qu'agents de contraste pour l'IRM, pour l'hyperthermie magnétique, voire pour les deux, en tant qu'agents dits théranostiques (utilisés en thérapie et diagnostic).

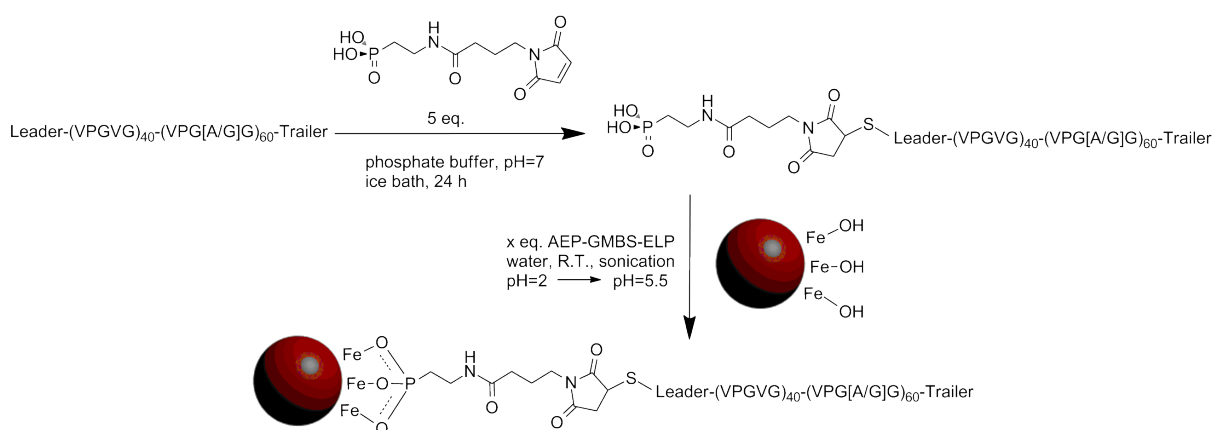


Figure 2 Schéma de synthèse convergente présentant le greffage d'un dibloc ELP*_{40-60-Tat} sur des IONPs.

La deuxième grande étape de ce projet était la fonctionnalisation des nanoparticules en modifiant leurs surfaces. L'objectif était d'apporter de la stabilité aux cœurs magnétiques en solution et potentiellement en conditions biologiques. La surface des nanoparticules a d'abord été modifiée par un aminosilane, suivi d'une molécule de liaison avant le greffage final d'un polymère ou d'un ELP. L'aminosilane a permis de faire le lien entre la surface inorganique d'oxyde de fer et la couronne organique à greffer. La bonne affinité du groupement silanol envers l'oxyde de fer a permis l'attachement de cet agent de surface, et ainsi introduit des groupements amines sur les IONPs. En sélectionnant une molécule de liaison appropriée, les polymères et polypeptides d'intérêt ont été liés de manière covalente avec les amines présentes à la surface des nanoparticules. L'aminosilane commercial AEAPTS et la molécule de liaison GMBS ont été utilisés pour greffer un ELP thermosensible mono-bloc (VPGIG)₂₀. L'AEAPTMS et une molécule de liaison synthétisée (acide azidoacétique) a permis de greffer le polymère thermosensible PDMAEMA. Ces modifications de surface se sont déroulées en trois étapes, avec des intermédiaires de réaction peu stables en solution. De plus, les caractérisations par des méthodes classiques (RMN, TLC) étaient impossibles du fait de l'immobilisation des molécules à analyser à la surface de nanoparticules solides et magnétiques. Des polymères et ELPs ont pu être entièrement modifiés avec une ancre phosphonate avant greffage en changeant de stratégie de synthèse. L'agent de surface acide aminoéthylphosphonique (AEP) a ainsi été utilisé à la place de l'AEAPTMS. Un polymère thiol-PEG a été modifié avec l'AEP et le GMBS (ensuite noté PEG*), purifié, puis greffé en une seule étape à la surface d'IONPs. Un ELP recombinant composé d'un dibloc (VPGVG)₄₀-(VPG(A/G)G)₆₀ et d'un peptide de pénétration cellulaire dérivé du Tat a également été modifié en introduisant une ancre phosphonate (ensuite noté ELP*_{40-60-Tat}). Le bloc (VPGVG)₄₀ de l'ELP a présenté des propriétés thermosensibles, avec une température de transition de 35 °C en solution. Le bloc (VPG(A/G)G)₆₀ de l'ELP hydrophile a permis d'apporter de la stabilité à la nanoparticule IONPs@ELP*_{40-60-Tat} cœur-écorce en solution. A notre connaissance, c'est la première fois que des ELPs ont été greffés à la surface de nanoparticules d'oxyde de fer. Une grande attention a

été portée sur la densité de greffage des chaînes PEG* et ELP*_{40-60-Tat}. Différents régimes de conformations de chaînes ont été explorés, présentant des chaînes greffées à une extrémité à la surface des IONPs et le reste de la chaîne étant étirée en solution, en faisant varier la quantité de chaînes par nanoparticule. Un paramètre dit « reduced tethered density » a permis d'évaluer le nombre de chaînes à greffer pour atteindre différents régimes de conformation, et prédire la stabilité des nanoparticules en solution. De plus, une sonde fluorescente DY700* a également été modifiée avec une ancre phosphonate et greffée à la surface des nanoparticules pour permettre leur suivi en fluorescence *in vitro* et *in vivo*.

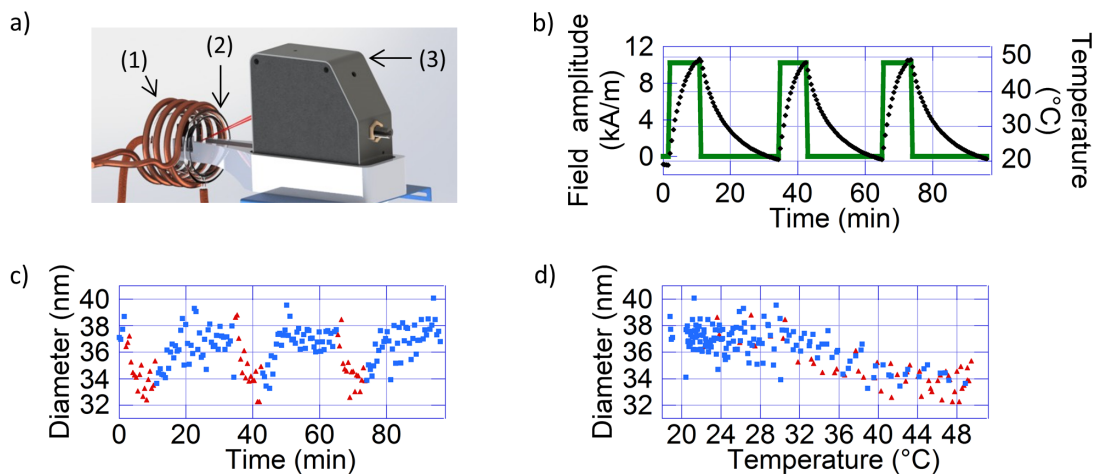


Figure 3 a) Illustration de l'instrument d'hyperthermie magnétique couplé avec une DLS: l'échantillon (IONPs@ELP*_{40-60-Tat} dispersé dans l'eau) contenu dans une cuvette a été placé dans une bobine d'induction à quatre spires (1), et thermalisé avec une double paroi en verre dans laquelle circulait de l'eau (2) tout en mesurant l'échantillon par DLS (3). **b)** La température de l'échantillon (losanges noirs) a été mesurée pendant l'application d'un profil de champs magnétiques (ronds verts). **c)** Les variations de diamètres hydrodynamiques (moyennés en intensité) ont été mesurés sous application de champs magnétiques (triangles rouges) ou sans application de champs magnétiques (carrés bleus). **d)** Les diamètres hydrodynamiques ont été représentés en fonction de la température sous application de champs magnétiques (triangles rouges) ou sans application de champs magnétiques (carrés bleus).

Un autre axe de cette thèse était de mesurer les variations de hauteur de brosses thermosensibles sous hyperthermie magnétique. Un instrument a été conçu spécialement pour ce besoin, couplant une bobine d'induction pour générer un champ magnétique alternatif à une sonde de température à fibre optique, et un appareil de diffusion dynamique de la lumière pour mesurer la réponse du système en variation de diamètre hydrodynamique et intensité diffusée. Cette approche unique a été démontrée comme étant prometteuse pour estimer la réponse de systèmes magnétiques et thermosensibles sous hyperthermie magnétique. Des nanoparticules cœur-écorce IONPs@PDMAEMA* ont été étudiées, montrant une agrégation réversible sous hyperthermie magnétique. D'autres systèmes magnétiques et thermosensibles ont été également mesurés par ce moyen : des micelles, des sphères creuses, et des microgels. Les nanoparticules hybrides IONPs@ELP*_{40-60-Tat} précédemment synthétisées ont été elles-aussi étudiées. Des variations importantes de température de l'ordre de 30 °C ont été mesurées, pouvant être obtenus en quelques minutes en appliquant un champ magnétique alternatif. De rapides diminutions de diamètres

hydrodynamiques ont été relevées par DLS, *in situ*, sous hyperthermie magnétique. Les variations de taille ont été comparées avec des modèles de brosses adaptés aux forts rayons de courbures présentés à la surface des nanoparticules. Nous avons démontré qu'à plus forte densité de greffage, les chaînes ELP*_{40-60-Tat} sont étirées, amenant à un plus large diamètre hydrodynamique. De plus grandes variations de hauteurs de brosses ont aussi été mesurées sous hyperthermie magnétique. Contrairement aux IONPs@PDMAEMA*, les diamètres ont diminué sous hyperthermie magnétique. Cela a été attribué à la déshydratation et raccourcissement du bloc (VPGVG)₄₀ et à l'effet stabilisant pour les IONPs du bloc (VPG(A/G)G)₆₀.

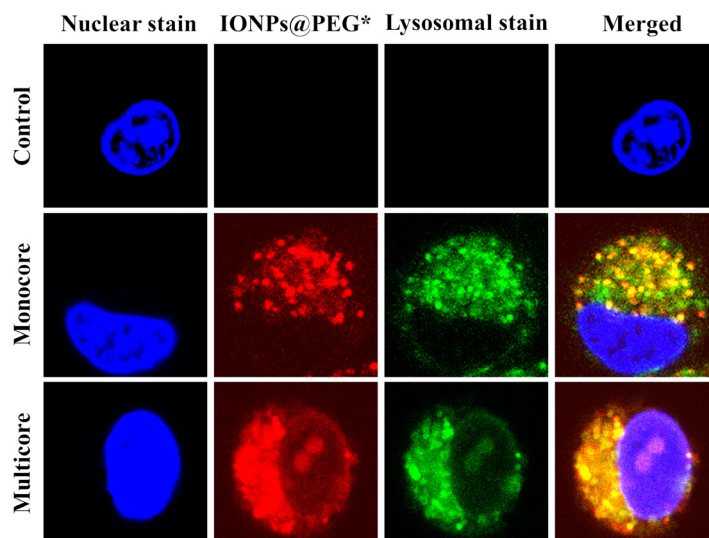


Figure 4 Distribution intracellulaire de IONPs@PEG* dans des cellules de glioblastome U87. Les cellules ont été incubées avec des IONPs@PEG* conjuguées à une sonde fluorescente DY700* (rouge) pendant 24 h à 100 $\mu\text{g}\cdot\text{mL}^{-1}$. Les cellules incubées ont ensuite été visualisées par microscopie à fluorescence confocale, avec un grandissement de 63 \times . Le noyau (bleu) a été marqué avec la sonde fluorescente Hoechst 33342 (2 $\mu\text{g}\cdot\text{mL}^{-1}$), les lysosomes (vert) avec le LysoTracker™ green (100 nM).

Les propriétés des nanoparticules hybrides IONPs@PEG* ont ensuite été évaluées *in vitro*. A l'origine, ces essais devaient être préliminaires et servir de contrôle à l'étude des nanoparticules IONPs@ELP*_{40-60-Tat}. Finalement nous avons décidé de faire une étude comparative de l'effet des monocœurs ou multicœurs sur l'internalisation cellulaire et la cytotoxicité. Les interactions des IONPs@PEG* avec des cellules humaines du cancer du cerveau (glioblastome) ont été étudiées. L'internalisation a été observée par microscopie optique, confocale et électronique, par cytométrie de flux et imagerie en fluorescence. Nous avons évalué l'influence de la dose de nanoparticules pendant l'incubation sur leurs internalisations dans les cellules. Nous avons observé que l'internalisation s'est déroulée probablement par micropinocytose, et que les nanoparticules se sont accumulées dans les lysosomes. Chaque cellule a ainsi internalisé quelques dizaines de millions de nanoparticules, sans impact visible sur la viabilité cellulaire. Par contre, après application d'un champ magnétique nous avons observé une forte cytotoxicité. Les nanoparticules multicœurs se sont révélées plus efficaces que les monocœurs pour traiter les cellules cancéreuses en culture, amenant à une mortalité cellulaire de près de 90 %.

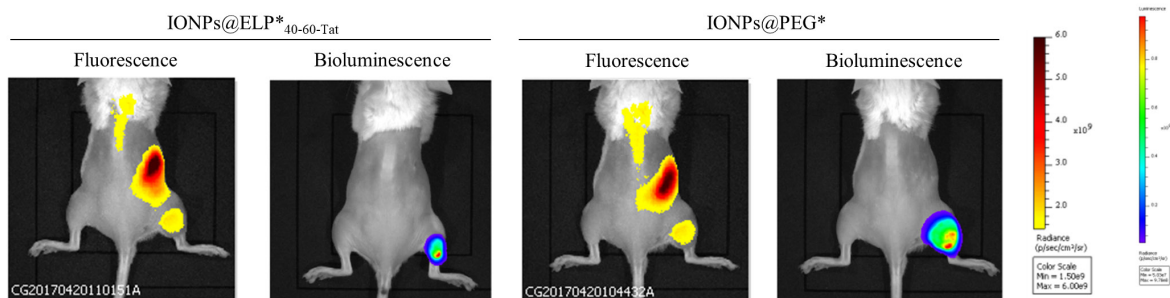


Figure 5 Signal de fluorescence des IONPs@ELP*_{40-60-Tat} et IONP@PEG* 30 min après administration intraveineuse, et signal en bioluminescence des tumeurs.

Des expériences *in vitro* et *in vivo* ont ensuite été menées avec les nanoparticules IONPs@PEG* et IONPs@ELP*_{40-60-Tat}. L'effet de la modification de surface sur les interactions avec les cellules et tumeurs a été évalué, en utilisant des cœurs identiques. Ces tests d'internalisation cellulaire ont été effectués eux-aussi sur des cellules à glioblastome. Une internalisation cellulaire supérieure des IONPs@ELP*_{40-60-Tat} comparé aux IONPs@PEG* a été observée, probablement grâce à l'effet pénétrant du groupement Tat. L'internalisation dans les lysosomes a été démontrée par microscopie électronique sur des microtomes, et par microscopie confocale sur cellules vivantes. La toxicité cellulaire après application d'hyperthermie magnétique a été attribuée à la rupture des lysosomes et à la fuite de leur contenu dans le cytosol. Cette observation valide l'utilisation de nanoparticules magnétiques pour des applications de délivrance de principes actifs. Une des grandes problématiques de la vectorisation de médicaments étant le piégeage des médicaments dans les compartiments d'internalisation cellulaire, l'application d'un champ magnétique couplé à des vecteurs magnétique peut permettre leur libération dans le cytosol. Une autre observation intéressante a été le partage des nanoparticules entre cellules filles lors de divisions cellulaires. Ainsi, les champs magnétiques peuvent être potentiellement appliqués successivement sur des durées supérieures au cycle de vie des cellules. Des expériences préliminaires *in vivo* ont montré l'effet positif du Tat comparé aux brosses de PEG sur la bio-distribution des nanoparticules, avec une accumulation plus importantes des IONPs@ELP*_{40-60-Tat} dans les tumeurs.

Pour conclure, des nanoparticules IONPs@ELP*_{40-60-Tat} ayant des propriétés magnétiques, thermosensibles, et de pénétration de cellules ont été synthétisées. D'autres systèmes ont aussi été synthétisés et étudiés, principalement en tant que « prototypes ». La mise en place de synthèses, de méthodes, et de moyens de caractérisations sur des systèmes moins précieux a permis ensuite de mener une étude complète sur les IONPs@ELP*_{40-60-Tat}. Les cœurs d'oxyde de fer synthétisés par polyol ayant les morphologies les mieux définies et les meilleures propriétés magnétiques ont été réservées pour greffer l'ELP*_{40-60-Tat}. La stratégie de greffage convergente a été optimisée sur des brosses de PEG* pour comprendre les différents régimes de densité de greffage et de conformation de chaîne, avant d'appliquer ces principes à l'ELP*_{40-60-Tat}. De cette manière, des nanoparticules hybrides IONPs@ELP*_{40-60-Tat} ont été synthétisées, avec des propriétés d'intérêt en tant qu'agents de contraste

pour l'IRM et des applications en hyperthermie magnétique, comme montré avec des essais *in vitro* et des essais préliminaires *in vivo*. La délivrance de principes actifs reste cependant à démontrer en conditions biologiques.

Remerciements

Les résultats obtenus lors de cette thèse sont le fruit d'un travail collaboratif, je souhaite remercier l'ensemble des personnes qui ont contribué à ce projet. Je remercie Pr. Sébastien Lecommandoux qui m'a accueilli dans son équipe Polymer Self-Assembly and Life Sciences au sein du Laboratoire de Chimie des Polymères Organiques (LCPO). J'ai été heureux de faire partie de cette équipe dynamique. J'y ai trouvé tous les moyens et ressources nécessaires pour faire une recherche de qualité. Les équipements, instruments, produits chimiques, locaux mis à disposition permettent de travailler dans de bonnes conditions. Je remercie également Dr. Olivier Sandre, mon directeur de thèse qui m'a engagé et m'a confié un sujet de recherche pendant trois ans. Tu m'as patiemment formé à la démarche scientifique et m'a permis de faire mes premiers pas en tant que chercheur. Tu m'as transmis ton goût pour la science, ta curiosité. Tu as toujours pris plaisir à partager ta grande culture scientifique et t'es rendu disponible en toutes circonstances pour m'aider, et cela naturellement. J'ai beaucoup apprécié que tu m'inclues dans les collaborations en France et à l'étranger auxquelles tu as participé. Cela m'a permis de découvrir de nombreuses applications des nanoparticules magnétiques. Tu m'as envoyé en congrès à Bordeaux, Paris, Saint-Malo, Montpellier, Mons, Bilbao, Kyoto, et Washington. J'ai pu rencontrer des communautés scientifiques, ce qui a été très bénéfique pour le projet. Je te remercie de ta confiance. Même si je ne continue pas dans la recherche académique, je garde un grand bout de cet héritage scientifique qui me sera extrêmement utile pour la suite. Je remercie Dr. Elisabeth Garanger, ma co-directrice de thèse pour sa participation dans ce projet. Tu es intervenue un peu plus tard lorsque j'ai commencé à avoir mes premiers résultats et plus de maturité sur mon sujet. Tu m'as permis de structurer mes idées, remettre en question des points clefs, et ajouter de la cohérence au projet. Tu m'as appris à communiquer plus efficacement et à valoriser intelligemment mes résultats. Ta présence et ton dynamisme ont apporté un souffle nouveau au milieu de ma thèse. Je remercie également Dr. Franck Couillaud, qui m'a accueilli à temps partiel pour ma dernière année de thèse dans son laboratoire de biologie. Grâce à toi, j'ai appris des quantités de choses en culture cellulaire et sur le cancer. J'ai adoré participer aux discussions de ton équipe aux pauses du matin et du midi, et découvrir de nouvelles facettes de la science en dehors de la chimie et physique. J'ai été très heureux que tu acceptes de faire partie de mon jury de thèse car tu as été à ta façon mon troisième encadrant. Je remercie également Pr. Bertrand Garbay pour toutes les discussions que l'on a eues ensemble. Tu donnes beaucoup de ton temps pour aider les autres autour de toi et faire en sorte que les jeunes chercheurs que nous sommes grandissent encore davantage. Merci d'avoir donné de ton temps, j'ai essayé d'apprendre le plus possible de nos échanges.

Je remercie le Ministère de l'Éducation Nationale et de la Recherche pour avoir financé ma thèse. Je suis profondément reconnaissant d'avoir pu bénéficier du système éducatif public français de mes 3 ans à mes 26 ans. De la primaire au collège, lycée, classe préparatoire, école d'ingénieur jusqu'à la thèse. De mon institutrice qui m'a appris à tenir un crayon pour écrire mes premières lettres jusqu'à

mes directeurs de thèse qui m'ont appris à être un chercheur. Je compte rendre à la société ce qu'elle a investi avec moi.

Je remercie Anthony Keyes qui a été un étudiant de stage talentueux et volontaire. Emmanuel Ibarboure pour les images de confocal de qualité qui ont fait d'excellentes illustrations. On a été l'un comme l'autre passionnés de voir des divisions cellulaires, des ruptures de lysosomes sous nos yeux. Anne-Laure Wirotius pour l'aide apportée pour interpréter des spectres RMN. Rosine Petittdemange pour m'avoir formé à la culture de bactéries. Dr. Eneko Garayo, Irati Rodrigo, Pr. Jose Angel Garcia, et Pr. Fernando Plazaola pour les mesures magnétiques sur les nanoparticules magnétiques, qui nous ont permis de connaître davantage les matériaux que j'ai synthétisés. Pr. Elizabeth Gillies, Dr. Bo Fan, Dr. John Trant, et Dr. Andrew Wong pour les collaborations fructueuses avec les polymères synthétiques thermosensibles. Dr. Sarah MacEwan et Pr. Ashutosh Chilkoti pour la collaboration avec les ELPs. Coralie Genevois et Pauline Jean-Jean qui se sont beaucoup investies sur la partie biologie du projet. Merci à Coralie de m'avoir patiemment formé à la culture cellulaire et Pauline pour les études *in vivo*. Sabrina Lacomme et Etienne Gontier pour leur investissement dans la préparation de grande qualité des échantillons pour la TEM. Boris Pedrono, Thomas Bayle, David Jacob pour toute leur aide sur l'appareil hyperthermie/DLS. Dr. Christophe Schatz et Dr. Jean-François Le Meins pour leurs expertises en DLS et physique des polymères qui ont été très utiles pour ce projet. Gérard Dimier et Cédric Le Coz pour leur aide en TGA. Loïc Petrault pour la gestion et approvisionnement des produits chimiques. Bernard de Jéso pour m'avoir formé à le RMN de paillasse. Claude le Pierres pour toute son aide et sa patience pour les ordres de mission. Corinne Goncalves de Carvalho, Catherine Roulinat, et Dominique Richard pour le soutien administratif.

Des remerciements plus personnels cette fois. Camille Geffroy t'as été superbe pendant ces trois ans, deux doctorants sous le même toit au 21 rue des 3 Conils. On s'est bien soutenu moralement, je te dois une grande partie des choses qui ont réussi pendant cette thèse. Tu as été géniale pendant les derniers mois de ma thèse pendant l'écriture du manuscrit et pendant la préparation de la défense. Hélène Meheust, tu sors vraiment du panier avec tes qualités. Si je devais trouver quelqu'un qui fait l'unanimité au laboratoire, ce serait toi. Merci à Louis Beauté et Ariane Peyret, les deux collègues proches du bureau. Vous avez donné du sens à l'expression « tout seul on va plus vite, à plusieurs on va plus loin ». Vous avez été ma force motrice pendant ces trois années. J'ai beaucoup appris de ton sens du relationnel Louis, de ton intelligence sociale, de ton attitude positive. Ariane, je me suis découvert un sens de la compétition stimulé par tes grandes ambitions. Lorsque l'on a réussi tous les deux à transformer les frictions inévitables en quelque chose de positif ça nous a tou deux tirés vers le haut. Je crois que ta thèse et la mienne n'auraient jamais été les mêmes si l'on ne s'était pas mutuellement poussé en dehors de nos zones de confort. Julien Rosselgong (oui j'écris les noms de famille pour m'en souvenir dans 10 ans), tu es juste quelqu'un de formidable, merci encore d'avoir pris le temps de lire ma thèse et de l'avoir corrigé lorsque je me sentais un peu délaissé. Je vais me

souvenir pendant longtemps des discussions philosophiques aux fermetures de bars et de tes conseils sur La Vie. Cony Gauche, tu m'as manqué quand tu es partie au Brésil, j'aimais beaucoup passer du temps avec toi et Medhi Neqal quand on était tous les trois dans la même équipe. Merci à tous les autres copains pour les bons moments passés ensemble : Michèle Dai, Guillaume Goudounet, Martin Fauquignon, Vangelis Georgilis, Ye Xiao, Coralie Lebleu, Laura Rodrigues, Gaëlle Le Fer, Monica Bravo Anaya. Camille Bakkali-Hassani, Quentin Sobczak, Julien Bosson, Sofiem Garmendia, Arthur Werner, Geoffrey Hibert, Alex Rakotoveloa, Florian Le Goupil, Anna Hofmann, Dounia Arcens, Martin Camus, Boris Bizet, Pierre-Luc Durand, Léa Bonnot, Pierre Berto, Quentin Passet, Etienne Savonnet, Ségolène Antoine, Cindy Gomes Correia, Fiona Magliozzi, Konstantinos Kallitsis.

Enfin, je remercie mes parents Marie-Claude et Bertrand, qui m'ont toujours poussé à donner le meilleur. Vous avez su encourager mes passions et aspirations, et avez soutenu mes choix. Merci à ma sœur Mélodie pour son soutien et son sens de l'attention, et à mes grands-parents Mado, Michel, Paulette pour leur bienveillance.

TABLE OF CONTENTS

<u>General introduction</u>	1
<u>List of abbreviations</u>	7
<u>Chapter I: Bibliography</u>	11
<u>1. Introduction on nanomedicine</u>	13
<u>2. Synthesis of iron oxide nanoparticles</u>	14
<u>2.1. Main characteristics of iron oxide nanoparticles</u>	14
<u>2.2. Co-precipitation method</u>	17
<u>2.3. Nano-template methods</u>	18
<u>2.4. Hydrothermal method</u>	19
<u>2.5. Thermal decomposition method</u>	20
<u>2.6. Polyol method</u>	22
<u>2.7. Combustion methods</u>	24
<u>2.8. Conclusion on the synthesis of iron oxide nanoparticles</u>	24
<u>3. Applications of iron oxide nanoparticles in nanomedicine</u>	25
<u>3.1. MRI contrast agents</u>	25
<u>3.2. Magnetic hyperthermia agents</u>	28
<u>3.3. Drug delivery systems</u>	30
<u>4. Review of anchoring groups used for the surface modification of iron oxide nanoparticles</u>	32
<u>4.1. Catechols</u>	33
<u>4.2. Carboxylic acids</u>	33
<u>4.3. Silanes</u>	34
<u>4.4. Phosphonic acids</u>	36
<u>5. Considerations for the surface modification of iron oxide nanoparticles with polymers</u>	37
<u>5.1. Grafting to versus grafting from strategies</u>	37
<u>5.2. Commonly used heterofunctional linkers</u>	37

5.3.	<u>Surface modification with polymers for biological applications</u>	39
5.4.	<u>Brush theory: flat surface</u>	39
5.5.	<u>Brush theory: curvature effect</u>	41
6.	<u>Brief overview of thermosensitive polymers</u>	42
6.1.	<u>Thermosensitive synthetic polymers</u>	42
6.2.	<u>Thermosensitive elastin-like polypeptides</u>	44
7.	<u>Nanoparticles in biological media</u>	48
7.1.	<u>Improving the stability of nanomedicines in physiological conditions</u>	48
7.2.	<u>Targeting solid tumors and metastasis</u>	49
7.3.	<u>Understanding the mechanism of cell uptake</u>	50
8.	<u>References</u>	53

Chapter II: Exploration of chemical routes toward iron oxide nanoparticles of different sizes, morphologies, and magnetic properties..... 63

1.	<u>Introduction</u>	65
2.	<u>Synthesis by co-precipitation</u>	65
2.1.	<u>Experimental section</u>	66
2.1.1.	<u>Materials</u>	66
2.1.2.	<u>Synthesis of IONPs by co-precipitation</u>	66
2.1.3.	<u>Size grading by magnetic sedimentation</u>	67
2.2.	<u>Results and discussion</u>	67
2.2.1.	<u>Synthesis</u>	67
2.2.2.	<u>Size-grading</u>	68
2.2.3.	<u>Morphologies of the iron oxide nanocrystals</u>	69
3.	<u>Polyol synthesis</u>	70
3.1.	<u>Experimental section</u>	71
3.1.1.	<u>Materials</u>	71
3.1.2.	<u>Synthesis of IONPs</u>	71
3.1.3.	<u>Sample nomenclature</u>	72

3.1.4.	<u>Transmission Electron Microscopy (TEM)</u>	73
3.1.5.	<u>Dynamic Light Scattering (DLS) and Zetametry</u>	73
3.1.6.	<u>Proton relaxometry</u>	73
3.1.7.	<u>Magnetic fluid hyperthermia</u>	74
3.1.8.	<u>Static (DC) magnetization</u>	74
3.1.9.	<u>Zero field cooling – field cooling (ZFC-FC) magnetometry</u>	74
3.1.10.	<u>Equivalent iron titration in IONP suspensions</u>	75
3.2.	<u>Results and discussion</u>	75
3.2.1.	<u>Influence of the conditions of reaction over the morphology of iron oxide nanoparticles</u> 75	
3.2.2.	<u>Colloidal stability and heating properties</u>	82
3.2.3.	<u>In-depth investigation of the heating properties</u>	85
3.2.4.	<u>Study of the magnetization properties</u>	88
3.2.5.	<u>Iron oxide nanoparticles as MRI contrast agents</u>	91
4.	<u>Conclusion</u>	93
5.	<u>References</u>	95
 <u>Chapter III: Surface functionalisation of iron oxide nanoparticles</u>		99
1.	<u>Introduction</u>	101
2.	<u>Direct adsorption of polyions</u>	102
2.1.	<u>Adsorption of poly(acrylic acid)</u>	102
2.1.1.	<u>Materials and methods</u>	102
2.1.2.	<u>Results and discussion</u>	102
2.2.	<u>Adsorption of Rhodamine123-modified poly(acrylic acid)</u>	103
2.2.1.	<u>Materials and methods</u>	103
2.2.2.	<u>Results and discussion</u>	104
3.	<u>Divergent synthesis or “grafting from”</u>	105
3.1.	<u>Grafting of PDMAEMA</u>	106
3.1.1.	<u>Materials and methods</u>	106

3.1.2.	<u>Results and discussions</u>	107
3.2.	<u>Grafting of a thermosensitive elastin-like polypeptide</u>	111
3.2.1.	<u>Materials and methods</u>	111
3.2.2.	<u>Results and discussion</u>	112
4.	<u>Convergent synthesis or “grafting to”</u>	115
4.1.	<u>Grafting of poly(ethylene glycol) and a fluorescent dye onto iron oxide nanoparticles</u>	116
4.1.1.	<u>Materials and methods</u>	116
4.1.2.	<u>Results and discussion</u>	117
4.2.	<u>Grafting of a thermosensitive diblock elastin-like polypeptide</u>	123
4.2.1.	<u>Materials and methods</u>	123
4.2.2.	<u>Results and discussion</u>	124
5.	<u>Conclusion</u>	129
6.	<u>References</u>	131

Chapter IV: A unique set-up to measure in real time the thermosensitive properties of nano-objects under magnetic hyperthermia

1.	<u>Introduction</u>	135
2.	<u>Materials and methods</u>	136
2.1.	<u>Presentation of magnetic hyperthermia coupled with DLS set-up</u>	136
2.2.	<u>Proton relaxometry</u>	137
2.3.	<u>TEM measurements</u>	139
2.4.	<u>Transition Temperature Measurement</u>	139
3.	<u>Magnetic and thermo-sensitive magnetic micelles</u>	139
3.1.	<u>Materials and methods</u>	139
3.2.	<u>Results and discussion</u>	140
4.	<u>Magnetic and thermo-sensitive nanorattles</u>	143
5.	<u>Magnetic and thermo-sensitive microgels</u>	145
6.	<u>Iron oxide nanoparticles grafted with PDMAEMA</u>	147
7.	<u>Iron oxide nanoparticles grafted with a single block (VPGIG)₂₀ elastin-like polypeptide</u>	155

8.	<u>Iron oxide nanoparticles grafted with diblock ELPs</u>	157
9.	<u>Study of iron oxide nanoparticles grafted with a diblock ELP as drug delivery agents</u>	164
9.1.	<u>Materials and methods</u>	164
9.2.	<u>Results and discussion</u>	165
10.	<u>Conclusion</u>	167
11.	<u>References</u>	169

Chapter V: Glioblastoma cell death induced by magnetic hyperthermia: monocoresh vs. multicore nanoparticles..... 173

1.	<u>Introduction</u>	175
2.	<u>Materials and methods</u>	176
2.1.	<u>Surface modification of monocoresh and multicore iron oxide nanoparticles</u>	176
2.2.	<u>Cell line generation and culture</u>	177
2.3.	<u>Incubation of cells with iron oxide nanoparticles</u>	177
2.4.	<u>Laser scanning confocal microscopy</u>	177
2.5.	<u>Flow cytometry</u>	178
2.6.	<u>Fluorescence and bioluminescence imaging</u>	178
2.7.	<u>Transmission electron microscopy</u>	178
2.8.	<u>Magnetic hyperthermia</u>	179
3.	<u>Results and discussion</u>	179
3.1.	<u>Monocoresh and multicore nanoparticles modified with a brush of poly(ethylene glycol) and a fluorescent probe</u>	179
3.2.	<u>Interaction of nanoparticles with U87 glioblastoma cancer cells</u>	181
3.2.1.	<u>Observation of nanoparticles-cells interactions by fluorescence imaging</u>	181
3.2.2.	<u>Observation of nanoparticles-cells interactions by bright field microscopy and flow cytometry</u>	182
3.2.3.	<u>Observation of nanoparticles-cells interactions by confocal microscopy</u>	184
3.2.4.	<u>Observation of nanoparticles-cells interactions by transmission electron microscopy</u>	186
3.3.	<u>Effect of magnetic hyperthermia over the cells' viabilities</u>	189
4.	<u>Conclusion</u>	191

5. <u>References</u>	192
----------------------------	-----

Chapter VI: Magnetic iron oxide nanoparticles grafted with a thermosensitive elastin-like polypeptide and a cell penetrating peptide : an *in vitro* and *in vivo* study..... 195

1. <u>Introduction</u>	197
------------------------------	-----

2. <u>Materials and methods</u>	198
---------------------------------------	-----

2.1. <u>IONP synthesis</u>	198
----------------------------------	-----

2.2. <u>Transmission electron microscopy on nanoparticles</u>	199
---	-----

2.3. <u>Dynamic light scattering</u>	199
--	-----

2.4. <u>TGA</u>	200
-----------------------	-----

2.5. <u>ATR-IR</u>	200
--------------------------	-----

2.6. <u>Cell line generation and culture</u>	200
--	-----

2.7. <u>Incubation of cells with IONPs</u>	200
--	-----

2.8. <u>Laser scanning confocal microscopy (LSCM)</u>	200
---	-----

2.9. <u>Fluorescence and bioluminescence imaging</u>	201
--	-----

2.10. <u>Transmission electron microscopy on cells</u>	201
--	-----

2.11. <u>Magnetic hyperthermia (MH)</u>	201
---	-----

3. <u>Results and discussion</u>	202
--	-----

3.1. <u>Synthesis strategy of the thermosensitive, cell-penetrating, fluorescent and magnetic nanoparticles</u>	202
---	-----

3.2. <u>Nanoparticles interactions with U87 glioblastoma cells</u>	205
--	-----

3.3. <u>Effect of magnetic hyperthermia on cells</u>	209
--	-----

3.4. <u>Biodistribution of intravenously administered nanoparticles in mice</u>	212
---	-----

3.5. <u>Treatment by intravenous (systemic) administration</u>	216
--	-----

3.6. <u>Treatment by intra-tumoral administration</u>	219
---	-----

4. <u>Conclusion</u>	222
----------------------------	-----

5. <u>References</u>	224
----------------------------	-----

<u>Conclusion and prospects</u>	227
---------------------------------------	-----

GENERAL INTRODUCTION

Nanomedicine is the medical application of nanotechnology. Alternatively, a nanomedicine designates a medicine (a drug) that is encapsulated within a nanocarrier, also called nanovector when exhibiting specific targeting properties. Nanoparticles used for this application have by definition at least one dimension in the range of 1 to 100 nanometers, which allows them to circulate in the body and cross biological membranes. A significant attention given to nanoparticles dedicated to the diagnosis and treatment of cancer led to the development of locally or systemically injectable dispersions of multimodal nano-objects to probe, sense, or treat cancer cells. A wide variety of nanocarriers were developed, based on liposomes, polymers, micelles, nanoparticles, and antibodies. These were designed with the aim of bringing functionalities such as cancer targeting capabilities, bioimaging properties (*e.g.* by MRI), and drug delivery properties. The delivery of therapeutic agents can be achieved by active means, with for instance nanomaterials responsive toward internal or external triggers. The drug delivery by “smart” materials is expected to achieve a better targeting effect toward cancer cell with a local liberation where the therapeutic agents are needed. This would allow overcoming current problematics such as the bio-distribution and pharmacokinetics of hydrophobic, thus poorly soluble, anti-cancerous drug. This shall permit an increased efficacy of treatments as well as the reduction of the dose and hence of secondary effects. The use of magnetic drug delivery systems presents several benefits, by allowing the triggered release of a drug by external application of a magnetic field, able to penetrate deep into tissues compared to light or ultrasound actuation for example. The chemotherapy can be coupled with a magnetic hyperthermia therapy in a synergistic manner when the elevation of temperature is significant to sensitize the tumor cells to a chemo- or radiotherapy, or to trigger the thermal transition of the carrier. Iron oxide nanoparticles (IONPs) are good candidates for this application as they are biocompatible, biodegradable, and present contrasting properties for MR imaging. The morphologies of iron oxide nanocrystals can be optimized by adjusting synthesis conditions. This potentially leads to hyperthermia agents demonstrating large specific absorption rates, meaning that they convert efficiently the electromagnetic energy into thermal energy at the tumor location.

This doctoral project was dedicated to bring new advancements to iron oxide based nanomedicine. The main objective of this project was to synthesize drug delivery platforms that have both magnetic and thermosensitive capabilities, applied to the field of cancer diagnosis and treatment. IONPs presenting strong heating properties under application of an external alternating magnetic field were synthesized. As in the field of nanotechnology the control over the morphologies dictates the properties of the materials, an efficient route had to be employed to prepare the IONPs. Another criterion was the amount of IONPs produced by individual batches. Synthesis at gram-scale was needed for both physics characterization and *in vitro/in vivo* investigations, which demand significant amounts of material for preclinical studies that have to be repeated on several animals. At the

beginning of this project, we have used the water-based co-precipitation route that led to ~100 g of IONPs. These IONPs however exhibited very broad size distributions. A multi-step size-grading method was applied post-synthesis, leading to a non-satisfying improvement on the quality of the samples. We therefore decided to explore another synthesis pathway which led to lower quantities than the co-precipitation method, but allowed obtaining better defined nanoparticle morphologies. IONPs were produced with the aim of obtaining good control over their morphologies, size-distributions, crystallinity, heating properties under application of magnetic hyperthermia. Selecting conditions of polyol synthesis such as solvents and amounts of water added led to a control over the nucleation and growth of iron oxide nanocrystals. The size of the nanocrystals could be tuned from 4 nm up to 37 nm, with a low standard deviation and either monocoreshell or multicore morphologies. Their properties as MRI contrast agents were assessed and compared, to possibly lead to theranostic agents that could be employed both for the diagnostic by MR imaging and treatment of cancer by magnetic hyperthermia. The stability of the nanoparticles dispersed in solution was evaluated, both in pH buffers and in a cell culture medium, as it strongly influences their properties. Every effort was made to obtain nanocrystal surfaces free of organic molecules and fully available for subsequent surface modification.

Different anchor groups were tested for surface modifications, such as carboxylic acids, silanes, and phosphonic acids. They allowed grafting molecules of interest at the surface of IONPs, by bridging the gap between the inorganic core and the organic shell. Different molecules and macromolecules were grafted, such as fluorescent probes (rhodamine, DY700), a thermosensitive polymer poly(dimethylaminoethyl methacrylate) (PDMAEMA), a stealth polymer poly(ethylene glycol) (PEG), and thermosensitive elastin-like polypeptides (ELPs) fused with a cell-penetrating peptide (CPP) Tat. Two types of bioconjugation strategies of the IONPs with the organic shells were tried out: the divergent and the convergent grafting approaches. The divergent strategy was used in the first steps of the project, when developing surface modifications with silanes. Due to their propensity to self-polymerize and form oligomers, it was not possible to perform chemical modifications using silane anchor groups before final bioconjugation with the IONPs. The silane terminated anchor groups had to be grafted first on the IONPs, and the final shell was constructed by successive covalent assembly of heterofunctional linkers and macromolecules. Switching to relatively chemically inert phosphonate anchor groups led to the possibility of using a convergent strategy, with a chemical modification of fluorescent probes, polymers and polypeptides beforehand, in a step prior their bioconjugation with IONPs. This made possible the characterization of the chemically modified (macro)molecules by classical methods such as TLC, mass-spectrometry, NMR, and IR spectroscopies. The bioconjugation of the (macro)molecules with the IONPs was finally carried in a single step, in mild conditions of reaction, leading to readily stable dispersions of nanoparticles. The newly formed hybrid core-shell structures presented new properties: magnetism due to their iron oxide

core, and thermosensitive, cell-penetrating, stealth, fluorescent properties depending on the surface modification selected. This led to the equivalent of Swiss-knives multi-potent nano-objects for medical applications.

The magnetic and thermosensitive properties were assessed using an in-house set-up, coupling a dynamic light-scattering (DLS) apparatus with magnetic hyperthermia. This novel and unique set-up allowed measuring simultaneously the temperature of the solutions dispersing the nanoparticles using an optical fiber probe, and measuring the hydrodynamic diameter of the nano-objects using DLS in backscattered light mode (165° angle). This instrumentation was used to assess the magnetic and thermosensitive properties of IONPs grafted with PDMAEMA first, and then with ELPs. Various potential drug delivery systems obtained through different collaborations with other laboratories were also characterized using this combined DLS-magnetic hyperthermia set-up. Thermosensitive “self-immolative” poly(ethylene oxide)-*block*-poly(ethyl glyoxylate)-*block*-poly(ethylene oxide) (PEG5k-PEtG50k-PEG5k) copolymers received from the research group of Elizabeth R. Gillies (Western University, Department of Chemistry, London, Canada) were mixed with surfactant-coated IONPs by a nanoprecipitation process to produce magnetic micelles responsive to magnetic hyperthermia. Magnetic and thermosensitive hollow capsules of silica-containing iron oxide covered by a layer of poly(*N*-isopropylacrylamide) (PNIPAM) were received from the team of Markus Gallei (Technische Universität Darmstadt, Ernst-Berl-Institute for Chemical Engineering and Macromolecular Science, Darmstadt, Germany). They proved to be thermoresponsive under magnetic hyperthermia by undergoing large variations of diameter. Thermosensitive microgels obtained by precipitation copolymerization of oligo(ethylene glycol) methyl ether methacrylate, di(ethylene glycol) methyl ether methacrylate, oligo(ethylene glycol)diacrylate and methacrylic acid loaded with IONPs were received from the team of Pr. Laurent Billon (Université de Pau et des Pays de L'Adour, Equipe de Physique et Chimie des Polymères, Pau, France). These magnetic microgels underwent large variations of volume under magnetic hyperthermia. These collaborations allowed studying the properties of different designs with magnetic and thermosensitive properties: micelles, capsules, microgels. These systems illustrate the large variety of strategies that are currently developed for drug delivery applications.

The doctoral project that was oriented toward inorganic chemistry, surface chemistry, physical characterization and instrumentation later took a turn toward medical applications of the newly designed systems. IONPs grafted with PEG for stealth purposes and a DY700 probe for tracking of the nanoparticles were produced. The monocoresh and multicore morphologies of the iron oxide cores were tested *in vitro* conditions to compare their cytotoxic effect on cancerous glioblastoma cells after application of magnetic hyperthermia treatment. This study was performed in the group of Franck Couillaud (Imagerie moléculaire et thérapies innovantes en oncologie (IMOTION), Bordeaux, France). A strong emphasis was placed on deciphering the internalization pathway of the nanoparticles inside the cells. Comparing results obtained by flow cytometry, transmission electron microscopy

(TEM), laser scanning confocal microscopy (LSCM), fluorescence and bioluminescence imaging allowed to gain core insight on the fate of internalized IONPs. A macropinocytosis internalization pathway was evidenced by observing the deformations of cells' membranes by TEM on cell microtomes, and the nanoparticles were shown to end-up inside lysosomes. The preparation of the TEM samples was performed by Sabrina Lacomme and Etienne Gontier (Bordeaux Imaging Center, Bordeaux, France) within a frame of collaboration with them. The influences of core morphologies, doses administrated during incubation, and effect of magnetic hyperthermia treatment on the cell viability were compared and quantified. The best efficacies were obtained with multicore morphologies, independent on the range of doses explored, with cytotoxic effects leading to decreases of up to 90 % of cell viability.

Following the study of IONPs core morphologies effect on internalization of nanoparticles and cytotoxicity, the surface modification effect was examined. The surface of monocoresh IONPs was modified with a diblock ELP_{40-60-Tat} providing both thermosensitive and cell-penetrating properties. The superior internalization of the ELP_{40-60-Tat} modified nanoparticles compared to a more classical PEG surface modification was demonstrated. The internalization pathway in lysosomes was described both by TEM and confocal imaging on cells. The nanoparticles were shown to liberate the content of the lysosomes under magnetic hyperthermia, by rupture of their membranes. The fate of the IONPs in cells from their internalization to the application of the treatment illustrated the strong advantage of magnetic nanoparticles for drug delivery applications, as they were able to liberate the content trapped inside lysosomes using an external trigger. Interestingly, we could image cellular division where the lysosomes and nanoparticles were equally shared and passed along among daughter cells. This allows the potential treatment of several generations and/or successive application of magnetic hyperthermia on time scales superior to the cells' life cycles. The biodistributions of nanoparticles modified with PEG or ELP_{40-60-Tat} was studied by intravenous administration in mice bearing a subcutaneous xenograft model of a brain tumor. The IONPs which surface was modified with ELP_{40-60-Tat} proved to accumulate more in tumors compared to PEG, with a larger cell internalization attributed to the Tat cell-penetrating peptide. As it is a major challenge in the drug delivery field, the fraction of administered dose effectively reaching the tumors was shown however to be insufficient to lead to a significant reduction in tumor activity by application of magnetic hyperthermia treatment. A local administration by intratumoral injection led to a greater accumulation of nanoparticles in the area to treat. A larger effect on tumor activity was evidenced, more pronounced in the case of ELP_{40-60-Tat} modified nanoparticles.

The content of the thesis is described in detail in the following six chapters, starting with an overview of literature. This allows the reader to understand the context of the research and to discern the novelties of the hybrid core/shell inorganic/organic nanoparticles synthesized and their associated properties. An in-detail description of the synthesis of IONPs derives from a review on fundamental

and advances in magnetic hyperthermia that was written at the beginning of this thesis. The overview of literature is followed by five chapters reporting materials, methods, experimental results and discussions on the issues listed beforehand. The majority of the content of experimental chapters was adapted from five articles published or submitted, hence the choice of presentation. This summary of three years' of data was non-chronologically divided in five parts for better clarity. The experimental chapters are ordered to present *i)* the chemical routes towards iron oxide nanoparticles of different sizes and morphologies, *ii)* the surface functionalization of iron oxide nanoparticles, *iii)* the magnetic and thermosensitive properties of drug delivery systems, *iv)* *in vitro* internalization of monocoresh and multicore IONPs modified with PEG in glioblastoma cancerous cells and their cytotoxic effect under magnetic hyperthermia treatment, *v)* and finally *in vitro* and *in vivo* internalization of IOPNs grafted with ELP_{40-60-Tat} in glioblastoma cancerous cells and tumors, and their cytotoxic effect under magnetic hyperthermia treatment.

LIST OF ABBREVIATIONS

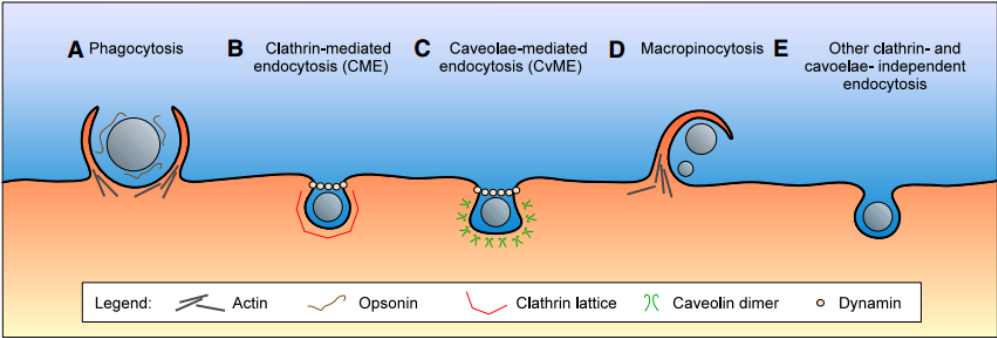
Σ	Reduced tethered density
τ	Delay time
θ_F	Angle of the polarization of light
A	Area of hysteresis loop
AC	Alternative current
AMF	Alternating magnetic field
APMS	3-aminopropyl-methylsiloxane
APTS	3-aminopropyl-triethoxysilane
AEAPTMS	3-(2-aminoethylamino)propyltrimethoxysilane
AEP	2-aminoethylphosphonic acid
AZ	Azidoacetic acid
ATCC	American Tissue Culture Collection
ATRP	Atom transfer radical polymerization
ATR-IR	Attenuated total reflection infrared
B_0	Static magnetic field
B_1	Transverse magnetic field
BSA	Bovine serum albumin
BLI	Bioluminescence imaging
χ	Magnetic susceptibility
CMT	Critical micellar temperature
CMV	Cytomegalovirus
CPP	Cell penetrating peptide
CPMG	Car-Purcell-Meiboom-Gill
CuAAC	Copper assisted azide-alkyne cycloaddition
Cryo-TEM	Cryogenic transmission electron microscopy
CTAB	Cetyltrimethylammonium
DC	Direct current
DCM	Dichloromethane
DEG	Diethylene glycol
DLS	Dynamic light scattering
DMSO	Dimethyl sulfoxide
DIPEA	Diisopropylethylamine
DMF	Dimethyl formamide
EDTA	Ethylenediaminetetraacetic acid
EDC	<i>N</i> -(3-dimethylaminopropyl)- <i>N'</i> -ethylcarbodiimide hydrochloride
EG	Ethylene glycol
ELP	Elastin-Like polypeptide
EPR	Enhanced permeability and retention
f	Frequency
FACS	Fluorescence-activated cell sorting
FBS	Fetal bovine serum
FUS	Focused ultrasound surgery
FRI	Fluorescence reflectance imaging
FC	Field-cooled
FDA	Food and drug administration
FWR	Feed weight ratio

GMBS	<i>N</i> - γ -maleimidobutyryl-oxysuccinimide ester
HEPES	4-(2-hydroxyethyl)-1-piperazineethanesulfonic acid
H_{an}	Anisotropy of magnetic field
H_{app}	Magnetic field applied
HIV	Human immunodeficiency virus
HPLC	High-performance liquid chromatography
IEP	Isoelectric point
ICP-MS	Inductively coupled plasma mass spectrometry
ILP	Intrinsic loss power
IONP	Iron Oxide Nanoparticle
IR	Infrared
IPTG	Isopropyl b-D-1-thiogalactopyranoside
ITC	Inverse transition cycling
k_a	Acid dissociation constant
LCST	Lower critical solution temperature
LSCM	Laser Scanning Confocal Microscopy
M_d	Specific magnetization per magnetic domain
MH	Magnetic Hyperthermia
MES	2-(<i>N</i> -morpholino)ethanesulfonic acid
MNP	Magnetic nanoparticles
MPI	Magnetic particle imaging
M_r	Remnant magnetization
MRI	Magnetic Resonance Imaging
M_{xy}	Transverse magnetization
M_z	Longitudinal magnetization
MTT	3-(4,5-dimethylthiazol-2-yl)-2,5-diphenyltetrazolium bromide
NHS	<i>N</i> -hydroxysuccinimide
NMDEA	<i>N</i> -methyldiethanolamine
NMR	Nuclear Magnetic Resonance
NIR	Near infrared
NP	Nanoparticle
PB	Phosphate buffer
PAA	Poly(acrylic acid)
PDEAAm	Poly(<i>N,N'</i> -diethylacrylamide)
PDI	Polydispersity index
PDMAEMA	Poly(dimethylaminoethyl methacrylate)
PEI	Polyethyleneimine
PEtG	Poly(ethyl glyoxylate)
PDMS	Poly(dimethylsiloxane)
PEG	Poly(ethylene glycol)
PG	1,2-propylene glycol
PNIPAM	Poly(<i>N</i> -isopropylacrylamide)
OD	Optical density
pH(I)	pH at the isoelectric point
POxa	Poly(oxazoline)
PVA	Poly(vinyl alcohol)
PVP	Polyvinylpyrrolidone
pKa	Logarithmic acid dissociation constant

RD	Recycling delay
RF	Radiofrequency
r_1	Longitudinal relaxivity index
r_2	Transverse relaxivity index
ROS	Reactive oxygen species
RAFT	Reversible addition-fragmentation chain transfer
rpm	Rotations per minute
R_g	Radius of gyration
ROI	Region of interest
SAM	Self-assembled monolayer
SAR	Specific absorption rate
SANS	Small angle neutron scattering
SDS-PAGE	Sodium dodecyl sulfate polyacrylamide gel electrophoresis
SEC	Size exclusion chromatography
SPM	Superparamagnetic
T_1	Longitudinal relaxation time
T_2	Transverse relaxation time
Tat	Trans-activator of transcription
TCEP	tris(2-carboxyethyl)phosphine
TE	Echo time
TEM	Transmission Electron Microscopy
TETA	Triethylene tetramine
TGA	Thermogravimetric analysis
THF	Tetrahydrofuran
Tris	Tris(hydroxymethyl)aminomethane
TLC	Thin layer chromatography
TMAOH	Tetramethylammonium hydroxide
UCST	Upper critical solution temperature
UUSPIO	Ultra-ultra-small superparamagnetic iron oxide nanoparticles
VSM	Vibrating sample magnetometer
WHO	World health organization
ZFC	Zero-field-cooled

CHAPTER I

BIBLIOGRAPHY



1. Introduction on nanomedicine

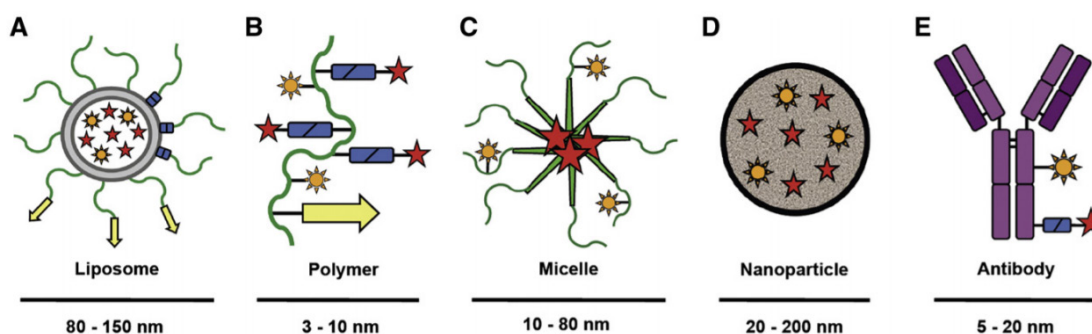


Figure 1 Systems and strategies used for drug targeting to tumors. A–E: Drug targeting systems. Liposomes and liposomal bilayers are depicted in gray, polymers and polymer-coatings in green, linkers allowing for drug release and for sheddable stealth coatings in blue (rectangles), targeting ligands in yellow (arrows), antibodies and antibody fragment in purple, imaging agents to monitor biodistribution and target site accumulation in orange (suns), and conjugated or entrapped (chemo-) therapeutic agents in red (stars).[1]

Nanotechnology dedicated to the field of health-care led to the emergence of another discipline called nanomedicine at the beginning of the 21st century.[2] It is a large industry, with sales reaching up to \$43.2 billion in 2010 and with a compound annual growth rate of 14.1%.[3] This high market progression and value can be explained by the polyvalence of nanomedicine, which finds applications in multiple stages of health care, from diagnostics to therapy. The objects described in nanomedicine have by definition a size between 1 and 100 nm, so approximately from the size of a protein to the size of a pore of a cell, enabling them to progress in living tissues.[4, 5] A significant effort of research and development from academy and industry is put toward cancer diagnosis and treatment, as it is the second cause of death in Europe and North-America, after cardiovascular diseases. According to the World Health Organization (WHO), the United Nations public health arm, 8.2 million people worldwide died from cancer in 2012, and 30% of cancers could be prevented. *GLOBOCAN 2012: estimated cancer incidence, mortality and prevalence worldwide in 2012* is a study carried out by the WHO; it shows that the strongest cancer incidences are in Australia, New-Zealand, Northern America and Europe, and that men are significantly more prone to cancer than women. The products aimed to treat cancer represent 45% of the products in clinical development. Different systems and strategies have been developed for drug targeting to tumors (**Figure 1**). These systems can be tentatively sorted into five categories: liposomes, polymers, micelles, nanoparticles, and antibodies.[1] Major pharmaceutical groups have a strong interest toward nanomedicine and dedicate significant efforts in drug delivery systems to target specific areas in the body and to reduce cytotoxic side effects of the treatments. This interest concerns AstraZeneca, Cytimmune, Bind Therapeutics AMGEN, and Pfizer among others, which understood that nanodelivery could be a way to use previous powerful cancer treatment candidates that have not obtained approval because of their non-specific toxicity and strong side effects.[6] Governmental and extra-governmental organizations try to unite research and forerunner industrial efforts to the field of nanotechnology for health. A

Nanomedicine European Technology platform regrouping experts and industrials has been created in 2005 and approved by the European Commission. In the USA the American Society for Nanomedicine is a professional, academic and medical society dedicated to advancing research in nanomedicine. In France, the French Society for Nanomedicine was created in 2014, in continuation to the “Groupe Thématique de Recherche sur la Vectorisation” founded by Pr. Patrick Couvreur in 1986. These organizations aim to establish a clear strategic vision, to decrease the fragmentation in nano-medical research, help public and private funding and boost innovation.

This thesis is devoted to the development of drug nano-carriers that have both thermosensitive and magnetic properties, allowing a release of the drug under magnetic hyperthermia (MH). Iron oxide nanoparticles (IONPs) are prominent candidates for this application as they combine diagnostic and therapeutic properties. Their applications as drug-carriers,[7] contrast agents for magnetic resonance imaging (MRI),[7] and/or magnetic heating agents [8] have already been demonstrated.

2. Synthesis of iron oxide nanoparticles

The choice of the magnetic material to be employed in MH is virtually infinite since, in principle, every magnetic compound can be synthesized under nanoparticulate form by chemical or physical procedures. However, a set of factors has to be taken into account for accomplishing safety requirements, especially biocompatibility. In this sense, iron oxides feature as the most attractive candidates and are reviewed in details thereafter.

2.1. Main characteristics of iron oxide nanoparticles

Iron is the fourth most common element in the Earth's crust, existing in oxidation states from -2 to +6 with common oxidation states of +2 and +3. Ochre composed of antiferromagnetic iron oxo-hydroxide magnetic nanoparticles (MNPs) (acicular haematite nano-spindles, goethite nano-laths, wüstite nanospheres) have been used as natural pigment since early ages of mankind, and thus can be considered as the forerunners of manufactured and environmental MNPs.[9] Iron oxide-based MNPs combine several physicochemical aspects leading to attractive properties. These MNPs typically have two or three dimensions under 100 nm, which provides a high surface-to-volume ratio and leads to different properties than those of bulk iron oxide materials. Human metabolism maintains the homeostasis of iron, controlling this necessary (but potentially toxic in excess) element. The human body is able to tolerate the oral administration of iron at 5 mg per kg of body mass,[10] well below the limit of acute toxicity in the range of 300-600 mg per kg of body mass as determined on Wistar rats with FeSO_4 as the source of iron.[11] This “iron pool” of the organism consists of both molecular iron ions (hemoglobin) and in nanoparticulate forms (ferritin), as a protein capsid encapsulating an antiferromagnetic ferrihydrite core. This unique biocompatibility feature, along with their magnetic properties, make IONPs excellent candidates for biomedical applications such as contrast agents for

MRI, cell labeling, magnetic separation, drug delivery assisted by direct current (DC) or alternative current (AC) magnetic fields or magnetic heating mediators.[12] The following discussion will be mainly focused on MH in this section, and the materials reviewed will mostly consist in either pure iron oxides or ferrites of the general formula MFe_2O_4 where M stands for another transition metal, or two different metals in the case of either mixed ferrites $(M,M')Fe_2O_4$ or core-shells $MFe_2O_4@M'Fe_2O_4$ (core@shell).

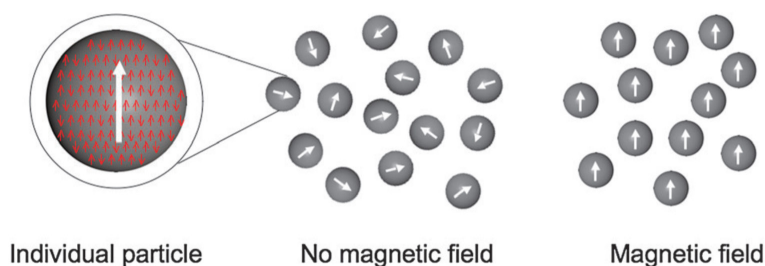


Figure 2 Schematic representation of a superparamagnetic particle. Note that although the moments within each particle are ordered (red arrows), the net magnetic moment of a system containing MNPs will be zero in the zero field and at high enough temperatures. In the presence of a field, there will be a net statistical alignment of magnetic moments, magnetization being defined as the volumic concentration of oriented moments.[13]

Frenkel and Dorfman were the first to predict in 1930 that a particle of a ferromagnetic material below a critical size consists of a single magnetic domain.[14] It is now accepted that a ferromagnetic particle of iron oxide with a radius under 30 nm is composed of a single domain particle,[15] meaning that under any magnetic field it will maintain a state of uniform magnetization (*i.e.* all the magnetic moments within the particles are pointing towards the same direction) (**Figure 2**). A colloidal assembly of this type of nanoparticles suspended in a liquid is considered “ferrofluid” as long as it stays in a monophasic state (no sedimentation or aggregation). At thermal equilibrium and under no external magnetic field applied, there is no net magnetization of the ferrofluid due to thermal agitation leading to random orientation of the grains and thus of their magnetic moments when considering the whole population of IONPs. The magnetization of single domains particles in thermodynamic equilibrium is identical to that of paramagnetic atoms or ions, except that extremely large moments are involved, of several hundred to thousands of Bohr magnetons.[16] Such thermal equilibrium, termed *superparamagnetism* follows the so-called Langevin’s theory of paramagnetism when the IONPs are in a dilute state where dipolar interactions can be neglected.[17] The properties exhibited by iron oxide NPs make them good candidates for either diagnosis or therapy as MRI contrast agents to assist diagnosis and for radiofrequency MH to remove cancerous cells by applying a thermal shock mediated by the IONPs. It is possible to engineer theranostic systems in which both these applications are integrated in the same nanostructure for simultaneous detection and treatment of diseases.[18]

Superparamagnetic IONPs can be obtained by various physical or chemical methods. Among others, the physical ones consist in top-down processes such as laser-induced ablation of macroscopic

targets of iron or iron oxides[19] resulting in polycrystalline IONPs with wide size distributions, or mechanical milling of bulk iron oxide[20] with subsequent mechano-chemical effect reducing the degree of crystallinity as compared to the starting material (also existent in other compounds[21]). Moskowitz and Rosensweig, in collaboration with the National Aeronautics and Space Administration (NASA), were the first in 1965 to prepare ferrofluids intended for magnetically driven pumps in the Explorer-17 satellites, by a grinding procedure of iron oxide powders for several weeks in the presence of surfactants.[22] Twelve years later, the 1st International Advanced Course on the Thermomechanics of Magnetic Fluids took place in 1977 in Italy, gathering experimentalists and theorists from both sides of “the iron curtain”, launching the cycle of the International Conference on Magnetic Fluids that still takes place regularly.

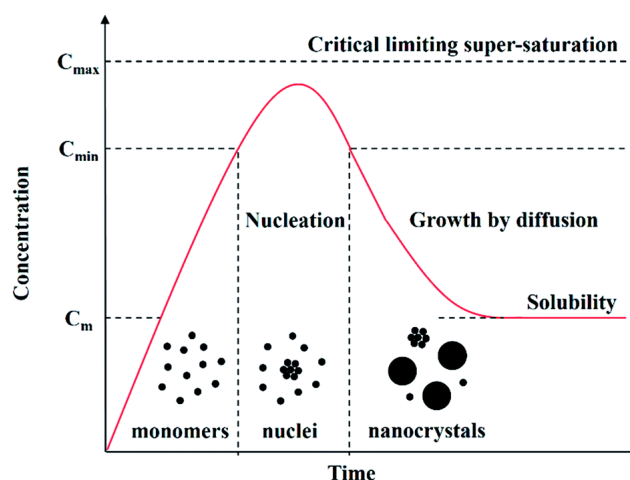


Figure 3 Plot of La Mer model for the generation of atoms, nucleation, and subsequent growth of colloidal synthesis (LaMer and Dinegar 1950).[23]

Bottom-up processes, consisting in the synthesis of IONPs from iron ions or molecular precursors, offer the great advantage over physical methods of controlling the composition, size and shape to achieve the desired properties by adjusting reaction parameters. The synthesis routes comprise the aqueous ferrous and ferric salts alkaline co-precipitation, the thermal decomposition of organometallic complexes, the alkaline hydrolysis in a polyol solvent, and the post-synthesis hydrothermal treatment (*i.e.* under high pressure) are among the most described in the list. These methods will be described in further details thereafter. In all synthesis methods, the so-called “LaMer model” is often evoked to interpret the size distributions of the synthesized IONPs. Originally established to describe the mechanism of formation of monodisperse hydrosols,[24] it was extensively used to explain the formation of any type of IONPs from (poly)atomic precursors. This model states that different processes are involved during the precipitation of IONPs: nucleation, crystal growth, and Ostwald ripening (**Figure 3**). Ideally, nucleation and crystal growth steps are separated, meaning that a burst of nucleation occurs at the early stage of the synthesis, followed by crystal growth through diffusion of the reactants to the nuclei. Because the physical properties of the nanocrystals are strongly dependent on their shape, size and size distributions, many publications have reported different

synthetic pathways in order to produce good quality materials with narrow size distributions, leading to controlled magnetic behaviors. Some of these findings are reported below.

2.2. Co-precipitation method

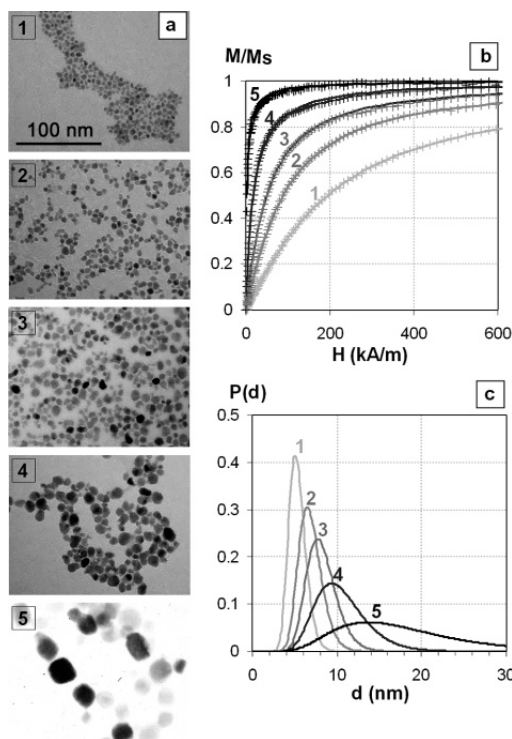


Figure 4 a) Transmission electron microscopy (TEM) images of iron oxide nanoparticles synthesized by aqueous alkaline coprecipitation followed by a size-sorting method based on ionic force induced phase-separation of (1) 5.3 ± 1.0 nm, (2) 6.7 ± 1.4 nm, (3) 8 ± 1.7 nm, (4) 10.2 ± 2.9 nm, and (5) 16.5 ± 7.5 nm. **b)** Magnetization M of samples no. 1-5 normalized to magnetization saturation M_s as a function of the applied magnetic field is well fitted by Langevin's law weighted by the log normal distribution of particle diameter (solid lines). **c)** Size distributions deduced from the fit of magnetization curves for samples no. 1-5.[25]

The alkaline co-precipitation of ferrous and ferric salts is widely used because it is a convenient and reproducible pathway to synthesize IONPs and obtain them directly dispersed in aqueous media. It is commonly referred to as “Massart’s method”, as Massart reported it first in 1981.[26] A variant was proposed quite simultaneously by Molday and Mackenzie in presence of a polysaccharide (Dextran).[27] This aqueous route to colloidal magnetite can be scaled-up to produce even kilograms of IONPs; thus, it is the method used by industries to produce commercial iron oxide contrast agents with well-adjusted parameters such as the mixing and addition rates of reactants to produce perfectly calibrated and reproducible batches. The precursors used are ferric (Fe^{3+}) and ferrous (Fe^{2+}) chlorides, sulfates or nitrates, first dissolved in an acidic aqueous solution to prevent the individual precipitation of hydroxides whose solubility products are very high, respectively $\text{pKs}=34$ for $\text{Fe}(\text{OH})_2$ and $\text{pKs}=44$ for $\text{Fe}(\text{OH})_3$, respectively. Then they are “co-precipitated” (meaning the two valences of iron ions together) under the addition of a strong base (commonly NH_4OH or NaOH), according to the reaction:



Controlling the salt metathesis of iron precursors into iron hydroxides followed by sol-gel reaction is not a straightforward task because it occurs instantaneously upon mixing; thus, the conditions have to be adequately set. The $\text{Fe}^{3+}/\text{Fe}^{2+}$ ratio, the nature of the anions in the salts, along with the final pH of the solution (dictated by the molar ratio R of OH^- ions to total iron ions compared to the stoichiometric value $R = 8/3$), temperature, mixing rates, ionic strength and optional presence of ligands (citrate, tartrate, etc.) greatly affect the nature of the nanocrystals obtained, including their size and shape. Magnetite (Fe_3O_4) is commonly synthesized this way, but an inadequate procedure can also lead to other non-magnetic iron oxo-hydroxide phase (goethite $\alpha\text{-FeOOH}$ or akaganeite $\text{Fe}_8\text{O}_8\text{OH}_8\text{Cl}_{1.35}$) or oxide (hematite $\alpha\text{-Fe}_2\text{O}_3$) phase.[28] Maghemite ($\gamma\text{-Fe}_2\text{O}_3$) can be obtained from magnetite by simple oxidation in an acidic medium with Fe^{3+} nitrate salts, or by leaving magnetite nanocrystals in contact with oxygen from ambient air, accelerating the formation of the thermodynamically favored maghemite compound.

The use of stabilizers during the co-precipitation process has been reported as a way to produce good quality materials with a narrower size distribution. Efficient stabilizers include poly(vinyl alcohol) (PVA), tri-sodium salt citrate, tartrate, or other multivalent carboxylate ions. An important criterion toward the selection of these organic additives is their hydrophilic or lipophilic affinity, which determines the final solubility of the IONPs in organic or aqueous solvents. For biomedical applications, hydrophilic ligands are used to ease the dispersion of the resulting particles in aqueous systems. Regarding shape and size control, co-precipitated samples under electron microscope usually exhibit “rock-like” IONPs with broad size-dispersity, corresponding to diameters ranging from 5 to 15 nm. As a post-synthesis process, a size-grading procedure based on the addition of an electrolyte allows to obtain narrow size-dispersities. The addition of an electrolyte in excess screens out the electrostatic repulsions between the iron oxide MNPs and leads to a liquid-liquid phase separation in two fractions respectively named S (“supernatant”) and C (“culot”), which are enriched with the lower sizes (respectively larger sizes) fractions of the initial distribution as shown in **Figure 4**. This was the method employed in one of the first articles describing the size effects on magnetic heating efficiency,[29] in agreement with Rosensweig’s linear relaxation model.[30]

2.3. Nano-template methods

Several template synthesis methods have been described in the literature in order to orient the particles’ geometry and to narrow the size distribution, as compared to co-precipitation in batch leading to a broad range of diameters. The use of pre-existing nanostructures as nano-molds was recently reviewed for organic templates, *i.e.* surfactants and polymers.[31] Inorganic templates such as mesoporous silica matrixes synthesized by the sol-gel route have also been tried out, since they enable to perform combustion synthesis at temperatures as high as 400°C while avoiding the issue of

aggregation and sintering of the nanocrystals.[31] Regarding micro-emulsions, these are composed of a nano-sized, thermodynamically stable dispersion of two immiscible solvents (water / oil) stabilized with a surfactant (dodecyl sulfate, Triton X-100, etc.) that can be used as medium to produce IONPs. In water-in-oil micro-emulsions, the iron precursor is solubilized in the water droplets forming confined reactors. The molar ratio of water-to-surfactant determines the size of the reverse micelles. Upon addition of a strong base, co-precipitation is initiated. The precipitating agent can be introduced directly in the emulsion of precursors or as a stabilized emulsion. In the latter case, the droplets containing the iron salts and the droplets containing the base collide and coalesce together, allowing the formation of IONPs. Since the size of the micelles is in the nanometer range, IONPs as small as 7.4 nm can be produced.[32] However, this method requires large amounts of solvents for small yields with a relatively low control of shape, crystallinity and monodispersity.

2.4. Hydrothermal method

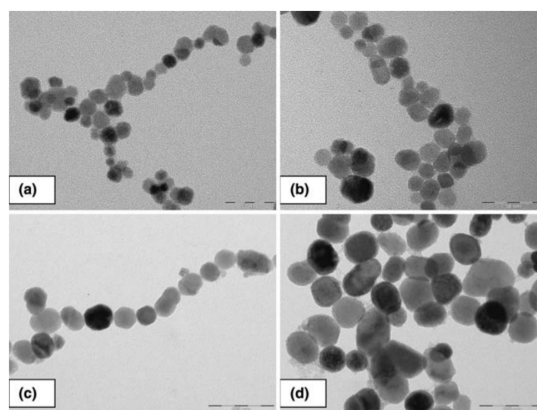


Figure 5 TEM images of γ -Fe₂O₃ particles obtained by using an hydrothermal treatment ($T = 200$ °C) for **a)** $t = 2$ h, pH = 12 (soluble particles); **b)** $t = 2$ h, pH = 12 (insoluble fraction); **c)** $t = 24$ h, pH = 12; **d)** $t = 2$ h, pH = 14. [22]

Single crystals can be synthesized from aqueous solutions at mild temperature and then transferred into a Teflon-lined stainless autoclave to perform a hydrothermal treatment. Combining a high temperature (usually around 200°C) and a high vapor pressure, such treatment favors the Ostwald ripening, by which the smallest crystallites are dissolved into the largest ones, increasing the average size and the crystallinity. This cost-effective and environmentally friendly route initially developed by von Schafhäütl in 1845 to grow microscopic quartz crystals has been used to produce various ferrites,[33, 34] magnetite[24, 35] and maghemite[22] nanocrystals with good water solubility and high crystallinity. Typically ferric and ferrous salts are mixed with a controlled molar ratio in an aqueous solution and precipitated upon addition of a base, similarly as in the co-precipitation method. The MNPs are then transferred into an autoclave for further aging at temperatures ranging from 150°C to 200°C under pressure. Starting with nanocrystals of 12 nm, the hydrothermal treatment leads to particles of 39 nm with ferrimagnetic behavior at room temperature.[24] The hydrothermal method leads to MNPs with very large sizes, good crystallinity and high saturation magnetization. However,

although the nucleation and growth steps are well separated (different conditions of temperature and pressure), the particles after hydrothermal treatment exhibit rounded (as opposed to faceted) yet rather ill-defined shapes as depicted in **Figure 5**. Therefore, this method still needs adjustments to limit the growth at the step of quasi-spherical particles of intermediate sizes (e.g. 20 nm).

2.5. Thermal decomposition method

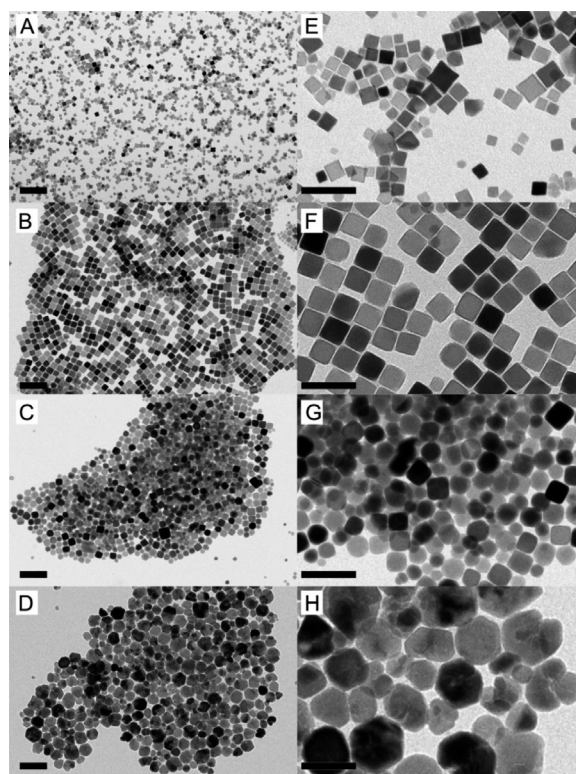


Figure 6 TEM images of iron oxide nanocubes for cube edge lengths of **A)** 12 ± 1 nm, **B)** 19 ± 3 nm, **C)** 25 ± 4 nm, and **D)** 38 ± 9 nm. Panels from **E-H)** (scale bars of 50 nm) are higher magnifications of samples shown in panels from A to D (scale bar of 100 nm). [36]

Originally introduced by Heyon[27] and concomitantly by Sun[29], the thermal decomposition of various organometallic complexes (iron pentacarbonyl,[27] acetylacetonate,[29] oleate,[30] or stearate[31]) in apolar organic solvents in the presence of ligands (oleic acid and/or oleyl amine) was reported as a synthesis path leading to the best geometrically-defined nanocrystals. These syntheses are performed at reflux of high boiling point solvents, commonly 1-octadecene ($T_{eb} = 318^\circ\text{C}$), octyl ether ($T_{eb} = 288^\circ\text{C}$), or diphenyl ether ($T_{eb} = 268^\circ\text{C}$). Several morphologies can be obtained from perfectly spherical[27, 29-31] to slightly polyhedral,[31] or prismatic[8] and cubic[37-39] by controlling the synthesis parameters. As seen on **Figure 6**, the nanocube morphology decreases the surface disorder and/or spin canting effect, which was interpreted as the origin of the observed decrease of the magnetic anisotropy constant as compared to a spherical particle of same volume,[40] and possibly of the overall magnetic heating properties of the dispersions.[41, 42] For all these syntheses, the reactants can be introduced following a “hot injection” protocol at the high reaction temperature, leading to a rapid formation of nuclei called “burst”, caused by the sudden

supersaturation of the solution with precursors. Alternatively, reactants can be introduced following a “heating-up” protocol: the solvent, the precursors and the ligands are mixed at a lower temperature before being heated at a controlled rate up to the reaction temperature, leading to the formation of nanocrystals. Compared to other routes, the thermal decomposition method has the superior advantage to dissociate the nucleation step and crystal-growth step which occur at different temperatures (ca. 200-240°C for the decomposition of the organometallic complex leading to precursors and up to 300°C for the growth, respectively). Whatever the source of iron (FeCO_5 , $\text{Fe}(\text{acac})_3$, FeCl_3 , etc.), it has been hypothesized that at the temperature at which pyrolysis occurred, iron carboxylate salts of the ligand used (e.g. iron oleate) were the real precursors.[43] Iron oleate complex can be produced before reaction from the inexpensive $\text{FeCl}_3 \cdot 6\text{H}_2\text{O}$ chemical[44] but it has to be purified beforehand in order to remove chlorine anions from the medium. Fatty acids such as oleic, decanoic or lauric acid, possibly mixed with fatty amines like oleylamine or hexadecylamine, are used as surfactants chemisorbed on the surface of the MNPs: first they can orient towards a specific morphology of the MNPs by blocking the growth of certain crystallographic facets compared to others; then, at the end of reaction, they assist the MNPs’ dispersion in organic solvents, and prevent aggregation by pointing outside into the solvent their non-polar chains. It should be noted however that the seed-and-growth technique consisting in adding more precursors to initially synthesized seeds enables to increase the sizes, but an imperfect epitaxial growth (i.e. internal defects existing within the crystals) can result in poor magnetic response.[45]

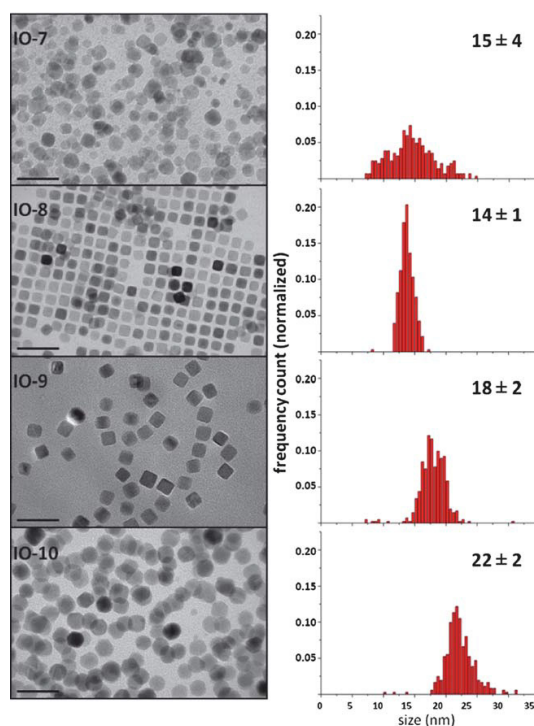


Figure 7 TEM micrographs and normalized size distribution histograms of iron oxide nanoparticles synthesized in 1-octadecene. Scale bars of 50 nm.[46]

In principle, the ratio of organometallic reagents, surfactant(s) and solvent drives the morphology and sizes obtained, but also other parameters like increasing the reaction time in absence of stirring as indicated in **Figure 7**.^[44] In some cases, further oxidation improves the crystallinity of the nanograins,^[27] as it is also the case by applying a magnetic hyperthermia treatment that acts as an annealing process.^[45] MNPs obtained this way are dispersible in polar solvents and are not water miscible, which is a limitation for biological applications. Following a ligand-exchange strategy, fatty acids can be exchanged with polar molecules, such as tetramethylammonium hydroxide (TMAOH) followed by adsorption of a synthetic polypeptide with a poly(aspartic acid) block,^[47] or chemical grafting of charged organosilanes.^[48] Amphiphilic polymers can also be used as phase transfer agents while keeping a good size-dispersity and colloidal dispersion, such as poly-(maleic anhydride *alt*-1-octadecene).^[49] The use of multidendate ligands such as meso-2,3-dimercaptosuccinic acid has also been reported.^[44, 50]

Lee *et al.* described the synthesis of ferrite@ferrite core-shell MNPs by thermal decomposition of $MnCl_2$ and $Fe(acac)_3$ in the presence of oleic acid, oleylamine and trioctylamine and $CoFe_2O_4$ seeds suspended in hexane.^[51] The magnetically hard core coupled with the magnetically soft shell leads to an exchange interaction resulting in thirty-four times enhancement of the specific absorption rate (*SAR*, physical magnitude related to MNPs heat dissipation which is discussed in details in the next sections) with respect to the commercial FDA approved iron oxide Feridex™ MNPs at same field intensity and frequency. This approach was further extended by Gavrilov-Isaac *et al.* who recently described the synthesis of trimagnetic multishell $MnFe_2O_4@CoFe_2O_4@NiFe_2O_4$ in order to tune the coercive field and, ultimately, *SAR*.^[52]

2.6. Polyol method

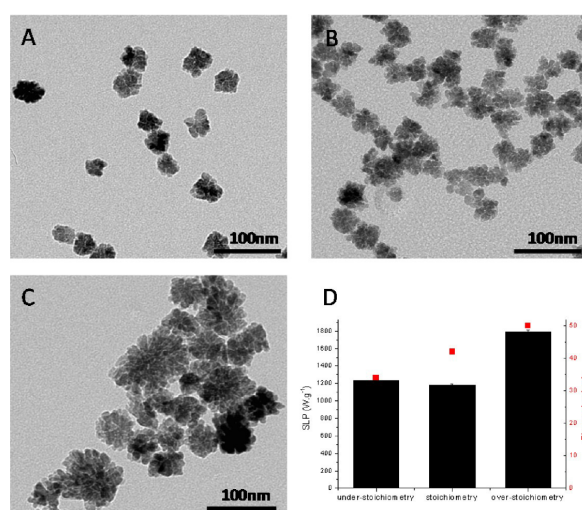


Figure 8 A-D) TEM micrographs of nanoflowers with sizes tuned by adjusting NaOH equivalents relative to iron chloride precursors. **D)** SLP (black bars) and mean diameter (red squares) of the samples.^[53]

In this method, the metal precursors (acetates or chlorides) are added to a polyol solvent (diol, triol), usually diethylene glycol (DEG), 1,2-propylene glycol (PG) or ethylene glycol (EG), exhibiting good chelating properties and stabilizing the precursors. Iron hydroxide precursors can be produced *in situ* by addition of NaOH to the ferrous and ferric iron chlorides (one equivalent relatively to chloride anions). Heating and mixing the solution helps to solubilize the precursors before reaching temperatures higher than 150°C, at which the polyol molecules chelated to the metal cations undergo a nucleophilic substitution reaction by water molecules (**Figure 9**), with the formation of a hydroxide according to the following scheme:

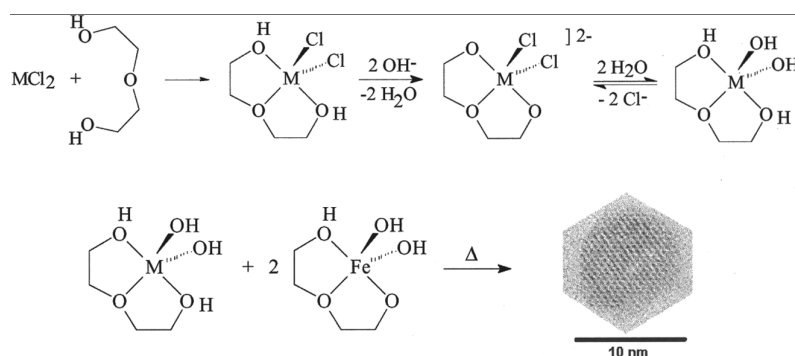


Figure 9 Proposed scheme for complex formation and its hydrolysis in DEG solution.[54]

Where M represents a divalent metal cation (*e.g.* Fe^{2+} , Co^{2+} ...). The mononuclear hydroxide reactive intermediates $M(OH)_2$ and $2 Fe(OH)_3$ react to yield MFe_2O_4 and $8 H_2O$ as in the co-precipitation reaction, the difference being that the organic ligands are coordinating the iron oxide surface. The equation also shows the necessity of a small amount of water, thus heating is carried at reflux rather than in an open vessel. After cooling down to room temperature, nanocrystals are extracted before being dispersed in water. The approach is similar to the thermal decomposition method previously described, except that the as-produced MNPs have a polar surface and are readily dispersible in aqueous solvents. The oxidized products of the polyol still attached as a corona wrapping the magnetic cores can be removed by extensive washings for further functionalization of the iron oxide surface. Magnetite, maghemite, nickel ferrite and cobalt ferrite have been reported to be synthesized this way with adjustable sizes and hyperthermia response at industrial scale.[55]

It has also been reported that the reaction of iron (II) and (III) chloride salts in NaHDEG with traces of water produce well-defined nanocrystals later dispersible in water.[56] NaHDEG is prepared by reaction of metallic sodium with DEG. This synthesis produces small crystals between 3 and 8 nm, thus more interesting as MRI contrast agents than as heat mediators. Cobalt ferrite ($CoFe_2O_4$) MNPs of different size grades from 5.4 to 40 nm were also synthesized in DEG from Co^{2+} and Fe^{3+} acetate complexes and further made hydrophilic or lipophilic with suitable phosphonic and hydroxamic acids.[57] But the polyol route can also lead to much larger MNPs, in particular to flower-like assemblies of smaller iron oxide crystallites. These so-called nanoflowers, as depicted on **Figure 8**, are multi-cores but behaving as magnetic single domains of size equivalent to the outer diameter, thus

presenting very high *SAR* values. They can be synthesized from iron chlorides precursors in a mixture of DEG with an organic base such as *N*-methyldiethanolamine (NMDEA)[58, 59] or tetraethylene tetramine (TETA)[60]. Another study shows that these structures result from well oriented attachment of the cores into flower-like clusters when the reaction is carried in EG and poor oriented attachment of the individual grains when the reaction is carried in PG.[61] This is explained by the formation rate of nanocrystals: in EG the formation and growth is slower, allowing the MNPs to assemble and organize by rotation resulting in crystal alignment and oriented aggregation, while in PG the mesostructure is less coherent and stable, with possible Ostwald ripening process meaning re-dissolution of the non-aligned crystals and growth of the organized crystals, the end-product being large MNPs exhibiting pores and magnetic multi-domains.

2.7. Combustion methods

Iron oxides can be produced in ultrafine (nanometric) powder from a gas reactant (FeCO_3) by laser-assisted pyrolysis,[62, 63] however post-treatments are necessary to collect the MNPs in a non-aggregated state.[64] An exothermic, fast and self-sustaining combustion reaction between +III manganese and a mixture of lanthanide nitrates and glycine also called Glycine Nitrate Process (GNP) can produce $\text{La}_{0.82}\text{Sr}_{0.18}\text{MnO}_{3+\delta}$ (lanthanum strontium manganite) MNPs, with a perovskite structure and a mean crystallite size of 22 nm.[65] This method leads to aggregated MNPs as the final product is composed of dry MNPs; milling steps can be performed to favor their disaggregation. These ferromagnetic particles are of particular interest for MH as their Curie temperature can be well adjusted by the lanthanide composition, thereby leading to “self-limited” nano-heaters. However, the high toxicity of lanthanides and manganese cations leads to the necessary coating of these MNPs by an inert shell such as silica in order to be used in biomedical applications.

2.8. Conclusion on the synthesis of iron oxide nanoparticles

To complete this overview of synthesis routes towards MNPs and, more particularly, iron oxide MNPs, some of them in this panel have been optimized to achieve larger scale. With this goal of scale-up in mind, microwave heating has been tried out instead of conventional heating in order to perform a homogeneous heating even with a large batch, as for the thermal decomposition of $\text{Fe}(\text{acac})_3$ [66] and the alkaline co-precipitation.[67] Overall, all these syntheses present various advantages and limitations, and a compromise must be chosen between the amount of MNPs produced and the degree of control of sizes and/or shapes and, of utmost importance for MH, of their magnetic properties. One more aspect needing to be highlighted in this part deals with the coating methods of MNPs. This is not only important to disperse them in hydrophilic media for biological applications, but also on the physical point of view, to tune the average distance between the MNPs in the dispersion: the ratio of mean particle diameter to their average center-to-center distance indeed controls the amplitude of their magnetic dipolar interaction, scaling like the 3rd power of this ratio for

ferri- or ferromagnetic MNPs, and the 6th power for SPM MNPs.[68] As will be developed later, these dipolar interactions that are weak in dilute individually dispersed MNPs, and on the contrary very high in densely clustered MNPs, have a non-negligible impact on the MH efficiency by slowing down the relaxation dynamics of the moments and/or increasing the shape component of the magnetic anisotropy and the hysteresis losses. Finally, a parameter that needs to be taken into account when going for biological tests is the availability of a sufficient amount of MNPs (meaning a few grams) in order to perform all the control experiments, especially when experimenting on animals. More precisely, one can estimate that 1 mg nanoparticles are sufficient and safe (ten-fold lower than the toxic dose) for an injection to a mouse (20 g average body weight), but 25 mg is required for a rat (500 g) and 100 mg for a rabbit (2 kg). Considering that dozens of animals are needed to obtain a significant statistics of tumor decrease results, one comes to the conclusion that between several tens and hundred grams of well-defined iron oxide cores must be synthesized, in a reproducible way. In the case of a clinical assay on humans, the need is even at the kg level. This is crucial to obtain the authorization of a magnetic nanoparticle system on market, as it has been already delivered in the past for iron oxide based contrast agents (e.g. ResovistTM, EndoremTM).

3. Applications of iron oxide nanoparticles in nanomedicine

The properties exhibited by magnetic iron oxides nanoparticles make them good candidates for either diagnosis or therapy. Iron oxide nanoparticles fit as MRI contrast agents to help diagnosis and for hyperthermia to treat cancerous cells by heat. It is possible to engineer theranostic systems in which both of these applications are coupled, allowing the detection and treatment of diseases.[18] MH is sometimes coupled to chemotherapy, by complex design of systems both magnetic and carrying drugs.

3.1. MRI contrast agents

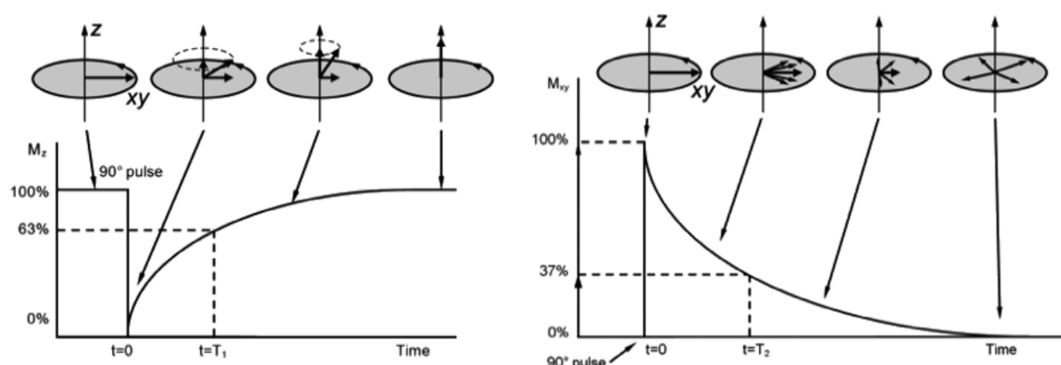


Figure 10 Return of the M_z vector along the longitudinal axis because of T1 relaxation. T2 (spin-spin) relaxation time = measure of the time required to regain decoherence of the transverse M_{xy} nuclear spin magnetization.[69]

MRI is based on the principal of NMR spectroscopy, *i.e.* on the dynamical response of an assembly of protons of molecules constituting the tissues (mostly water and fat membranes), which nuclear magnetic moments are magnetized by a strong static magnetic field (B_0). Thanks to an alternating magnetic field (B_1) transverse to B_0 , also called radiofrequency pulse, the population of nuclear spins is set into an out-of-equilibrium state. The recovery of the longitudinal (M_z) and transverse (M_{xy}) components of the magnetization through time occur with characteristic decay times, respectively T_1 (spin-lattice relaxation time) and T_2 (spin-spin relaxation time), as represented in **Figure 10**.

Table 1 T_1 and T_2 values of different tissues at 1.5 T.[32]

Tissue	T_1 (ms)	T_2 (ms)
Skeletal muscle	870	47
Myocardium	600	40
Liver	490	43
Fat	260	84
Blood	1,210	35
Venous arterial blood	1,210	250

In the late seventies, Mansfield in the UK and Lauterburg in the USA introduced a way to code 3D images by the appropriate application of tridimensional gradients of B_0 , correlating the free induction decays to their spatial origin and processing the data with a computer. Tissues can be differentiated depending on these variables, for instance blood vessels from the organs, or grey matter from white matter in the brain. Examples of values are reported in **Table 1**. Contrary to X-ray tomography, MRI enables to image soft tissues like muscles or the brain, with sub-mm resolution (almost single cell detection in its latest developments).

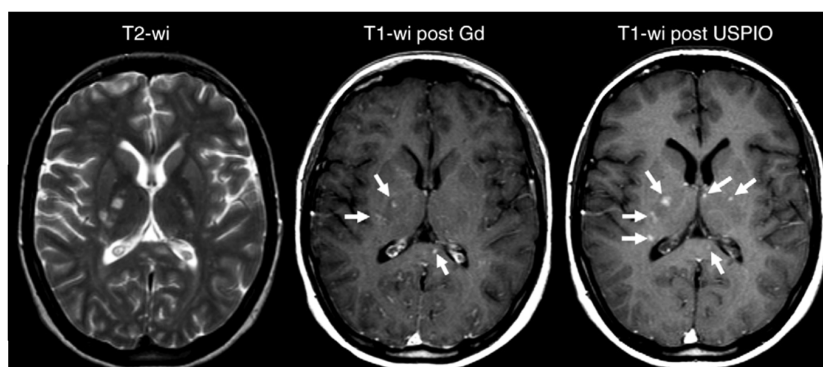


Figure 11 Mismatch between gadolinium- and ferumoxtran-10 enhanced images obtained at baseline in a 23-year-old woman with active relapsing-remitting multiple sclerosis without disease-modifying treatment. Left, axial unenhanced T_2 -weighted image shows multiple hyperintense lesions. Middle, axial gadolinium-enhanced T_1 -weighted image shows three enhanced lesions (arrows). Right, axial T_1 -weighted image obtained 24–48 hours after injection of Ferumoxtran-10 shows the same three lesions along with three additional active lesions that enhanced only with ferumoxtran-10 (arrows).[34]

The introduction of superparamagnetic nanoparticles induces local magnetic field gradients which accelerate the loss of phase coherence of the proton spins contributing to the NMR signal, improving the relaxation mechanism and contrast, as seen on **Figure 11**. [70, 71] The spin-lattice and

spin-spin relaxation enhancements per millimol of iron in the suspension are quantified by the relaxivities r_1 and r_2 . Depending on their r_1 and r_2 values, IONPs are often referred to as T_1 or T_2 -type agents, meaning that they are respectively prone to brighten or darken areas of images where they are localized. They therefore improve the contrast of the images and help localize abnormalities. Iron oxide contrast agents have been marketed in the 2000-2010 decade under various names as Feridex, Resovist, Sinerem, Lumirem and Clariscan. Feridex is a T_2 contrast agent composed of iron oxide nanoparticles coated with a low molecular weight dextran, with a size of 120 to 180 nm. Resovist is a T_1 contrast agent also composed of iron oxide nanoparticles coated with carboxydextrane, with a hydrodynamic diameter ranging from 45 to 60 nm.[72] Usually, individually dispersed iron oxide cores with a hydrodynamic diameter below 40 nm are called USPIO (“Ultra-small Superparamagnetic Iron Oxide”), whereas multicore clusters with diameters in the range of 100-200 nm are called SPIO or SPION (“Superparamagnetic Iron Oxide Nanoparticles”). Sinerem is an example of USPIO used for brain imaging (because its small size enables it to cross a damaged Brain Blood Barrier in case of brain tumor), whereas Endorem is used for liver imaging (due to its strong uptake by healthy Kupfer cells, but not by liver tumors, making them appear brighter than the healthy part of the liver). More recently, UUSPION (standing for “Ultra-Ultra-small Superparamagnetic Iron Oxide Nanoparticles”) have been introduced by Tromsdorf *et al.*: such single core nanoparticles with very small hydrodynamic diameter obtained by an efficient stealth polymer grafter (*e.g.* PEG) have a small value of the r_2/r_1 ratio (around 2-3), enabling to perform positive MRI contrast.[33] Since then, a few other studies describe the synthesis of polymer brush around iron oxide nanoparticles for positive contrast, using silane coupling and “grafting to” reaction. Brougham *et al.* described a grafting process of 3-aminopropyl-triethoxysilane (APTS) over the surface of iron oxide nanocrystals followed with polymerization from the free primary amines of a precursor with clickable alkyne groups.[73] This strategy allows the functionalization of the polymer with targeting agents through simple click chemistry.

3.2. Magnetic hyperthermia agents

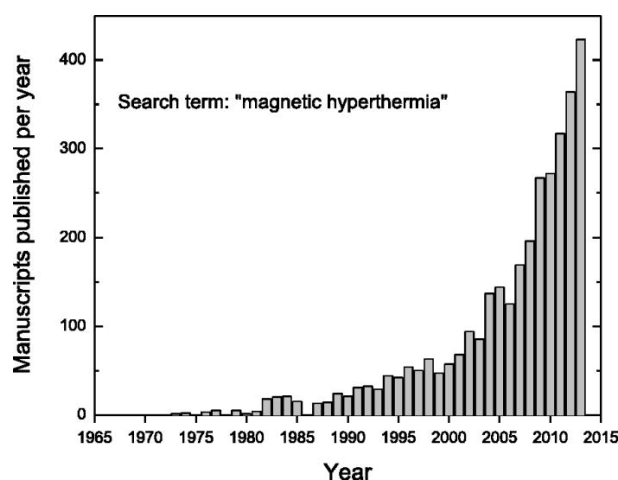


Figure 12 Number of published scientific manuscripts during the period 1973–2013 using the search term “magnetic hyperthermia.”

In medical oncology, the term *hyperthermia* refers to a therapeutic modality by which a given region of interest is subjected to a temperature increased above 40 °C.[35] Historically, it is believed that the oldest description about the use of hyperthermia is in Edwin Smith's surgical papyrus indicating the treatment of breast cancer. A more recent modality is the magnetic hyperthermia, where the temperature increase is produced by applying an alternating magnetic field (AMF) to a magnetic material, typically iron oxide. A brief analysis about MH literature illustrated in **Figure 12** shows that in the period 1973–2013, more than 3000 scientific manuscripts were published about MH, followed by an exponential growth as of the beginning of XXIst century. As can be seen, MH has never been so much in the spotlight as now. As in many other areas (materials science,[74] energy,[75] or health[76]) the progresses made in nanotechnology have taken MH to a much higher degree of development. For example, the application of MNPs in medicine is moving towards targeting body regions otherwise difficult to reach, and chemical manipulation at the nanoscale has conferred the ability to conjugate biomolecules like antibodies for a more effective therapy or to accomplish specific targeting.

Considering the extent of the treated region, hyperthermia can be classified into three types: *i*) whole body hyperthermia (achieved by using thermal chambers or blankets), *ii*) partial hyperthermia (applied to treat locally advanced cancer by perfusion or microwaves), and *iii*) local hyperthermia (mainly for smaller volumes than organs). The temperature increase in local hyperthermia—the one most frequently evaluated—might be accomplished by distinct approaches based on the use of ultrasound, microwaves, or near-infrared radiation.[37, 38] Even though these modalities have been incorporated into the clinical practice to treat a relatively wide range of cancer types, nowadays MH has some fundamental advantages over these when locally dealing with solid tumors: *i*) the AMF penetration depth is higher than any other activation mechanism (light or acoustic waves), allowing to reach deeper tissues; *ii*) administration of MNPs in a wide concentration range that may stay at the tumor site for repeated therapy sessions; *iii*) size-driven magnetic properties at the nanoscale

determining the heating capabilities; *iv*) precise control of size and morphology as well as surface modification for diverse goals including biocompatibility, providing chemical groups for attaching biomolecules, and minimizing blood proteins adsorption.

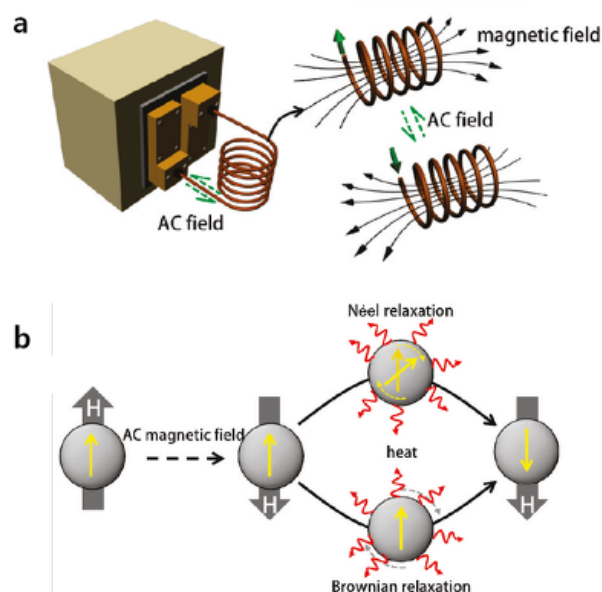


Figure 13 a) Instrumentation to generate an alternating field. **b)** Néel and Brownian relaxation processes of magnetic moments involved in heat dissipation during magnetic hyperthermia.[18]

The use of MNPs as a minimally invasive agent was initially addressed by Gilchrist *et al.* in 1957 giving rise to MH.[39, 40] This seminal work pointed out some challenges which are still under discussion by the scientific community concerning the application of MH in living beings: *i*) the heat release should be the highest possible at the lowest particles dose; *ii*) safety of AMF (with high voltages producing eddy currents in conducting media); *iii*) reliability for providing a precisely controlled intratumoral heat exposure mediated by MNPs. With the proposition of MH as a potential cancer treatment, the establishment of new materials and devices has been addressed with a continuous effort. It is possible to heal cancerous tissues by injecting magnetic nanoparticles in areas to treat and making them oscillate and generate heat locally with an alternative exterior magnetic field (**Figure 13**). Malignant tumors are composed of cells which have grown anarchically, poorly irrigated by blood vessels. Holding for 30 min or more a therapeutic threshold temperature of 42°C affects mainly these cells which evacuate the excess of heat less efficiently than healthy ones.[12] It has been recognized promising for cancer therapy, particularly in synergy with chemo- or radio-therapy.

After six decades of research, MH has taken an important step toward clinical applications. A. Jordan *et al.* have tested MH followed by radiotherapy on patients suffering from glioblastoma multiforme (**Figure 14**). Although this method is not able to cure the disease, there is evidence suggesting superiority of this new therapy, the overall survival from the time point of primary diagnosis of glioblastoma is of 23.2 months, which is substantially higher than the median 14.6

months in the reference group.[8] It has passed a phase II clinical trial on humans for glioblastoma in 2011 and is now authorized on market.

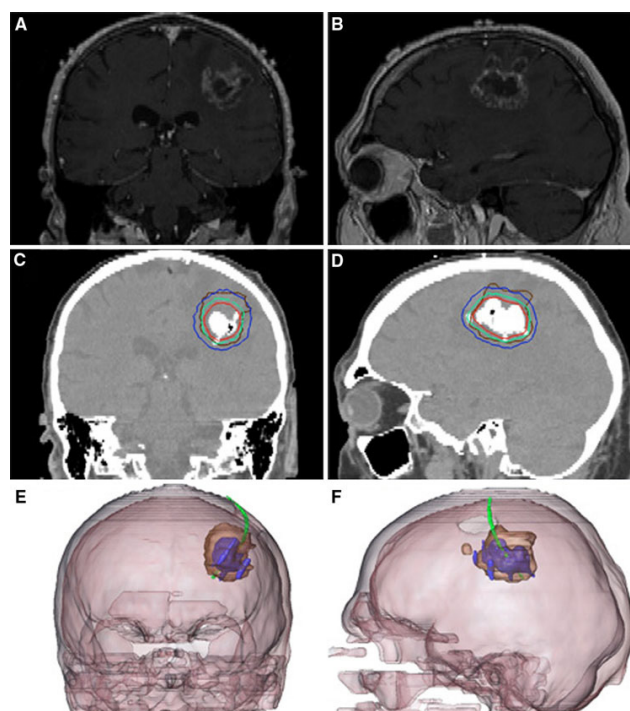


Figure 14 a,b) Pre-treatment brain MRI. c,d) Post-instillation CT showing magnetic nanoparticle deposits as hyperdense areas. Isothermal lines indicate calculated treatment temperatures between 40°C (blue) and 50 °C (red). The brown line represents the tumor area. e,f) 3-D reconstruction of fused MRI and CT showing the tumor (brown), magnetic fluid (blue) and thermometry catheter (green).[8]

Nevertheless the heat provided this way is difficult to calculate and locally probing the temperature is one of the challenges of this method. One convenient way to measure the temperature is to use a thermometry catheter with a small outside diameter implanted in the target area, but it makes the intervention invasive.

3.3. Drug delivery systems

As a large percentage of drug molecules developed by the pharmaceutical industry is poorly water soluble,[77] strategies have to be put in place to improve their delivery. This field of research is extensively growing, especially since one of the main challenges of cancer treatment has been described as the transport of the drugs.[78] Obstacles such as insolubility of the drug, inaccessibility of the tumor leading to limited therapeutic activity, and side-effects leading to damage to healthy tissues have to be overcome. Macromolecular drug carriers can benefit from the enhanced permeability and retention (EPR) effect and preferentially accumulate in the tumors (**Figure 15**). Complex assembly designs can couple the loading of a drug with active tumor targeting or cell-penetrating properties, stealth properties for improved circulation in the body, and so on. Different main classes of carriers are actively studied, such as liposomes, which can encapsulate large aqueous volumes and possibly

multiple drugs, and that have already reached the market.[79] Microemulsions are already historically extensively used in the pharmaceutical industry and used for drug delivery.[80]

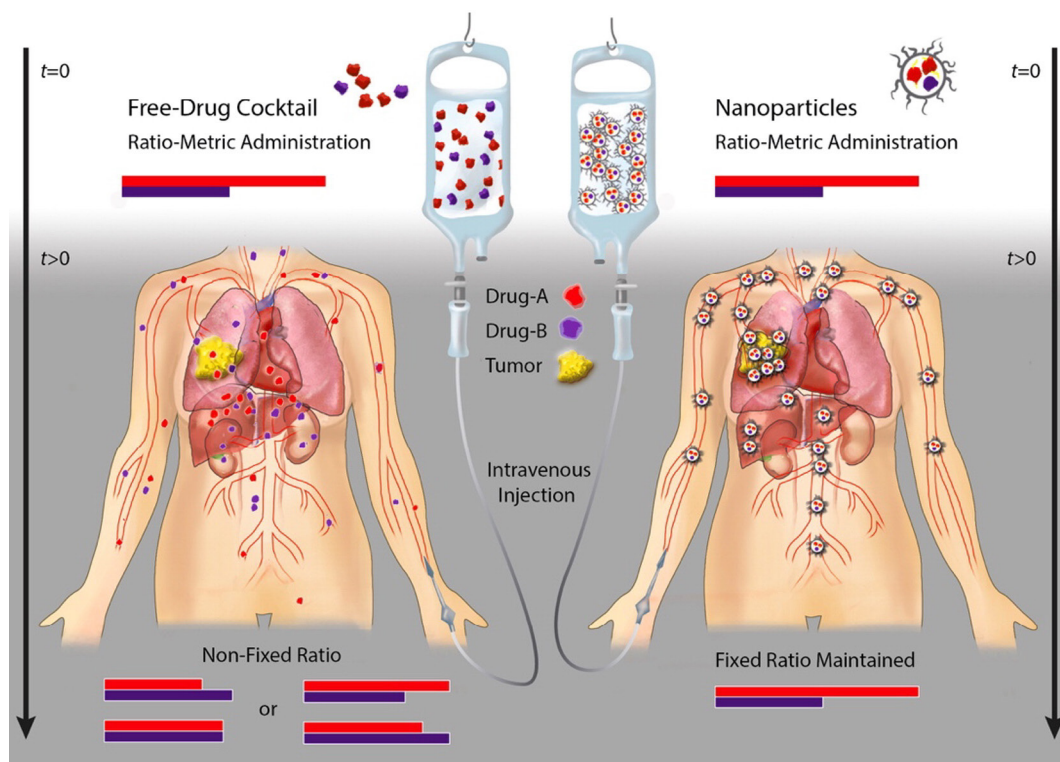


Figure 15 Illustration of potential benefits of using nanocarriers for ratio-metric delivery of synergistic drug combination for cancer treatment in clinical applications. Alteration of pharmacokinetics and biodistribution of ratiometric drug combination delivered by free solution. Upon intravenous (*i.v.*) administration, traditional free drug combination fails to maintain desired drug ratio (*e.g.* 2:1) before reaching the tumor.[81]

Polymeric nanoparticles are also extensively studied candidates thanks to the versatility of polymers that can be engineered and the resulting structures; from micelles to nanogels to nanocapsules.[82, 83] A strong emphasis is put on the biocompatibility and biodegradability of the materials used. The choice of drug encapsulated is rather large, and depends on the targeted application, but most of the drugs reported are in relation with cancer treatment, such as paclitaxel,[84] doxorubicin[85] and other intercalating anthracyclins. A variety of receptors can be targeted to improve the uptake in targeted tissues,[82] and diverse internal or external triggers are used to deliver the cargo, but we will focus here on magnetic and thermosensitive systems.

MH allows the penetration of deep tissues. This ability coupled to a magnetic mediator converting the radiofrequency into heat and a thermo-responsive carrier allows the theoretical treatment of any part of the body. The concepts of drug releasing by AMF have been presented in different reviews.[86, 87] The best candidates for the magnetic mediator part are still iron oxide nanoparticles, thanks to their biocompatibility, large surface to volume ratio and outstanding performances as heating mediators. The thermosensitive drug carriers can either rely on destabilization of membranes,[88] LCST properties (**Figure 16**),[89-91] cleavable bonds sensitive to temperature or pH.[92]

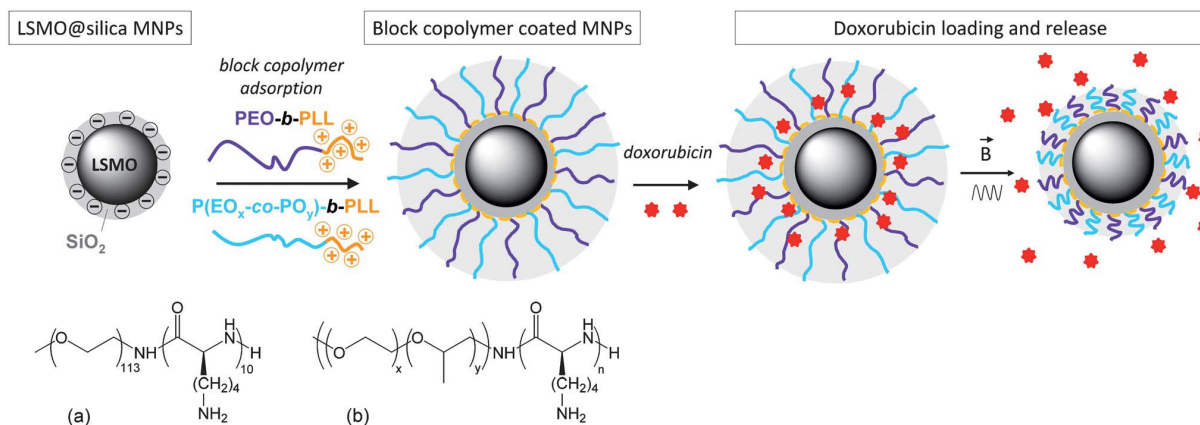


Figure 16 Magnetic and thermosensitive drug carrier based on a LCST polymer[91]

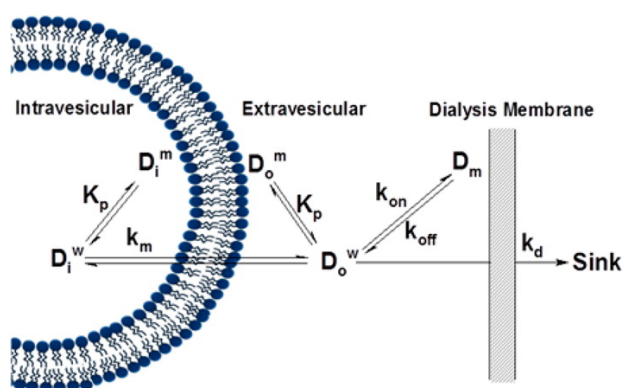


Figure 17 Determination of drug release kinetics.[93]

The kinetics of release by drug delivery systems is commonly evaluated by dynamic dialysis, by studying the diffusion of the drug from the dialysis chamber to the sink receiver. The drug content as a function of time is quantified in the receiver, allowing the evaluation of the kinetic of release. This system is limited to sustained drug delivery systems, as in the case of fast delivery the apparent kinetic of liberation depends on the drug transport across the dialysis membrane (**Figure 17**).[93] Evaluation of the kinetics of release in cells or in-vivo is quite complicated, with few methods available as High-performance liquid chromatography (HPLC) quantification of plasma and tissues.[94] Most of the time articles report the effect of the drug quantified as a cell viability percentage, or tumor volume to assess the release.

4. Review of anchoring groups used for the surface modification of iron oxide nanoparticles

As the particles are made of extremely divided matter, they exhibit large surface to volume ratio. The surface of the nanoparticles often needs to be modified in order to preserve their magnetic properties for the targeted applications, or to bring new functionalities. The chemical modification of iron oxide nanoparticles therefore leads to core-shell structures. The shell can be another layer of

inorganic material such as silica[95] or gold[96] for example. In the scope of this thesis, strategies to build an organic shell and yield hybrid inorganic-organic nanoparticles with iron oxide cores are discussed hereafter. Several chemical moieties can be added through surface modification of the IONPs with surface-complexing agents. The most widely used anchoring groups for iron oxide nanoparticles are catechols, carboxylates, silanes and phosphonates (**Figure 18**). These chemical functionalities are often terminated with another chemical moiety in order to pursue the surface modification of the IONPs, or are directly attached to the molecule of interest. They often act as a bridge between the inorganic iron oxide core and the organic shell.

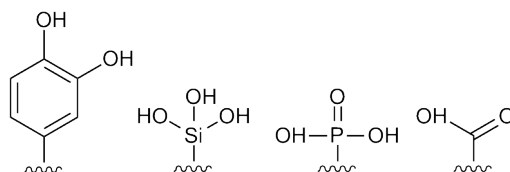


Figure 18 Common anchoring groups used to modify the surface of iron oxide nanoparticles. From left to right: catechol, silane (trimethylsiloxane in this case), phosphonic acid and carboxylic acid anchor groups.

4.1. Catechols

The catechol function is derived from mussel adhesive protein. This chemical function can bind to the surface of IONPs through direct chelating bond of the surface ferric irons. Dopamine is a natural molecule that presents a catechol function and, through chemical modification of its primary amine, other molecules can be chemically grafted onto the IONPs.[97] Dopamine is fairly unstable and can polymerize, meaning that molecules prepared beforehand for surface modification can react among themselves and form oligomers. Dopamine modification of IONPs often leads to the formation of clusters. This property is of interest for applications as enzyme immobilization for heterogeneous catalysis.[98] This clustering effect can be also advantageously used for the recovery of molecules in solution or treatment of wastewater.[99] In this case, the aggregated IONPs can be easily recovered with a permanent magnet. Stable IONPs in solution are preferred for biomedical applications, so that their magnetic properties used for magnetic hyperthermia or MRI are preserved. Other surface modifications strategies than catechols are therefore preferred.

4.2. Carboxylic acids

The thermal decomposition synthesis of IONPs often makes use of oleic acid.[27] This leads to nanocrystals readily capped with an organic layer. The oleic acid ligand is grafted with its carboxylic moiety onto the surface of the IONPs, and such nanoparticles can be dispersed in apolar solvents. The ligand needs to be exchanged with a hydrophilic capping agent to transfer them in aqueous solvents. Another surface modification making use of carboxylates is the citrate adsorption. This anion can be introduced directly in the reaction medium during the synthesis of the nanocrystals. Citrate anions were shown to influence the size of IONPs produced by co-precipitation in water,

leading to fine nanocrystals with diameters as small as 2 nm.[100] These anions can also be introduced with the IONPs as a post-synthesis step. In this case, the nanoparticles are produced by coprecipitation, purified, and capped with tri-sodium citrate as a final step.[101] The dispersions obtained are stable over long periods of time, with preserved magnetic properties for MR imaging and cell labeling. The adsorption of citrate modifies the point of zero charge of the IONPs, from the neutral pH region to acidic values of around 2.[102] With a $pK_{a1}=3.1$, $pK_{a2}=4.8$, and $pK_{a3}=6.4$, the citrate ions remain charged over a large range of pH, making citrate-modified IONPs stable at physiological pH and saline conditions. Another way to increase the charge of the IONPs for biomedical application is the coating with polyelectrolytes such as polyacrylic acid (PAA). PAA provides strong adsorption (resisting to dilution) and electro-steric repulsion between the IONPs, overcoming van der Waals and magnetic dipole-dipole attractive forces. Compared to smaller multivalent ligands like citric acid, the PAA coating offers superior stability, especially in high salinity buffers[103] and impedes the adsorption of blood plasma proteins.[104] In practical terms, PAA chains are adsorbed at acidic pH on the positively charged MNPs before modifying the pH to neutral or basic values, a process referred to as “precipitation-redispersion”.

4.3. Silanes

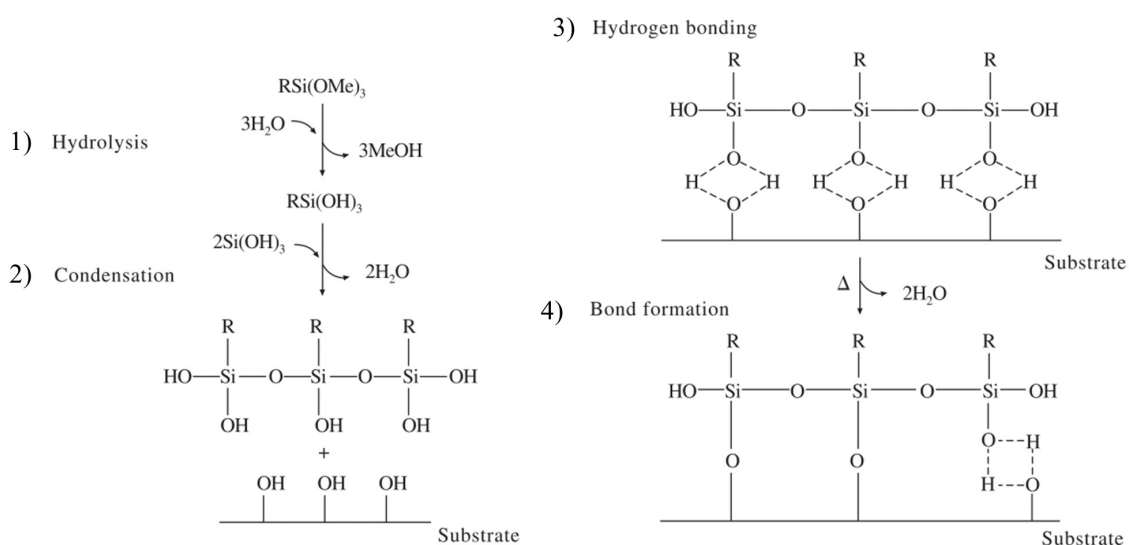


Figure 19 Hydrolytic Deposition of Silanes (adapted from: B. Arkles, CHEMTECH, 7, 766, 1977)

Several publications report ways for the silanization of superparamagnetic iron oxide nanoparticles.[105, 106] An organosilane presents two classes of functionality and has for general formula $R_n\text{SiX}_{(4-n)}$ with R being a non-hydrolysable organic alkane with desired characteristic and X is an hydrolysable group like acyloxy, halogen, alkoxy. Organosilanes with short alkoxy chemical functions are easier to hydrolyze. Therefore, methoxysilane is the most easily hydrolysable chemical function and is widely used (**Figure 19**). Also the surface modifications are often carried in methanol, matching the solvent with the leaving group of the alkoxy silane. The alkoxy silanes undergo hydrolysis

forming silanols, which can polymerize and condense on the surface of the IONPs presenting hydroxyl groups (either the original Fe-OH moieties of the raw iron oxide surface or the Si-OH brought by an intermediate silica shell). There is a competition between the condensation of silanols on the surface of nanoparticles and self-polymerization. For this reason, the amount of water available must be controlled as it determines the degree of polymerization and affects the outcome of the reaction. Multilayers are often obtained and present complex network structures, loose, intermixed or both.[107]

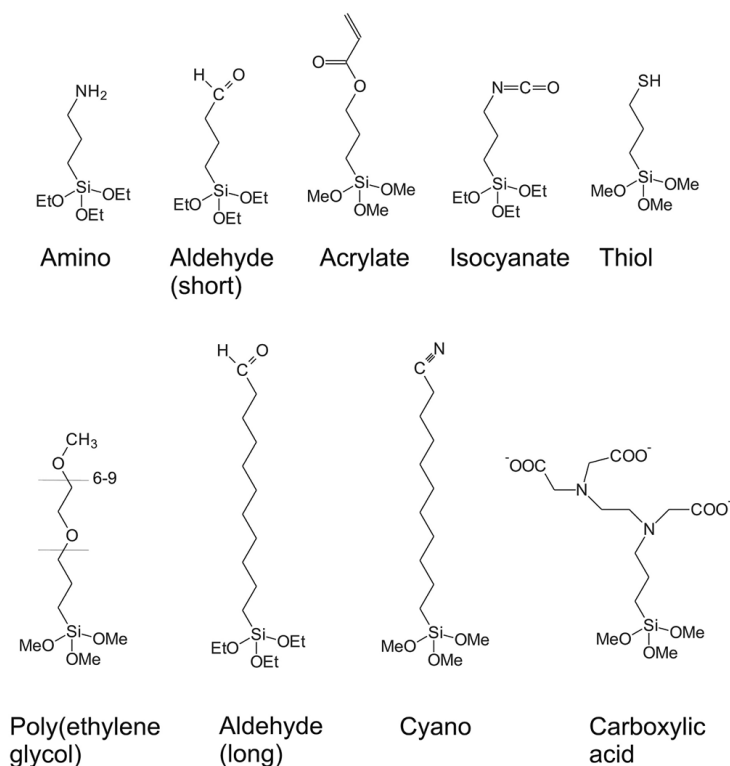


Figure 20 Structures of various silanes.[108]

One interesting silane coupling agent is the APTS, a substance which is approved by the Food and Drug Administration (FDA). Its terminal amine function allows a good stabilization of IONPs in aqueous media by increasing their hydrophilic character. Also the ability of the amine to bond with proteins, drugs or biomolecules lead to interesting bio applications.[109] Many different types of silanes exist aside from APTS, and are widely available in the market. These silanes can present different end-groups and be of interest by offering multiple possibilities for following grafting steps (**Figure 20**). These end-groups can be aldehydes, amines, acrylate, isocyanate, thiol, cyano or carboxylic functions, and are selected depending on the next reaction steps to be carried.[108] As silanes self-polymerize, the surface modification of the IONPs is often done by different grafting steps, building a shell in successive reactions starting from the silane. This divergent synthesis strategy often leads to aggregates when the conditions of reaction are not suitable for the stability of the IONPs. The IONPs have a tendency to aggregate when they are reacted in unsuitable solvents, or if they are grafted with intermediary destabilizing chemical moieties.

4.4. Phosphonic acids

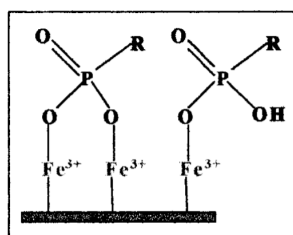


Figure 21 Two possible binding schemes for phosphonate ions to surface Fe³⁺ ions.[110]

One of the earliest reports on the surface modification of iron oxide nanoparticles with a phosphonic anchor group describes the use of an octadecanephosphonic acid (**Figure 20**).[110] This self-assembled monolayer (SAM) was shown to start decomposing and desorbing at temperatures as high as 340 °C. Two bonding schemes are possible; a phosphonate symmetrically grafted through its two oxygen atoms, or a phosphonate bonded through a single atom. The authors have shown through comparison with an alkanesulfonic acid that the binding with two atoms is the most probable. One strategy to increase the grafting efficiency on IONPs is to use multivalent phosphonate polymers. Torrisi *et al.* reported a graft copolymer with PEG pendant groups and phosphonate moieties that enable to make PEG coating very resistant to blood protein adsorption with outstanding stability in cell culture media supplemented with serum.[111] Another possibility is to use phosphonic anchors in a block structure instead of along the polymer backbone, to produce brushes at the surface of the IONPs.[112] Other innovative designs are PEG oligomers with dendritic architecture strongly anchored to the iron oxide surface through a phosphonate ligand thereby bringing good stability properties *in vivo*. [113] Using a mono- or biphosphonate anchor group led to comparable results in terms of stability or MRI properties.[114] This result suggests that a phosphonate anchor group is sufficient to efficiently and permanently graft a macromolecule at the surface of IONPs, and makes them suitable for biomedical applications. The grafting process can be tentatively assessed by IR spectroscopy if the strength of the signal is sufficient to be observed. The bands characteristic of P=O and P-O or Fe-O-P are in the range of 1200-800 cm⁻¹ which is usually crowded with other resonance bands.[115] Advantageously, the phosphonic acid moieties are fairly unreactive toward other chemical species, making them interesting candidates for the chemical modification of molecules prior to the grafting onto IONPs. In addition, they are highly water soluble and stable.

5. Considerations for the surface modification of iron oxide nanoparticles with polymers

5.1. Grafting to *versus* grafting from strategies

Core-shell hybrid nanoparticles with an inorganic core and organic shell of polymer brush find applications in nanoelectronics, catalysis, biosensing and drug delivery among many others. Two techniques are offered in order to functionalize a nanoparticle with a polymer: the “grafting to” and the “grafting from” methods. In the “grafting from” technique the polymer chain grows in situ from the surface of the nanoparticles with the help of initiators, by reversible addition-fragmentation chain transfer (RAFT) or atom transfer radical polymerization (ATRP).[116] A wide variety of initiators is available, depending on the material at the surface to modify and the polymer to synthesize. The polymer brushes produced are generally of high density as the grafted layer is swollen by the monomer solutions. The chains growths are limited by the diffusion of monomers only in the case of large grafting densities. While the grafting from technique has been performed on a wide variety of nanoparticles, it has been rarely experimented on magnetic nanoparticles.[117] These reactions of polymerization have to take place in conditions suitable for IONPs stability in order to access all the material surface available and build homogeneous core-shell structures. Furthermore, the magnetic properties of the IONPs prevent the characterization by NMR, and the immobilization of the chains hinders the characterization by size exclusion chromatography (SEC) or mass spectrometry. Broader molecular mass distributions are to expect, because of high local concentrations of polymer chains. These arguments explain why the synthesis of polymers and the study of their properties are often done beforehand, in a step prior to the grafting onto IONPs. In the “grafting to” method, end-functionalized polymers react with surface groups of nanoparticles. It is an easy and intuitive technique that allows a good control on the final core-shell structure. Sometimes the steric crowding of reactive surface sites by already attached polymeric chains leads to low grafting densities.

5.2. Commonly used heterofunctional linkers

There is a need to use intermediates to build shells on nanoparticles when there is no direct compatibility between the solid phase and the molecules to be attached on it. Click chemistry coupling reactions are commonly used in building blocks strategies. “Click chemistry” is a term describing chemistry tailored to generate substances quickly and reliably by joining units together. The term has been coined by Sharpless and Kolb to refer to reactions that are “modular, wide in scope, high yielding, create only inoffensive by-products that can be removed without chromatography by simple means, are stereospecific, simple to perform and that require benign or easily removed solvent”.[118] This chemistry is inspired by nature, which has a preference for heteroatoms bonds over carbon bonds when it comes to the assembly of small building blocks, like nucleic acids, polysaccharides and

proteins. Click chemistry is generally exothermic and performed in water, a green solvent, which acts as a heat sink for handling heat output. The best example of click reactions is Huisgen's 1,3-dipolar cycloaddition of alkynes and azides, forming triazoles, with copper(I) as a catalyst. It meets the requirements of click chemistry, there are no protecting groups needed, and it leads to a complete conversion and selectivity.

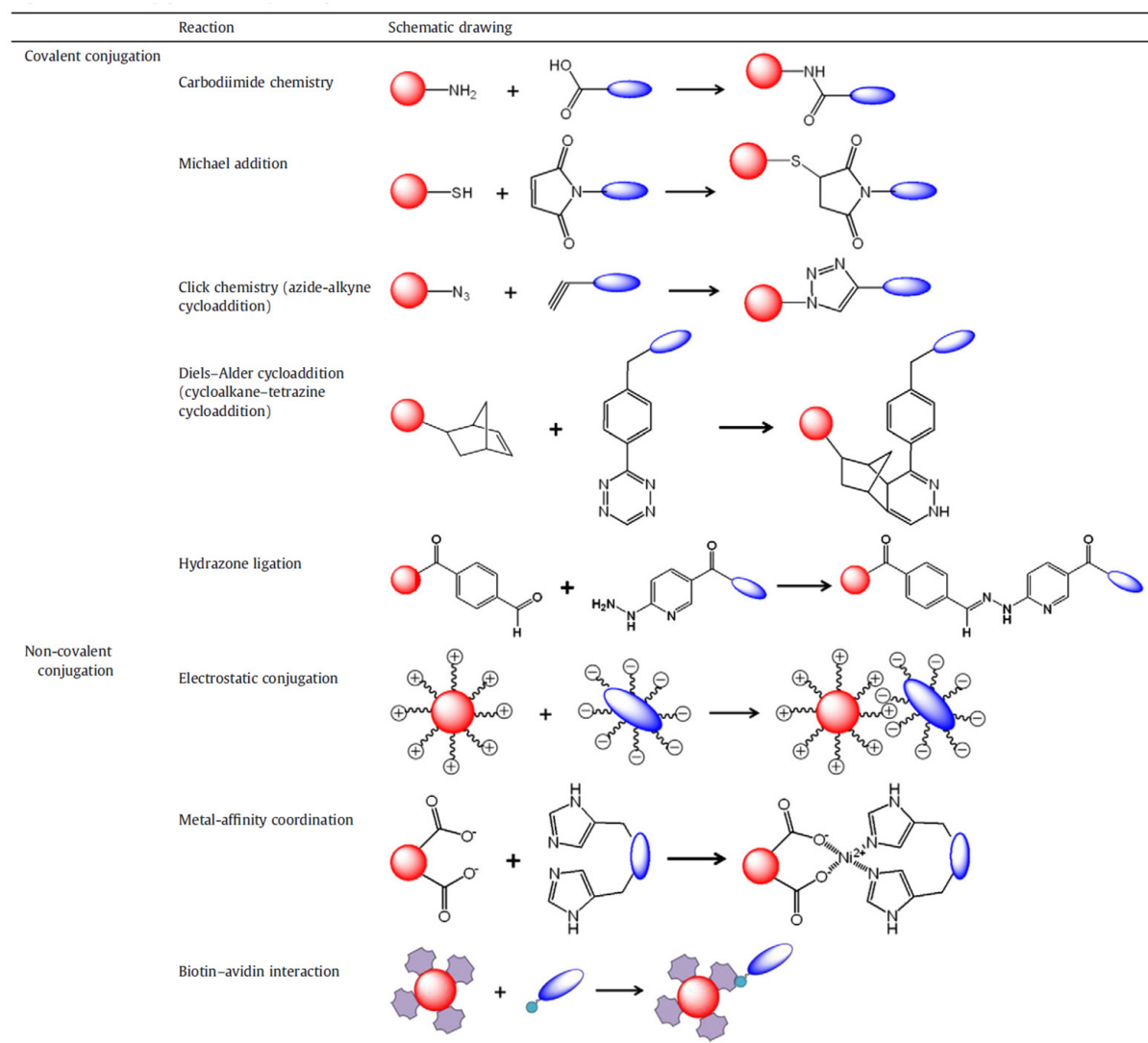


Figure 22 Representative bioconjugation chemistry of inorganic NPs.[119]

Thanks to the large quantity of possible starting materials it is possible to build a vast library of product compounds with biological potential and medical chemistry applications [120]. These bioconjugation strategies are illustrated in **Figure 22**. Another widely used synthesis pathway is the formation of amide bond. It is quite a convenient reaction to couple a carboxylic function and a primary or secondary amine. In this reaction, coupling agents like *N*-(3-dimethylaminopropyl)-*N'*-ethylcarbodiimide hydrochloride (EDC) and *N*-hydroxysuccinimide (NHS) are often used to improve the reaction's kinetic and yield. A study by Nakajima and Ikada accepted as true and often referenced to enlightens the reactions conditions, mechanisms and the stability of the resulting product.[121] This

bond is stable in a wide range of pH and temperature, making it a robust bond for targeted applications. Diels-Alder cycloadditions and hydrazone ligations are interesting chemical bonds in a strategy of drug release due to their thermosensitive properties. They allow the release of a drug through the local increased temperature at the surface of IONPs upon applying an external magnetic field. Finally, Michael addition type reactions are useful to chemically modify thiols from the cysteines of proteins, antibodies or polypeptides.

5.3. Surface modification with polymers for biological applications

Several natural and synthetic polymers have been tested to modify the surface of IONPs to improve their colloidal stability *in vitro* (in pH buffers, then in cell culture media supplemented with serum proteins) and eventually *in vivo* (in blood circulation), while being biocompatible: polysaccharides (*e.g.* Dextran[122]), PEG, poly(oxazoline) (POxa)[123] have been investigated among others for giving “stealth” properties to NPs, *i.e.* repulsion towards certain proteins of blood serum (opsonins), whose role is to mark foreign bodies by strongly adsorbing onto their surface so that they are recognized by white blood cells and go through elimination pathways. Once the circulation half-life is improved, it is possible to graft ligands with a specific affinity toward target sites, or to direct them near the tumor site with an external static or AMF gradient. IONPs must be stabilized in aqueous media in order to be used in MH applications, *i.e.* they must exhibit and keep a proper state of dispersion under given physicochemical conditions (pH, ionic strength, adsorbing proteins, etc.) and under an applied static field or AMF, whatever the field strength.

5.4. Brush theory: flat surface

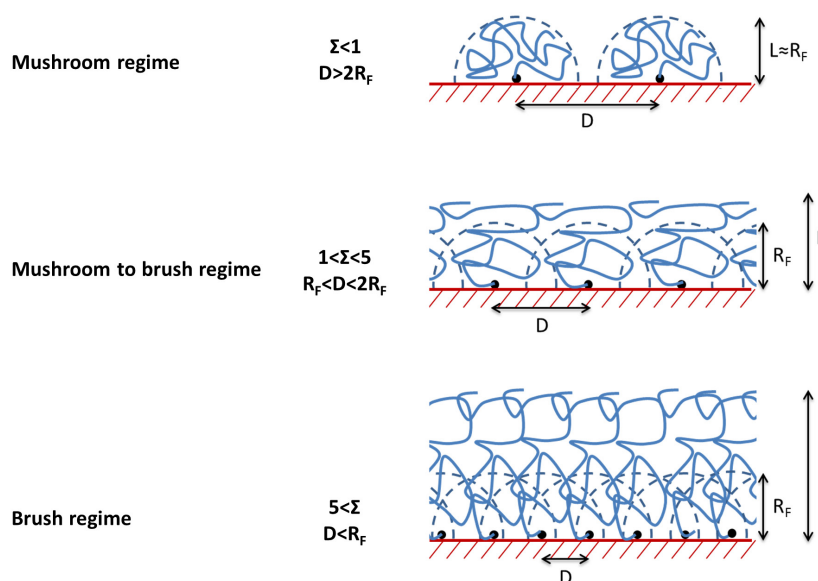


Figure 17. Conformation of a chain grafted onto a surface as a function of grafting density.

Molecular chains grafted at the surface of IONPs adopt different conformations depending on the grafting densities (**Figure 17**). In the case of a free chain in a good solvent, the volume occupied

by a polymer chain is a sphere with a gyration (Flory) radius of $R_g = aN^{3/5}$, where N is the number of repeating units and a is the monomer size. Three regimes can be identified when one end of the chain is tethered while the other part is able to occupy a volume available in the solvent. At low grafting density the chains are sufficiently far from each other, the distance between two grafting points is superior to 2 times the radius of gyration. The chains do not interact, and the thickness of the layer is approximately equivalent to the radius of gyration. At higher grafting densities the distance between grafting points is shortened, being inferior to a radius of gyration. The chains then interpenetrate and interact. This results in a true brush, a monolayer of elongated chains. At intermediate regime the chains are partially elongated. Several parameters can be calculated to estimate the quantity of IONP and polymer to react. Among them there is the ratio of organic material (% w/w), the grafting density, and the number of chains per IONP.

Table 2 Conformation of tethered chains depending on the reduced tethered density.

reduced tethered density value	regime
$\Sigma < 1$	mushroom
$1 < \Sigma < 5$	mushroom to brush transition
$\Sigma > 5$	brush

The reduced tethered density Σ is a convenient dimensionless parameter to estimate the regime of chains conformation (**Table 2**). The reduced tethered density Σ was introduced by Brittain *et al.* to describe the brush regime with a single adimensional parameter. Σ represents “the number of chains that occupy an area that a free non-overlapping polymer chain would normally fill under the same experimental conditions”. It is calculated as-follow:

$$\Sigma = \frac{\pi \cdot R_g^2}{D^2} \quad \begin{array}{l} R_g \text{ radius of gyration} \\ D \text{ distance between grafting points} \end{array}$$

While in the case of PEG, the radius of gyration is calculated using scaling laws either reported by Devanand[124]:

$$R_g = 0.0215 \cdot M_w^{0.583} \quad M_w \text{ molecular weight}$$

Or the scaling law reported by Le Coeur *et al.*[125]:

$$R_g = 0.665 \cdot M_w^{0.452} \quad M_w \text{ molecular weight}$$

These two scaling laws have different parameters but both lead to the same value $R_g = 3.4$ nm for PEG at $6,000 \text{ g}\cdot\text{mol}^{-1}$ for example. The limit between the mushroom and mushroom to brush transition is set for $\Sigma=1$, which corresponds to an inter-chains distances of 6.8 nm when considering a gyration radius of 3.4 nm. Brittain *et al.* described the transition from mushroom to the true brush regime.[126] They stressed that the term « polymer brush » should only refer to grafted

chains extended in the third regime, at $\Sigma > 5$. Hence, the term “polymer brush” should not be a synonym for a tethered polymer layer.

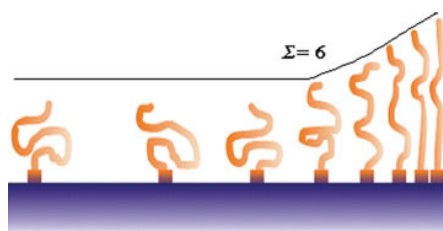


Figure 23 Transition between the “mushroom” regime and “true brush” regime.[126]

At high grafting densities, the polymers chains interact and extend due to steric interactions (Figure 23). They lose their random-walk isotropic configuration of free chains and stretch perpendicularly to the interface. This results in an increase of the thickness of the grafted monolayer.

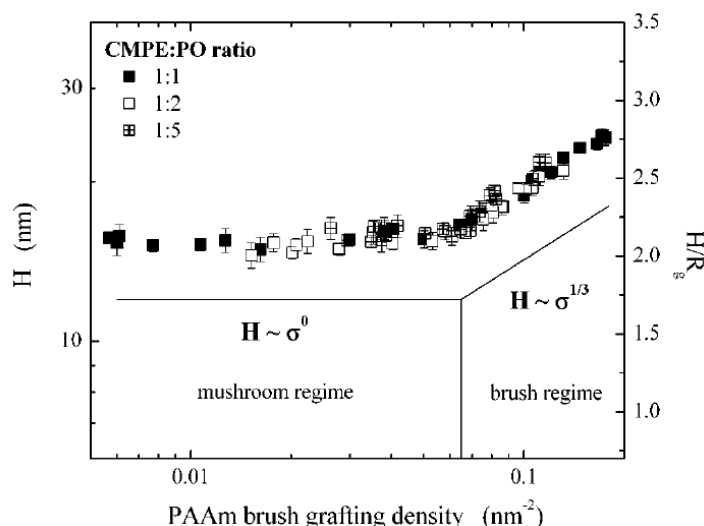


Figure 24 Wet thickness of the PAAm brush (H) as a function of the PAAm brush grafting density. [127]

The extension of surface-anchored polyacrylamide (PAAm) chains was experimentally demonstrated by Wu *et al.*[127] The so-called mushroom and brush regimes are directly observable on Figure 24.

5.5. Brush theory: curvature effect

For nanoparticles with high curvatures (small radii), the polymer brush chains can explore more space than when tethered on infinite curvatures (planar) surfaces. In this case, the conformations of the chains are more difficult to describe. There is a local gradient of concentration of polymer chains, with a decreasing concentration at a distance from the surface. Vogiatzis *et al.* represented this local density of a polymer in proximity with the surface of a nanoparticle.[128] They used a Monte Carlo simulation to model the conformation of the grafted polystyrene chains in a polymer melt. They calculated the height of grafted polymer brushes, either by considering a sphere in which 99 % of the grafted materials can be found, or a sphere defined by the root mean square rms height $\langle h^2 \rangle^{1/2}$ of the

brush. These findings are reported in **Figure 25**, showing that the brush thickness depends on the grafting density and the molecular weight of the polymer.

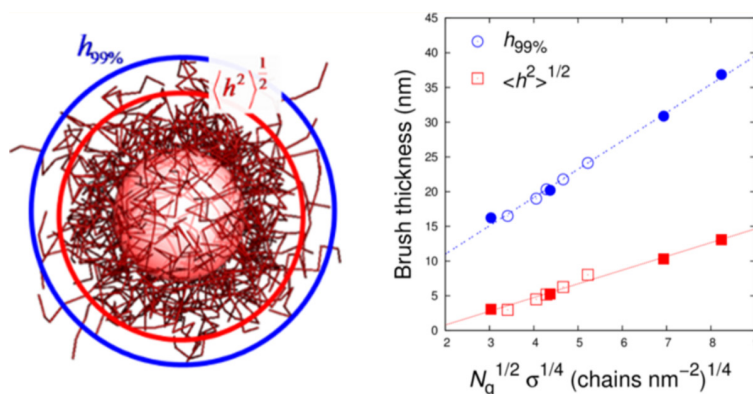


Figure 25 The calculated brush thickness (either $\langle h^2 \rangle^{1/2}$ or $h^{99\%}$) is plotted versus the square root of the degree of polymerization of grafted chains, $N_g^{1/2}$, times the fourth root of the grafting density, $\sigma^{1/4}$. In this model the nanoparticles have a radius of 8 nm.[128]

For systems consisting of a spherical hard core grafted with polymer chains in aqueous solutions, the hydrodynamic diameters provided by the DLS measurement most probably represent the diameter of the core added to the thickness of the hydrated brushes. The hydrated shell thickness can be estimated using formulas introduced by Birshtein and Zhulina. They described the curvature of a polymer brush around a spherical particle for the Theta solvent regime[129]. The effect of grafting density governing the tethered chains conformation is of crucial importance for the stability of nanoparticles in biological media. IONPs grafted with PEG were shown to withstand precipitation at specific weight fractions of iron oxide and polymer.[130] The steric repulsion between IONPs brought by the PEG brush was able to hinder van der Waals forces and magnetic dipole/dipole attractions. This facilitated the use of these nanoparticles as MRI contrast agents to detect lymph nodes, thanks to their increased stability in the bloodstream.

6. Brief overview of thermosensitive polymers

6.1. Thermosensitive synthetic polymers

Many applications can be considered thanks to the functionalization of nanoparticles with polymers, among them it is possible to immobilize active molecules in polymer brushes [131, 132], to graft ligands to improve their intracellular uptake and ability to target cancerous cells [133, 134] and to use them as stable imaging agents [10, 135, 136]. The grafting of thermosensitive polymers has been investigated in the field of nanomedicine. Stimuli-responsive polymers are defined as polymers that undergo relatively large and abrupt, physical or chemical changes in response to small external changes in the environmental conditions. Their chain conformation, interactions between chains, or interactions between chains and solvents are sensitive to physical or chemical stimuli.[137] These stimuli-responsive polymers are usually used in the form of hydrogels, micelles, or shells of

nanoparticles. Thermoresponsive polymers exhibit a critical solution temperature, at which the polymer phase separates from the solvent. When the polymer and the solvent form a phase separation occurs upon increasing temperature then the polymer exhibits a lower critical solution temperature (LCST) (**Figure 26 a**). When the opposite situation is observed, the polymer exhibits an upper critical solution temperature (UCST) (**Figure 26 b**).

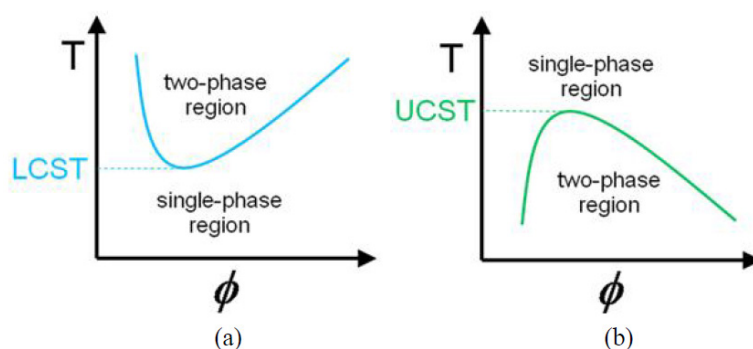


Figure 26 Temperature vs. polymer volume fraction. **a)** LCST behavior and **b)** UCST behavior.[138]

Several thermoresponsive polymers have been described in the literature, such as poly(*N*-isopropylacrylamide) (PNIPAM), triblock PEO-PPO-PEO copolymers (Pluronic, Poloxamers), poly(*N,N'*-diethylacrylamide) (PDEAAM) among others. Thermosensitive core-shell nanoparticles with inverse dependence of particle size with temperature have been reported, with non-magnetic or magnetic cores.[139] Systems containing a magnetic core and a thermosensitive polymer shell with a LCST a few degrees (Celsius) above the human body temperature are of interest as magnetic drug-targeting delivery systems and MRI contrast agents.[140]

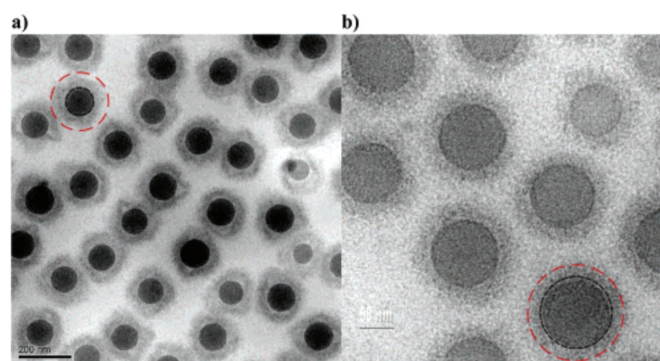


Figure 27 Cryo-TEM micrographs of a 0.2 wt % aqueous suspension of the PS/PNIPAM core-shell particles. The sample was maintained at **a)** 23 and **b)** 45 °C before vitrification. The core consists of polystyrene and the corona of cross-linked PNIPAM with BIS. The circle around the core marks the core radius determined by dynamic light scattering in solution. The circle around the entire particle gives the hydrodynamic radius R_H of the core-shell particles, again determined by dynamic light scattering.[141]

DLS measurement of hydrodynamic diameters and scattered intensities upon macroscopic temperature variations is a convenient way to measure the thermoresponsive properties of such core-shell nanoparticles. The measurement has a nanometric resolution and the set-up is automatized on Malvern instruments for example. Kurzhals *et al.* reported IONPs grafted with PNIPAM that

underwent colloidal aggregation upon heating.[142] They evidenced that the assembly of nanoparticles is reversible upon cooling of the solution, and that the thermoresponsiveness of the system depends on the topology of the shell of PNIPAM (grafted vs. free polymer chains). Polo-Corrales *et al.* reported an original system to evidence variations of temperature produced at the surface of IONPs under MH.[143] They used thermoresponsive fluorescent polymers grafted at the surface of IONPs, measured their fluorescence signal under MH and compared the values with calibration curves. They could evidence a surface temperature above the temperature of the surrounding medium. Cryogenic transmission electron microscopy (cryo-TEM) has also been reported as a powerful tool to observe a thermosensitive shell at shrunken or swollen states. Crassous *et al.* produced solid cores of poly(styrene) with a shell of cross-linked PNIPAM, and imaged the conformation of the shell in swollen and dehydrated states by vitrifying the sample followed by observation by cryo-TEM.[141] The diameters obtained were similar to that measured by DLS.

6.2. Thermosensitive elastin-like polypeptides

6.2.1. Chemical structure and thermosensitive properties

Elastin-like polypeptides (ELPs) are polypeptides whose composition is inspired by the hydrophobic domain of human tropoelastin. A pentapeptide of composition Val-Pro-Gly-Xaa-Gly (VPGXG) forms the repeated unit of an ELP, with Xaa (X) being a guest residue which can be any amino acid except proline. ELPs are interesting materials for drug delivery applications as they exhibit a lower critical temperature phase transition behavior. ELPs aggregate into coacervates above a characteristic cloud point temperature (transition temperature T_t). This transition is fully reversible, leading to the re-solubilization of the ELP chains when the temperature of the aqueous solution is returned below the T_t . The value of T_t for a specific ELP sequence depends on the composition of the repeated units; hydrophobic guest residues (valine, leucine) lower the T_t while hydrophilic ones (glycine, serine) elevate it.[144] Also, an increased molecular weight of the ELP chain results in a decrease of T_t . [145] Other extrinsic factors shift the T_t , such as the salt concentration in solution, nature of the salts,[146] the concentration of ELP, and pH if the sequence contains guest residues that can be protonated. The ELPs mainly find applications in medicine in the fields of drug delivery, tissue engineering and regenerative medicine as scaffolds.[147]

6.2.2. Biosynthesis of elastin-like polypeptides

ELPs are mainly produced by biosynthesis, by encoding protein-based polymer sequences at the gene level. This allows controlling the composition of polymer subunits (VPGXG)_n, as well as the chains lengths (number of repetition n).[145, 147] The ELPs obtained by genetic engineering therefore present perfectly defined chemical structures, which would be impossible to achieve through chemical polymerization. For these reasons and due to the perfect batch to batch reproducibility, the biosynthesis method is preferred over the solid phase peptide synthesis (SPPS). Although, one minor

drawback of the biosynthesis method is its lack of versatility; changing the chemical structure of an ELP to tune its properties means changing the whole gene sequence. Alternatively, the ELPs chains can be chemically modified post-synthesis to adjust their temperature responsive behavior.[148] ELPs of high molecular weight can be produced with yields in the order of $100 \text{ mg}\cdot\text{L}^{-1}$.

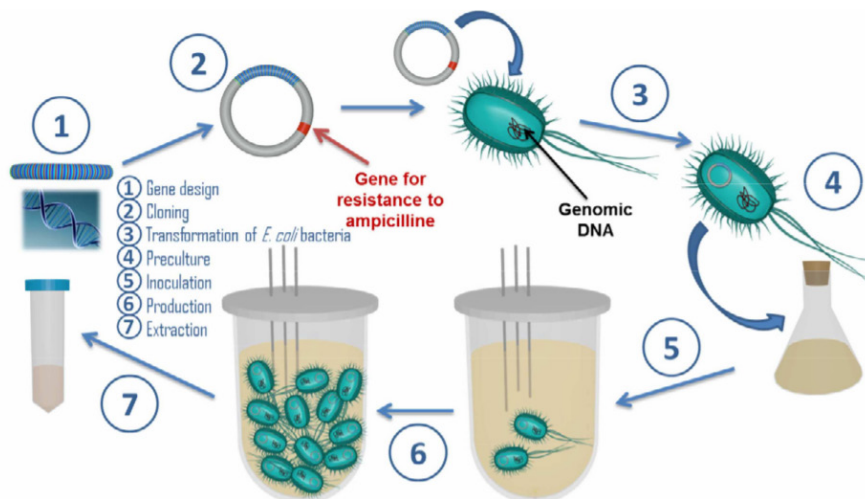


Figure 28 Biosynthesis of a recombinant ELP. (Illustration from R. Petitdemail PhD thesis).

The ELP genes are typically expressed in *E. Coli*, through the insertion of a plasmid (**Figure 28**). The bacteria are then fermented in the appropriate growth medium, leading to the development of the colony and the production of the ELP (following the strategy of production). The extraction and purification steps makes use of the thermosensitive properties of the ELP, through a separation process called inverse transition cycling (ITC), a method reported by McPherson *et al.*[149]. The bacteria are collected by centrifugation. Following the application of freezing/thawing cycles and sonication, the ELP can be extracted from the lysate. Four steps are applied successively: *i*) the ELP is aggregated by raising the temperature of the solution and adding salt; *ii*) the ELP is pelleted by centrifugation and the supernatant is discarded, removing soluble contaminants; *iii*) the ELP is recovered by addition of a fresh solvent in cold conditions and agitation; *iv*) the non-soluble contaminants are pelleted by centrifugation, leaving the purified ELP in the supernatant. The ITC process is repeated a determined number of times, leading to an increased purity of the product.

6.2.3. Macromolecular self-assembly for drug delivery applications

ELPs are promising materials for drug delivery applications. Macromolecular assemblies can be obtained by taking advantage of the thermosensitive properties of the ELPs. Unimers of ELP self-assemble into coacervates when the solution is heated-up above the T_t . Bioactive molecules can be trapped in these ELP structures for a later sustained release in biological media.[150] In this case, the thermosensitive property of the ELPs is used for the formation of objects of several hundreds of nanometers, but does not serve as a trigger for the delivery.

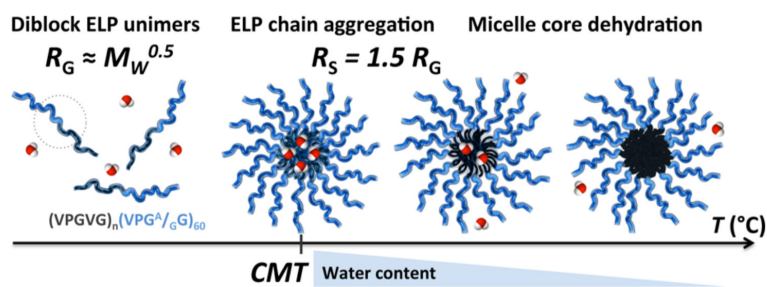


Figure 29 Proposed self-assembly mechanism of formation of diblock ELP nanoparticles.[151]

More complex systems of diblock ELPs with a hydrophobic ELP segment fused to a hydrophilic ELP block lead to the formation of dispersible objects of smaller dimensions (**Figure 29**).[151] Soluble unimers self-assemble into mono-disperse spherical micelles above their critical micellar temperature (CMT). These assemblies are directed by the selective dehydration of the hydrophobic segment which form the core of the micelles, while the hydrophilic segment remains solvated and stabilizes the self-assembly. The lengths and compositions of the two blocks of the ELP influence the dimensions of the micelles as well as the CMT. The nano-objects can be stabilized by cross-linking to withstand interactions with bovine serum albumin (BSA).[152] They can also be decorated with tumor targeting ligands by addition of a terminal peptide to the diblock ELP.[153] Therapeutic cargos can be loaded in the micelles and delivered in a sustainable way.[154] Other systems based on ELPs were tried out, such as ELP-functionalized dendrimers or liposomes, but to the best of our knowledge, no bio-conjugations of ELPs with IONPs were reported. Aside from the passive diffusion of drugs loaded in micelles, covalent bonding of the drugs with ELPs was reported. In this case, the drug was grafted onto the ELP, leading to the formation of star-like micelles.[155] Relatively large amounts of drug, close to 5 wt.% could be loaded by chemical conjugation. The mechanism of release in cells in *in vitro* conditions is still to be unraveled, as the drug was able to find its way to the nucleus. The ELP-drug assembly possibly underwent enzymatic degradation inside endosomes and/or lysosomes. Other systems relying on the thermosensitive properties of the ELPs to design smart drug carriers have been reported in several reviews.[156, 157] These designs are commonly micelles with thermosensitive coronas or micelles with thermosensitive cores.

6.2.4. Improving the cell uptake

ELPs can be fused to cell penetrating peptides (CPPs) and/or tumor targeting peptides. Several cases are presented thereafter to illustrate such strategies.

The fusion of ELPs with targeting peptides can enhance the intracellular drug delivery of ELP-based drug carriers. Sarangthem *et al.* reported the fusion by recursive directional ligation of a tumor targeting peptide AP1 with an ELP (VPGVG)₁₂ referred to as V₁₂. [158] The fusion of AP1 led to an enhanced tumor-specific targeting and improved uptake in different cancer cell lines *in vitro* compared to an ELP (VPGVG)₁₄ referred to as V₁₄ (**Figure 30**). This proves that the internalization of ELP-

based nanovectors for drug delivery can be increased by the construction of ELPs comprising tumor targeting or cell-penetrating peptides.

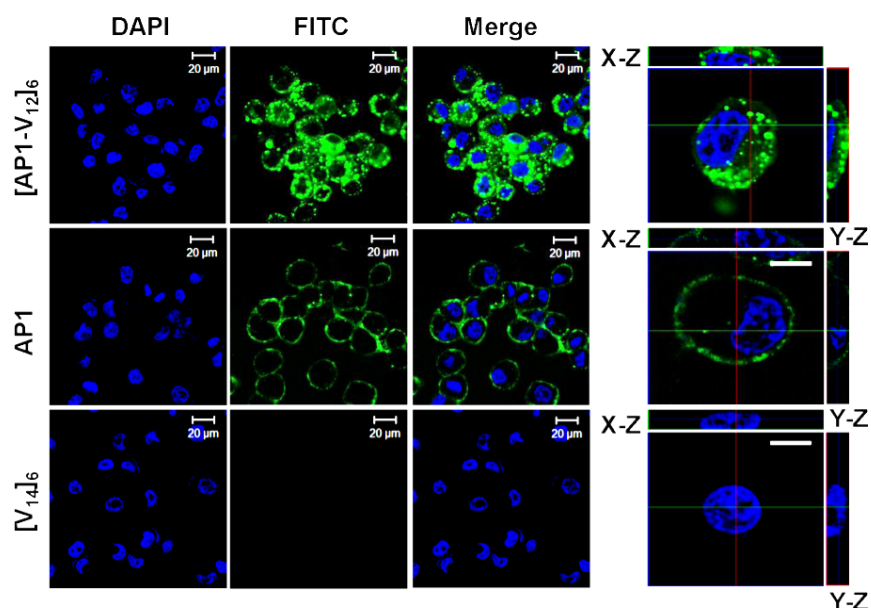


Figure 30 Confocal laser scanning microscopic images of H226 cancer cells treated with 10 mM of $[AP1-V_{12}]_6$, AP1, or $[V_{14}]_6$ at 37 °C (AP1 is a tumor targeting peptide, V_{12} is an ELP $(VPGVG)_{12}$, V_{14} is an ELP $(VPGVG)_{14}$). Representative confocal images of three experiments (scale bar 20 mm). Right panels: Examination of $[AP1-V_{12}]_6$, AP1 and $[V_{14}]_6$ cellular location by Z-section scanning of confocal microscopic images. Representative confocal images of three experiments (scale bar 10 mm).[158]

Interestingly, in this example AP1 binds to the surface of the cells while $[AP1-V_{12}]_6$ binds to and penetrates the cells. This illustrates that the molecular construction is important to direct interactions in biological media, but the assembly into objects of nanometer size strongly influences the uptake and internalization pathway in cells, as described in the next section.

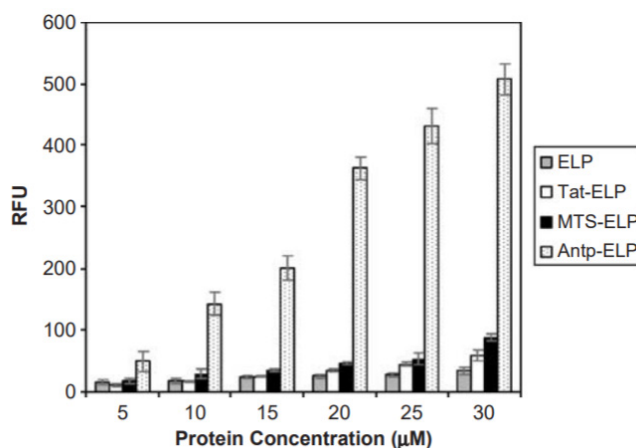


Figure 31 Effect of CPP-ELP-fluorescein concentration on cellular uptake as expressed in relative fluorescence units (RFU) normalized to uptake of 5 μM ELP. Increasing concentrations of polypeptides were incubated with HeLa cells at 37 °C for 1 h. Results are represented as mean±SEM of three independent experiments.[159]

CPPs are interesting for drug delivery applications as they translocate through the cellular plasma membrane. They can be coupled to oligonucleotides, nanoparticles or proteins. CPPs have been shown

to increase the uptake of ELP assemblies inside cells. Massodi *et al.* compared the effect of three different cell-penetrating peptides fused with ELPs on HeLa cells *in-vitro* conditions (**Figure 31**).[159] They studied a CPP derived from the Drosophila transcription factor Antennapedia (Antp), another CPP derived from the HIV-1 transactivator of transcription (Tat), and a third CPP derived from the Kaposi fibroblast growth factor (MTS). The increased cell uptake was several fold superior to that of ELP alone. The performance of MTS and Tat were moderate, while Antp showed a large penetration effect. Walker *et al.* produced ELPs fused to CPPs and conjugated with a thermosensitive hydrazone bond to the anticancer drug doxorubicin.[160] They evaluated the efficacy of three different CPPs to penetrate MCF-7 breast cancer cells: Bac (derived from the bacteriocin family of antimicrobial peptides), Tat, and SynB1 (from protegrins found in porcine leukocytes). They demonstrated that the three different CPP-ELP-Dox conjugates delivered doxorubicin to the nucleus of the cells. However, Bac and Tat CPPs significantly contributed to the cytotoxic effects observed, in addition to the contribution of Dox. Josephson *et al.* reported Tat peptides and dextran grafted onto IONPs.[161] Such nanoparticles were internalized into lymphocytes over 100-fold more efficiently than non-modified nanoparticles.

7. Nanoparticles in biological media

7.1. Improving the stability of nanomedicines in physiological conditions

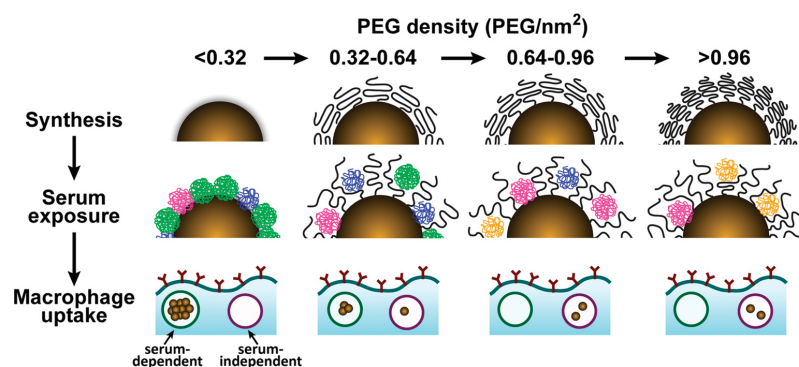


Figure 32 Schematic illustrating the influence of PEG density on serum protein adsorption to gold nanoparticles and their subsequent uptake by macrophages. The top panel shows as-synthesized gold nanoparticles grafted with PEG at increasing density. As PEG density increases, PEG volume decreases as a result of PEG–PEG steric interactions. The middle panel illustrates how PEG density determines the amount and relative abundance of serum proteins adsorbed to the gold nanoparticle surface after serum exposure.

Understanding the body response toward invasive foreign nanoparticles helps designing strategies to treat specific cells, tissues or organs. The clearance process is composed of two steps; the opsonization process in the blood stream and the cellular uptake by endocytosis/phagocytosis, or other pathways. During the opsonization process plasma proteins circulating in the blood recognize invasive entities and adsorb onto their surfaces, acting as markers to help macrophages and plasma membrane receptors to eliminate unwanted entities. When nanoparticles are injected in the blood, they attract different types of plasma proteins depending on their surface properties, charge density, size and

morphologies (**Figure 32**). After this first step the nanoparticles endure phagocytosis and endocytosis or macropinocytosis leading to their elimination from circulation and concentration in organs with high phagocytosis activity. This explains why nanoparticles tend to concentrate mainly in the liver 80/90%, spleen 5-8% and bone marrow 1-2%.[162] It is possible to take advantage of this process to specifically deliver therapeutic agents in phagocytic cells and their related organs, in a passive targeting way. A way to improve circulating time would be to tackle the immune system by injecting a large placebo amount of nanoparticles prior the injection of nanoparticles of interest (in that case magnetic nanoparticles), or injecting species destroying liver and spleen macrophages.[10] Mistreating the defense system of a body already suffering from a disease cannot be a viable strategy. To rather achieve active targeting there is a need to engineer nano-objects in order to attain other organs by searching inspiration in naturally circulating nano-objects such as blood cells. It seems that the smaller, the more neutral and the more hydrophilic the carrier surface, the longer its plasma life. For a dual nanoparticle with a core and a shell, the engineering of the surface with hydrophilic macromolecules helps reducing plasma adsorption.[163] Polysaccharides (e.g. Dextran) and poly(ethers) (e.g. poly(ethylene oxide)) have been investigated for giving long circulation times to nanoparticles. Once the circulating life time is improved it is possible to graft ligands with a specific affinity toward target sites, though the formation of a protein corona seems to impair the availability of the ligands at the surface of the nanoparticles. Another strategy is to direct the nanoparticles with an external magnetic field if they present magnetic properties. There is a crucial need to minimize aggregation and biofouling. The solution is engineering the surface of the IONPs to make them stable for a long period of time in physiological conditions, meaning high salt and protein concentrations.[164] IONPs reaching these characteristics are often referred as stealth.

7.2. Targeting solid tumors and metastasis

The EPR effect is a concept by which particles accumulate preferentially in tumor tissues as compared to healthy tissues (**Figure 33**). The blood vessels formed to carry nutritional and oxygen supply to the quickly growing tumor cells present defects. Their vasculatures exhibit wide fenestrations and lumen, leading to extravasation of fluids and accumulation of particles and macromolecules. A lack of lymphatic drainage is furthermore added to this permeation property. According to the EPR concept, particles having appropriate sizes and able to circulate for long durations in the blood flow passively target tumors. Following the discovery of the EPR effect in the 1980s by Maeda, and its strong support by preclinical studies, multiple nanovectors were developed to increase the specific delivery of drugs to tumors. This theoretically allows increasing the dose in the region of interest. Liposomal doxorubicin (Doxil, Janssen Biotech, Inc) exhibits enhanced tumor targeting, with a clearance half-life 100 fold greater than free doxorubicin.[165] Unfortunately, clinical studies on other forms of nano-sized drug delivery systems later indicated that EPR is not as reliable as thought and strongly depends on the tumor type. In addition, there is a significant difference of EPR

effect between preclinical studies on rodent models and clinical studies on human.[166] Nevertheless, a wide library of nanomedicines without active targeting properties is used clinically and show benefits when used for specific types of tumors.[167] The nanovectors can be micelles, nanoparticles, polymer-drug conjugates or liposomes, evidencing the diversity of possible designs.

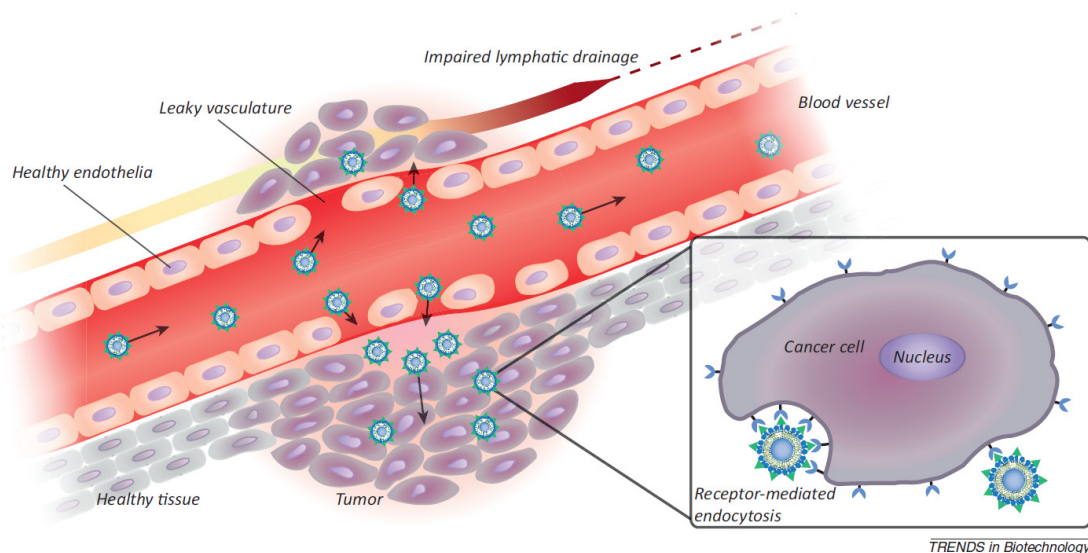


Figure 33 Passive targeting of nanoparticles to tumors through the enhanced permeability and retention (EPR) effect. Angiogenic vessels in rapidly growing tumors are abnormally constructed with large vascular fenestrae and impaired lymphatic drainage. As a result, particles <200 nm preferentially accumulate in the tumor interstitium. Post-extravasation, intracellular uptake of ligand-targeted liposomes is facilitated by receptor-mediated endocytosis.[165]

Different strategies were developed in order to target cancerous cells on humans, while relying less on the EPR effect. A different class of nanomedicines with active targeting properties makes use of ligands such as antibodies or peptides. They are grafted at the surface of the nanovectors and bind on receptors of the target site. They can target receptors of cancer cells (folate, transferrin, galactosamine) and improve the uptake. Smart systems delivering drugs upon exposure to external stimuli (heat, light, ultrasound, and magnetic fields) can be used to even further improve the selective local administration of a drug. It is tempting to design complex nanovectors able to fulfill all these requirements, but so far, the best solutions for tumor treatment came from the simplest strategies.[1, 167] Additional challenges can arise depending on the location of the tumor. For example, glioblastoma is a cancer that begins in the brain. Nanovectors therefore need to cross the blood-brain barrier (BBB) to reach their target. This selective and semi-permeable membrane separates the circulating blood from the brain extracellular fluid. Only nanoparticles of small size (tens of nanometers) can cross the barrier and access the tumors.

7.3. Understanding the mechanism of cell uptake

Different methods can be used to study the interactions between nanoparticles and cells. Fluorescence microscopy is widely used, preferentially on live-cells to avoid fixation artifacts. TEM

allows observing structures smaller than with visible light, providing images with satisfying resolution.

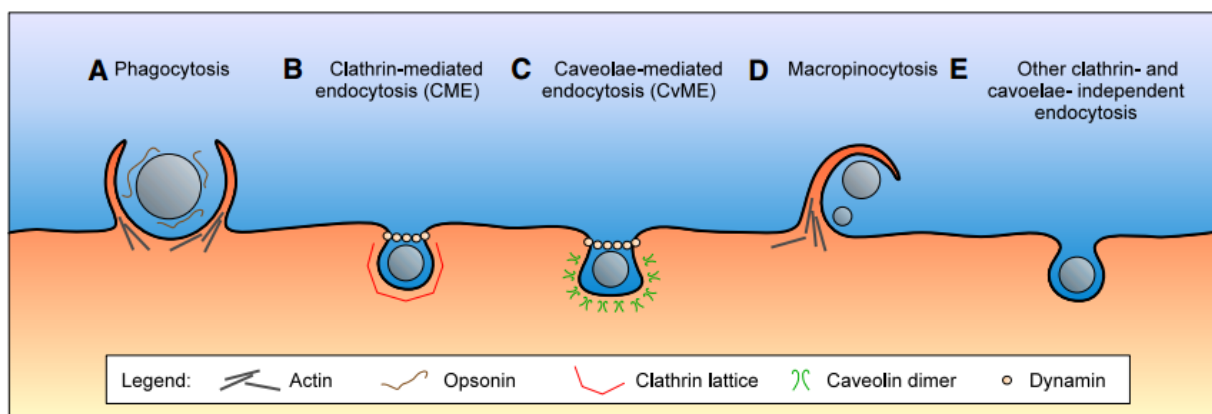


Figure 34 Principal nanocarrier internalization pathways in mammalian cells. **A** Phagocytosis is an actin-based mechanism occurring primarily in professional phagocytes, such as macrophages, and closely associated with opsonization. **B** Clathrin-mediated endocytosis is a widely shared pathway of nanoparticle internalization, associated with the formation of a clathrin lattice and depending on the GTPase dynamin. **C** Caveolae-mediated endocytosis occurs in typical flaskshaped invaginations of the membrane coated with caveolin dimers, also depending on dynamin. **D** Macropinocytosis is an actin-based pathway, engulfing nanoparticles and the extracellular milieu with a poor selectivity. **E** Other endocytosis pathways can be involved in the nanoparticle internalization, independent of both clathrin and caveolae.[168]

The cell uptake mainly depends on the physicochemical properties of the nanoparticles.[169] Several parameters of importance were reported such as the size, shape, rigidity, charge and surface chemistry. Dimensions larger than 200 nm leads to phagocytosis, smaller dimensions usually lead to endocytosis (**Figure 34**). The influence of the shape is still debated, but spherical nanoparticles seem to internalize more efficiently. The surface charge seems to influence the uptake as cationic nanoparticles have better affinity with cellular membranes. The surface chemistry dictates the protein corona formation and opsonin-driven phagocytosis, and the nanoparticles are most likely taken up when a critical concentration is reached at the surface of the cells. This could explain the relatively high local concentrations of nanoparticles inside endocytic compartments.

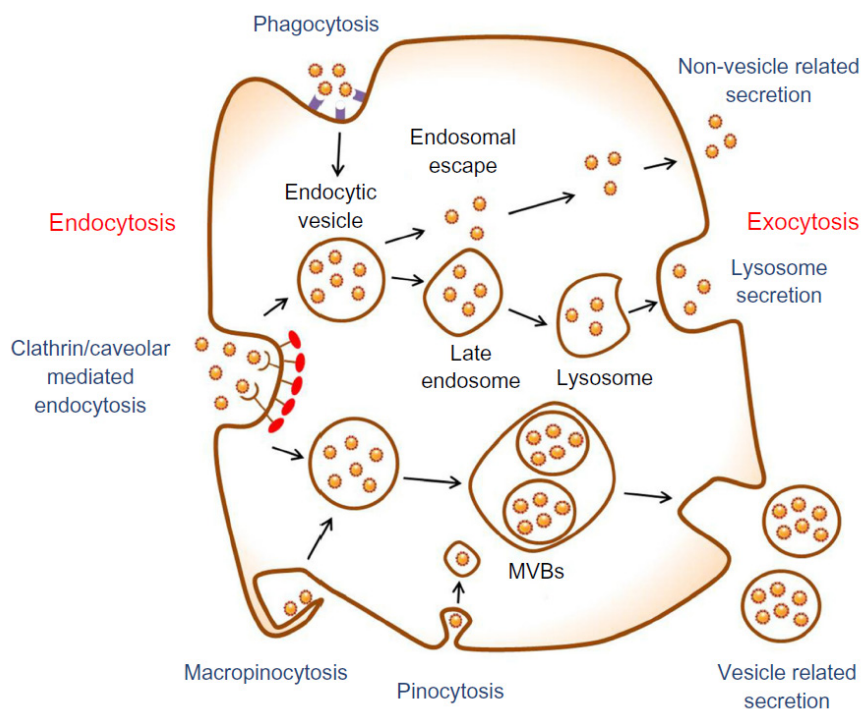


Figure 35 Schematic of endocytosis and exocytosis patterns of nanoparticles. Nanoparticles enter the cell via four types of pathway: clathrin/caveolar-mediated endocytosis, phagocytosis, macropinocytosis, and pinocytosis. Nanoparticles exit the cell via three types of pathway: lysosome secretion, vesicle-related secretion, and non-vesicle-related secretion.[170]

Nanoparticles uptaken by cells end-up in specific compartments depending on their internalizations pathways. The organelles are transported inside the cytosol through motor-dependent movement or by diffusion, and vesicles can undergo fusion events (**Figure 35**). In general, exogenous materials tend to accumulate in the perinuclear region. As reported by Collinet *et al.*, there is a strong correlation between the endosome distance from the nucleus, their number inside the cells, and their size.[171] The internalization compartments have their own characteristic pH values, lysosome being acidic, with a pH value of 4.5. This property can be exploited for drug delivery applications using pH sensitive triggers.

8. References

1. Lammers, T., F. Kiessling, W.E. Hennink, and G. Storm, *Drug targeting to tumors: Principles, pitfalls and (pre-) clinical progress*. Journal of Controlled Release, 2012. **161**(2): p. 175-187.
2. Krukemeyer, M., V. Krenn, F. Huebner, W. Wagner, and R. Resch, *History and Possible Uses of Nanomedicine Based on Nanoparticles and Nanotechnological Progress*. J Nanomed Nanotechnol, 2015. **6**(6): p. 2157-7439.
3. *Nanotechnology in Medical Applications: The Global Market*. BCC Research Market Forecasting, 2010.
4. Moghimi, S.M., A.C. Hunter, and J.C. Murray, *Nanomedicine: current status and future prospects*. FASEB Journal, 2005. **19**(3).
5. Hillaireau, H. and P. Couvreur, *Nanocarriers' entry into the cell: relevance to drug delivery*. Cell. Mol. Life Sci., 2009. **66**: p. 2873-2896.
6. *Applications des nanotechnologies à la médecine*. leem Comité Biotech, 2013.
7. Mejías, R., S. Pérez-Yagüe, L. Gutiérrez, L.I. Cabrera, R. Spada, P. Acedo, C.J. Serna, F.J. Lázaro, Á. Villanueva, M.d.P. Morales, and D.F. Barber, *Dimercaptosuccinic acid-coated magnetite nanoparticles for magnetically guided in vivo delivery of interferon gamma for cancer immunotherapy*. Biomaterials, 2011. **32**(11): p. 2938-2952.
8. Maier-Hauff, K., F. Ulrich, D. Nestler, H. Niehoff, P. Wust, B. Thiesen, H. Orawa, V. Budach, and A. Jordan, *Efficacy and safety of intratumoral thermotherapy using magnetic iron-oxide nanoparticles combined with external beam radiotherapy on patients with recurrent glioblastoma multiforme*. Journal of Neuro-Oncology, 2011. **103**(2): p. 317-324.
9. Cornell, M. and U. Schwertmann, *The Iron Oxides*. 1996, Wiley-VCH: Weinheim.
10. Mornet, S., S. Vasseur, F. Grasset, and E. Duguet, *Magnetic nanoparticle design for medical diagnosis and therapy*. Materials Chemistry, 2004. **14**: p. 2161-2175.
11. Berkovitch, M., A. Livne, G. Lushkov, M. Segal, C. Talmor, Y. Bentur, J. Klein, and G. Koren, *The efficacy of oral deferiprone in acute iron poisoning*. The American Journal of Emergency Medicine, 2000. **18**(1): p. 36-40.
12. Pankhurst, Q.A., J. Connolly, J.S. K., and J. Dobson, *Applications of magnetic nanoparticles in biomedicine*. J. Phys. D: Appl. Phys., 2003. **36**: p. 167-181.
13. Colombo, M., S. Carregal-Romero, M.F. Casula, L. Gutierrez, M.P. Morales, I.B. Bohm, J.T. Heverhagen, D. Prosperi, and W.J. Parak, *Biological applications of magnetic nanoparticles*. Chemical Society Reviews, 2012. **41**(11): p. 4306-4334.
14. Frenkel, J. and J. Dorfman, *Spontaneous and induced magnetisation in ferromagnetic bodies*. Nature, 1930. **126**: p. 274-275.
15. Vergés, M.A., R. Costo, A.G. Roca, J.F. Marco, G.F. Goya, C.J. Serna, and M.P. Morales, *Uniform and water stable magnetite nanoparticles with diameters around the monodomain-multidomain limit*. Journal of Physics D: Applied Physics, 2008. **41**(13): p. 134003.
16. Ortega, R.A. and T.D. Giorgio, *A mathematical model of superparamagnetic iron oxide nanoparticle magnetic behavior to guide the design of novel nanomaterials*. Journal of Nanoparticle Research, 2012. **14**(12).
17. Bean, C.P. and J.D. Livingston, *Superparamagnetism*. Journal of Applied Physics, 1959. **30**.
18. Yoo, D., J.-H. Lee, T.-H. Shin, and J. Cheon, *Theranostic Magnetic Nanoparticles*. Accounts of chemical research, 2011. **44**(10): p. 863-874.
19. Iwamoto, T. and T. Ishigaki, *Fabrication of iron oxide nanoparticles using laser ablation in liquids*. Journal of Physics: Conference Series, 2013. **441**(1): p. 012034.
20. Arbain, R., M. Othman, and S. Palaniandy, *Preparation of iron oxide nanoparticles by mechanical milling*. Minerals Engineering, 2011. **24**(1): p. 1-9.
21. Périgo, E.A., S.C. Silva, E.M.B.d. Sousa, A.A. Freitas, R. Cohen, L.C.C.M. Nagamine, H. Takiishi, and F.J.G. Landgraf, *Properties of nanoparticles prepared from NdFeB-based compound for magnetic hyperthermia application*. Nanotechnology, 2012. **23**(17): p. 175704.

22. Horner, O., S. Neveu, S. de Montredon, J.-M. Siaugue, and V. Cabuil, *Hydrothermal synthesis of large maghemite nanoparticles: influence of the pH on the particle size*. Journal of Nanoparticle Research, 2009. **11**(5): p. 1247-1250.
23. Nguyen, T.-D. and T.-O. Do, *Size- and Shape-Controlled Synthesis of Monodisperse Metal Oxide and Mixed Oxide Nanocrystals*, in *Nanocrystal*, Y. Masuda, Editor. 2011, InTech: Rijeka. p. Ch. 02.
24. Daou, T.J., G. Pourroy, S. Bégin-Colin, J.M. Grenèche, C. Ulhaq-Bouillet, P. Legaré, P. Bernhardt, C. Leuvrey, and G. Rogez, *Hydrothermal Synthesis of Monodisperse Magnetite Nanoparticles*. Chemistry of Materials, 2006. **18**(18): p. 4399-4404.
25. Fortin, J.-P., C. Wilhelm, J. Servais, C. Ménager, J.-C. Bacri, and F. Gazeau, *Size-Sorted Anionic Iron Oxide Nanomagnets as Colloidal Mediators for Magnetic Hyperthermia*. Journal of the American Chemical Society, 2007. **129**(9): p. 2628-2635.
26. Massart, R., *Preparation of aqueous magnetic liquids in alkaline and acidic media*. IEEE Transactions on Magnetics, 1981. **17**(2): p. 1247-1248.
27. Hyeon, T., S.S. Lee, J. Park, Y. Chung, and H.B. Na, *Synthesis of Highly Crystalline and Monodisperse Maghemite Nanocrystallites without a Size-Selection Process*. Journal of the American Chemical Society, 2001. **123**(51): p. 12798-12801.
28. Abou-Hassan, A., O. Sandre, and V. Cabuil, *Microfluidic Synthesis of Iron Oxide and Oxyhydroxide Nanoparticles*, in *Microfluidic Devices in Nanotechnology*. 2010, John Wiley & Sons, Inc. p. 323-360.
29. Sun, S. and H. Zeng, *Size-Controlled Synthesis of Magnetite Nanoparticles*. Journal of the American Chemical Society, 2002. **124**(28): p. 8204-8205.
30. Park, J., K. An, Y. Hwang, J.-G. Park, H.-J. Noh, J.-Y. Kim, J.-H. Park, N.-M. Hwang, and T. Hyeon, *Ultra-large-scale syntheses of monodisperse nanocrystals*. Nat Mater, 2004. **3**(12): p. 891-895.
31. Baaziz, W., B.P. Pichon, S. Fleutot, Y. Liu, C. Lefevre, J.-M. Grenèche, M. Toumi, T. Mhiri, and S. Begin-Colin, *Magnetic Iron Oxide Nanoparticles: Reproducible Tuning of the Size and Nanosized-Dependent Composition, Defects, and Spin Canting*. The Journal of Physical Chemistry C, 2014. **118**(7): p. 3795-3810.
32. van Geuns, R.-J.M., P.A. Wielopolski, H.G. de Bruin, B.J. Rensing, P.M.A. van Ooijen, M. Hulshoff, M. Oudkerk, and P.J. de Feyter, *Basic principles of magnetic resonance imaging*. Progress in Cardiovascular Diseases, 1999. **42**(2): p. 149-156.
33. Tromsdorf, U.I., O.T. Bruns, S.C. Salmen, U. Beisiegel, and H. Weller, *A Highly Effective, Nontoxic T1 MR Contrast Agent Based on Ultrasmall PEGylated Iron Oxide Nanoparticles*. Nano Letters, 2009. **9**(12): p. 4434-4440.
34. Tourdias, T., S. Roggerone, M. Filippi, M. Kanagaki, M. Rovaris, D.H. Miller, K.G. Petry, B. Brochet, J.-P. Pruvo, E.-W. Radüe, and V. Dousset, *Assessment of Disease Activity in Multiple Sclerosis Phenotypes with Combined Gadolinium- and Superparamagnetic Iron Oxide-enhanced MR Imaging*. Radiology, 2012. **264**(1): p. 225-233.
35. Dahl, O. and J. Overgaard, *A Century With Hyperthermic Oncology In Scandinavia*. Acta Oncologica, 1995. **34**(8): p. 1075-1083.
36. Guardia, P., R.D. Corato, L. Lartigue, C. Wilhelm, A. Espinosa, M. Garcia-Hernandez, F. Gazeau, L. Manna, and T. Pellegrino, *Water-Soluble Iron Oxide Nanocubes with High Values of Specific Absorption Rate for Cancer Cell Hyperthermia Treatment*. ACS Nano, 2012. **6**(4): p. 3080-3091.
37. Liu, X., H.-j. Chen, X. Chen, Y. Alfadhl, J. Yu, and D. Wen, *Radiofrequency heating of nanomaterials for cancer treatment: Progress, controversies, and future development*. Applied Physics Reviews, 2015. **2**(1): p. 011103.
38. *Front Matter*, in *Physics of Thermal Therapy*. 2012, Taylor & Francis. p. i-xvi.
39. Gilchrist, R.K., R. Medal, W.D. Shorey, R.C. Hanselman, J.C. Parrott, and C.B. Taylor, *Selective Inductive Heating of Lymph Nodes*. Annals of Surgery, 1957. **146**(4): p. 596-606.
40. Ivkov, R., *Magnetic nanoparticle hyperthermia: A new frontier in biology and medicine?* International Journal of Hyperthermia, 2013. **29**(8): p. 703-705.
41. Martinez-Boubeta, C., K. Simeonidis, A. Makridis, M. Angelakeris, O. Iglesias, P. Guardia, A. Cabot, L. Yedra, S. Estradé, F. Peiró, Z. Saghi, P.A. Midgley, I. Conde-Leborán, D.

- Serantes, and D. Baldomir, *Learning from Nature to Improve the Heat Generation of Iron-Oxide Nanoparticles for Magnetic Hyperthermia Applications*. 2013. **3**: p. 1652.
42. Guardia, P., R. Di Corato, L. Lartigue, C. Wilhelm, A. Espinosa, M. Garcia-Hernandez, F. Gazeau, L. Manna, and T. Pellegrino, *Water-Soluble Iron Oxide Nanocubes with High Values of Specific Absorption Rate for Cancer Cell Hyperthermia Treatment*. ACS Nano, 2012. **6**(4): p. 3080-3091.
 43. Yu, W.W., J.C. Falkner, C.T. Yavuz, and V.L. Colvin, *Synthesis of monodisperse iron oxide nanocrystals by thermal decomposition of iron carboxylate salts*. Chemical Communications, 2004(20): p. 2306-2307.
 44. Salas, G., C. Casado, F.J. Teran, R. Miranda, C.J. Serna, and M.P. Morales, *Controlled synthesis of uniform magnetite nanocrystals with high-quality properties for biomedical applications*. Journal of Materials Chemistry, 2012. **22**(39): p. 21065-21075.
 45. Levy, M., A. Quarta, A. Espinosa, A. Figuerola, C. Wilhelm, M. García-Hernández, A. Genovese, A. Falqui, D. Alloyeau, R. Buonsanti, P.D. Cozzoli, M.A. García, F. Gazeau, and T. Pellegrino, *Correlating Magneto-Structural Properties to Hyperthermia Performance of Highly Monodisperse Iron Oxide Nanoparticles Prepared by a Seeded-Growth Route*. Chemistry of Materials, 2011. **23**(18): p. 4170-4180.
 46. Salas, G., C. Casado, F.J. Teran, R. Miranda, C.J. Serna, and M.P. Morales, *Controlled synthesis of uniform magnetite nanocrystals with high-quality properties for biomedical applications*. J. Mater. Chem., 2012. **22**: p. 21065-21075.
 47. Euliss, L.E., S.G. Grancharov, S. O'Brien, T.J. Deming, G.D. Stucky, C.B. Murray, and G.A. Held, *Cooperative Assembly of Magnetic Nanoparticles and Block Copolypeptides in Aqueous Media*. Nano Letters, 2003. **3**(11): p. 1489-1493.
 48. De Palma, R., S. Peeters, M.J. Van Bael, H. Van den Rul, K. Bonroy, W. Laureyn, J. Mullens, G. Borghs, and G. Maes, *Silane Ligand Exchange to Make Hydrophobic Superparamagnetic Nanoparticles Water-Dispersible*. Chemistry of Materials, 2007. **19**(7): p. 1821-1831.
 49. Pellegrino, T., L. Manna, S. Kudera, T. Liedl, D. Koktysh, A.L. Rogach, S. Keller, J. Rädler, G. Natile, and W.J. Parak, *Hydrophobic Nanocrystals Coated with an Amphiphilic Polymer Shell: A General Route to Water Soluble Nanocrystals*. Nano Letters, 2004. **4**(4): p. 703-707.
 50. Chen, Z.P., Y. Zhang, S. Zhang, J.G. Xia, J.W. Liu, K. Xu, and N. Gu, *Preparation and characterization of water-soluble monodisperse magnetic iron oxide nanoparticles via surface double-exchange with DMSA*. Colloids and Surfaces A: Physicochemical and Engineering Aspects, 2008. **316**(1): p. 210-216.
 51. Lee, J.-H., J.-t. Jang, J.-s. Choi, S.H. Moon, S.-h. Noh, J.-w. Kim, J.-G. Kim, I.-S. Kim, K.I. Park, and J. Cheon, *Exchange-coupled magnetic nanoparticles for efficient heat induction*. Nat Nano, 2011. **6**(7): p. 418-422.
 52. Gavrillov-Isaac, V., S. Neveu, V. Dupuis, D. Taverna, A. Gloter, and V. Cabuil, *Synthesis of Trimagnetic Multishell MnFe₂O₄@CoFe₂O₄@NiFe₂O₄ Nanoparticles*. Small, 2015. **11**(22): p. 2614-2618.
 53. Hugounenq, P., M. Levy, D. Alloyeau, L. Lartigue, E. Dubois, V. Cabuil, C. Ricolleau, S. Roux, C. Wilhelm, F. Gazeau, and R. Bazzi, *Iron Oxide Monocrystalline Nanoflowers for Highly Efficient Magnetic Hyperthermia*. J. Phys. Chem. C, 2012. **116**(29): p. 15702-15712.
 54. Caruntu, D., Y. Remond, N.H. Chou, M.-J. Jun, G. Caruntu, J. He, G. Goloverda, C. O'Connor, and V. Kolesnichenko, *Reactivity of 3d Transition Metal Cations in Diethylene Glycol Solutions. Synthesis of Transition Metal Ferrites with the Structure of Discrete Nanoparticles Complexed with Long-Chain Carboxylate Anions*. Inorganic Chemistry, 2002. **41**(23): p. 6137-6146.
 55. Baldi, G., D. Bonacchi, F. Innocenti, G. Lorenzi, M. Bitossi, P. Ferruti, E. Ranucci, A. Ricci, and F.M. Comes, *Magnetic nanoparticles for the application in hyperthermia, preparation thereof and use in constructs having a pharmacological application*. 2008, Google Patents.
 56. Kucheryavy, P., J. He, V.T. John, P. Maharjan, L. Spinu, G.Z. Goloverda, and V.L. Kolesnichenko, *Superparamagnetic Iron Oxide Nanoparticles with Variable Size and an Iron Oxidation State as Prospective Imaging Agents*. Langmuir, 2013. **29**(2): p. 710-716.

57. Baldi, G., D. Bonacchi, M.C. Franchini, D. Gentili, G. Lorenzi, A. Ricci, and C. Ravagli, *Synthesis and Coating of Cobalt Ferrite Nanoparticles: A First Step toward the Obtainment of New Magnetic Nanocarriers*. Langmuir, 2007. **23**(7): p. 4026-4028.
58. Caruntu, D., G. Caruntu, Y. Chen, C.J. O'Connor, G. Goloverda, and V.L. Kolesnichenko, *Synthesis of Variable-Sized Nanocrystals of Fe₃O₄ with High Surface Reactivity*. Chemistry of Materials, 2004. **16**(25): p. 5527-5534.
59. Hugounenq, P., M. Levy, D. Alloyeau, L. Lartigue, E. Dubois, V. Cabuil, C. Ricolleau, S. Roux, C. Wilhelm, F. Gazeau, and R. Bazzi, *Iron Oxide Monocrystalline Nanoflowers for Highly Efficient Magnetic Hyperthermia*. The Journal of Physical Chemistry C, 2012. **116**(29): p. 15702-15712.
60. Ramesh, R., M. Rajalakshmi, C. Muthamizhchelvan, and S. Ponnusamy, *Synthesis of Fe₃O₄ nanoflowers by one pot surfactant assisted hydrothermal method and its properties*. Materials Letters, 2012. **70**: p. 73-75.
61. Cheng, C., F. Xu, and H. Gu, *Facile synthesis and morphology evolution of magnetic iron oxide nanoparticles in different polyol processes*. New Journal of Chemistry, 2011. **35**(5): p. 1072-1079.
62. Bi, X.-X., B. Ganguly, G.P. Huffman, F.E. Huggins, M. Endo, and P.C. Eklund, *Nanocrystalline α -Fe, Fe₃C, and Fe₇C₃ produced by CO₂ laser pyrolysis*. Journal of Materials Research, 1993. **8**(7): p. 1666-1674.
63. Veintemillas-Verdaguer, S., M.P. Morales, and C.J. Serna, *Continuous production of γ -Fe₂O₃ ultrafine powders by laser pyrolysis*. Materials Letters, 1998. **35**(3): p. 227-231.
64. Popovici, E., F. Dumitrache, I. Morjan, R. Alexandrescu, V. Ciupina, G. Prodan, L. Vekas, D. Bica, O. Marinica, and E. Vasile, *Iron/iron oxides core-shell nanoparticles by laser pyrolysis: Structural characterization and enhanced particle dispersion*. Applied Surface Science, 2007. **254**(4): p. 1048-1052.
65. Epherre, R., E. Duguet, S. Mornet, E. Pollert, S. Louguet, S. Lecommandoux, C. Schatz, and G. Goglio, *Manganite perovskite nanoparticles for self-controlled magnetic fluid hyperthermia: about the suitability of an aqueous combustion synthesis route*. Journal of Materials Chemistry, 2011. **21**(12): p. 4393-4401.
66. Bilecka, I., M. Kubli, E. Amstad, and M. Niederberger, *Simultaneous formation of ferrite nanocrystals and deposition of thin films via a microwave-assisted nonaqueous sol-gel process*. Journal of Sol-Gel Science and Technology, 2011. **57**(3): p. 313-322.
67. Blanco-Andujar, C., D. Ortega, P. Southern, Q.A. Pankhurst, and N.T.K. Thanh, *High performance multi-core iron oxide nanoparticles for magnetic hyperthermia: microwave synthesis, and the role of core-to-core interactions*. Nanoscale, 2015. **7**(5): p. 1768-1775.
68. van Leeuwen, M.E. and B. Smit, *What makes a polar liquid a liquid?* Physical Review Letters, 1993. **71**(24): p. 3991-3994.
69. Sharma, H.A., *MRI physics - basic principles*. Acta Neuropsychiatrica, 2009. **21**(4): p. 200-201.
70. Atle, B. and J. Lars, *The utility of superparamagnetic contrast agents in MRI: theoretical consideration and applications in the cardiovascular system*. NMR Biomed, 2004. **17**: p. 465-477.
71. Wáng, Y.X.J. and J.-M. Idée, *A comprehensive literatures update of clinical researches of superparamagnetic resonance iron oxide nanoparticles for magnetic resonance imaging*. Quantitative Imaging in Medicine and Surgery, 2017. **7**(1): p. 88-122.
72. Wang, Y.-X., *Superparamagnetic iron oxide based MRI contrast agents: Current status of clinical application*. Quant Imaging Med Surg, 2011. **1**: p. 35-40.
73. Borase, T., T. Ninjbadgar, A. Kapetanakis, S. Roche, R. O'Connor, C. Kerskens, A. Heise, and D. Brougham, *Stable Aqueous Dispersions of Glycopeptide-Grafted Selectably Functionalized Magnetic Nanoparticles*. Angewandte Chemie, 2013. **52**(11): p. 3164-3167.
74. Lee, J., S. Mahendra, and P.J.J. Alvarez, *Nanomaterials in the Construction Industry: A Review of Their Applications and Environmental Health and Safety Considerations*. ACS Nano, 2010. **4**(7): p. 3580-3590.
75. Lenert, A., D.M. Bierman, Y. Nam, W.R. Chan, I. Celanovic, M. Soljagic, and E.N. Wang, *A nanophotonic solar thermophotovoltaic device*. Nat Nano, 2014. **9**(2): p. 126-130.

76. Riehemann, K., S.W. Schneider, T.A. Luger, B. Godin, M. Ferrari, and H. Fuchs, *Nanomedicine—Challenge and Perspectives*. Angewandte Chemie International Edition, 2009. **48**(5): p. 872-897.
77. Hu, J., K.P. Johnston, and R.O. Williams, *Nanoparticle Engineering Processes for Enhancing the Dissolution Rates of Poorly Water Soluble Drugs*. Drug Development and Industrial Pharmacy, 2004. **30**(3): p. 233-245.
78. Robert, C., C.S. Wilson, A. Venuta, M. Ferrari, and C.D. Arreto, *Evolution of the scientific literature on drug delivery: A 1974–2015 bibliometric study*. Journal of Controlled Release, 2017. **260**: p. 226-233.
79. Allen, T.M. and P.R. Cullis, *Liposomal drug delivery systems: From concept to clinical applications*. Advanced Drug Delivery Reviews, 2013. **65**(1): p. 36-48.
80. Callender, S.P., J.A. Mathews, K. Kobernyk, and S.D. Wettig, *Microemulsion utility in pharmaceuticals: Implications for multi-drug delivery*. International Journal of Pharmaceutics, 2017. **526**(1–2): p. 425-442.
81. Zhang, R.X., H.L. Wong, H.Y. Xue, J.Y. Eoh, and X.Y. Wu, *Nanomedicine of synergistic drug combinations for cancer therapy – Strategies and perspectives*. Journal of Controlled Release, 2016. **240**: p. 489-503.
82. Masood, F., *Polymeric nanoparticles for targeted drug delivery system for cancer therapy*. Materials Science and Engineering: C, 2016. **60**: p. 569-578.
83. Kumari, A., S.K. Yadav, and S.C. Yadav, *Biodegradable polymeric nanoparticles based drug delivery systems*. Colloids and Surfaces B: Biointerfaces, 2010. **75**(1): p. 1-18.
84. Fonseca, C., S. Simões, and R. Gaspar, *Paclitaxel-loaded PLGA nanoparticles: preparation, physicochemical characterization and in vitro anti-tumoral activity*. Journal of Controlled Release, 2002. **83**(2): p. 273-286.
85. Indulekha, S., P. Arunkumar, D. Bahadur, and R. Srivastava, *Dual responsive magnetic composite nanogels for thermo-chemotherapy*. Colloids and Surfaces B: Biointerfaces, 2017. **155**: p. 304-313.
86. Mertz, D., O. Sandre, and S. Bégin-Colin, *Drug releasing nanoplatfoms activated by alternating magnetic fields*. Biochimica et Biophysica Acta (BBA) - General Subjects, 2017. **1861**(6): p. 1617-1641.
87. Ulbrich, K., K. Holá, V. Šubr, A. Bakandritsos, J. Tuček, and R. Zbořil, *Targeted Drug Delivery with Polymers and Magnetic Nanoparticles: Covalent and Noncovalent Approaches, Release Control, and Clinical Studies*. Chemical Reviews, 2016. **116**(9): p. 5338-5431.
88. Sanson, C., O. Diou, J. Thévenot, E. Ibarboure, A. Soum, A. Brûlet, S. Miraux, E. Thiaudière, S. Tan, A. Brisson, V. Dupuis, O. Sandre, and S. Lecommandoux, *Doxorubicin Loaded Magnetic Polymersomes: Theranostic Nanocarriers for MR Imaging and Magneto-Chemotherapy*. ACS Nano, 2011. **5**(2): p. 1122-1140.
89. Sun, P., Y. Zhang, L. Shi, and Z. Gan, *Thermosensitive Nanoparticles Self-Assembled from PCL-b-PEO-b-PNIPAAm Triblock Copolymers and their Potential for Controlled Drug Release*. Macromolecular Bioscience, 2010. **10**(6): p. 621-631.
90. Liu, T.-Y., S.-H. Hu, K.-H. Liu, R.-S. Shaiu, D.-M. Liu, and S.-Y. Chen, *Instantaneous Drug Delivery of Magnetic/Thermally Sensitive Nanospheres by a High-Frequency Magnetic Field*. Langmuir, 2008. **24**(23): p. 13306-13311.
91. Louguet, S., B. Rousseau, R. Epherre, N. Guidolin, G. Goglio, S. Mornet, E. Duguet, S. Lecommandoux, and C. Schatz, *Thermoresponsive polymer brush-functionalized magnetic manganite nanoparticles for remotely triggered drug release*. Polymer Chemistry, 2012. **3**(6): p. 1408-1417.
92. Kievit, F.M., F.Y. Wang, C. Fang, H. Mok, K. Wang, J.R. Silber, R.G. Ellenbogen, and M. Zhang, *Doxorubicin loaded iron oxide nanoparticles overcome multidrug resistance in cancer in vitro*. Journal of Controlled Release, 2011. **152**(1): p. 76-83.
93. Modi, S. and B.D. Anderson, *Determination of Drug Release Kinetics from Nanoparticles: Overcoming Pitfalls of the Dynamic Dialysis Method*. Molecular Pharmaceutics, 2013. **10**(8): p. 3076-3089.

94. Alhareth, K., C. Vauthier, C. Gueutin, G. Ponchel, and F. Moussa, *HPLC quantification of doxorubicin in plasma and tissues of rats treated with doxorubicin loaded poly(alkylcyanoacrylate) nanoparticles*. *Journal of Chromatography B*, 2012. **887**: p. 128-132.
95. Jiang, F., Y. Fu, Y. Zhu, Z. Tang, and P. Sheng, *Fabrication of iron oxide/silica core-shell nanoparticles and their magnetic characteristics*. *Journal of Alloys and Compounds*, 2012. **543**: p. 43-48.
96. Wang Wang, J. Luo, Q. Fan, M. Suzuki, I.S. Suzuki, M.H. Engelhard, Y. Lin, N. Kim, J.Q. Wang, and C.-J. Zhong, *Monodispersed Core-Shell Fe₃O₄@Au Nanoparticles*. *The Journal of Physical Chemistry B*, 2005. **109**(46): p. 21593-21601.
97. Xu, C., K. Xu, H. Gu, R. Zheng, H. Liu, X. Zhang, Z. Guo, and B. Xu, *Dopamine as A Robust Anchor to Immobilize Functional Molecules on the Iron Oxide Shell of Magnetic Nanoparticles*. *J. Am. Chem. Soc.*, 2004. **126**(32): p. 9938-9939.
98. Gao, X., K. Ni, C. Zhao, Y. Ren, and D. Wei, *Enhancement of the activity of enzyme immobilized on polydopamine-coated iron oxide nanoparticles by rational orientation of formate dehydrogenase*. *Journal of Biotechnology*, 2014. **188**: p. 36-41.
99. Long, Y., L. Xiao, and Q. Cao, *Co-polymerization of catechol and polyethylenimine on magnetic nanoparticles for efficient selective removal of anionic dyes from water*. *Powder Technology*, 2017. **310**: p. 24-34.
100. Bee, A., R. Massart, and S. Neveu, *Synthesis of very fine maghemite particles*. *Journal of Magnetism and Magnetic Materials*, 1995. **149**(1-2): p. 6-9.
101. Saraswathy, A., S.S. Nazeer, M. Jeevan, N. Nimi, S. Arumugam, V.S. Harikrishnan, P.R.H. Varma, and R.S. Jayasree, *Citrate coated iron oxide nanoparticles with enhanced relaxivity for in vivo magnetic resonance imaging of liver fibrosis*. *Colloids and Surfaces B: Biointerfaces*, 2014. **117**: p. 216-224.
102. Kotsmar, C., K.Y. Yoon, H. Yu, S.Y. Ryoo, J. Barth, S. Shao, M. Prodanović, T.E. Milner, S.L. Bryant, C. Huh, and K.P. Johnston, *Stable Citrate-Coated Iron Oxide Superparamagnetic Nanoclusters at High Salinity*. *Industrial & Engineering Chemistry Research*, 2010. **49**(24): p. 12435-12443.
103. Safi, M., H. Sarrouj, O. Sandre, N. Mignet, and J.F. Berret, *Interactions between sub-10-nm iron and cerium oxide nanoparticles and 3T3 fibroblasts: the role of the coating and aggregation state*. *Nanotechnology*, 2010. **21**(14): p. 145103.
104. Jedlovszky-Hajdú, A., F.B. Bombelli, M.P. Monopoli, E. Tombácz, and K.A. Dawson, *Surface Coatings Shape the Protein Corona of SPIONs with Relevance to Their Application in Vivo*. *Langmuir*, 2012. **28**(42): p. 14983-14991.
105. Campelj, S., D. Makovec, and M. Drogenik, *Functionalization of magnetic nanoparticles with 3-aminopropyl silane*. *Journal of Magnetism and Magnetic Materials*, 2009. **321**(10): p. 1346-1350.
106. Takafuji, M., S. Ide, H. Ihara, and Z. Xu, *Preparation of Poly(1-vinylimidazole)-Grafted Magnetic Nanoparticles and Their Application for Removal of Metal Ions*. *Chem. Matter.*, 2004. **16**(10): p. 1977-1983.
107. Arkles, B., *Silane Coupling Agents: Connecting Across Boundaries*. Gelest, 2006(v2.0).
108. Palma, R.D., S. Peters, M.V. Bael, H.V.d. Rul, K. Bonroy, W. Laureyn, J. Mullens, G. Borghs, and G. Maes, *Silane Ligand Exchange to Make Hydrophobic Superparamagnetic Nanoparticles Water-Dispersible*. *Chem. Matter.*, 2007. **19**(7): p. 1821-1831.
109. Mohapatra, S., N. Pramanik, S. Mukherjee, S.K. Ghosh, and P. Pramanik, *A simple synthesis of amine-derivatised superparamagnetic iron oxide nanoparticles for bioapplications*. *Journal of Materials Science*, 2007. **42**(17): p. 7566-7574.
110. Yee, C., G. Kataby, A. Ulman, T. Prozorov, H. White, A. King, M. Rafailovich, J. Sokolov, and A. Gedanken, *Self-Assembled Monolayers of Alkanesulfonic and -phosphonic Acids on Amorphous Iron Oxide Nanoparticles*. *Langmuir*, 1999. **15**(21): p. 7111-7115.
111. Torrisi, V., A. Graillet, L. Vitorazi, Q. Crouzet, G. Marletta, C. Loubat, and J.F. Berret, *Preventing Corona Effects: Multiphosponic Acid Poly(ethylene glycol) Copolymers for Stable Stealth Iron Oxide Nanoparticles*. *Biomacromolecules*, 2014. **15**(8): p. 3171-3179.

112. Eamegdool, S.S., M.W. Weible, B.T.T. Pham, B.S. Hawkett, S.M. Grieve, and T. Chan-ling, *Ultrasmall superparamagnetic iron oxide nanoparticle prelabelling of human neural precursor cells*. *Biomaterials*, 2014. **35**(21): p. 5549-5564.
113. Walter, A., C. Billotey, A. Garofalo, C. Ulhaq-Bouillet, C. Lefèvre, J. Taleb, S. Laurent, L. Vander Elst, R.N. Muller, L. Lartigue, F. Gazeau, D. Felder-Flesch, and S. Begin-Colin, *Mastering the Shape and Composition of Dendronized Iron Oxide Nanoparticles To Tailor Magnetic Resonance Imaging and Hyperthermia*. *Chemistry of Materials*, 2014. **26**(18): p. 5252-5264.
114. Walter, A., A. Garofalo, P. Bonazza, F. Meyer, H. Martinez, S. Fleutot, C. Billotey, J. Taleb, D. Felder-Flesch, and S. Begin-Colin, *Effect of the Functionalization Process on the Colloidal, Magnetic Resonance Imaging, and Bioelimination Properties of Mono- or Bisphosphonate-Anchored Dendronized Iron Oxide Nanoparticles*. *ChemPlusChem*, 2017. **82**(4): p. 647-659.
115. Tudisco, C., F. Bertani, M.T. Cambria, F. Sinatra, E. Fantechi, C. Innocenti, C. Sangregorio, E. Dalcanale, and G.G. Condorelli, *Functionalization of PEGylated Fe₃O₄ magnetic nanoparticles with tetrakisphosphonate cavities for biomedical application*. *Nanoscale*, 2013. **5**(23): p. 11438-11446.
116. Wu, L., U. Glebe, and A. Boker, *Surface-initiated controlled radical polymerizations from silica nanoparticles, gold nanocrystals, and bionanoparticles*. *Polymer Chemistry*, 2015. **6**(29): p. 5143-5184.
117. Xiao, Z.-P., K.-M. Yang, H. Liang, and J. Lu, *Synthesis of Magnetic, Reactive, and Thermoresponsive Fe₃O₄ Nanoparticles via Surface-Initiated RAFT Copolymerization of N-Isopropylacrylamide and Acrolein*. *Journal of Polymer Science*, 2010. **48**(3): p. 542-550.
118. Kolb, H.C. and K.B. Sharpless, *The growing impact of click chemistry on drug discovery*. *Drug Discovery Today*, 2003. **8**(24): p. 1128-1137.
119. Nam, J., N. Won, J. Bang, H. Jin, J. Park, S. Jung, S. Jung, Y. Park, and S. Kim, *Surface engineering of inorganic nanoparticles for imaging and therapy*. *Advanced Drug Delivery Reviews*, 2013. **65**(5): p. 622-648.
120. Tron, G.C., T. Pirali, and R.A. Billington, *Click chemistry reactions in medicinal chemistry: Applications of the 1,3-dipolar cycloaddition between azides and alkynes* *Medicinal Research Reviews*, 2008. **28**(2): p. 278-308.
121. Naoki, N. and I. Yoshito, *Mechanism of Amide Formation by Carbodiimide for Bioconjugation in Aqueous Media*. *Bioconjugate Chem.*, 1995. **6**: p. 123-130.
122. Molday, R.S. and D. Mackenzie, *Immunospecific ferromagnetic iron-dextran reagents for the labeling and magnetic separation of cells*. *Journal of Immunological Methods*, 1982. **52**(3): p. 353-367.
123. Morgese, G., B. Shirmardi Shaghasemi, V. Causin, M. Zenobi-Wong, S.N. Ramakrishna, E. Reimhult, and E.M. Benetti, *Next-Generation Polymer Shells for Inorganic Nanoparticles are Highly Compact, Ultra-Dense, and Long-Lasting Cyclic Brushes*. *Angewandte Chemie International Edition*, 2017. **56**(16): p. 4507-4511.
124. Devanand, K. and J.C. Selser, *Asymptotic behavior and long-range interactions in aqueous solutions of poly(ethylene oxide)*. *Macromolecules*, 1991. **24**(22): p. 5943-5947.
125. Le Coeur, C., J. Teixeira, P. Busch, and S. Longeville, *Compression of random coils due to macromolecular crowding: Scaling effects*. *Physical Review E*, 2010. **81**(6): p. 061914.
126. Brittain, W.J. and S. Minko, *A structural definition of polymer brushes*. *Journal of Polymer Science Part A: Polymer Chemistry*, 2007. **45**(16): p. 3505-3512.
127. Wu, T., K. Efimenko, and J. Genzer, *Combinatorial Study of the Mushroom-to-Brush Crossover in Surface Anchored Polyacrylamide*. *Journal of the American Chemical Society*, 2002. **124**(32): p. 9394-9395.
128. Vogiatzis, G.G. and D.N. Theodorou, *Structure of Polymer Layers Grafted to Nanoparticles in Silica-Polystyrene Nanocomposites*. *Macromolecules*, 2013. **46**(11): p. 4670-4683.
129. Birshtein, T.M. and E.B. Zhulina, *Conformations of star-branched macromolecules*. *Polymer*, 1984. **25**(10): p. 1453-1461.
130. Masoudi, A., H.R. Madaah Hosseini, M.A. Shokrgozar, R. Ahmadi, and M.A. Oghabian, *The effect of poly(ethylene glycol) coating on colloidal stability of superparamagnetic iron oxide*

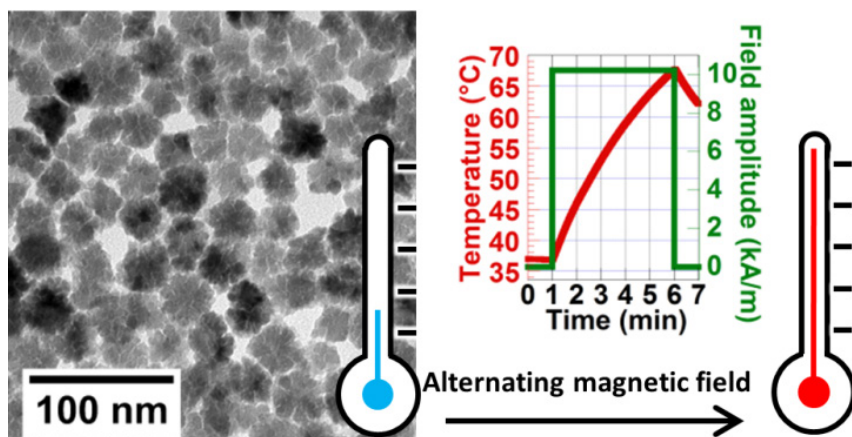
- nanoparticles as potential MRI contrast agent*. International Journal of Pharmaceutics, 2012. **433**(1): p. 129-141.
131. Galeotti, F., F. Bertini, and G. Scavia, *A controlled approach to iron oxide nanoparticles functionalization for magnetic polymer brushes*. Journal of Colloid and Interface Science, 2011.
 132. Robbes, A.-S., F. Cousin, and F. Meneau, *Controlled grafted brushes of polystyrene on magnetic γ -Fe₂O₃ nanoparticles via nitroxide-mediated polymerization*. Soft Matter, 2012.
 133. Zhang, Y., N. Kohler, and M. Zhang, *Surface modification of superparamagnetic magnetite nanoparticles and their intracellular uptake*. Biomaterials, 2002.
 134. Kohler, N., G. Fryxell, and M. Zhang, *A bifunctional Poly(ethylene glycol) Silane Immobilized on Metallic Oxide-Based Nanoparticles for Conjugation with Cell Targeting agents*. Journal of the American Chemical Society, 2004.
 135. Corot, C., P. Robert, and J.-M. Idee, *Recent advances in iron oxide nanocrystal technology for medical imaging*. Advanced Drug Delivery Reviews, 2006.
 136. Gupta, A.K. and M. Gupta, *Synthesis and surface engineering of iron oxide nanoparticles for biomedical applications*. Biomaterials, 2005.
 137. Gil, E.S. and S.M. Hudson, *Stimuli-responsive polymers and their bioconjugates*. Prog. Polym. Sci., 2004. **29**: p. 1173-1222.
 138. Ward, M.A. and T.K. Georgiou, *Thermoresponsive Polymers for Biomedical Applications*. Polymers, 2011. **3**(3): p. 1215-1242.
 139. Lopez, R.G., I.A. Facundo, M.J. Soria, and M.G. Rosales, *Synthesis and characterization of thermosensitive core-shell polymeric nanoparticles*. Polym. Bull., 2011. **67**: p. 985-995.
 140. Zhang, J.L., R.S. Srivastava, and R.D.K. Misra, *Core-Shell Magnetite Nanoparticles Surface Encapsulated with Smart Stimuli-Responsive Polymer: Synthesis, Characterization, and LCST of Viable Drug-Targeting Delivery System*. Langmuir, 2007. **23**(11): p. 6342-6351.
 141. Crassous, J.J., M. Ballauff, M. Drechsler, J. Schmidt, and Y. Talmon, *Imaging the Volume Transition in Thermosensitive Core-Shell Particles by Cryo-Transmission Electron Microscopy*. Langmuir, 2006. **22**(6): p. 2403-2406.
 142. Kurzhals, S., N. Gal, R. Zirbs, and E. Reimhult, *Aggregation of thermoresponsive core-shell nanoparticles: Influence of particle concentration, dispersant molecular weight and grafting*. Journal of Colloid and Interface Science, 2017. **500**(Supplement C): p. 321-332.
 143. Polo-Corrales, L. and C. Rinaldi, *Monitoring iron oxide nanoparticle surface temperature in an alternating magnetic field using thermoresponsive fluorescent polymers*. Journal of Applied Physics, 2012. **111**(7): p. 07B334.
 144. Urry, D.W., *Physical Chemistry of Biological Free Energy Transduction As Demonstrated by Elastic Protein-Based Polymers*. The Journal of Physical Chemistry B, 1997. **101**(51): p. 11007-11028.
 145. Meyer, D.E. and A. Chilkoti, *Quantification of the Effects of Chain Length and Concentration on the Thermal Behavior of Elastin-like Polypeptides*. Biomacromolecules, 2004. **5**(3): p. 846-851.
 146. Cho, Y., Y. Zhang, T. Christensen, L.B. Sagle, A. Chilkoti, and P.S. Cremer, *Effects of Hofmeister Anions on the Phase Transition Temperature of Elastin-like Polypeptides*. The Journal of Physical Chemistry B, 2008. **112**(44): p. 13765-13771.
 147. Kowalczyk, T., K. Hnatuszko-Konka, A. Gerszberg, and A.K. Kononowicz, *Elastin-like polypeptides as a promising family of genetically-engineered protein based polymers*. World Journal of Microbiology & Biotechnology, 2014. **30**(8): p. 2141-2152.
 148. Petitdemange, R., E. Garanger, L. Bataille, W. Dieryck, K. Bathany, B. Garbay, T.J. Deming, and S. Lecommandoux, *Selective Tuning of Elastin-like Polypeptide Properties via Methionine Oxidation*. Biomacromolecules, 2017. **18**(2): p. 544-550.
 149. McPherson, D.T., J. Xu, and D.W. Urry, *Product Purification by Reversible Phase Transition Following Escherichia coli Expression of Genes Encoding up to 251 Repeats of the Elastomeric Pentapeptide GVGVP*. Protein Expression and Purification, 1996. **7**(1): p. 51-57.
 150. Bessa, P.C., R. Machado, S. Nürnberger, D. Dopler, A. Banerjee, A.M. Cunha, J.C. Rodríguez-Cabello, H. Redl, M. van Griensven, R.L. Reis, and M. Casal, *Thermoresponsive*

- self-assembled elastin-based nanoparticles for delivery of BMPs*. Journal of Controlled Release, 2010. **142**(3): p. 312-318.
151. Garanger, E., S.R. MacEwan, O. Sandre, A. Brûlet, L. Bataille, A. Chilkoti, and S. Lecommandoux, *Structural Evolution of a Stimulus-Responsive Diblock Polypeptide Micelle by Temperature Tunable Compaction of its Core*. Macromolecules, 2015. **48**(18): p. 6617-6627.
 152. Kim, W., J. Thévenot, E. Ibarboure, S. Lecommandoux, and E.L. Chaikof, *Self-Assembly of Thermally Responsive Amphiphilic Diblock Copolypeptides into Spherical Micellar Nanoparticles*. Angewandte Chemie International Edition, 2010. **49**(25): p. 4257-4260.
 153. Dreher, M.R., A.J. Simnick, K. Fischer, R.J. Smith, A. Patel, M. Schmidt, and A. Chilkoti, *Temperature Triggered Self-Assembly of Polypeptides into Multivalent Spherical Micelles*. Journal of the American Chemical Society, 2008. **130**(2): p. 687-694.
 154. Shi, P., S. Aluri, Y.-A. Lin, M. Shah, M. Edman, J. Dhandhukia, H. Cui, and J.A. MacKay, *Elastin-based protein polymer nanoparticles carrying drug at both corona and core suppress tumor growth in vivo*. Journal of Controlled Release, 2013. **171**(3): p. 330-338.
 155. McDaniel, J.R., S.R. MacEwan, M. Dewhurst, and A. Chilkoti, *Doxorubicin-conjugated chimeric polypeptide nanoparticles that respond to mild hyperthermia*. Journal of Controlled Release, 2012. **159**(3): p. 362-367.
 156. McDaniel, J.R., M.W. Dewhurst, and A. Chilkoti, *Actively targeting solid tumours with thermoresponsive drug delivery systems that respond to mild hyperthermia*. International Journal of Hyperthermia, 2013. **29**(6): p. 501-510.
 157. MacEwan, S.R. and A. Chilkoti, *Applications of elastin-like polypeptides in drug delivery*. Journal of Controlled Release, 2014. **190**: p. 314-330.
 158. Sarangthem, V., Cho, E. A., Bae, S. M., Singh, T. D., Kim, S. J., Kim, S., Park, R. W., *Construction and application of elastin like polypeptide containing IL-4 receptor targeting peptide*. PLoS ONE, 2013. **8**(12).
 159. Massodi, I., G.L. Bidwell, and D. Raucher, *Evaluation of cell penetrating peptides fused to elastin-like polypeptide for drug delivery*. Journal of Controlled Release, 2005. **108**(2): p. 396-408.
 160. Walker, L., E. Perkins, F. Kratz, and D. Raucher, *Cell penetrating peptides fused to a thermally targeted biopolymer drug carrier improve the delivery and antitumor efficacy of an acid-sensitive doxorubicin derivative*. International Journal of Pharmaceutics, 2012. **436**(1): p. 825-832.
 161. Josephson, L., C.-H. Tung, A. Moore, and R. Weissleder, *High-Efficiency Intracellular Magnetic Labeling with Novel Superparamagnetic-Tat Peptide Conjugates*. Bioconjugate Chemistry, 1999. **10**(2): p. 186-191.
 162. Monfardini, C. and V. Francesco, *Stabilization of substances in circulation*. Bioconjugate Chem., 1998. **9**: p. 418-450.
 163. Walkey, C.D., J.B. Olsen, H. Guo, A. Emili, and W.C.W. Chan, *Nanoparticle Size and Surface Chemistry Determine Serum Protein Adsorption and Macrophage Uptake*. Journal of the American Chemical Society, 2012. **134**(4): p. 2139-2147.
 164. Lee, H., E. Lee, D.K. Kim, N.K. Jang, Y.Y. Jeong, and S. Jon, *Antibiofouling Polymer-Coated Superparamagnetic Iron Oxide Nanoparticles as Potential Magnetic Resonance Contrast Agents for in Vivo Cancer Imaging*. Journal of American Chemical Society, 2006. **128**(22): p. 7383-7389.
 165. Noble, G.T., J.F. Stefanick, J.D. Ashley, T. Kiziltepe, and B. Bilgicer, *Ligand-targeted liposome design: challenges and fundamental considerations*. Trends in Biotechnology, 2014. **32**(1): p. 32-45.
 166. Nichols, J.W. and Y.H. Bae, *EPR: Evidence and fallacy*. Journal of Controlled Release, 2014. **190**: p. 451-464.
 167. Danhier, F., *To exploit the tumor microenvironment: Since the EPR effect fails in the clinic, what is the future of nanomedicine?* Journal of Controlled Release, 2016. **244**: p. 108-121.
 168. Hillaireau, H. and P. Couvreur, *Nanocarriers' entry into the cell: relevance to drug delivery*. Cellular and Molecular Life Sciences, 2009. **66**(17): p. 2873-2896.

169. Panariti, A., G. Miserocchi, and I. Rivolta, *The effect of nanoparticle uptake on cellular behavior: disrupting or enabling functions?* Nanotechnology, Science and Applications, 2012. **5**: p. 87-100.
170. Oh, N. and J.-H. Park, *Endocytosis and exocytosis of nanoparticles in mammalian cells.* International Journal of Nanomedicine, 2014. **9**(Suppl 1): p. 51-63.
171. Collinet, C., M. Stoter, C.R. Bradshaw, N. Samusik, J.C. Rink, D. Kenski, B. Habermann, F. Buchholz, R. Henschel, M.S. Mueller, W.E. Nagel, E. Fava, Y. Kalaidzidis, and M. Zerial, *Systems survey of endocytosis by multiparametric image analysis.* Nature, 2010. **464**(7286): p. 243-249.

CHAPTER II

EXPLORATION OF CHEMICAL ROUTES TOWARD IRON OXIDE NANOPARTICLES OF DIFFERENT SIZES, MORPHOLOGIES, AND MAGNETIC PROPERTIES



1. Introduction

Magnetic iron oxide nanoparticles (IONPs) find applications in the medical field as diagnostic tools and innovative therapies. They provide contrast enhancing properties in magnetic resonance imaging (MRI), and also serve as local heat mediators in magnetic hyperthermia (MH) and for the triggered delivery of drugs.[1] As IONPs are biocompatible, they stand among the best candidates over other alternative magnetic nanomaterials for health applications. Various synthetic pathways have been explored for their production,[2] the most common ones being the alkaline co-precipitation,[3] the polyol process,[4] the thermal degradation of organometallic precursors,[5] and the hydrothermal method.[6] The co-precipitation and polyol pathways have their own advantages and limits. The co-precipitation can be scaled-up to produce dozens of grams of IONPs at the lab scale but has low control over the morphology of resulting nanocrystals. The polyol synthesis achieves a better control over the morphology, but necessitates organic solvents as well as high temperature conditions to carry out the reaction. These two methods are thereafter explored and their advantages for IONPs production are compared.

2. Synthesis by co-precipitation

Because the physical properties of iron nanocrystals are strongly dependent on their shape, size and size-distribution, significant effort has been dedicated to produce good quality materials with narrow size-distributions, leading to optimal magnetic behaviors.[7] Among them, co-precipitation is widely used because it is a facile and convenient path to synthesize IONPs in a reproducible way. The precursors used are chloride, sulfate or nitrate iron II and iron III salts that are precipitated in aqueous solution upon the addition of a base. The nature of the salts, along with the pH of the solution, temperature and ionic strength influence the morphologies of the nanocrystals, regarding their size and shape. Magnetite Fe_3O_4 or maghemite $\gamma\text{-Fe}_2\text{O}_3$ nanoparticles are commonly synthesized using this procedure. Maghemite can be obtained from magnetite by simple oxidation in acidic medium with iron III nitrate salts, or by drying magnetite nanocrystals and letting them in contact with oxygen from ambient air, accelerating the formation of the thermodynamically favored maghemite compound. The use of stabilizers during the co-precipitation process has been reported to produce good quality materials with a narrow size-distribution. Examples of reported stabilizers are trisodium salt citric acid, polyvinylpyrrolidone (PVP), cetyltrimethylammonium (CTAB).[8, 9] An important criterion toward the selection of these organic additives is their hydrophilic or lipophilic affinity, determining the final solubility of the IONPs in organic or aqueous solvents. For medical applications hydrophilic salts are generally used due to their hydrophilicity. In this work, superparamagnetic IONPs dispersed in water, meaning dispersions of IONPs in solutions with large magnetic susceptibilities but no apparent magnetizations were produced. They were synthesized according to Massart's alkaline co-precipitation of ferrous and ferric chloride salts in water .[14] The magnetite (Fe_3O_4) IONPs obtained

were further oxidized into maghemite ($\gamma\text{-Fe}_2\text{O}_3$) by treatment with a boiling FeNO_3 solution. This gave a dispersion of superparamagnetic IONPs stable in a pH range 1.5–2.5 after several washings with acetone to remove excess ions. This dispersion remained in a monophasic state under the application of a magnetic field of arbitrary value. A size sorting procedure was then applied, as described in a previous work.[15] This procedure is based on the screening of the electrostatic repulsions between IONPs by excess addition of electrolyte (here HNO_3). The two phases were then separated over a strong ferrite permanent magnet (Calamit™). The concentrated bottom phase (referred to as C) was enriched in larger IONPs while the upper dilute supernatant (referred to as S) contained in average smaller IONPs. Proceeding this way multiple times, different fractions were obtained.

2.1. Experimental section

2.1.1. Materials

IKA Eurostar power control-visc and Scientifica LH VELP overhead mechanical stirrers allowed homogenizing solutions. An IKA C-MAG HS 7 was used for heating and magnetic stirring. A HANNA HI 9125 pH/ORP meter allowed the determination of pH of solutions. A KNF laboport pump was used to separate supernatants from precipitates by Buchner filtration. Iron dichloride tetra-hydrate powder ($\text{FeCl}_2 \cdot 4\text{H}_2\text{O}$), iron tri-chloride hexa-hydrate 45% solution ($\text{FeCl}_3 \cdot 6\text{H}_2\text{O}$), ammonia 28% solution (NH_4OH), hydrochloric acid 37% solution (HCl), nitric acid 69% solution (HNO_3), acetone ($(\text{CH}_3)_2\text{CO}$), and iron (III) nitrate powder ($\text{Fe}(\text{NO}_3)_3$) were from Sigma Aldrich. The water used was MilliQ (18 M Ω). Reagent grade diethyl ether anhydrous was from Baker.

2.1.2. Synthesis of IONPs by co-precipitation

The reactants were prepared by introducing 180 g of $\text{FeCl}_2 \cdot 4\text{H}_2\text{O}$, 100 mL of HCl and 500 mL of distilled water in a 1 L beaker. A magnetic stirring bar was used to ease the dissolution of $\text{FeCl}_2 \cdot 4\text{H}_2\text{O}$. 715 mL of $\text{FeCl}_3 \cdot 6\text{H}_2\text{O}$ were added into a 5 L beaker, later used for the reaction. After the complete dissolution of FeCl_2 , the solution obtained was poured onto the 5 L beaker, the resulting solution was completed at 3 L with distilled water and a mechanic agitator was used at 800 rotations per minute (rpm). At first, magnetite Fe_3O_4 nanocrystals were synthesized from an alkaline co-precipitation. 1 L of a concentrated ammonia solution (7 mol) was quickly added onto the acidic iron salts mixture, which produced a black solid suspension almost instantaneously. After 30 minutes of stirring at 800 rpm, the Fe_3O_4 IONPs were attracted by a strong ferrite magnet (152*101*25.4 mm³, Calamit Magneti, Milano-Barcelona-Paris). Then, the supernatant (2.25 L) containing non-magnetic ferrihydrites (reddish flakes) was discarded using water pump vacuum. The magnetic precipitate (black) was washed with 1 L of water, stirred for 10 min. Then the beaker was placed over the strong magnet for magnetic sedimentation. The clear supernatant was discarded using water pump vacuum. After sedimentation on the ferrite magnet, the flocculate was acidified with 0.26 L of nitric acid (69 %) and stirred 30 min after being completed up to 2 L with water. The ferrofluid was flocculated

using nitric acid. In order to completely oxidize magnetite into maghemite, the solid phase was separated from the supernatant (1.5 L, red) and immersed in a boiling solution of ferrite nitrate (0.8 mol). After 30 min under stirring at 90-100 °C, the suspension turned into the red color characteristic of maghemite $\gamma\text{-Fe}_2\text{O}_3$. Finally, free ions in excess were removed by washing with water, acetone and diethyl-ether. This stable ferrofluid was stirred during 10 min, after which 360 mL of concentrated nitric acid were added to destabilize the suspension and repeat two times the steps of sedimentation and suction. After having introduced 1 L of acetone and stirred the ferrofluid during 10 min, the IONPs were sedimented over a magnet and the supernatant was discarded. This step was followed by a stirring of 10 min after the addition of 500 mL of diethyl-ether, which purpose was to remove acetone. The IONPs were sedimented and the supernatant was discarded. Finally the IONPs were readily dispersed in water to form a true “ionic-ferrofluid” made of maghemite IONPs. The iron oxide surface bears positive charges due to adsorption of protons in acidic media, in that case a dilute HNO_3 solution at pH between 1.2 and 1.7. Therefore the ferrofluid remains in a monophasic state under the application of a magnetite field of arbitrary value.

2.1.3. Size grading by magnetic sedimentation

The ferrofluid underwent a size-sorting procedure based on the de-phasing of the liquid by screening of the stabilizing charges of the IONPs. A controlled amount of HNO_3 was added to the ferrofluid, leading to a change of color from deep black to brown as the ferrofluid partially flocculated. The dispersion was then put over a permanent magnet for approximately 15 minutes leading to a dephasing, with a dilute supernatant of IONPs on top (S) and a concentrated precipitate at the bottom (C). The two phases were separated, the supernatant was isolated and the sediment was redispersed by addition of water. This process was repeated again for each of the two phases, leading to 4 fractions of ferrofluids (S1S2, S1C2, C1S2, C1C2).

2.2. Results and discussion

2.2.1. Synthesis

Iron oxide nanocrystals were produced by co-precipitation of ferrous and ferric salts in alkaline aqueous solution. This is a convenient synthesis with affordable reactants and solvents. The whole process can be scaled-up and produced in batches, with a control over the variability of the product by adjusting addition rates, order of addition, and mixing process. The introduction of iron II and III chloride precursors with the ammonium hydroxide solution spontaneously led to the formation of a solid precipitate. The reaction most probably took place in two steps. At first the iron salt precursors underwent a salt metathesis reaction, also called double replacement reaction. Counter-ions were exchanged leading to iron hydroxides as intermediates of reaction. These intermediates promptly produced nanocrystals according to the following reaction:



Iron II precursors had to be protected from oxidation to control the equivalents described in the chemical equation. In the lab, the synthesis was carried in large volumes of water (5 L beaker), not previously degassed. As it technically difficult to prevent the oxidation from occurring, an excess of iron II precursors was added (1.7), to try reaching the correct equivalents during the co-precipitation step. The excess amount was empirically set depending on the conditions of reaction. This was a first limitation to the co-precipitation synthesis. Non-desired species as goethite α -FeOOH, akaganeite $\text{Fe}_8\text{O}_8\text{OH}_8\text{Cl}_{1.35}$, or hematite α - Fe_2O_3 phase were eliminated by addition of a strong acid (nitric acid), and/or elimination of the supernatant. The partially oxidized magnetite Fe_3O_4 product was completely oxidized into the more thermodynamically favored maghemite γ - Fe_2O_3 phase. Samples produced in large quantities by co-precipitation synthesis were often stored for long durations and used in different projects. Hence, magnetite nanoparticles were oxidized into maghemite in order to characterize and store samples in the long haul.

2.2.2. Size-grading

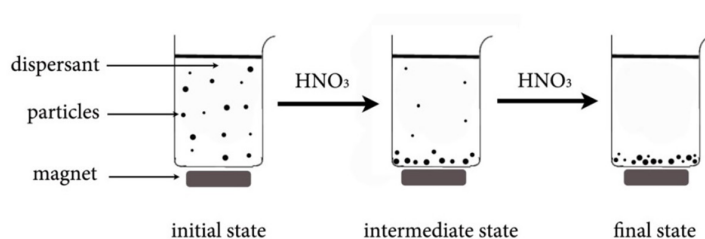


Figure 1 Scheme of the size-grading procedure of iron oxide nanoparticles by addition of nitric acid and sedimentation over a permanent magnet.

A size-grading procedure was carried on the sample in order to refine the size distributions, and produce batches of various average diameters. Nanoparticles with larger diameters could be used for magnetic hyperthermia applications as they typically presented higher specific absorption rates. Nanoparticles with smaller diameters were for example chemically modified and incorporated in membranes of polymersomes for drug delivery applications. The size-grading procedure relied on the screening of electrostatic charges stabilizing the nanoparticles by addition of salts (nitric acid). At intermediates states, larger nanoparticles were more susceptible to destabilize, aggregate, and could be collected by a permanent magnet, as illustrated in **Figure 1**.

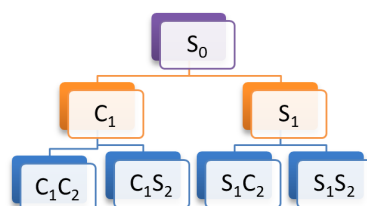


Figure 2 Scheme of the different fractions that are obtained after reiterating the size-grading procedure.

The two fractions were separated, leading to a supernatant (dilute fraction, referred to as S) enriched in smaller nanoparticles, and a culot (concentrated fraction, referred to as C) enriched in larger nanoparticles that could be redispersed by addition of water, diluting the salts and reducing the screening of charges. This procedure could be reproduced an arbitrary number of times to further refine the size-distributions (**Figure 2**). It was applied three times, leading to a total of 4 fractions (C1C2, C1S2, S1C2, S1S2).

2.2.3. Morphologies of the iron oxide nanocrystals

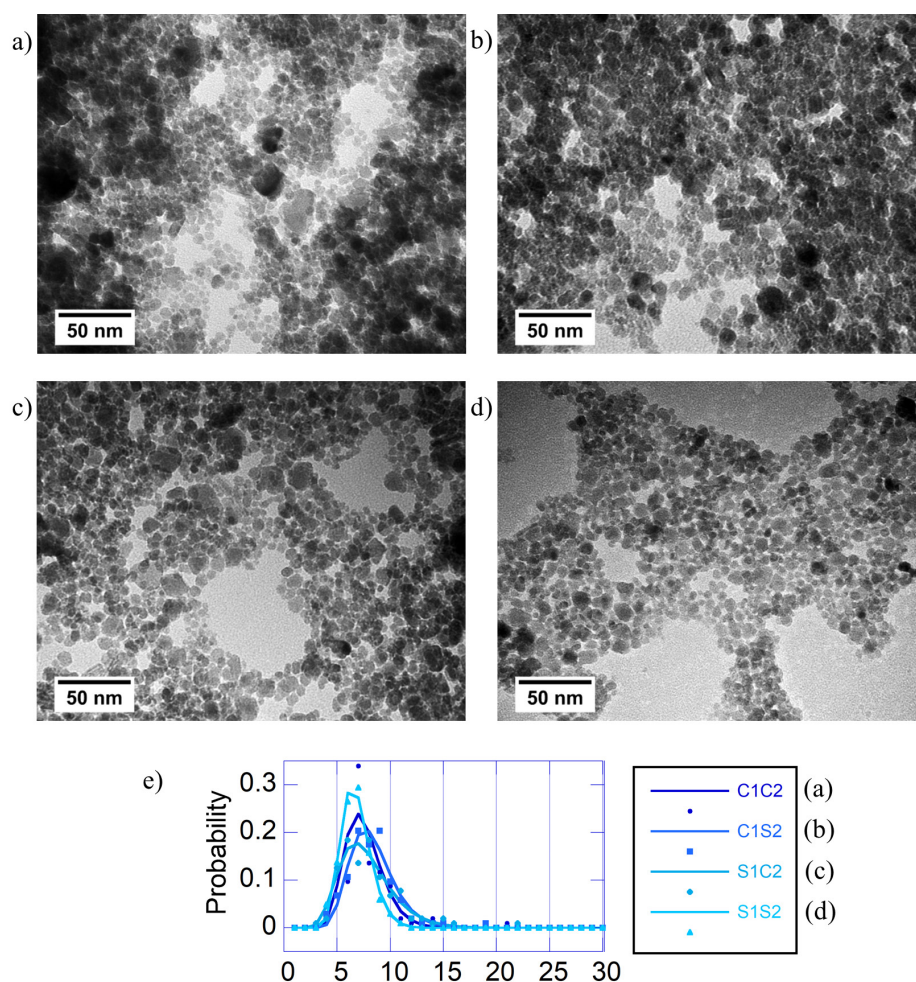


Figure 3 TEM micrographs of the different fractions obtained after the size-sorting process. **a)** C1C2, **b)** C1S2, **c)** S1C2, and **d)** S1S2 fractions. **e)** Corresponding size distributions.

The different fractions were imaged by TEM to observe the morphologies of the IONPs (**Figure 3 a-d**). Visually, the fractions C1C2 and C1S2 presented large faceted objects as well as smaller spherical IONPs. The fractions S1S2 and S1C2 contained more homogeneous spherical IONPs. The size distributions of the four different fractions were estimated by measuring the diameters of the IONPs on TEM micrographs, and size-histograms were fitted to a log-normal distribution law.

Table 1 Mean size and standard deviations of the four fractions obtained after the size-sorting process.

Fraction	Mean size (nm)	Standard deviation (nm)
C1C2	7.4	1.7
C1S2	8.1	2
S1C2	7.5	2.4
S1S2	6.7	1.4

Mean sizes $d_0 = \langle d \rangle$ (number-averages) and standard deviations $\sigma = \langle (d - \langle d \rangle)^2 \rangle^{1/2}$ were calculated using the classical Gaussian statistics formulas. The results obtained for C1C2 had to be cautiously interpreted. The TEM micrographs showed aggregates of large IONPs that were tedious to measure, leading to an underestimate of the mean size. The mean sizes of the samples decreased for fractions collected in the supernatants, from 8.1 nm for C1S2 to 6.7 nm for S1S2. This was expected according to the principle of the size-grading process, which separated larger IONPs in the culots and smaller IONPs in the supernatants.

The co-precipitation pathway yielded large quantities (several grams) of material in a convenient way. Affordable and common chemicals were used both for the production and purification of the IONPs. Nevertheless, there was a lack of control over the morphologies of the IONPs, and a size-grading procedure was compulsory to try refining the product. Samples with mean sizes below 7 nm could be obtained with relatively narrow size-distributions, while samples with mean sizes superior to 8 nm were considered poly-dispersed and broad in size-distributions. Smooth spheres with controlled diameters were needed in order to build core-shell structures with controlled grafting densities for the next steps of the project. We moved to the polyol synthesis to answer this need and produce IONPs of various diameters while keeping narrow size-distributions.

3. Polyol synthesis

The polyol route is a versatile method to produce gram-scale batches of IONPs with well-defined morphologies and magnetic properties. In this work, the influences of the water amount and temperature at which it was injected in the reflux system were investigated. Distinct morphologies of IONPs were obtained, from ultra-ultra-small superparamagnetic iron oxide nanoparticles (UUSPIOs), namely smooth mono-core spheres down to 4 nm in diameter, to larger multi-core raspberry-like ones up to 37 nm. Well-defined multi-core assemblies with narrow grain size dispersity were successfully synthesized. Other strategies were reported to directly produce raspberry-like structures in water such as the co-precipitation performed in presence of excess polysaccharide,[10] or in a microwave reactor.[11] The polyol synthesis of multi-core IONPs was introduced by Caruntu *et al.*[4] In this reaction, the solvent acted simultaneously as a complexing agent for iron chloride precursors and as high boiling point solvent, with reflux temperatures usually in the range of 220 °C. Multi-core IONPs are to date amongst the most efficient for heating under an applied alternating magnetic field (AMF)

and as negative (transverse T_2) MRI contrast agents, as previously reported.[12] At equivalent concentrations of iron, the outstanding heating properties of these assemblies of small grains into larger raspberry-like structures were related to a frustrated super-spin glass state.[13] Regarding the synthesis mechanistic pathway, tentative descriptions of the intermediary states of reaction were proposed,[14] together with the role of the polyol solvent in orienting the morphology.[15] Different reaction conditions were studied in the literature, with variable parameters such as the choice of the polyol solvent,[15] temperature and pressure,[16] reaction time and heating ramp slope,[17] alkaline pH,[18] and presence of adsorbed capping agents.[19] The main applications envisioned for multi-core IONPs are as nanoheaters for MH and efficient negative (T_2) contrast agents for MRI, as ascribed to their large magnetic moment and large intrinsic magnetization M_d (magnetic mono-domain moment divided by the particle volume). The main challenge to overcome for utilizing these superior magnetic properties in biological media was to prevent particle aggregation that could be evidenced by a non-reversible magnetization curve in static magnetic field. With large magnetic moments, multi-core IONPs experimented strong magnetic dipolar interactions. Moreover, the coating of their surface by a residual organic layer could render them difficult to peptize as stable aqueous colloidal suspensions, especially in physiological media. In the course of this section, the crucial role of water in the polyol synthesis is described. An extensive study describing how the amount and way of adding water in the synthesis influenced the final nanoparticle (NP) morphology is reported here. A library of water-dispersible IONPs was successfully synthesized, with tunable diameters from ~ 4 to ~ 37 nm and superior magnetic properties for MFH and MRI. A diverse and large library of samples was obtained by varying the nature of solvents and the amounts of added water while keeping all other parameters constant. The different morphologies led to magnetic IONPs suitable for important biomedical applications such as magnetic hyperthermia, MRI contrast agent, or both.

3.1. Experimental section

3.1.1. Materials

Nitric acid (HNO_3 , 70%) was from Fisher. Ethyl acetate (>99.5%) was from Sigma Aldrich. Acetone (technical grade), ethanol (96%), and diethyl ether (100%) were from VWR. *N*-methyldiethanolamine (NMDEA, 99%) was from Acros Organics Diethylene glycol (DEG, 99%), sodium hydroxide microprills (NaOH, 98%), iron(III) nitrate nonahydrate ($\text{Fe}(\text{NO}_3)_3 \cdot 9\text{H}_2\text{O}$, >98%), and iron(II) chloride tetrahydrate ($\text{FeCl}_2 \cdot 4\text{H}_2\text{O}$, 98%) were from Alfa Aesar. Iron(III) chloride hexahydrate ($\text{FeCl}_3 \cdot 6\text{H}_2\text{O}$, >97%) was from Panreac.

3.1.2. Synthesis of IONPs

IONPs were produced by adapting reaction conditions reported by Caruntu *et al.*: [4] 80 mL of either pure DEG or a mixture of DEG and NMDEA with volume ratios 1:1 v/v were introduced in a three-neck round bottom flask flushed with nitrogen and stirred with a magnetic stir bar for one hour

under inert atmosphere. 1.08 g (4 mmol) of $\text{FeCl}_3 \cdot 6\text{H}_2\text{O}$ and 0.40 g (2 mmol) of $\text{FeCl}_2 \cdot 4\text{H}_2\text{O}$ were then dissolved overnight. In the meantime, 0.64 g (16 mmol) of NaOH was dissolved under magnetic stirring in 40 mL of either pure DEG or a 1:1 v/v mixture of DEG and NMDEA in a separate three-neck round bottom flask. The NaOH solution was flushed by bubbling nitrogen for one hour before mixing with the mixed iron(II,III) chloride solution. The color quickly turned from yellow to deep green. The mixture was then heated up to 220 °C (temperature ramp in around 30 min) with an electronically controlled Digi-Mantle™ heating mantle (OMCA0250, Electrothermal™) set at full power, before allowing the reaction to occur for a determined period of time, either with or without agitation at 500 rpm by a mechanical stirring Teflon shaft inserted through the condenser aperture. IONPs were then separated over a strong permanent ferrite magnet (152×101×25.4 mm³, Calamit Magneti™, Milano-Barcelona-Paris), washed three times with a mixture of ethanol and ethyl acetate (1:1 v/v), once with 10 % nitric acid, twice with acetone, and twice with diethyl ether. NPs were then readily redispersed in water by stirring in open air to remove volatile solvents. At this stage, a black monophasic dispersion of IONPs was obtained. 8.6 g of iron(III) nitrate was then added as a strong oxidant by heating at 80 °C for 45 min while mechanically stirring.[20] The colloidal solution then turned from clear black to clear brown-orange. The IONPs were flocculated by addition of 10 % nitric acid and finally washed twice with acetone and twice again with diethyl ether. At this stage a deep orange-black dispersion of IONPs was obtained. The fluid was attracted by permanent magnets while staying in a single liquid phase, confirming that a true “ferrofluid” was obtained.

3.1.3. Sample nomenclature

Each final product was designated according to the main synthesis parameters, *i.e.* the solvent (*D* for pure DEG, *N* for DEG/NMDEA 1:1), the volume of water in μL added to 120 mL of solvent (the subscript *HI* or *HU* being added to specify if water was injected to the reaction mixture at solvent reflux – hot injection – or by heating-up from room temperature, respectively), and the reaction time. For example, the sample name *N500_{HU}-5h* indicated that 500 μL of H_2O were added to 120 mL DEG/NMDEA (1:1) and the reaction mixture was heated up to reflux for 5 hours. The sample name *D5000_{HI}-20m* indicated that 5,000 μL of H_2O were added through a septum to 120 mL of iron(II,III) precursors in boiling DEG, then let for 20 min before cooling).

Table 2 Batch names and their corresponding conditions of synthesis. *reaction performed under “natural mixing” *i.e.* by diffusion and convection yet no stirring.

Batch name	Nomenclature
15ff	N1000 _{HU} -5h
17ff	D5000 _{HI} -20m
25ff	N500 _{HU} -4h
30ff	N1000 _{HU} -5h
31ff	N500 _{HU} -1h
32ff	N500 _{HU} -5h
34ff	N100 _{HU} -5h*
35ff	N100 _{HU} -5h
36ff	N100 _{HU} -5h

3.1.4. Transmission Electron Microscopy (TEM)

TEM was performed on a Hitachi™ H7650 microscope with an acceleration voltage of 80 kV. TEM images were acquired with an ORIUS™ SC1000 large format (11 MPx) camera. Samples were prepared by nebulizing IONP dispersions at 1 g·L⁻¹ concentration on Formvar™ carbon-coated 200 mesh copper grids from Agar Scientific™ and leaving them to dry at room temperature. IONP size distributions were obtained by measuring more than 100 IONPs with the ImageJ freeware (<https://imagej.nih.gov/ij/>). Size-histograms were fitted to a log-normal distribution law of diameters $P(d)$ with optimized values of median diameter α and non-dimensioned width β :

$$P(d) = \frac{1}{d \cdot \beta \sqrt{2\pi}} \cdot \exp\left(\frac{-(\ln(d) - \ln(\alpha))^2}{2\beta^2}\right)$$

In addition, the mean sizes $d_0 = \langle d \rangle$ (number-averages) and standard deviations $\sigma = \langle (d - \langle d \rangle)^2 \rangle^{1/2}$ were calculated using the classical Gaussian statistics formulas.

3.1.5. Dynamic Light Scattering (DLS) and Zetametry

A Nanosizer™ Nano ZS90 from Malvern™, UK, was used to measure ζ potentials, Z-average hydrodynamic diameters (D_h), and polydispersity indexes (PDI). The 2nd order Cumulant fit was used for analysing DLS data into a size distribution (the PDI being defined as the ratio of the 2nd order coefficient to the square of the 1st order one in the series[21]). The Smoluchowski equation was used to convert the measured electrophoretic mobility into a ζ potential value in mV.

3.1.6. Proton relaxometry

Samples were prepared at concentrations of 6 mM_{Fe}. NMR tubes (7.5 mm outer diameter) were filled with 1 mL of each sample, and inserted in a Bruker™ mq60 relaxometer equipped with a

60 MHz / 1.41 Tesla magnet. The samples were left to thermalize to 37 °C using a Julabo™ f25 ED circulation bath. Following recommended protocols in proton relaxometry,[22] longitudinal T_1 relaxation times were measured using an inversion-recovery sequence of first duration of $\sim 0.1 \times T_1$ and final duration of $\sim 3 \times T_1$ with a recycling delay (RD) of $\sim 5 \times T_1$ between two of the 10 acquisition points, 4 scans and an automatic RF receiver gain. Transverse T_2 relaxation times were measured using Carr-Purcell-Meiboom-Gill (CPMG) sequence, with delay time τ of 0.04 ms between the 90° rotation to transverse plane and the 180° focusing pulse, a duration time of $3 \times T_2$, RD of $5 \times T_1$, and automatic receiver gain. The number of acquisition points was set by dividing the duration time by the delay time τ .

3.1.7. Magnetic fluid hyperthermia

IONPs were dispersed at concentrations of 3 g·L⁻¹ in diluted HNO₃ (at pH~2) to preserve their colloidal stability. The samples were placed in 500 μ L plastic cuvettes, whose caps were pierced with a needle to introduce a fiber optics temperature probe of 420 μ m outer diameter (medical range OTG-M420 fiber, Opsens™, Québec, QC, Canada) and measure temperature profiles *versus* time. Samples were thermalized at 37 °C using a glass-water jacket connected to a temperature bath until reaching equilibrium. The heat generation by magnetic NPs was triggered using an induction coil (4-turn of 3.5 mm diameter hollow – 0.4 mm wall – copper tubing, 55 mm outer diameter, 48 mm inner diameter, 34.5 mm height) fed by a Minimax Junior™ ITS 3.5 kW generator (Seit Elettronica™, Italy) applying an AMF at maximum amplitude H_{app} of 10.2 kA·m⁻¹ and at a frequency f of 755 kHz as determined by finite element modelling.[23] The amplitude and frequency of the magnetic field were corroborated by measuring the electromotive force in a scout coil (turn of 17.5 mm diameter) and an oscilloscope (Agilent™ 54641 A). The AMF was applied for 5 min while recording the elevation of temperature and measuring its slope at early times (within first 5 s).

3.1.8. Static (DC) magnetization

DC magnetization curves of the NP aqueous dispersions were obtained up to 1.8 Tesla on a homemade vibrating sample magnetometer (VSM) at the SGIker facility (UPV/EHU). The magnetic field was measured by a gaussmeter whereas the signal was conditioned by a Stanford™ SR810DSP lock-in amplifier controlled by a PC under a LabVIEW™ program.

3.1.9. Zero field cooling – field cooling (ZFC-FC) magnetometry

ZFC-FC experiments were conducted on a magnetic property measurement system (MPMS™ 7T from Quantum Design™, San Diego, CA, USA). This ultrasensitive magnetometer was previously calibrated by Y₃Fe₅O₁₂ garnet 1 mm diameter sphere (standard reference materials 2853) and reset after each measurement. Estimates of the blocking temperature were made according to a previously published protocol.[24, 25]

3.1.10. Equivalent iron titration in IONP suspensions

The equivalent iron molarity [Fe] was measured by a disruptive photometric assay, using the characteristic absorption peak at 350 nm of the $[\text{Fe}(\text{Cl})_6]_3^-$ complex when an aliquot of the suspension was dissolved in concentrated hydrochloric acid (HCl 5 M), according to previous calibration law $\text{OD}_{350\text{nm}, 2\text{mm}} = 0.5043 \times [\text{Fe}]_{\text{mM}} + 0.0172$. Then [Fe] was converted into iron oxide weight assuming pure $\gamma\text{-Fe}_2\text{O}_3$ composition ($\sim 80 \text{ g}\cdot\text{mol}^{-1}$).

3.2. Results and discussion

In the course of this work, it was postulated that water traces were incorporated in the highly hygroscopic polyol solvent and that this initial water content in the mixture before reaction was a key parameter to produce well-defined magnetic IONPs. This led us to an extensive study on the role of controlled additions of water in the synthesis of IONPs in a mixture of polyols (DEG, NMDEA). Different batches of IONPs were thereby produced by varying reaction parameters such as reaction time, solvent system, amount and timing of injections of water traces, *i.e.* hot injection at solvent reflux *vs.* heating-up of the reaction mixture including water. Since the two major biomedical applications of IONPs are for MH and as MRI contrast agents, well-defined IONPs suitable for these two applications were produced. Large (several tens of nm) IONPs were obtained for MH, while UUSPIOs of a few nm were synthesized for being used as positive MRI contrast agents with T_1 -weighted sequences.[26-29]

3.2.1. Influence of the conditions of reaction over the morphology of iron oxide nanoparticles

The main reaction parameter to control IONP morphology (and therefore magnetic properties) was the solvent composition. A mixture of DEG and NMDEA (1:1 volume ratio) was used to yield large IONPs, while UUSPIO NPs were produced in pure DEG. In both cases, the same quantity and stoichiometric ratio of iron(II,III) chlorides and hydroxides were used ($\text{Fe}^{3+}/\text{Fe}^{2+}/\text{OH}^-$ 2:1:8, *i.e.* one hydroxide anion per chloride).

Reactants were heated from room temperature (RT) to reflux (approximately 30 min to reach 220 °C) to obtain IONPs. Traces of water were injected to the reaction mixture either at RT before heating (*heating-up, HU*) or at reflux (*hot injection, HI*). Solvents used for the syntheses were freshly ordered and preserved from moisture. In the case of the DEG/NMDEA solvent system, traces of water were injected in different amounts, from 100 μL to 2 mL, into 120 mL of the total polyol solvent mixture, representing 0.083 % to 1.67 % volume ratios (v/v) or 5.5 to 11 mmol H_2O , *i.e.* stoichiometric (not catalytic) water quantity compared to the total iron(II,III) salts (6 mmol). Lower water amounts did not allow producing IONPs, while larger quantities of water led to ill-defined IONPs.

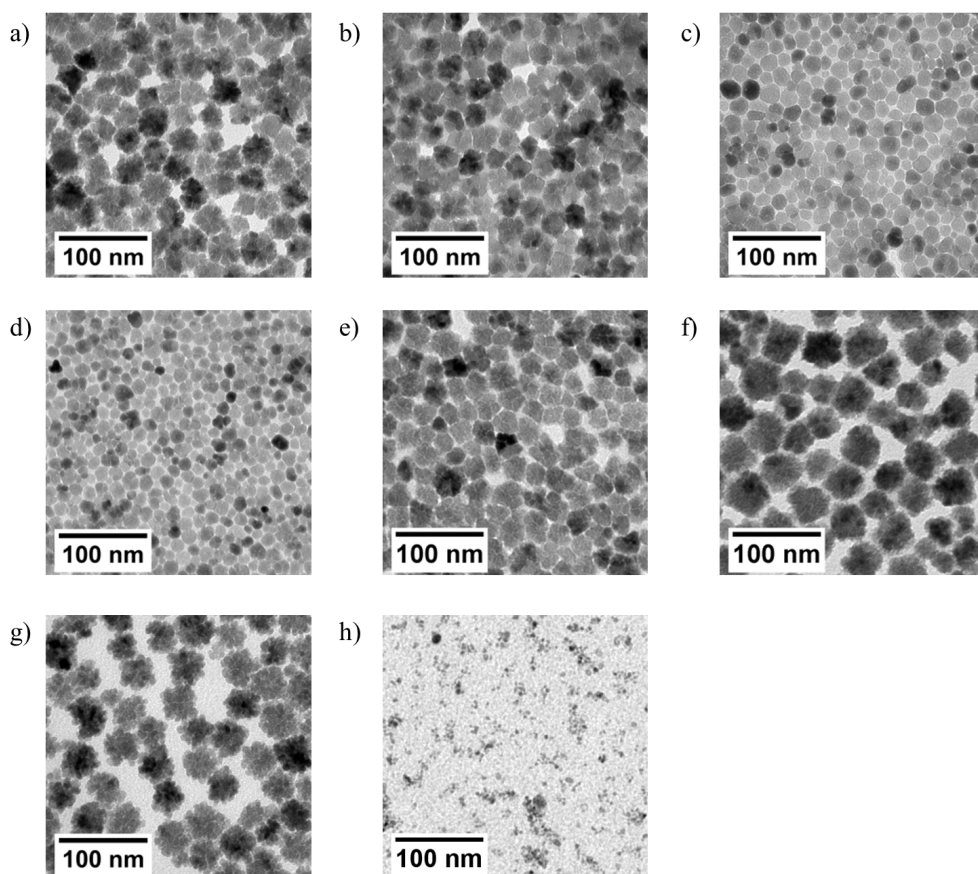


Figure 4 TEM micrographs of γ - Fe_2O_3 IONPs of mono- or multi-core morphology: **a)** 36ff (32.3±5.0 nm), **b)** 35ff (29.1±4.4 nm), **c)** 34ff (18.5±3.2 nm), **d)** 32ff (14.5±3.4 nm), **e)** 31ff (27.5±4.2 nm), **f)** 30ff (46.9±8.5 nm), **g)** 15ff (36.9±4.8 nm), and **h)** 17ff (4.3±1.1 nm). TEM sizes in parentheses correspond to the mean outer diameters and respective standard deviations.

As seen on data (**Figure 4** and **Table 2**), optimal control, in terms of size-distribution and morphology homogeneity, was achieved when mixing a determined amount of water in the solvent system with the precursors before heating (*HU*), as supposedly ascribed to a more homogeneous composition of the starting mixture.

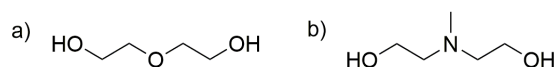


Figure 5 Chemical structures of **a)** diethylene glycol and **b)** N-methyldiethanolamine

Surprisingly, using anhydrous iron(III) chloride instead of the hexahydrate compound did not allow producing magnetic IONPs, even when traces of water were added before heating (*HU*). This evidenced the critical role of water and its necessary presence in the starting iron salt precursors for the positive outcome of the reaction. In the polyol (DEG/NMDEA) synthesis, the solvents (**Figure 5**) acted simultaneously as multivalent chelators for iron(II,III) cations, as well as a high boiling temperature medium to achieve a good control over the nucleation and separation from growth of IONPs. The chloride counter-ions of the iron(II,III) salts were thus exchanged by complexing solvent molecules and subsequently by hydroxide anions or by water molecules when adding the NaOH solution.

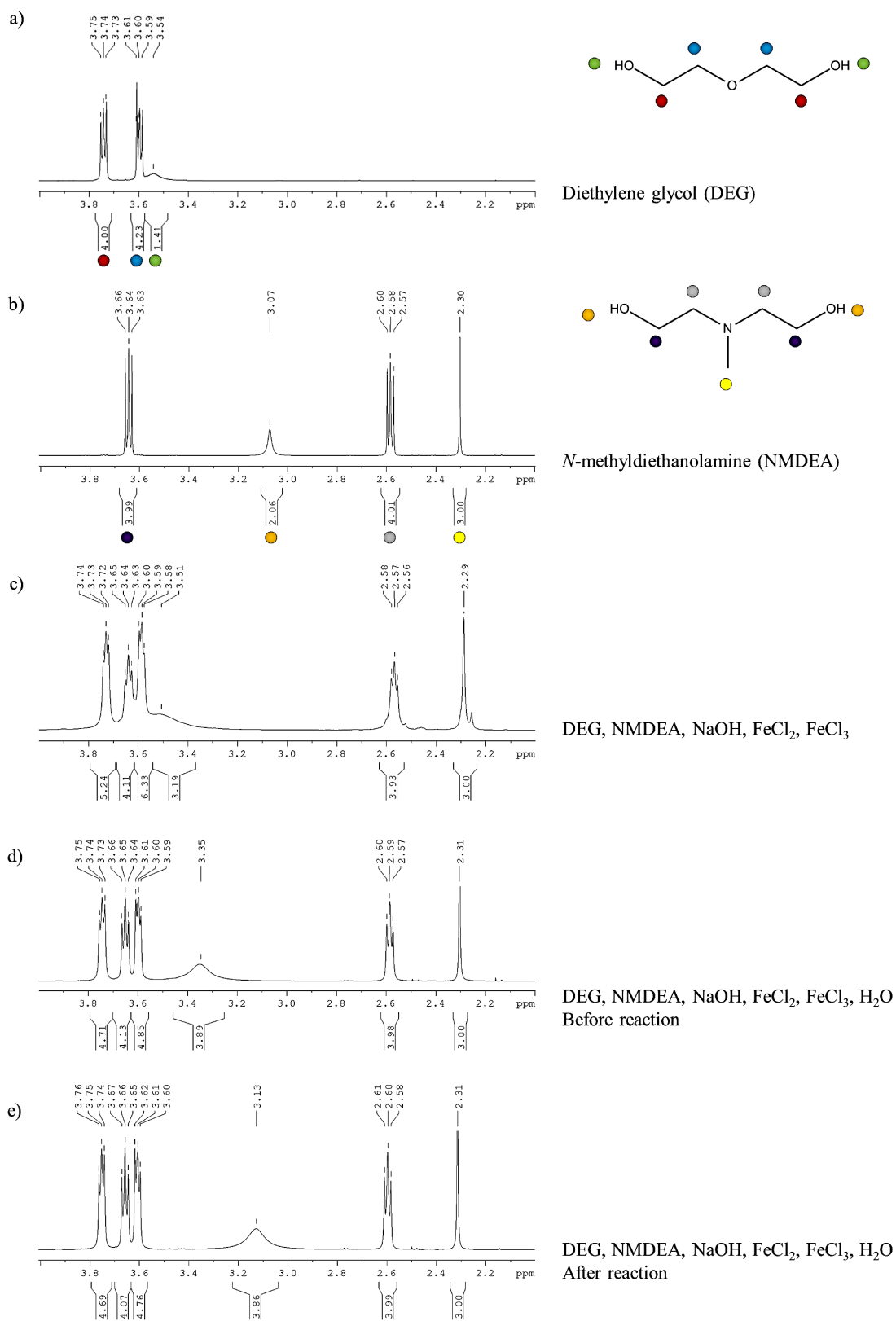


Figure 6 NMR analyses of **a)** DEG, **b)** NMDEA and of **c)** the medium of synthesis before addition of water, after addition of water **d)** before and **e)** after reaction. Addition of water shifted the peak corresponding to hydroxyls, which was further shifted after reaction, most likely due to a variation of pH. The solvents did not undergo degradation during the reaction.

Caruntu *et al.* described that the actual precursors of inorganic polymerization are iron(II,III) hydroxides in which the metallic centres are also chelated by DEG.[14] Therefore, the polyol route is also referred to in literature as a “forced hydrolysis” mechanism. This salt metathesis could be observed visually when mixing the reactants from the color changes of the organometallic solution turning into a black colloidal suspension of magnetite (Fe_3O_4) NPs. Studying the medium of synthesis by ^1H NMR spectroscopy helped understanding the mechanism of reaction (**Figure 6**). It was observed that controlled water addition shifted the broad peak attributed to the labile protons of hydroxyl groups in DEG and NMDEA (at respectively 3.43 and 3.07 ppm). Apart from further shifting of this labile protons peak ascribed to pH variation occurring during the synthesis (hydroxyl groups being converted into oxides), the NMR spectrum did not show any evidence of polyol molecules degradation. It is worth noting that the IONPs were, in most cases, covered by a layer of chelating solvent molecules even after several washing steps using a mixture of ethanol and ethylacetate.[17] This affected the colloidal stability of the samples, and their ability to be oxidized by the boiling $\text{Fe}(\text{NO}_3)_3$ addition.[20]

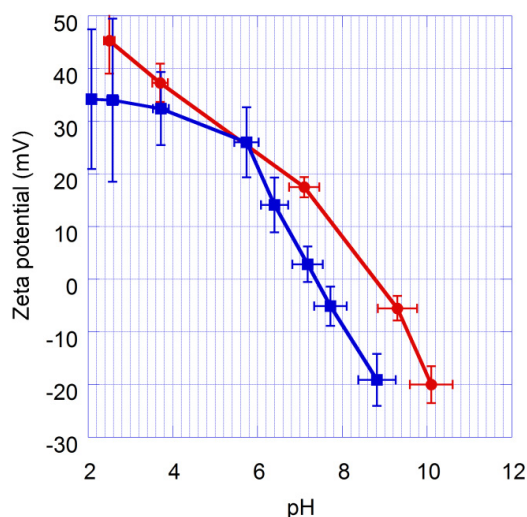


Figure 7 Zeta (ζ) potential measurement of IONPs which surfaces were partially cleaned after the polyol synthesis (red circles), with an isoelectric point (IEP) estimated to be at around $\text{pH}=9$, evidencing the presence of amine moieties of NMDEA of the solvent molecules chelated on the IONPs. IONPs fully cleaned (blue squares), with an IEP estimated to be around $\text{pH}=7$, which was consistent with values previously reported for a bare surface of iron oxide NPs (*i.e.* covered only with neutral hydroxyl groups).

During the oxidation step, the sample color was expected to turn from black to dark red as IONPs were oxidized from magnetite to maghemite. In some cases, especially for multi-core IONPs, the color of the colloidal solution remained black. This protective layer of DEG and NMDEA at the surface of IONPs was also evidenced by ζ potential measurement at varying pH (**Figure 7**). The isoelectric point (IEP) of maghemite was expected at around $\text{pH}=7$, while the IEP of IONPs still covered by a layer of solvent ligands was shifted to about $\text{pH}=9$, which was consistent with the expected pK_a value of the tertiary amine in NMDEA. Washing IONPs by a precipitation-redispersion process in aqueous alkaline media revealed to be an efficient means to completely remove the

remainder of chelated solvents as evidenced by the curve of ζ vs. pH after extensive washing on **Figure 7**.

In the case of the sole DEG solvent, amounts of water as large as 5 mL, representing 4.2 % of the total solvent volume or 275 mmol H₂O molecules, were injected at reflux temperature with a syringe needle through a septum (*hot injection, HI*), generating much smaller IONPs, with diameters typically in the order of 3-5 nm. The fast introduction of a water excess at high temperature immediately generated a sudden nuclei burst, with a solution turning from deep green to black. This hot injection method led to UUSPIOs as there was a limited quantity of precursors in solution available for crystal growth. The time-scale of reaction was usually much shorter than when synthesizing larger IONPs in DEG/NMDEA. Typically, reactions in sole DEG were completed after only 15-20 min. When letting an aliquot of the reaction mixture at rest over a strong permanent magnet, the supernatant became colorless, evidencing the total conversion of the colored iron(II,III) organometallic precursors into a colloidal magnetite phase.

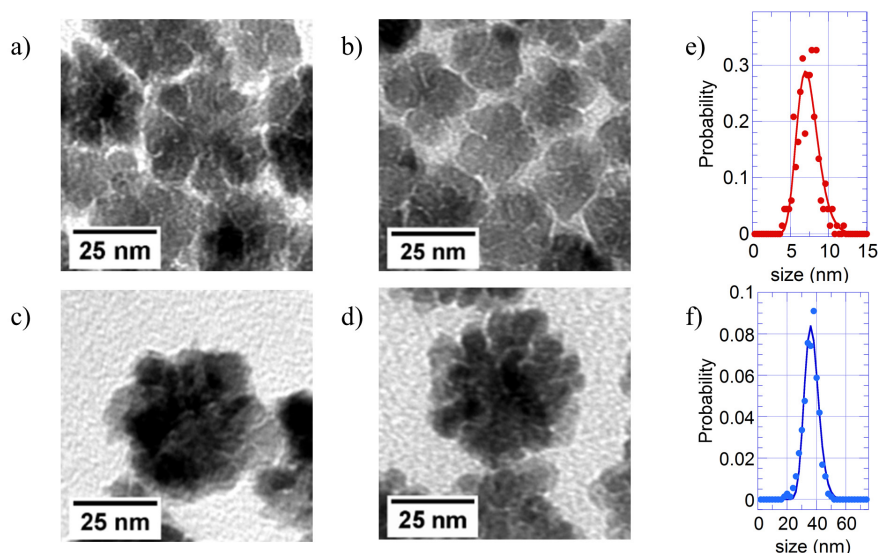


Figure 8 High magnification TEM micrographs of γ -Fe₂O₃ multi-core IONPs: **a)** 36ff, **b)** 35ff, **c)** 30ff, and **d)** 15ff. Distribution of **e)** grain sizes of the 15ff batch (7.4 ± 1.4 nm), and **f)** outer diameter (36.9 ± 4.8 nm), measured on TEM micrographs and log-normal fits.

The final products of all the different batches greatly differed in sizes and shapes according to the solvent composition: only DEG or DEG/NMDEA, or amount and timing of water addition. Mono-core IONPs as well as more complex structures previously reported as “multi-core IONPs” were obtained. TEM images enabled to determine both the overall diameters and the individual grain sizes for these multi-core IONPs. Mono-core IONPs were produced with adjustable sizes from ~4 nm to ~20 nm when the mixture was left at rest during all the reaction (under ‘natural convection’), while multi-core IONPs were obtained when the mixture was continuously homogenized with a stirring shaft, with sizes from ~27 to ~37 nm (**Figure 4**). The size-histograms could be well-fitted using a log-

normal distribution law of parameters α and β (**Figure 8**). In order to express diameters as $d_0 \pm \sigma$, the mean values d_0 along with standard deviations σ were calculated according to the following formulas:

$$d_0 = \langle d \rangle = \alpha e^{\frac{\beta^2}{2}} \quad \text{and} \quad \sigma^2 = \langle (d - d_0)^2 \rangle = d_0^2 (e^{\beta^2} - 1)$$

Size distributions characterized by β parameters below 0.2 were considered sufficiently narrow and suitable for further characterization. The condition *NI00_{HU}-5h*, using mechanical stirring, proved to be both optimal and robust for the reproducible synthesis of multi-core IONPs as evidenced by the similar TEM images obtained for the 35ff and 36ff batches (**Figure 8**). In contrast, similar conditions without stirring (*NI00_{HU}-5h**) led to smooth spherical iron oxide NPs (34ff) of narrow size-distribution 18.5 ± 3.2 nm as determined by TEM analysis, or 18.8 ± 6.5 nm as obtained by fitting the DC magnetization curve (**Figure 16**). This observation highlights the critical role of mixing (diffusion-reaction vs. active stirring) as experimental parameter on the resulting IONP morphology.

Important characteristics of the IONPs were reported in the **Table 3**. Mean diameter d_0 and standard deviation σ obtained by particle counting on TEM images on more than 100 nanoparticles (figures in parentheses correspond to the inner core size of nanoflowers when it could be measured; an asterisk indicates a lower statistics); the initial temperature slope during 5 s under an AMF $H_{\text{app}}=10.2$ kA·m⁻¹ at $f=755$ kHz and at 3 g·L⁻¹ iron oxide; the specific absorption rate (normalized by the mass of iron oxide); the Z-average hydrodynamic diameter (D_h) and polydispersity index (PDI), the r_1 and r_2 relaxivities and their ratio (measured at 37°C and under 1.41 Tesla). Lines in italics correspond to nanoflowers (otherwise nanospheres). Bold lines indicate samples analyzed in details in main text. Missing values correspond to measurements that were not performed because samples were estimated not interesting enough, or because of absence of colloidal stability due to a too large TEM size (e.g. 9ff).

Table 3 Summary of characteristics of the sample library synthesised by the polyol route

Sample	$d_0 \pm \sigma$ (nm)	T slope ($^{\circ}\text{C}\cdot\text{s}^{-1}$)	SAR ($\text{W}\cdot\text{g}^{-1}$)	D_h (nm)	PDI	r_1 ($\text{s}^{-1}\cdot\text{mM}_{\text{Fe}}^{-1}$)	r_2 ($\text{s}^{-1}\cdot\text{mM}_{\text{Fe}}^{-1}$)	r_2/r_1
4ff	8.3±1.9	-	-	-	-	12.1	113.3	9.3
5ff	21.4±3	0.080	111	36.3	0.22	5.7	80.3	14.0
7ff	7.1±1.6*	0.022	31	32.0	0.14	18.3	170.6	9.3
9ff	60.0±7.4	-	-	-	-	-	-	-
12ff	10.0±2	0.052	72	44.2	0.18	22.0	149.6	6.8
13ff	11.7±4.7*	0.14	189	57.2	0.35	15.6	291.3	18.7
15ff	36.9±4.8 (7.4±1.4)	-	296	46.3	0.227	-	-	-
16ff	4.7±1.2	-	-	29.3	0.39	6.4	23.9	3.8
17ff	4.3±1.1	0.004	6	25.2	0.36	-	-	-
18ff	3.4±0.8	0.006	8	44.2	0.96	5.5	12.1	2.2
19ff	7.7±1.7	0.070	98	21.5	0.18	-	-	-
20ff	6.3±1.6	0.016	22	16.2	0.21	-	-	-
21ff	11.2±1.9	0.060	84	26.9	0.14	17.9	145.3	8.1
22ff	12.1±3.1	0.14	189	42.8	0.14	10.6	118.5	11.2
25ff	14.2±3.2	0.090	125	55.2	0.26	19.7	267.7	13.6
26ff	-	0.088	123	35.7	0.10	16.0	219.1	13.7
27ff	-	0.11	150	49.6	0.11	12.5	194.2	15.5
29ff	25.9±4.5 (12.1±1.9)	0.13	178	36.5	0.16	-	-	-
31ff	27.5±4.2	0.19	268	33.3	0.08	13.1	341.9	26.1
32ff	14.5±3.4	0.096	134	20.6	0.13	25.9	203.4	7.8
33ff	21.6±5.5	0.10	145	44.7	0.12	5.9	140.6	23.8
34ff	32.3±5.0	0.15	206	29.9	0.19	12.2	163.1	13.4
35ff	29.1±4.4	0.19	265	35.7	0.13	6.2	170.0	27.3
36ff	32.3±5.0	0.17	237	71.0	0.37	0.86	22.3	25.9

3.2.2. Colloidal stability and heating properties

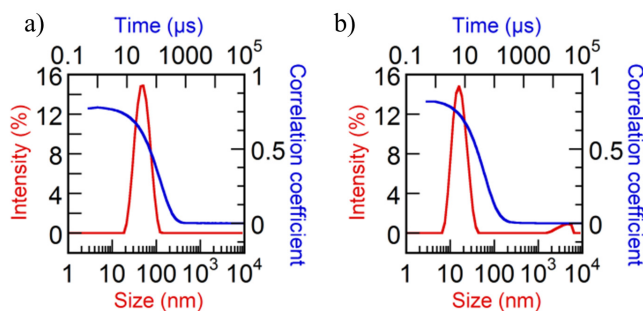


Figure 9 DLS correlograms and intensity-averaged distribution of diameters of a) 35ff multi-core IONPs ($D_h=36$ nm, PDI=0.13), and b) 20ff UUSPIO mono-core IONPs ($D_h=16$ nm, PDI=0.21). Values in parentheses correspond to the Z-average hydrodynamic diameter (D_h), obtained from the 2nd order cumulant fit, and polydispersity index (PDI).

The dispersion state of the different IONP batches synthesized was probed by dynamic light scattering (DLS) in a weakly acidic aqueous medium (pH~2) (**Figure 9**). The fit of correlograms by the 2nd order cumulant method provided the Z-average hydrodynamic diameter (D_h) and polydispersity index (PDI). Typical values of Z-average diameters were in the order of 30 nm, ranging from 16 to 55 nm when considering all synthesized batches (**Figure 10**). For instance, the Z-average hydrodynamic diameter of 35ff multi-core IONPs was measured at $D_h=36$ nm (PDI=0.13), while 20ff UUSPIO mono-core IONPs were sized at $D_h=16$ nm (PDI=0.21). Hydrodynamic diameters estimated by DLS are always found larger than diameters determined by TEM due to the dried state of the TEM sample. In addition, the data was represented in intensities (%) and not in numbers (%), which tended to overestimate the Z-average diameters. The DLS sizes however better represented the real dispersion state of IONPs, by evidencing the presence of aggregates.

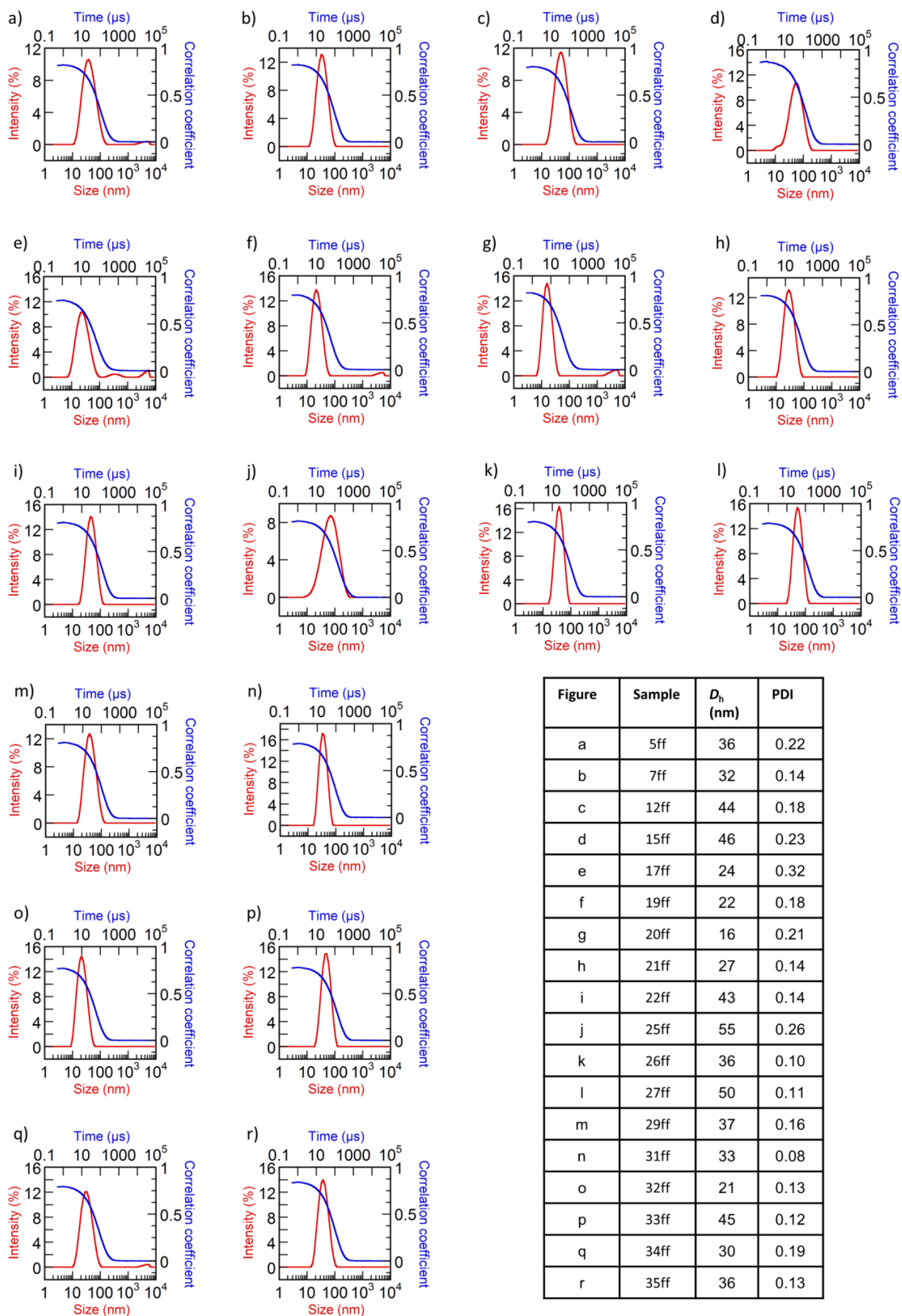


Figure 10 DLS correlagrams and intensity-averaged distributions of diameters. The 2nd order cumulant fit led to the Z-average hydrodynamic diameter (D_h) and polydispersity index (PDI).

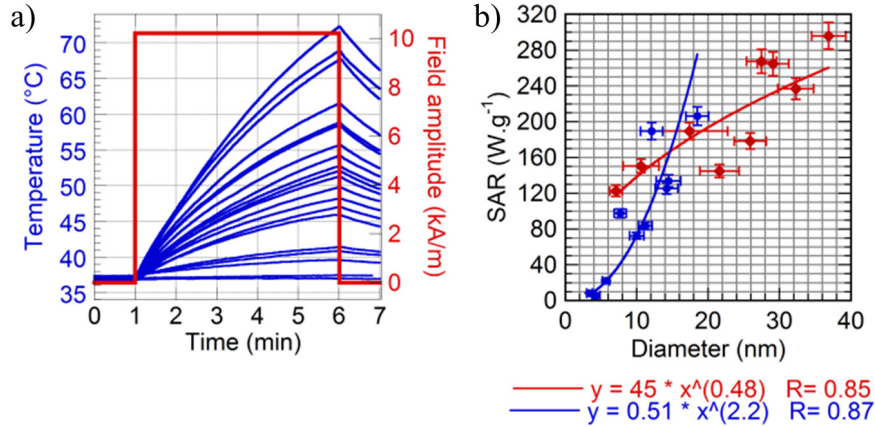


Figure 11 a) Temperature profiles vs. time of different samples of iron oxide concentration set at $3 \text{ g}\cdot\text{L}^{-1}$, under application of an AMF at $H_{\text{app}}=10.2 \text{ kA}\cdot\text{m}^{-1}$ and $f=755 \text{ kHz}$. **b)** Deduced SAR vs. mean diameter (determined by TEM) for mono-core (blue) and multi-core IONPs (red). Solid lines are power law fits of exponents 2.2 and 0.48, respectively.

The efficiency of the different IONP batches for magnetic hyperthermia was evaluated by applying an AMF for 5 min and by recording the temperature rise of the solvent, with iron oxide concentrations set to $3 \text{ g}\cdot\text{L}^{-1}$. While no significant heating under AMF was obtained for a few samples like the 17ff UUSPIOs with the smallest size, a temperature rise from $37 \text{ }^\circ\text{C}$ to $70 \text{ }^\circ\text{C}$ was recorded for the largest dispersible multi-core IONPs 15ff (**Figure 11**). Therapeutic hyperthermia requires that IONPs heat cancerous tissues up to $43\text{--}44 \text{ }^\circ\text{C}$ to deposit a suitable “thermal dose”, usually by IONP intra-tumoral injection.[30] This temperature may potentially be reached *in vivo* with the best heating samples after few minutes, even at a concentration as low as the one used in our study ($3 \text{ g}\cdot\text{L}^{-1}$), assuming that their heating properties are preserved in physiological intracellular conditions.[31] The heating properties of our sample library were thus quantified using the specific absorption rate (SAR) determined experimentally using the commonly used formula:

$$SAR = \frac{\Delta T}{\Delta t_{t \rightarrow 0}} \cdot \frac{C_p}{m_{\text{Fe}_2\text{O}_3}}$$

where $(\Delta T/\Delta t)_{t \rightarrow 0}$ was the temperature raise slope at early times of AMF application (first 5 s) to simulate adiabatic conditions,[32] m was the mass of IONPs in 1 mL of suspension and C_p was approximated by the specific heat of pure water.[2]

SAR has been used to evaluate the heating properties of the IONPs instead of the intrinsic loss power (ILP),[33] because the SAR variation with field intensity can depart significantly from a quadratic law. The plot of SAR at given field amplitude ($H_{\text{app}}=10.2 \text{ kA}\cdot\text{m}^{-1}$) and frequency ($f=755 \text{ kHz}$) vs. diameter measured by TEM clearly evidences a correlation between the SAR and IONP outer diameter measured by TEM (**Figure 11.b**). Nanospheres experimentally followed a quadratic law with diameter while multi-core IONPs follow a lower exponent (nearly square-root). This was qualitatively in agreement with the most advanced models on the optimal size of magnetic NPs for MH at given

values of their other physical properties (specific magnetization and magnetic anisotropy).[34] Results obtained on all batches evidence that all multi-core IONPs and mono-core IONPs larger than 12-14 nm were efficient nanoheaters, while UUSPIOs smaller than 5-6 nm did not generate sufficient heat but were likely useable as positive (T_1 -weighted) MRI contrast agents, as shown later in this section. Mono-core IONPs of intermediate diameters (10-14 nm) were ideal to be used both as nanoheaters for MH and as negative (T_2 -weighted) MRI contrast agents (*vide infra*), once coated with appropriate ligands, while larger ones were difficult to stabilise in physiological media.

3.2.3. In-depth investigation of the heating properties

An in-depth characterization of magnetic heating properties was carried out on selected IONP samples with interesting morphologies and core size in 20-40 nm range as evidenced by TEM, with outstanding heating efficiency ($SAR > 200 \text{ W}\cdot\text{g}^{-1}$ at $H_{\text{app}} = 10.2 \text{ kA}\cdot\text{m}^{-1}$ and $f = 755 \text{ kHz}$). Large mono-core IONPs (34ff) and multi-core IONPs of different grain size and increasing outer diameters (31ff, 35ff, and 15ff) were thus selected to be further examined with an in-house developed pick-up coil set-up, allowing SAR measurement on a broad range of AMF frequencies and amplitudes.[35] AC magnetization curves of IONPs are plotted on **Figure 12** versus amplitude H_{app} up to $21 \text{ kA}\cdot\text{m}^{-1}$ at fixed frequency ($f = 1030 \text{ kHz}$).

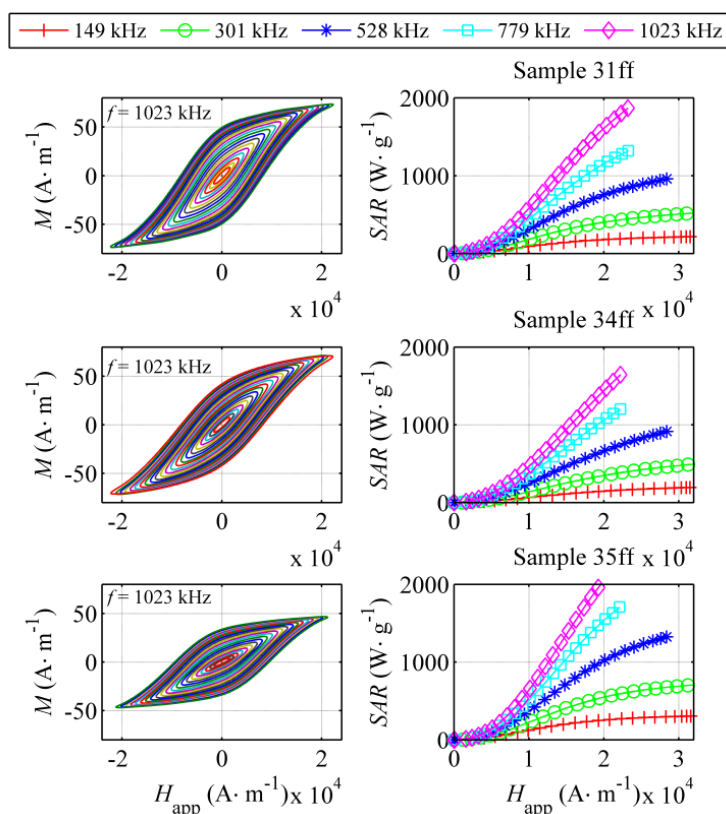


Figure 12 AC hysteresis loops of samples 31ff, 34ff and 35ff at 1023 kHz fixed frequency (left); SAR of samples 31ff, 34ff and 35ff versus field amplitude at different frequencies (right).

Such AC hysteresis loops reflected that magnetic moments of IONPs under AMF excitation oscillate with a phase lag relatively to the magnetic field, leading to a partial conversion of the radiofrequency magnetic energy into heat that then dissipated in the surrounding aqueous medium. Larger AC hysteresis loops areas were obtained at higher amplitudes H_{app} and higher frequencies, while stronger magnetic anisotropy of the materials tended to change the shapes of the curves from sigmoidal to more square-like shapes. Carrey *et al.* interpreted such dynamic hysteresis loops by a two-level Stoner-Wohlfarth model instead of the classical linear response theory involving Néel and Brown relaxation times of the magnetic moments.[34, 36, 37] The larger the surface of the hysteresis loops, the larger the energy dissipated by the IONPs per AMF cycle. These AC magnetization curves could be compared to the calorimetric experiments by multiplying the surface of the hysteresis loop with the frequency and by dividing by iron oxide concentration to get the *SAR*. The resulting values were then plotted as a function of frequency and amplitude, as shown in **Figure 12**.

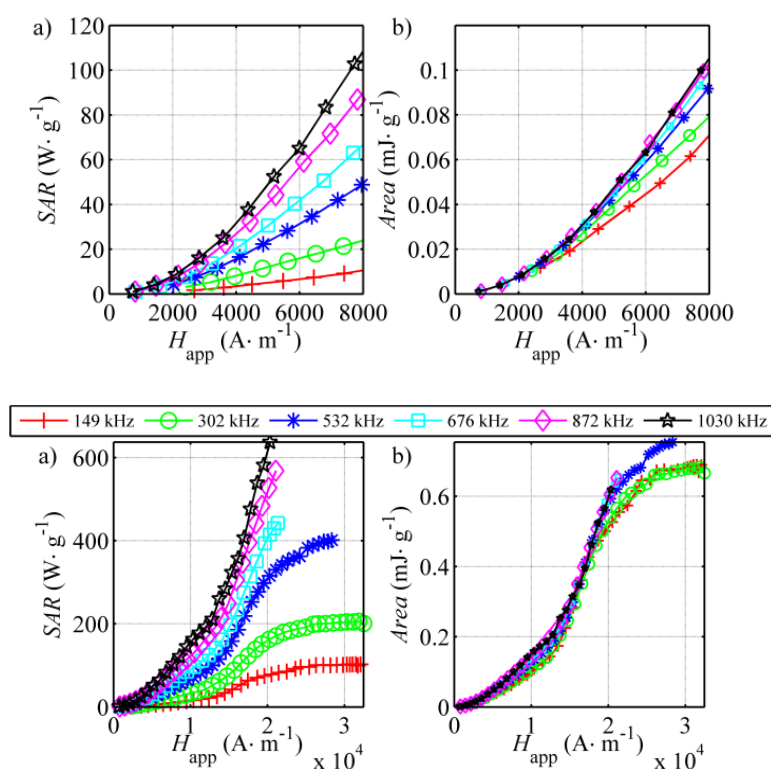


Figure 13 a) *SAR* and **b)** hysteresis loop area A vs. applied intensity H_{app} of the oxidized 15ff nanoflower batch.

SAR values as high as $2000 \text{ W}\cdot\text{g}^{-1}$ were obtained at a frequency of 1023 kHz and amplitude of $20 \text{ kA}\cdot\text{m}^{-1}$, although out-passing by a factor 4 the upper limit of $5 \times 10^9 \text{ A}\cdot\text{m}^{-1}\cdot\text{s}^{-1}$ of the $f \cdot H_{app}$ product recommended for human treatment by MH.[38] Whereas the *ILP* parameter was previously introduced in the literature by dividing the *SAR* with frequency and the square of H_{app} ,[1] the assumption that *SAR* is a quadratic function only works at low field amplitude (**Figure 13 a**). It has been therefore preferred to report the ratio (in $\text{J}\cdot\text{g}^{-1}$) of the *SAR* and frequency, which represented the area A of a hysteresis loop (*i.e.* thermal losses per AMF cycle). This enabled to directly compare the heating properties of the

magnetic IONPs synthesized in this chapter to different ones reported in literature, although measured under various conditions and setups. As reported by Carrey *et al.*,[34] the plot of hysteresis surface area *vs.* H_{app} expected for ferromagnetic NPs exhibits a sigmoidal shape: it started with a slow increase as long as the AMF amplitude was lower than the anisotropy field H_{an} of the nanomaterials, then increased rapidly (*i.e.* with an exponent larger than two, value expected for superparamagnetic IONPs), and finally plateaus in the high-field limit. The plot of A *vs.* H_{app} for the 15ff sample perfectly fitted this description (**Figure 13 b**), with a threshold anisotropy field $H_{an} \sim 10^4 \text{ A}\cdot\text{m}^{-1}$. The plateau value around $0.7 \text{ mJ}\cdot\text{g}^{-1}$ for the oxidized 15ff sample was not particularly outstanding as a maximal value of $1.8 \text{ mJ}\cdot\text{g}^{-1}$ was previously reported for IONPs obtained by coprecipitation followed by hydrothermal treatment.[39]

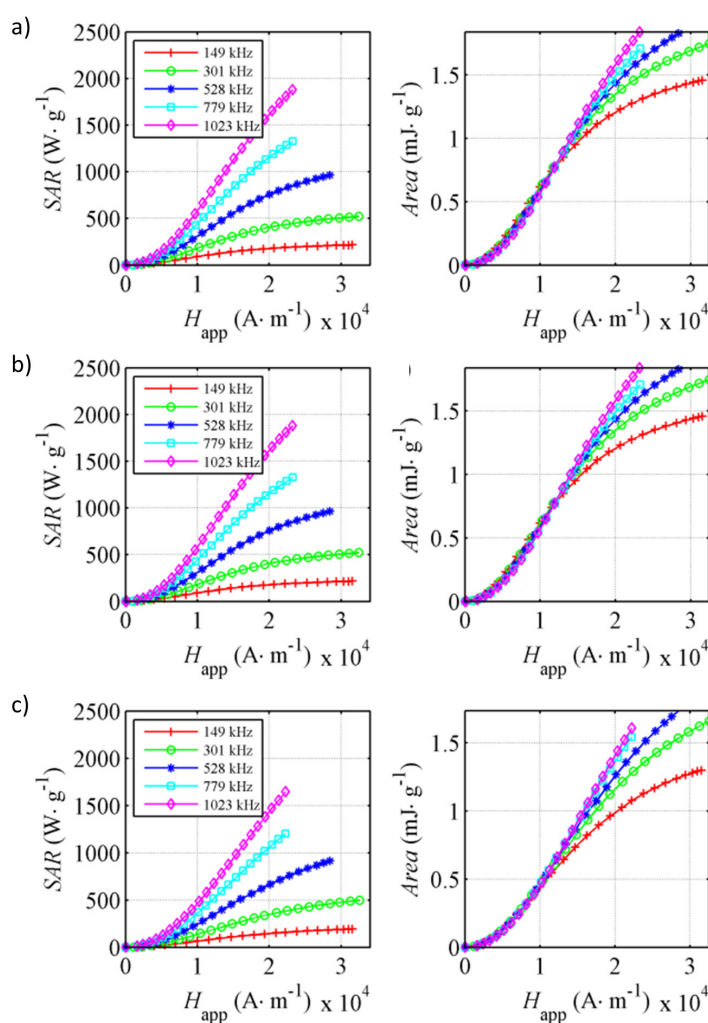


Figure 14 SAR (left) and hysteresis area (right) *versus* applied magnetic field amplitude (H_{app}) of sample **a)** 31ff (multi-core IONPs of $27.5 \pm 4.2 \text{ nm}$ outer diameter) **b)** 34ff (smooth nanospheres of $18.5 \pm 3.2 \text{ nm}$ diameter) **c)** 35 ff (multi-core IONPs of $29.1 \pm 4.4 \text{ nm}$ outer diameter).

The oxidized 15ff sample however illustrated the complex magnetic behaviour of multi-core IONPs reflected in the dependence of their hysteresis loss area A with the amplitude H_{app} of the AMF: for the six probed frequencies, the plots of the hysteresis area A vs. H_{app} collapsed almost perfectly on a unique master curve. The field dependence remains quadratic up to a threshold H_{app} ascribed to the anisotropy field H_{an} of the multi-core structure, characteristic of collective dynamics of sintered grains as in a multiple-domain magnet. For any applied AMF strength below H_{an} , multi-core IONPs exhibited pure superparamagnetic response as evidenced by the quadratic variation of their SAR vs. H_{app} plot, each of their magnetic mono-domains being excited individually by the AMF. Other IONP batches of lower outer sizes (below 30 nm) exhibited even superior plateau values of the hysteresis area per cycle vs. H_{app} (which exact value slightly varies with frequency), from $\sim 1.6 \text{ mJ}\cdot\text{g}^{-1}$ for 31ff multi-core IONPs (**Figure 14 a**) and 34ff smooth nanospheres (**Figure 14 b**) to $\sim 2.5 \text{ mJ}\cdot\text{g}^{-1}$ for 35ff multi-core IONPs (**Figure 13 c**) or a bit lower ($2 \text{ mJ}\cdot\text{g}^{-1}$) at the lowest frequency of 149 kHz. In comparison with data available in the literature, these were the highest hysteresis area values reported so far for synthetic magnetic IONPs, excluding the case of needle-like submicron $\gamma\text{-Fe}_2\text{O}_3$ particles commercialized for magnetic recording applications, that could reach hysteresis areas up to $8 \text{ mJ}\cdot\text{g}^{-1}$, but necessitated to apply an AMF stronger than a thrice higher threshold field, $H_{an}\sim 30 \text{ kA}\cdot\text{m}^{-1}$. [40]

3.2.4. Study of the magnetization properties

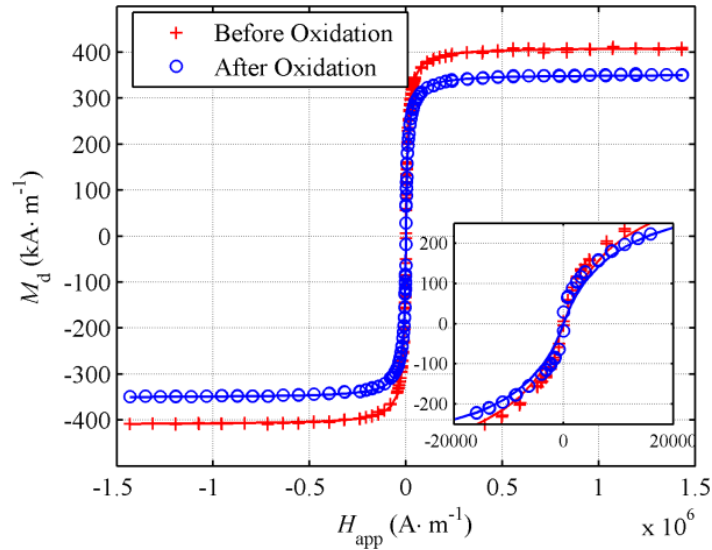


Figure 15 Static magnetization curve of 15ff multi-core IONPs measured by VSM before and after oxidation (red and blue curves, respectively). In a narrow range $-1.6 < H_{app} < 1.6 \text{ kA}\cdot\text{m}^{-1}$ only, the curves could be approximated by $M_d = \chi \cdot H_{app}$, the susceptibility reaching a value as high as $\chi = 59$ in both cases.

To get an insight into the peculiar structure-property relationships and complex magnetic behavior of multi-core IONPs, the DC magnetization curves of 15ff IONPs (with or without the oxidation step) were also measured with a lab-made vibrating sample magnetometer (VSM) setup (**Figure 15**). In both cases, the IONPs were dispersed in water acidified with dilute HNO_3 (pH \sim 2.5). The magnetization curve of both samples exhibited null coercive field ($H_c=0$) and zero remanence

($M_r=0$), which corresponded to pure superparamagnetic behavior. This evidences the good dispersion state of these IONPs in water, as a remanant magnetization would have been expected in case of an aggregated sample. The saturation magnetization of the non-oxidized sample obtained after synthesis and washings was $350 \text{ kA}\cdot\text{m}^{-1}$, slightly below the value $400 \text{ kA}\cdot\text{m}^{-1}$ of bulk magnetite (Fe_3O_4), as ascribed to spin-canting defects at the IONP surface,[41] or to partial oxidation already starting during the purification steps, as no particular precautions were taken to prevent it. In contrast, total oxidation of sample 15ff obtained by heating with iron(III) nitrate, led to a magnetization at saturation of $300 \text{ kA}\cdot\text{m}^{-1}$, which was the expected value for bulk maghemite ($\gamma\text{-Fe}_2\text{O}_3$).

All the IONP batches were thus oxidized intentionally to control the magnetic phase of the IONPs, despite lowering the magnetic saturation and presumably their heating efficiency for MH. All samples reported in this study exhibited similar saturation magnetization (**Figure 16**). A second useful information provided by VSM magnetometry could be obtained by fitting the DC magnetization curves by the Langevin function characteristic of superparamagnetism, convolved by a log-normal distribution of diameters to take into account size-dispersity.[24] The resulting magnetic domain diameters laid below the outer diameter measured by TEM for multi-core IONPs: $25.1\pm 12.0 \text{ nm}$ for 35ff, $21.9\pm 10.6 \text{ nm}$ for 31ff, while almost identical to TEM (within experimental uncertainty) for 34ff mono-core IONPs: $18.8\pm 6.5 \text{ nm}$.

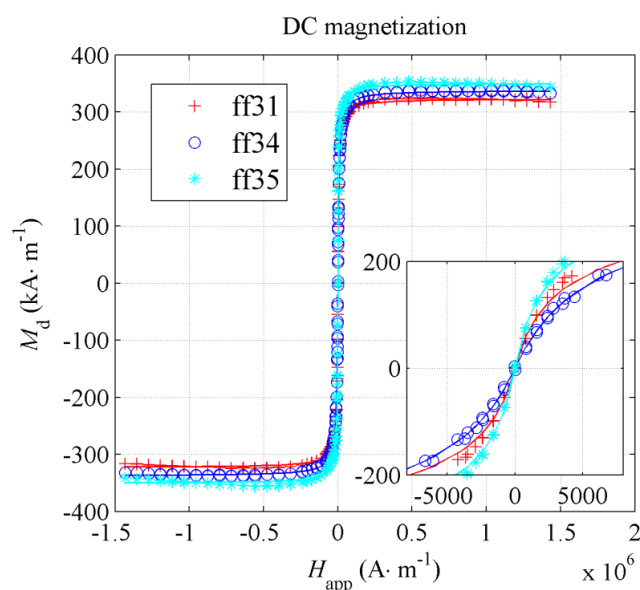


Figure 16 DC magnetization of samples 31ff, 34ff and 35ff measured by VSM. As the inset showed, they followed a superparamagnetic behavior. The signal was normalized by volume fraction calculated from the iron oxide concentration (assuming a mass density of $5 \text{ g}\cdot\text{cm}^3$) in order to derive the specific magnetization per domain, denominated M_d . In the linear region described by $M_d = \chi \cdot H_{app}$, (*i.e.* in a narrow range $-1.6 < H_{app} < 1.6 \text{ kA}\cdot\text{m}^{-1}$, the susceptibility value varied between $\chi=45$ (34ff), $\chi=68$ (31ff) and up to $\chi=100$ (35ff).

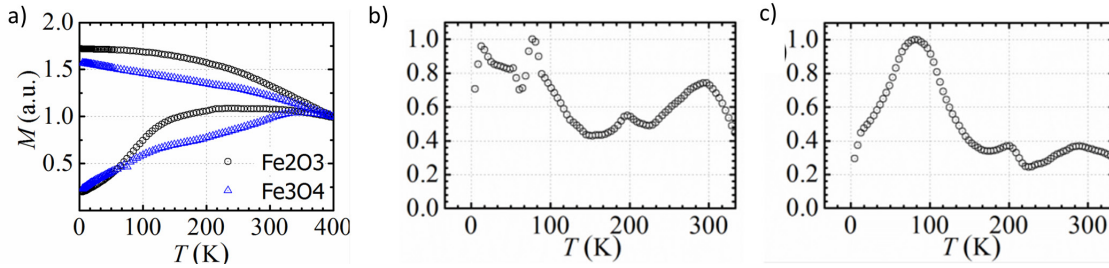


Figure 17 ZFC-FC measurement by MPMS magnetometry and derivative $d(M_{\text{FC}}-M_{\text{ZFC}})/dT$ of the FC-ZFC curve difference for un-oxidized Fe_3O_4 (a) and oxidized $\gamma\text{-Fe}_2\text{O}_3$ (b) 15ff nanoflowers. The peak near 90K was ascribed to the Verwey transition.

Sensitive magnetometry performed on the commercial MPMS system on the oxidized and non-oxidized 15ff multi-core IONPs (**Figure 17 a**) led to ZFC and FC magnetization curves *vs.* temperature both lower for the non-oxidized as compared to the oxidized 15ff NPs. Such non-classical ZFC-FC curve profile had already been reported for large (18 and 22 nm) Fe_3O_4 NPs synthesized by iron(III) oleate thermal decomposition,[42] and was partially explained by the so-called Verwey or charge ordering transition,[42, 43] when such IONPs underwent a slight crystallographic distortion from cubic, electrically conducting, to inverse spinel, electrically insulating, structure, this change of crystalline structure also impacted the magnetic properties. A suitable method to estimate the blocking temperature T_B , defined at the transition from the ferrimagnetic state to the superparamagnetic regime, consisted in plotting the derivative of the $M_{\text{FC}}-M_{\text{ZFC}}$ curve difference with respect to temperature.[25] For the two different batches (non-oxidized and oxidized 15ff), the plot exhibited three maxima (**Figure 17 c-d**). The peak near 90 K was ascribed to the Verwey transition of magnetite, yet it was not clear why it also appeared on the oxidized sample. The two other peaks corresponded to characteristic temperatures, respectively near 200 and 300 K. It is rather uncommon for a sample to exhibit two values of blocking temperatures. We hypothesized that $T_{B1} \approx 200$ K was ascribed to individual magnetic domains of diameter 7.4 ± 1.4 nm and $T_{B2} \approx 300$ K to the whole magnetic multi-core structure of outer diameter 36.9 ± 4.8 nm. The complete interpretation of these data, *e.g.* in term of superspin glass transition, would have necessitated complementary AC susceptometry experiments *vs.* temperature, to study the slow relaxation dynamics of the frustrated spins in multi-core multi-core IONPs as reported by Kostopoulou *et al.*,[13] but it was beyond the scope of these experiments.

3.2.5. Iron oxide nanoparticles as MRI contrast agents

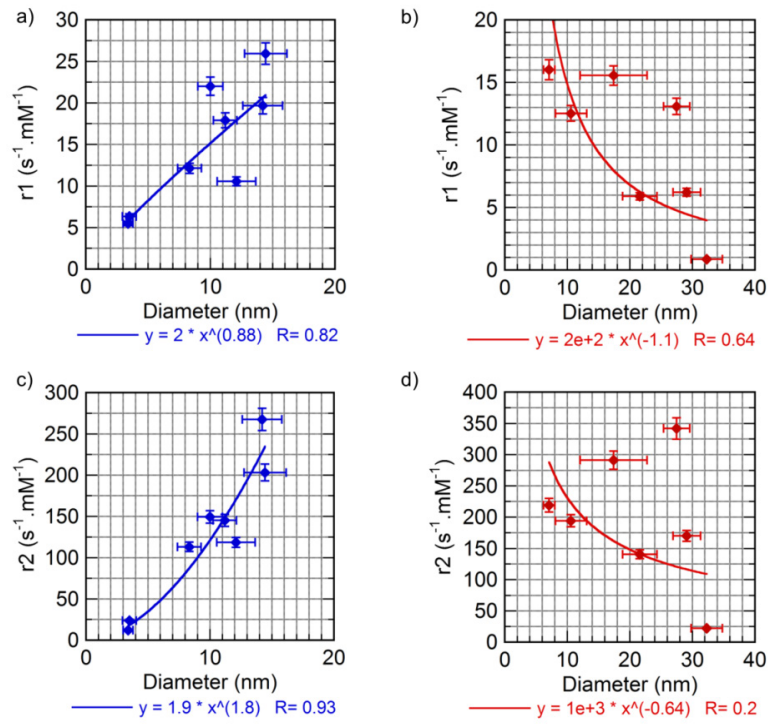


Figure 18 Longitudinal relaxivity of mono-core (a) and multi-core (b) IONPs. Transverse relaxivity of mono-core(c) and multi-core (d) IONPs. All measurements were performed at 37°C on a 1.41 Tesla / 60 MHz Bruker mq60 relaxometer.

In order to assess the efficiency of the different batches synthesized by the polyol route to relax nuclear spins of water protons, their transverse (r_2) and longitudinal (r_1) relaxivities were measured at physiological temperature (37 °C) with a 60 MHz relaxometer based on a 1.41 Tesla magnet (*i.e.* close to the 1.5 Tesla magnetic field of most clinical MRI machines used in hospitals) (**Figure 18**). Practically, the longitudinal (T_1) and transverse (T_2) relaxation times of water protons were measured with an inversion-recovery and a CPMG sequence, respectively at decreasing equivalent [Fe] concentrations starting from 6 mM, in acidified water to maintain colloidal stability. Relaxivities were obtained from the slope of the linear variation with [Fe] of the longitudinal (respectively transverse) decay rate of water proton spins, according to:[22]

$$\frac{1}{T_{i=1 \text{ or } 2}} = r_i \times [Fe] + \left(\frac{1}{T_{i=1 \text{ or } 2}}\right)_{\text{water}}$$

where $(1/T_i)_{\text{water}}$ represented the diamagnetic contribution of water.

In the “outer sphere” model of MRI contrast agents introduced by Ayant and Freed for paramagnetic agents, and adapted by Gillis *et al.* to superparamagnetic IONPs,[44] the increase relaxation rate $1/T_2$ compared to pure water originates from fluctuating dipolar interactions between nuclear spins of water protons and the electronic magnetic moment of IONPs. For a limited range of diameters called “motional averaging regime”, the superparamagnetic particle could be considered

immobile during the echo time (TE) of the sequence compared to random trajectories of water molecules diffusing all around the magnetic sphere. In this case, Vuong *et al.* have shown that r_2 follows a universal scaling law that is quadratic both with the magnetization and with the radius of the “outer sphere”, defined as the minimum approach distance between H₂O molecules and the IONP center.[45] For the IONP batches prepared in this study, the quadratic law was perfectly observed for the smooth sphere IONPs (**Figure 18 c**), validating the proton diffusive model. This brought additional evidence that no organic layer remains on their surface after the washing steps. If not, water protons could not reach IONP surface and the quadratic law would not be observed. In the case of multi-core IONPs, the variation of r_2 vs. size appeared erratic (**Figure 18 d**), presumably because of their rough geometry and very high specific area mentioned before, that could be up to 60% larger than the geometrical area of a smooth sphere. Proton relaxivity may have arisen by a combination of “outer sphere” and “inner sphere” mechanisms, meaning that water molecules could be transiently adsorbed in the porosity of multi-core IONPs, relaxation dynamics could therefore not be modeled by a single translational diffusion constant of water molecules around the particle.

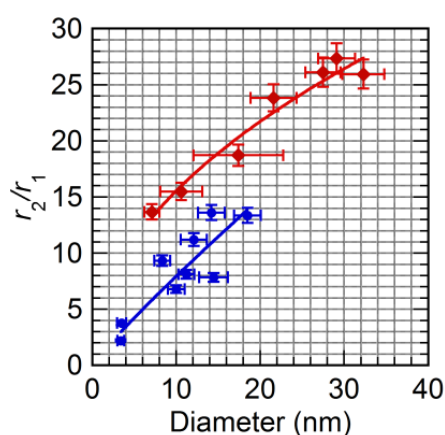


Figure 19 Ratio of transverse (r_2) to longitudinal (r_1) relaxivities at 1.41 T/60MHz (37°C) vs. average TEM diameters of IONPs, for nanosphere (blue) and nanoflower (red) samples. Solid lines are power law fits of exponents respectively 0.92 and 0.48.

The ratio of relaxivities r_2/r_1 is commonly used to determine whether IONPs are most suitable as T_1 (positive) or T_2 (negative) MRI contrast agents. With r_2/r_1 ratios larger than 5, most of the IONPs synthesized here were suitable as negative contrast agents for T_2 weighted MRI applications, such as commercial medical products Resovist®, Feridex®, Cliavist® or Clariscan®.[46] With much smaller r_2/r_1 ratios, UUSPIOs of just a few nm diameters synthesized in pure DEG would rather be perfectly suitable as T_1 -type, positive contrast agents. Such UUSPIO-based T_1 -type contrast agents not yet commercially available would however be an excellent alternative to gadolinium chelates currently used and suspected of toxicity.[47] Free gadolinium ions (*i.e.* not complexed by very strong ligands) are indeed nephrotoxic and neurotoxic, and undesirable side effects may arise in patients with renal insufficiency. Iron oxides having been proven perfectly safe in clinical use, these UUSPIOs are likely to find applications as alternative T_1 contrast agents in clinical MRI in a near future.

4. Conclusion

Two synthesis pathways to produce IONPs were presented in this chapter. The co-precipitation synthesis was an affordable method to produce nanoparticles with diameters in the order of 6-10 nm. Several grams of material could be yielded this way. Unfortunately, the control over their morphology (size, size-distribution) was not satisfying, even after a post-synthesis process of size-grading. Also larger and well-defined nanoparticles (in the range of 10-30 nm) with optimum heating properties were needed for magnetic hyperthermia applications, and smaller nanoparticles (in the range of 2-4 nm) were needed for specific applications in MR imaging. We decided to test the polyol synthesis which fulfilled our requirements for the targeted applications.

To conclude on the polyol pathway; we presented herein a comprehensive study of IONPs synthesis and characterization. IONPs were synthesized by the forced hydrolysis of iron(II, III) chlorides either in pure DEG polyol or in a mixture with NMDEA. The importance of controlling the amount and timing of water addition for a successful synthesis and proper control over IONP morphology has been demonstrated. A library of samples was obtained, ranging from “ultra-ultra-small” (~3 nm) UUSPIOs obtained by water “hot injection” in DEG at 220°C and fast growth (20 min), to large IONPs (up to 37 nm) obtained by a longer “heating up” protocol in a DEG/NMDEA 1:1 mixture. Depending on reaction conditions (natural mixing *vs.* mechanical stirring), either mono-core or multi-core morphologies were obtained. The structural and magnetic properties of these IONPs were extensively studied. They all exhibited superparamagnetic behavior characterized by a reversible magnetization curve in static magnetic field, with a strong saturation magnetization above $3 \times 10^5 \text{ A}\cdot\text{m}^{-1}$. On the physical point of view, the specific absorption rate (*SAR*) was first tested at given AMF conditions (755 kHz, $10.2 \text{ kA}\cdot\text{m}^{-1}$) and iron oxide concentration ($3 \text{ g}\cdot\text{L}^{-1}$). These parameters were also varied over a broad range of field strength and frequencies with the use of an AC magnetometer that is much faster than calorimetric experiments for estimating the *SAR*. The efficiency of most of synthesized batches as MRI contrast agents were also evaluated by proton relaxometry measurements. Several scaling laws were derived for the *SAR* and the relaxivity ratio r_2/r_1 , both being estimated at physiological body temperature (37 °C). At given AMF condition, the *SAR* exhibits quadratic variation with diameter for smooth nanospheres and slower variations (*viz.* square root) for multi-core IONPs. Transverse relaxivity r_2 exhibits also quadratic variation with diameter for smooth nanospheres, in line with the “motional averaging regime” of the “outer sphere” model of MRI contrast agents. The r_2/r_1 ratios, calculated to distinguish IONPs better suited as T_1 or T_2 MRI contrast agents, varies linearly on diameter for nanospheres, and with a lower exponent (*viz.* square root) for multi-core IONPs. In the case of the smallest diameter IONPs synthesized (USPIOs), their longitudinal relaxivity r_1 at 1.41 T associated with moderate r_2/r_1 ratio make them alternatives to gadolinium chelates as positive MRI contrast agents, with lower risk of side effects on patients. The AC hysteresis loops measured at

varying AMF frequency and intensity brought more information on the magnetic hyperthermia mechanisms. In the case of multi-core IONPs and large nanospheres, the *SAR* vs. field intensity curve showed an inflexion point between low and high fields. Below this threshold field, they presented perfect superparamagnetic behavior, whereas above this field they behaved more like ferromagnets. The threshold field could be associated with an anisotropy field as was done in the two-level Stoner-Wohlfarth model developed by Carrey *et al.* for blocked magnetic moments.[34] Besides these obvious applications as nanoheaters in magnetic field hyperthermia and as MRI contrast agents, other uses could be envisioned. These very large diameter IONPs yet forming stable colloidal suspensions exhibited extremely large magnetic susceptibility in DC magnetic field (χ up to 100), which could be a requested property for delicate experimental setups based on weak DC magnetic fields such as the “magnetic tweezers” to manipulate living tissues or embryos,[48] or micromechanical experiments to assess the flexural rigidity of magnetic wires.[49] Another application could also be magnetic particle imaging (MPI) that requires IONPs optimally in the 20-25 nm diameter range so that magnetization saturates at low field strengths.[50] Such versatility of sizes, morphologies and thus of physical properties was achieved by playing only on the nature of polyols as well as the amount and way of introducing water in the reaction vessel (“hot injection” vs. “heating up”), in solvent reflux conditions. In brief, robust, gram-scale and easily reproducible synthesis protocols were described to prepare from ultra-ultra-small superparamagnetic cores to very large size magnetic smooth nanospheres and multi-core IONPs, the latter offering among the highest magnetic heating properties reported so far for synthetic IONPs.

5. References

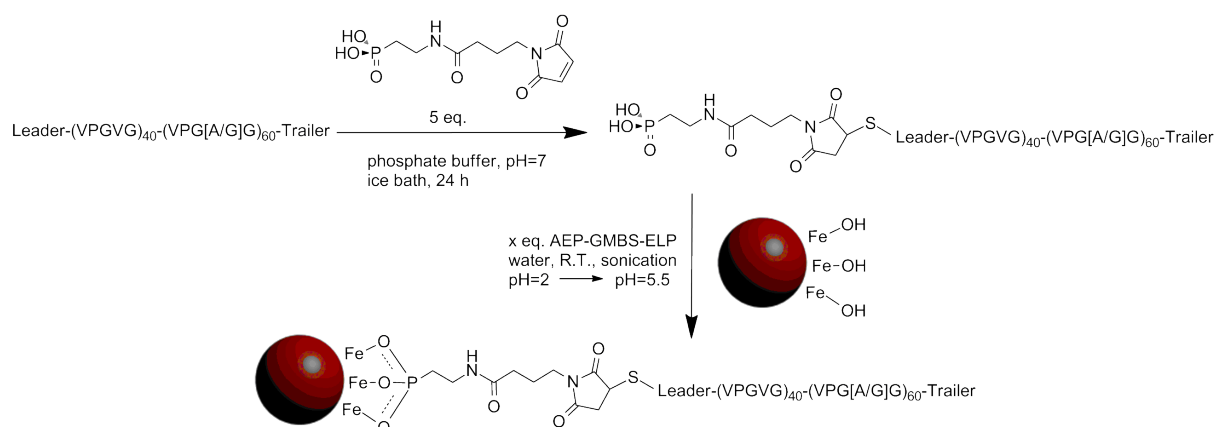
1. Hervault, A. and N.T.K. Thanh, *Magnetic nanoparticle-based therapeutic agents for thermo-chemotherapy treatment of cancer*. *Nanoscale*, 2014. **6**(20): p. 11553-11573.
2. Pérido, E.A., G. Hemery, O. Sandre, D. Ortega, E. Garaio, F. Plazaola, and F.J. Teran, *Fundamentals and advances in magnetic hyperthermia*. *Applied Physics Reviews*, 2015. **2**(4): p. 041302.
3. Massart, R., *Preparation of aqueous magnetic liquids in alkaline and acidic media*. *IEEE Transactions on Magnetics*, 1981. **17**(2): p. 1247-1248.
4. Caruntu, D., G. Caruntu, Y. Chen, C.J. O'Connor, G. Goloverda, and V.L. Kolesnichenko, *Synthesis of Variable-Sized Nanocrystals of Fe₃O₄ with High Surface Reactivity*. *Chemistry of Materials*, 2004. **16**(25): p. 5527-5534.
5. Hyeon, T., S.S. Lee, J. Park, Y. Chung, and H.B. Na, *Synthesis of Highly Crystalline and Monodisperse Maghemite Nanocrystallites without a Size-Selection Process*. *J. Am. Chem. Soc.*, 2001. **123**(51): p. 12798-12801.
6. Horner, O., S. Neveu, S.d. Montredon, J.-M. Siaugue, and V. Cabuil, *Hydrothermal synthesis of large maghemite nanoparticles: influence of the pH on the particle size*. *J. Nanopart. Res.*, 2009. **11**(5): p. 1247-1250.
7. Lu, A.-H., E.L. Salabas, and F. Schuth, *Magnetic Nanoparticles: Synthesis, Protection, Functionalization, and Application*. *Angewandte Chemie*, 2007. **46**(8): p. 1222-1244.
8. Bee, A., R. Massart, and S. Neveu, *Synthesis of very fine maghemite particles*. *Journal of Magnetism and Magnetic Materials*, 1995. **149**(1-2): p. 6-9.
9. Filippousi, M., M. Angelakeris, M. Katsikini, E. Paloura, I. Efthimiopoulos, Y. Wang, D. Zamboulis, and G. Van Tendeloo, *Surfactant Effects on the Structural and Magnetic Properties of Iron Oxide Nanoparticles*. *The Journal of Physical Chemistry C*, 2014. **118**(29): p. 16209-16217.
10. Shubitidze, F., K. Kekalo, R. Stigliano, and I. Baker, *Magnetic nanoparticles with high specific absorption rate of electromagnetic energy at low field strength for hyperthermia therapy*. *Journal of Applied Physics*, 2015. **117**(9): p. 094302.
11. Blanco-Andujar, C., D. Ortega, P. Southern, Q.A. Pankhurst, and N.T.K. Thanh, *High performance multi-core iron oxide nanoparticles for magnetic hyperthermia: microwave synthesis, and the role of core-to-core interactions*. *Nanoscale*, 2015. **7**(5): p. 1768-1775.
12. Lartigue, L., P. Hugounenq, D. Alloyeau, S.P. Clarke, M. Lévy, J.-C. Bacri, R. Bazzi, D.F. Brougham, C. Wilhelm, and F. Gazeau, *Cooperative Organization in Iron Oxide Multi-Core Nanoparticles Potentiates Their Efficiency as Heating Mediators and MRI Contrast Agents*. *ACS Nano*, 2012. **6**(12): p. 10935-10949.
13. Kostopoulou, A., K. Brintakis, M. Vasilakaki, K.N. Trohidou, A.P. Douvalis, A. Lascialfari, L. Manna, and A. Lappas, *Assembly-mediated interplay of dipolar interactions and surface spin disorder in colloidal maghemite nanoclusters*. *Nanoscale*, 2014. **6**(7): p. 3764-3776.
14. Caruntu, D., Y. Remond, N.H. Chou, M.-J. Jun, G. Caruntu, J. He, G. Goloverda, C. O'Connor, and V. Kolesnichenko, *Reactivity of 3d Transition Metal Cations in Diethylene Glycol Solutions. Synthesis of Transition Metal Ferrites with the Structure of Discrete Nanoparticles Complexed with Long-Chain Carboxylate Anions*. *Inorganic Chemistry*, 2002. **41**(23): p. 6137-6146.
15. Cheng, C., F. Xua, and H. Gu, *Facile synthesis and morphology evolution of magnetic iron oxide nanoparticles in different polyol processes*. *NewJ. Chem.*, 2011. **35**: p. 1072-1079.
16. Hachani, R., M. Lowdell, M. Birchall, A. Hervault, D. Mertz, S. Begin-Colin, and N.T.K. Thanh, *Polyol synthesis, functionalisation, and biocompatibility studies of superparamagnetic iron oxide nanoparticles as potential MRI contrast agents*. *Nanoscale*, 2016. **8**(6): p. 3278-3287.
17. Hugounenq, P., M. Levy, D. Alloyeau, L. Lartigue, E. Dubois, V. Cabuil, C. Ricolleau, S. Roux, C. Wilhelm, F. Gazeau, and R. Bazzi, *Iron Oxide Monocrystalline Nanoflowers for Highly Efficient Magnetic Hyperthermia*. *J. Phys. Chem. C*, 2012. **116**(29): p. 15702-15712.

18. Forge, D., A. Roch, S. Laurent, H. Tellez, Y. Gossuin, F. Renaux, L. Vander Elst, and R.N. Muller, *Optimization of the Synthesis of Superparamagnetic Contrast Agents by the Design of Experiments Method*. The Journal of Physical Chemistry C, 2008. **112**(49): p. 19178-19185.
19. Sakellari, D., K. Brintakis, A. Kostopoulou, E. Myrovali, K. Simeonidis, A. Lappas, and M. Angelakeris, *Ferrimagnetic nanocrystal assemblies as versatile magnetic particle hyperthermia mediators*. Materials Science and Engineering: C, 2016. **58**: p. 187-193.
20. Tourinho, F.A., R. Franck, and R. Massart, *Aqueous ferrofluids based on manganese and cobalt ferrites*. Journal of Materials Science, 1990. **25**(7): p. 3249-3254.
21. Koppel, D.E., *Analysis of Macromolecular Polydispersity in Intensity Correlation Spectroscopy: The Method of Cumulants*. The Journal of Chemical Physics, 1972. **57**(11): p. 4814-4820.
22. Henoumont, C., S. Laurent, and L. Vander Elst, *How to perform accurate and reliable measurements of longitudinal and transverse relaxation times of MRI contrast media in aqueous solutions*. Contrast Media & Molecular Imaging, 2009. **4**(6): p. 312-321.
23. Hemery, G., E. Garanger, S. Lecommandoux, A.D. Wong, E.R. Gillies, B. Pedrono, T. Bayle, D. Jacob, and O. Sandre, *Thermosensitive polymer-grafted iron oxide nanoparticles studied by in situ dynamic light backscattering under magnetic hyperthermia*. Journal of Physics D: Applied Physics, 2015. **48**(49): p. 494001.
24. Garaio, E., O. Sandre, J.-M. Collantes, J.A. Garcia, S. Mornet, and F. Plazaola, *Specific absorption rate dependence on temperature in magnetic field hyperthermia measured by dynamic hysteresis losses (ac magnetometry)*. Nanotechnology, 2015. **26**(1): p. 015704.
25. Bruvera, I.J., P. Mendoza Zélis, M. Pilar Calatayud, G.F. Goya, and F.H. Sánchez, *Determination of the blocking temperature of magnetic nanoparticles: The good, the bad, and the ugly*. Journal of Applied Physics, 2015. **118**(18): p. 184304.
26. Tromsdorf, U.I., O.T. Bruns, S.C. Salmen, U. Beisiegel, and H. Weller, *A Highly Effective, Nontoxic T1 MR Contrast Agent Based on Ultrasmall PEGylated Iron Oxide Nanoparticles*. Nano Letters, 2009. **9**(12): p. 4434-4440.
27. Ninjbadgar, T. and D.F. Brougham, *Epoxy Ring Opening Phase Transfer as a General Route to Water Dispersible Superparamagnetic Fe₃O₄ Nanoparticles and Their Application as Positive MRI Contrast Agents*. Advanced Functional Materials, 2011. **21**(24): p. 4769-4775.
28. Borase, T., T. Ninjbadgar, A. Kapetanakis, S. Roche, R. O'Connor, C. Kerskens, A. Heise, and D.F. Brougham, *Stable Aqueous Dispersions of Glycopeptide-Grafted Selectably Functionalized Magnetic Nanoparticles*. Angewandte Chemie International Edition, 2013. **52**(11): p. 3164-3167.
29. Hannecart, A., D. Stanicki, L. Vander Elst, R.N. Muller, S. Lecommandoux, J. Thevenot, C. Bonduelle, A. Trotier, P. Massot, S. Miraux, O. Sandre, and S. Laurent, *Nano-thermometers with thermo-sensitive polymer grafted USPIOs behaving as positive contrast agents in low-field MRI*. Nanoscale, 2015. **7**(8): p. 3754-3767.
30. Sandre, O., C. Genevois, E. Garaio, L. Adumeau, S. Mornet, and F. Couillaud, *In Vivo Imaging of Local Gene Expression Induced by Magnetic Hyperthermia*. Genes, 2017. **8**(2): p. 61.
31. Sanz, B., M.P. Calatayud, E. De Biasi, E. Lima, Jr., M.V. Mansilla, R.D. Zysler, M.R. Ibarra, and G.F. Goya, *In Silico before In Vivo: how to Predict the Heating Efficiency of Magnetic Nanoparticles within the Intracellular Space*. Sci Rep., 2016. **6**: p. 38733.
32. Iacob, N., G. Schinteie, P. Palade, C.M. Ticos, and V. Kuncser, *Stepped heating procedure for experimental SAR evaluation of ferrofluids*. The European Physical Journal E, 2015. **38**(6): p. 57.
33. Kallumadil, M., M. Tada, T. Nakagawa, M. Abe, P. Southern, and Q.A. Pankhurst, *Suitability of commercial colloids for magnetic hyperthermia*. Journal of Magnetism and Magnetic Materials, 2009. **321**(10): p. 1509-1513.
34. Carrey, J., B. Mehdaoui, and M. Respaud, *Simple models for dynamic hysteresis loop calculations of magnetic single-domain nanoparticles: Application to magnetic hyperthermia optimization*. Journal of Applied Physics, 2011. **109**(8): p. 083921.
35. Garaio, E., J.M. Collantes, J.A. Garcia, F. Plazaola, S. Mornet, F. Couillaud, and O. Sandre, *A wide-frequency range AC magnetometer to measure the specific absorption rate in*

- nanoparticles for magnetic hyperthermia*. Journal of Magnetism and Magnetic Materials, 2014. **368**: p. 432-437.
36. Lacroix, L.-M., R.B. Malaki, J. Carrey, S. Lachaize, M. Respaud, G.F. Goya, and B. Chaudret, *Magnetic hyperthermia in single-domain monodisperse FeCo nanoparticles: Evidences for Stoner–Wohlfarth behavior and large losses*. Journal of Applied Physics, 2009. **105**(2): p. 023911.
 37. Mehdaoui, B., A. Meffre, J. Carrey, S. Lachaize, L.-M. Lacroix, M. Gougeon, B. Chaudret, and M. Respaud, *Optimal Size of Nanoparticles for Magnetic Hyperthermia: A Combined Theoretical and Experimental Study*. Advanced Functional Materials, 2011. **21**(23): p. 4573-4581.
 38. Hergt, R. and S. Dutz, *Magnetic particle hyperthermia—biophysical limitations of a visionary tumour therapy*. Journal of Magnetism and Magnetic Materials, 2007. **311**(1): p. 187-192.
 39. Marciello, M., V. Connord, S. Veintemillas-Verdaguer, M.A. Verges, J. Carrey, M. Respaud, C.J. Serna, and M.P. Morales, *Large scale production of biocompatible magnetite nanocrystals with high saturation magnetization values through green aqueous synthesis*. Journal of Materials Chemistry B, 2013. **1**(43): p. 5995-6004.
 40. Kashevsky, B.E., S.B. Kashevsky, V.S. Korenkov, Y.P. Istomin, T.I. Terpinskaya, and V.S. Ulashchik, *Magnetic hyperthermia with hard-magnetic nanoparticles*. Journal of Magnetism and Magnetic Materials, 2015. **380**: p. 335-340.
 41. Baaziz, W., B.P. Pichon, S. Fleutot, Y. Liu, C. Lefevre, J.-M. Greneche, M. Toumi, T. Mhiri, and S. Begin-Colin, *Magnetic Iron Oxide Nanoparticles: Reproducible Tuning of the Size and Nanosized-Dependent Composition, Defects, and Spin Canting*. The Journal of Physical Chemistry C, 2014. **118**(7): p. 3795-3810.
 42. Salas, G., C. Casado, F.J. Teran, R. Miranda, C.J. Serna, and M.P. Morales, *Controlled synthesis of uniform magnetite nanocrystals with high-quality properties for biomedical applications*. Journal of Materials Chemistry, 2012. **22**(39): p. 21065-21075.
 43. Goya, G.F., T.S. Berquó, F.C. Fonseca, and M.P. Morales, *Static and dynamic magnetic properties of spherical magnetite nanoparticles*. Journal of Applied Physics, 2003. **94**(5): p. 3520-3528.
 44. Gillis, P., A. Roch, and R.A. Brooks, *Corrected Equations for Susceptibility-Induced T2-Shortening*. Journal of Magnetic Resonance, 1999. **137**(2): p. 402-407.
 45. Vuong, Q.L., J.-F. Berret, J. Fresnais, Y. Gossuin, and O. Sandre, *A Universal Scaling Law to Predict the Efficiency of Magnetic Nanoparticles as MRI T2-Contrast Agents*. Advanced Healthcare Materials, 2012. **1**(4): p. 502-512.
 46. Wang, Y.-X.J., *Superparamagnetic iron oxide based MRI contrast agents: Current status of clinical application*. Quantitative Imaging in Medicine and Surgery, 2011. **1**(1): p. 35-40.
 47. Thomsen, H.S., S.K. Morcos, and P. Dawson, *Is there a causal relation between the administration of gadolinium based contrast media and the development of nephrogenic systemic fibrosis (NSF)?* Clinical Radiology, 2006. **61**(11): p. 905-906.
 48. Serwane, F., A. Mongera, P. Rowghanian, D.A. Kealhofer, A.A. Lucio, Z.M. Hockenbery, and O. Campas, *In vivo quantification of spatially varying mechanical properties in developing tissues*. Nat Meth, 2017. **14**(2): p. 181-186.
 49. Gerbal, F. and Y. Wang, *Optical detection of nanometric thermal fluctuations to measure the stiffness of rigid superparamagnetic microrods*. Proceedings of the National Academy of Sciences, 2017. **114**(10): p. 2456-2461.
 50. Bauer, L.M., S.F. Situ, M.A. Griswold, and A.C.S. Samia, *High-performance iron oxide nanoparticles for magnetic particle imaging - guided hyperthermia (hMPI)*. Nanoscale, 2016. **8**(24): p. 12162-12169.

CHAPTER III

SURFACE FUNCTIONALIZATION OF IRON OXIDE NANOPARTICLES



1. Introduction

The chemical composition at the surface of bulk iron oxide has been examined, and reportedly exhibit iron and oxygen atoms, regularly arranged with local crystal defects.[1] The loss of crystal order leads to the integration of hydrogen in the chemical composition of the surface, and respecting the valency of the atoms produces Fe-O-H bonds. As IONPs exhibit high surface-to-volume ratios, a large numbers of hydroxyl groups are available at the surface for subsequent chemical modification. Molecules that have a strong affinity toward the iron oxide surface can be used to bring specific properties of interest to the IONPs. Chemical moieties such as phosphonates,[2] carboxylates,[3] as well as hydroxyls[4, 5] can form coordination bonds with the surface of maghemite or magnetite. The following sections describe the ligands that have been attached at the surface of the IONPs through direct chelation.

Several small molecules as well as natural and synthetic polymers conjugated to IONPs have been reported in the literature. They were able to improve the stability of IONPs in aqueous and biological media, or to bring new functionalities. Dextran,[6] poly(vinylpyrrolidone) (PVP),[7] poly(ethylene) glycol (PEG),[8] have been investigated among others to give “stealth” properties to IONPs. The resulting core-shell morphologies added increased circulation times to the functionalized IONPs in the blood as compared to bare IONPs, allowing the nanoparticles to reach their target organs. The chemical modification of IONPs can be achieved either by directly adsorbing molecules or macro-molecules at their surface when there is a direct compatibility, or by using ligands that help bridging the gap between the inorganic core and the organic shell. The grafting of the polymer can be achieved in multiple steps, by successive assembly of molecules, starting from the IONPs. This divergent strategy is also referred to “grafting from”. The grafting of the polymer can also be achieved in a one-step chemical modification of the surface of the nanoparticle using an appropriate intermediate, extratemporaneously synthesized. This other grafting strategy leads directly to a core-shell structure. This strategy is sometimes referred to ‘grafting to’, and has the major advantage of being convergent.

Here are reported first the grafting of poly(acrylic acid) (PAA) that acted as a stabilizing polymer, and the grafting of PAA-Rhodamine which imparted fluorescence and stability properties to the IONPs. PEG was grafted for its stealth property, a (VPGIG)₂₀ (referred to as ELP₂₀) mono-block elastin-like protein was conjugated for its thermosensitive property, a (VPGVG)₄₀-(VPG(A/G)G)₆₀ di-block elastin-like protein terminated with a Tat cell-penetrating peptide (referred to as ELP_{40-60-Tat}) was also grafted for its thermosensitive property. Finally, a DY-700 fluorescent probe was attached to allow the tracking of the IONPs in biological conditions. These molecules or bio-macromolecules brought additional functionalities to the magnetic properties of the nanoparticles. The new properties acquired by the IONPs will be presented in the followings chapters, while in the present one are discussed the different strategies of surface modifications as well as the necessary characterizations.

2. Direct adsorption of polyions

2.1. Adsorption of poly(acrylic acid)

PAA, or more precisely, sodium poly(acrylate) can be adsorbed at the surface of IONPs. This polyvalent molecule presents a logarithmic acid dissociation constant of $pK_a=4.2$, and chelates through its carboxylic acid groups at the surface of the IONPs.[9] Different molecular weights were available. In our case, a polymer with a molecular weight $M_w=5100 \text{ g}\cdot\text{mol}^{-1}$ was used. PAA was adsorbed at the surface of IONPs when nanoparticles stable in neutral pH were needed. This phenomenon was used to study the interaction of IONPs with vesicles at neutral pH, in collaboration with Mrs Er-Rafik (Institut Charles Sadron, Strasbourg, France). It was also employed as an intermediate before reaction with poly[dimethylsiloxane-*co*-(3-aminopropyl)methylsiloxane] PDMS-*co*-APMS to yield hydrophobic nanoparticles that could be incorporated in the hydrophobic part of the membrane of vesicles, made themselves by the self-assembly of PEO-PDMS-PEO (*block* or *graft*) copolymers.[10]

2.1.1. Materials and methods

1 L of an aqueous solution at $2 \text{ g}\cdot\text{L}^{-1}$ of PAA ($M_w=6,000 \text{ g}\cdot\text{mol}^{-1}$), pH fixed at $pH=2.5$ with nitric acid was freshly prepared in a 5 L beaker. IONPs produced by co-precipitation (fraction S1S2) were diluted with water acidified at $pH=2.5$ with dilute nitric acid to reach a volume of 1 L and a concentration of $2 \text{ g}\cdot\text{L}^{-1}$. The polymer solution was homogenized using a IKA Eurostar power control-visc overhead mechanical stirrers, agitation speed set at 400-500 rpm, and the IONP dispersion was added. Instantaneous flocculation of the IONPs occurred. They were then sedimented over a strong permanent magnet (Calamit Magneti, Milano-Barcelona-Paris). The supernatant was removed and replaced with few mL of MilliQ water. The pH of the solution was carefully adjusted to $pH=8$ using dilute ammonia, leading to a spontaneous redispersion of the chemically modified nanoparticles, labelled IONPs@PAA.

2.1.2. Results and discussion

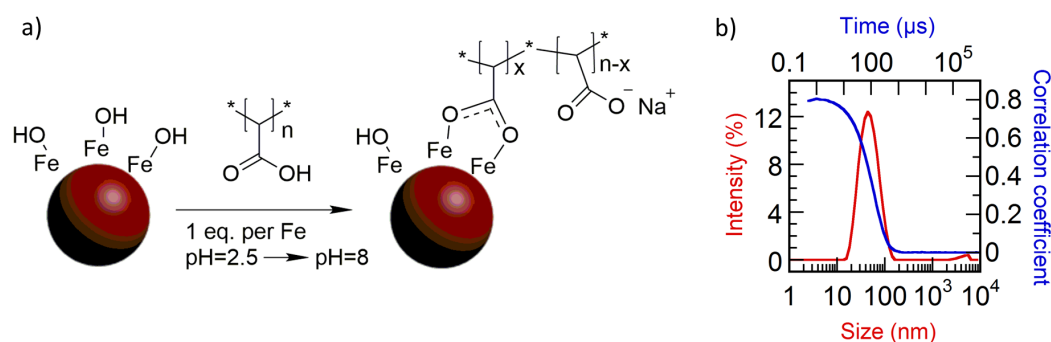


Figure 1 a) Synthetic scheme for the adsorption of PAA on IONPs and b) DLS diagram of the nanoparticles dispersed in aqueous conditions, at neutral pH.

PAA is an anionic polymer, making it a polyelectrolyte. Its degree of ionization varies over a large range of solution pH.[11] The surface modification of the IONPs with PAA took place in acidic conditions, with positively charged IONPs and mild negatively charged PAA polymer chains. The mixing of the two solutions led to a spontaneous change of stability of the IONPs, evidencing a fast interaction driven by attraction of the two reactants by their opposite charge signs. The IONPs readily flocculated, which could indicate a loss of electrostatic stability due to the compensation and/or screening of their surface charge density. The surface modification strategy reported here was optimized by adding IONPs to the solution of PAA, and by decreasing the concentrations of PAA and IONPs during reaction to $1 \text{ g}\cdot\text{L}^{-1}$. This allegedly prevented PAA chains from binding to more than one nanoparticle, and thus prevented irreversible aggregation. The IONPs were re-dispersed by renewing the supernatant which allowed removing the excess unreacted PAA. The solution pH was set in a range of 7-8 with dilute ammonia. The addition of a base led to a larger fractional charge of PAA, with a value of approximately 0.5 according to Swift *et al.*[11] Said differently, half of the carboxylic acids were protonated at this solution pH. The polymer chain could be potentially tethered at one end (**Figure 1 a**), though multiple sections alongside the chain were more probably grafted at the surface of the IONPs. The resulting IONPs grafted with PAA were stable in neutral conditions as evidenced by DLS (**Figure 1 b**).

2.2. Adsorption of Rhodamine123-modified poly(acrylic acid)

2.2.1. Materials and methods

50 mg of PAA ($M_w=5100 \text{ g}\cdot\text{mol}^{-1}$, $10 \text{ }\mu\text{mol}$, corresponding to 0.5 mmol of repeat unit) was dissolved in 5 mL of DMF. 1.6 mg (0.012 equiv., $0.8 \text{ }\mu\text{mol}$) of 1-ethyl-3-[3-(dimethylamino)propyl]carbodiimide (EDC) (Alfa Aesar, 98+ %) and 1.6 mg (0.02 equiv., $1.4 \text{ }\mu\text{mol}$) of *N*-hydroxysuccinimide (NHS) (Sigma Aldrich, 98 %) were added to the solution to produce the NHS-activated ester. Precised amounts of EDC and NHS were reacted using stock solutions at a concentration of $1 \text{ g}\cdot\text{L}^{-1}$. 0.8 mg (0.013 equiv., $6.9 \text{ }\mu\text{mol}$) of rhodamine123 (Acros Organics, 99+ %) dissolved in DMF was then added, mixed and let to react in order to yield rhodamine-modified PAA. Several PAA-rhodamine polymers were prepared this way with different targeted ratios of acrylic acid repeat units modified (0.1%, 1%, 5%, 10%) by adjusting equivalents of rhodamine, EDC and NHS with respect to PAA. The modified polymers were purified by dialysis against water and lyophilized. The grafting of PAA-Rhodamine was made in identical conditions as for unmodified PAA.

2.2.2. Results and discussion

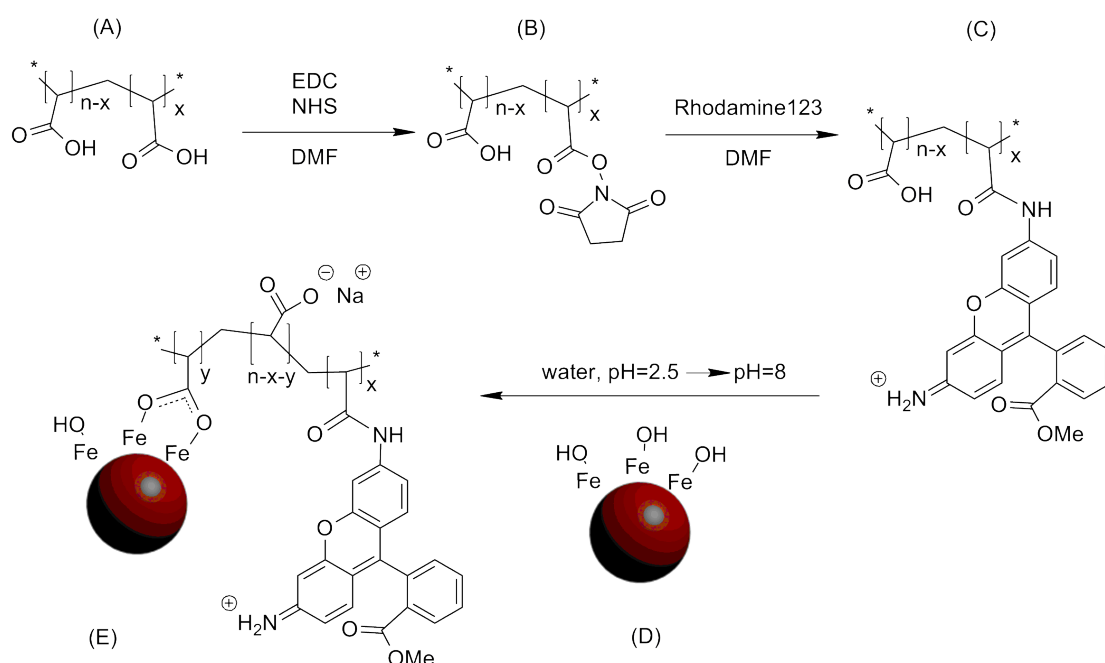


Figure 2 Chemical modification of PAA with Rhodamine123 and adsorption of the polymer on IONPs (coprecipitation, fraction S1S2).

PAA-Rhodamine was synthesized and grafted on IONPs (coprecipitation, fraction S1S2) to bring stability to the dispersion of nanoparticles and to allow the tracking of nanoparticles in solution (**Figure 2**). This was done with the purpose of monitoring the interaction of IONPs with vesicles' membranes by laser confocal scanning microscopy (LCSM). PAA (A) was reacted with EDC and NHS in DMF to produce a controlled fraction of repeat unit activated with NHS (B). Rhodamine123 then reacted with the NHS ester, resulting in the formation of an amide bond (C). Using DMF as a reaction solvent instead of water led to a better solubility of rhodamine123. PAA conjugated with rhodamine123 was then grafted onto IONPs (D) in order to bring strong electrostatic stability at neutral pH and fluorescence to the resulting core-shell IONPs (E).

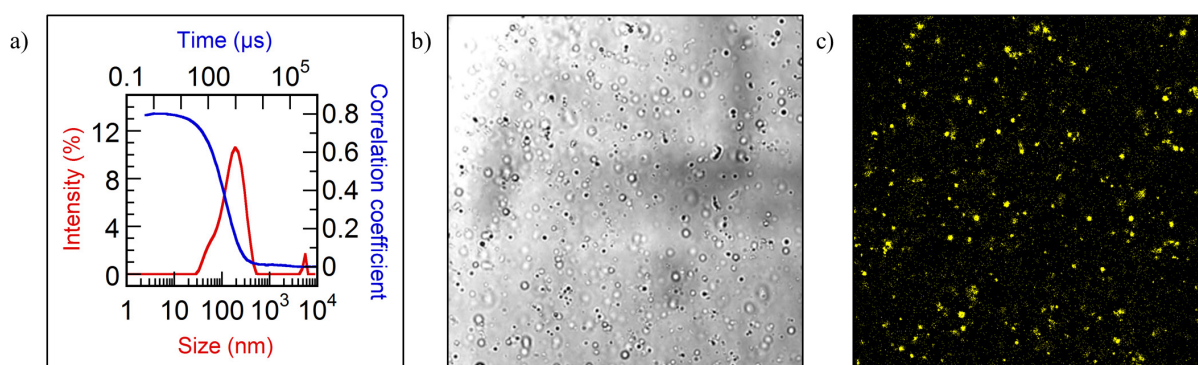


Figure 3 a) DLS diagram of the modified IONPs. **b)** IONPs grafted with the 1% rhodamine123-modified PAA were aggregated on purpose and observed with a confocal microscope in pseudo bright-field and **c)** fluorescence mode.

IONPs modified with PAA-rhodamine123 1% were stable in water at pH=7 (**Figure 3 a**). The core-shell IONPs@PAA-rhodamine123 were unstable in aqueous conditions at higher fractions of modified repeat unit (5%, 10%), probably because of the lower solubility of the fluorescent probe in water, leading to a more hydrophobic surface. The fluorescence was also confirmed by observation using a confocal microscope. A homogeneous fluorescent background was obtained when IONPs were stable and homogeneously distributed in the medium. The ionic strength of the solution was increased to screen the stabilizing electrostatic charges in order to aggregate the IONPs. Fluorescent aggregates were observed (**Figure 3 b,c**), proving that the fluorescence came from the polymer grafted at the surface of the IONPs and not from free polymer chains in solution. These IONPs were synthesized, characterized and sent to collaborators at the Institut Charles Sadron in order to study the interactions between IONPs and liposome cell-membrane models.

3. Divergent synthesis or “grafting from”

A synthetic polymer poly[2-(dimethylamino) ethyl methacrylate] (PDMAEMA) and a biopolymer (ELP) were covalently tethered onto the IONPs. In a conventional “grafting from” synthesis, an initiator would have been attached at the surface of the nanoparticle before polymerization. In this section the strategy was similar except that the polymers and biopolymers were already synthesized beforehand and grafted at the surface of IONPs after addition of an anchor group and a heterofunctional linker (**Figure 4**).

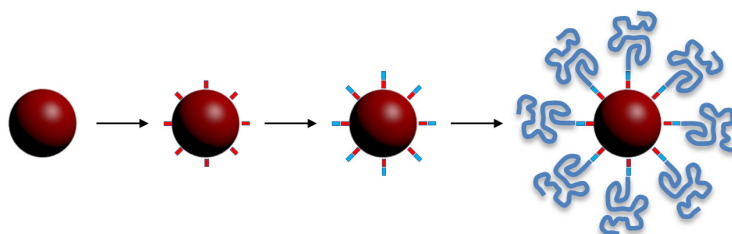


Figure 4 General principle of a divergent surface modification strategy.

An aminosilane acted as the first building block that bound to the surface of the IONPs and bridged the gap between the inorganic core and the organic shell to build up. Then a heterobifunctional-linker was added before final attachment with the macromolecule of interest. Two macromolecules were introduced: a synthetic pH and thermosensitive polymer PDMAEMA, and a recombinant thermosensitive elastin-like polypeptide (VPGIG)₂₀ (referred to as ELP₂₀). These two macromolecules afforded additional functionalities to the IONPs. The grafting is presented in this section while the studies of the resulting IONPs modified properties are described in Chapters IV, V and VI.

3.1. Grafting of PDMAEMA

PDMAEMA is a thermo- and pH-sensitive polycation that has been used in applications such as antibacterial surfaces.[10] The present work uses the thermal transitions (LCST) of the polymer chains grafted onto IONPs. A sol-gel route and copper assisted azide-alkyne cycloaddition (CuAAC) chemistry were used for grafting PDMAEMA chains onto iron oxide NPs.

3.1.1. Materials and methods

Sodium azide 99.5% (NaN_3) was provided by Sigma Aldrich. Water used was MilliQ™ (18 $\text{M}\Omega\text{-cm}$ conductivity). 3-(2-aminoethylamino)propyltrimethoxysilane 96% (AEAPTMS), and *N*-hydroxysuccinimide (NHS) were purchased from Alfa Aesar. Reagent grade anhydrous diethyl ether was from Baker. Bromoacetic acid, 1-ethyl-3-(3-dimethylaminopropyl) carbodiimide hydrochloride (EDC), diisopropylethylamine (DIPEA), ethylenediaminetetraacetic acid (EDTA) were from Acros Organics.

AEAPTMS (530 μL , 2.4 mmol, representing an excess of 20 added molecules per nm^2 for S1S2) was grafted onto IONPs (420 mg, 5.25 mmol of Fe), in a mixture of solvents (10% water 90% ethanol) in acidic conditions (arising from the low pH of the ferrofluid) at first to hydrolyse the alkoxy silane into a hydroxysilane, followed by condensation with the Fe-OH moieties of iron oxide in neutral conditions for an hour, and boiling at reflux for another hour, a protocol adapted from Duguet and Mornet's patent.[12] The sample was then washed multiple times with methanol by a precipitation-redispersion process before being redispersed in water with a pH corrected to a value of 3 with dilute HNO_3 .

Azidoacetic acid (AZ) was synthesized following a modified procedure from Srinivasan et al.[13] Sodium azide NaN_3 (107 mmol) was dissolved in 30 mL of distilled water and cooled down with an ice bath. Bromoacetic acid (51 mmol) was then added slowly and the mixture was let to warm to room temperature overnight. The chemical obtained *via* substitution was protonated by acidification and extracted in diethylether, dried over MgSO_4 and finally, after a rotavapor extraction of the solvent at 40°C and reduced pressure, a pale yellow oily liquid was obtained.

Typically 1 equiv. of azidoacetic acid (0.83 mg, 8 μmol) with respect to primary amines was added to the IONPs aqueous solution (12 mg, 75 μmol Fe). 2 equiv. of EDC (3.14 mg, 16 μmol) and 1 equiv. of NHS (0.94 mg, 8 μmol) were then added and the pH was adjusted to 5. An "active" NHS ester was produced *in situ*, reacting with the primary amines at the surface of the iron oxide IONPs to form amide bonds. The mixture was let to react for 6 h and dialyzed against 5 L of milliQ™ water.

Typically 1 equiv. of propargyl-terminated PDMAEMA (82 mg, 8.2 μmol), 2 equiv. of ascorbic acid (3.3 mg, 16.4 μmol), and 0.5 equiv. of CuSO_4 (0.65 mg, 4.1 μmol) were added to the IONPs (12 mg, 75 μmol of Fe) functionalized with the clickable azido moiety (by the previous step) in

DMF. The mixture was let to react overnight and dialyzed against 5 L of a 10 mM EDTA solution to complex and remove the copper salts, followed by pure water.

3.1.2. Results and discussions

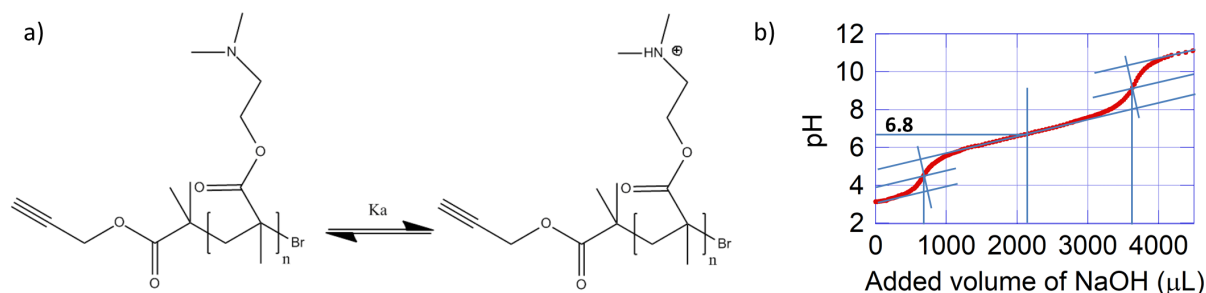


Figure 5 a) Equilibrium of charge of the tertiary amine. b) pH-metric titration of PDMAEMA chains by NaOH (0.3 M) for the determination of the $pK_a=9.5$ of the secondary amines moieties

The solution behaviour of PDMAEMA chains in water is known to be both thermo- and pH-sensitive. The tertiary amine of the PDMAEMA chains (**Figure 5 a**) was characterized by its respective value of dissociation constant pK_a . As determined by acid-base titration (**Figure 5 b**), half of amines were protonated at solution pH lower than their $pK_a=6.8$. This value was close to the reported value for PDMAEMA 7.5.[14] The pK_a values of tertiary amines usually are within the range of 10–11, which shifts to a lower value because of the neighboring group effect upon polymerization.

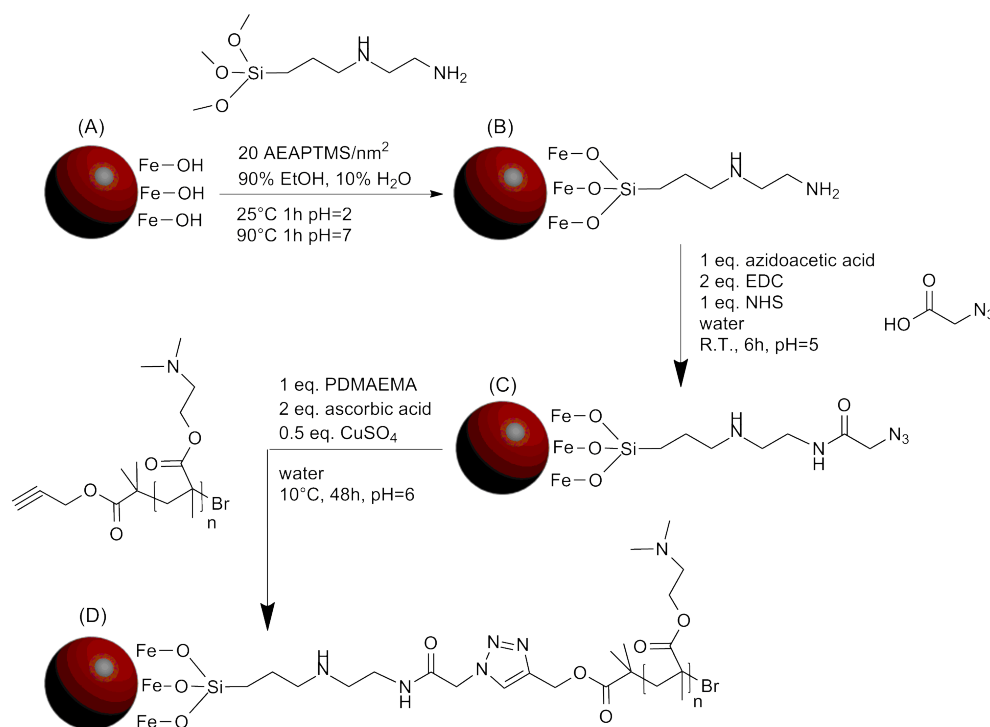


Figure 6 Scheme showing the successive reaction steps to build the magnetic thermosensitive IONPs. The original maghemite ($\gamma\text{-Fe}_2\text{O}_3$) IONPs (A) was reacted in a sol-gel reaction with the AEAPTMS organosilane to introduce primary amines (B). The IONPs were then grafted with an azide by formation of an amide bond facilitated by EDC and NHS (C). The IONPs were finally modified with the thermosensitive polymer PDMAEMA (D) using a copper assisted azide-alkyne cycloaddition (CuAAC).

The synthesis of IONPs with well-defined properties (chemical composition of their surface, hydrodynamic diameters, and polydispersity indexes) was mandatory to achieve the goal of *in situ* probing of their thermosensitive properties. First, superparamagnetic IONPs were synthesized using an alkaline co-precipitation procedure in water followed by an electrolyte-mediated magnetic sorting process. Then their surface was modified grafting the thermosensitive PDMAEMA chains, as illustrated in **Figure 6**. Bare IONPs exhibited hydroxyl functionalities (Fe–OH) at their surfaces (A), allowing the grafting of AEAPTMS by sol-gel chemistry (hydrolysis-condensation) (B). The amino groups on the grafted silanes were then coupled to the carboxylic acid groups of azidoacetic acid (abbreviated as AZ) using an NHS-mediated EDC coupling (C). Finally, the alkyne-terminated PDMAEMA was conjugated to the azides by a copper-mediated azide-alkyne cycloaddition reaction (D).

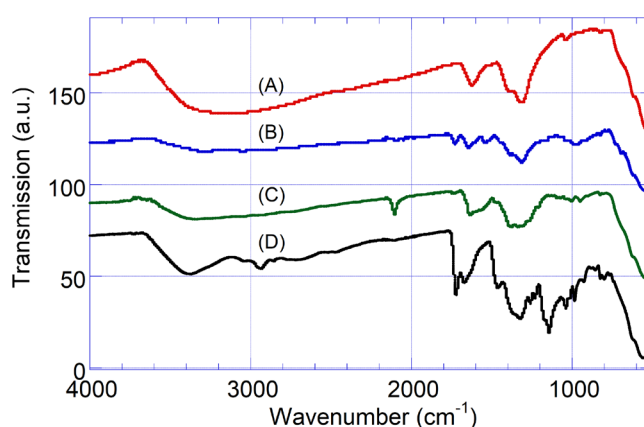


Figure 7 ATR-IR spectra of the reaction products (A) IONPs, (B) IONPs@AEAPTMS, (C) IONPs@AEAPTMS-AZ and (D) IONPs@AEAPTMS-AZ-PDMAEMA

The grafting steps were assessed by attenuated total reflectance infrared (ATR-IR) spectroscopy (**Figure 7**). The spectrum of the original ferrofluid presented peaks in the 3000-3500 cm^{-1} range attributed to the stretching vibrations of water. The peak at 1392 cm^{-1} was ascribed to elongation modes of adsorbed NO_3^- ions. The peak at 1627 cm^{-1} was ascribed to the bending vibration of water, and the large, strong peak starting at 536 cm^{-1} corresponded to the stretching vibration of the bond between oxygen and iron. This was explained by the hydration of the sample by remaining traces of water. This water was superficial rather than interstitial as there was evidence from TEM analysis that the IONPs consist of single spherical crystals with no visible defects. The signal from the Fe-O bond ensured the presence of hydroxyl groups on the surface of the IONPs, which were thereafter exploited as anchor groups for the silanization and subsequent functionalization. After grafting of AEAPTMS, new signals appeared in the IR spectrum. Barely visible peaks at 1114 and 1043 cm^{-1} were due to the stretching of C–N bonds and Si–O–Si bonds. Peaks at 2926 and 2853 cm^{-1} corresponded to the stretching of $-\text{CH}_3$ and $-\text{CH}_2-$ groups. The other peaks were already present before the reaction. These observations were consistent with the grafting of AEAPTMS, which exhibited aliphatic carbons and primary ($-\text{NH}_2$) and secondary ($-\text{NH}-$) amines. There was no sign of

alcohol groups, which suggested the conversion of the alkoxy silane into a silanol followed by chemical bonding with the hydroxyl groups on the surface of the IONPs was complete. Azidoacetic acid was grafted on the primary amines through an amide bond formation as a next step toward the synthesis of the thermosensitive IONPs. The IR spectrum remained roughly unchanged, but exhibited a strong sharp peak at 2015 cm^{-1} which was typical of an azide functional group. The spectrum showed broad bands ascribed to amide carbonyl groups in the $1650\text{--}1690\text{ cm}^{-1}$ range (amide band I for C=O, amide band II for N-H). Finally, the grafting of PDMAEMA resulted in a more complex spectrum. The disappearance of the azide peak suggested substantial conversion during the reaction. There was also a strong peak at approximately 1750 cm^{-1} , which likely corresponded to the carbonyl stretch of the amides. The peaks at $\sim 2500\text{ cm}^{-1}$ corresponded to amines or amine salts of the polymer.

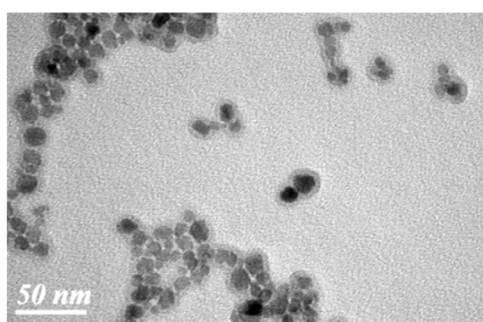


Figure 8 TEM micrograph showing IONPs@AEAPTMS-AZ-PDMAEMA exhibiting core-shell structure.

TEM micrographs evidenced iron oxide cores showing as dark spherical nano-objects, and the corona with a lighter shade of grey as shown in **Figure 8**. The difference of contrast between the core and the shell of the nanoparticles comes from the higher density of electrons of the inorganic iron oxide as compared to the carbon-based shell. The TEM micrograph allowed observing the final hybrid core/shell inorganic/organic morphologies of the nanoparticles. They appeared well-distributed in term of iron oxide core diameters and in term of corona thickness.

Laser light scattering velocimetry was an effective way to estimate the sign and intensity of the charge at the surface of IONPs by the readout of the Zeta potential, deduced from the electrophoretic mobility by the Smoluchowski equation. In the double-layer model of charged colloids, the Zeta potential is defined as the electric potential interface at the stationary layer, *i.e.* the shear plane inside the solvent in the motion of the IONPs relative to solvent under the action of the electromotive force. Charged particles were better dispersed in water because they bore charges of the same sign and thus exhibited repulsive interactions between each other. It is commonly accepted that an absolute value $|\text{Zeta}|=25\text{ mV}$ sets the limit between minimally and highly charged particles. Pristine IONPs bore hydroxyl groups at their surfaces and were uncharged at neutral pH, meaning that the isoelectric point of this amphoteric material was determined at $\text{pH(I)}\sim 7.5$ (equal number of Fe-O^- and Fe-OH^{2+} species). The iron oxide surface bore a positive charge in acidic media and a negative charge in basic media. However, in practice, to obtain $|\text{Zeta}|>25\text{ mV}$ and stable uncoated iron oxide colloids,

the pH had to be lower than 4 or higher than 10, while the ionic strength needed to remain limited, typically less than 20 mM, otherwise the electrostatic repulsions were screened by the electrolyte. Zetametry was a powerful tool to investigate the nature of the chemical functions grafted on the IONPs, first the primary and the secondary amines of the aminosilanes, and then the tertiary amines of the polymer chains.

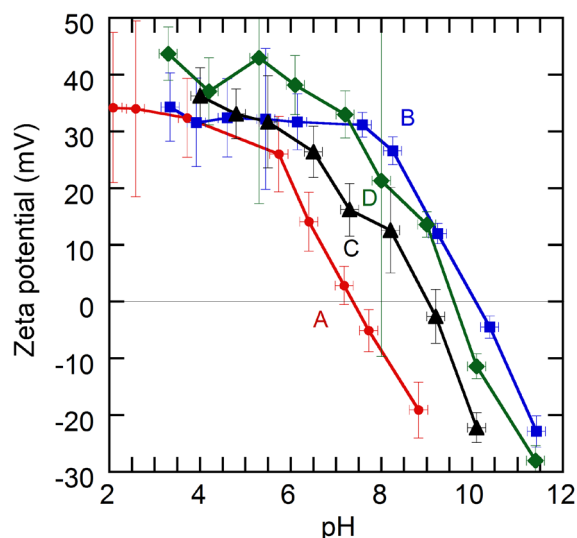


Figure 9 Zeta potential vs. pH for acidic IONPs (A, red circles), aminosilane grafted IONPs@AEAPTMS (B, blue squares), cross-linker grafted IONPs@AEAPTMS-AZ (C, black triangles) and finally thermosensitive IONPs@AEAPTMS-AZ-PDMAEMA (D, green diamonds). PDMAEMA-coated IONPs were charged over the whole acidic pH range up to pH=6.5.

Measurements of the Zeta potential *versus* pH for all of the coated IONPs showed that the isoelectric point was the highest (pH(I)~10) for the IONPs@AEAPTMS, while it decreased by one unit (pH(I)~9) for the final IONPs@AEAPTMS-AZ-PDMAEMA. As predicted, amine moieties lost their positive charge above the pKa, and the remaining negative charges must have arisen from still uncoated hydroxyl groups Fe-O⁻ or possibly from deprotonation of the N-H groups of the secondary amine or amide associated with the AEAPTMS linker. Compared to bare IONPs, grafted IONPs exhibited higher stability over a broader pH range because pure electrostatic repulsions were replaced by electro-steric repulsions, meaning that the organic chains at short distances could not interpenetrate, leading to better dispersed IONPs. The shift of the isoelectric point along the successive grafting steps could be ascribed to variation in the quantity of amines at the surface of the IONPs. The grafting of azidoacetic acid on the primary amines reduced the isoelectric point of the IONPs by approximately 0.5 pH units, because the azide function was neutral at all pH. Finally, the isoelectric point was further reduced by 0.5 pH units following grafting of PDMAEMA chains onto the IONPs using the azido moieties as anchor groups. This observation was consistent with the pKa value of PDMAEMA that had been determined to be 9.5 by acid-base titration (**Figure 5 b**). In addition, for a brush of PDMAEMA chains grafted at high density on IONPs such as in the current system, a curvature effect could further decrease the pKa, as previously reported for star-like PDMAEMA micelles.[15]

3.2. Grafting of a thermosensitive elastin-like polypeptide

The elastin-like polypeptide MW(VPGIG)₂₀C (later referred to as ELP₂₀) was bio-synthesized using an *Escherichia Coli* (*E. Coli*) strain, as previously reported by Bataille *et al.*[16] The recombinant expression of the hydrophobic ELP in *E. Coli* led to pure biodegradable polymers with thermosensitive properties, exhibiting a temperature of transition at around 15 °C in low salt buffer. The ELP₂₀ was therefore an interesting candidate for biomedical applications due to its physico-chemical properties. Coupling the ELP₂₀ with IONPs would theoretically lead to a biocompatible and biodegradable hybrid organic-inorganic core-shell nanoparticle with magnetic and thermosensitive properties.

3.2.1. Materials and methods

LB Broth (Lennox) was from Sigma Aldrich. The yeast extract was from Biokar diagnostics. D+ glucose, PBS 1X and isopropyl b-D-1-thiogalactopyranoside (IPTG) were from Euromedex. The autoclave Varioklav® was from Thermo Scientific. The incubator Innova® 43 was from New Brunswick. The spectrometer SpectraMax M2e was from Molecular Devices. The centrifuge Avanti J-E used to concentrate precultures and cultures was from Beckman Coulter. The centrifuge 5804 R used for other purposes was from Eppendorf. Complete Mini EDTA-free protease inhibitors were from Roche. The ultrasonic processor 75186 was from Vibra-Cell™. The oven was from Bioblock Scientific. *N,N*-diisopropylethylamine (DIPEA) was from Alfa Aesar. *N*- γ -maleimidobutyryloxysuccinimide ester (GMBS) was from TCI Europe. Dimethyl Sulfoxide (DMSO) was from Fisher.

Preculture media were prepared by dissolving 1 g of LB broth supplemented with 0.25 g of yeast extract and 0.05 g of D+ glucose in 50 mL of deionized water. Culture media were prepared by dissolving 20 g of LB broth supplemented with 5 g of yeast extract and 1 g of D+ glucose in 1 L of deionized water. The solutions were sterilised at 110 °C at high pressure for 30 min in an autoclave. Selected bacteria strains (R118 and R151) were used to inoculate the preculture media and ampicillin (50 μ L, 100 mg·mL⁻¹) was added. Bacteria were let to develop in an incubator at 180 rpm, 37 °C overnight. After approximately 14 h, 300 μ L of pre-culture media were diluted with 2700 μ L of water (dilution factor of 10). Optical densities at 600 nm (OD_{600nm}) were measured using a UV-Vis spectrometer. 1 mL of ampicillin (50 μ L, 100 mg·mL) was added to culture media, as well as correct volumes of precultures to reach an OD of 0.1, using the following formula:

$$V_{preculture} = \frac{V_{culture} \times OD_{culture}}{OD_{preculture}}$$

Samples were collected every hour to measure their OD_{600nm}. When their optical densities reached a value of 1.2, ELP production was initiated by addition of IPTG to a final concentration of 0.5 mM. The temperature of the incubator was decreased from 37 °C to 25 °C. 22 h after induction by IPTG, the cultures were harvested by centrifugation at 11000 rpm for 15 min at 4 °C. Supernatants

were discarded and pellets were stored overnight at $-80\text{ }^{\circ}\text{C}$. Pellets were later thawed at $-4\text{ }^{\circ}\text{C}$, 10 mL of PB 1X was added for every gram of bacteria, and solutions were supplemented with one tablet per 10 mL of Complete Mini EDTA-free protease inhibitors. Thereafter the samples were incubated overnight at $-80\text{ }^{\circ}\text{C}$ and slowly defrosted by incubation at $4\text{ }^{\circ}\text{C}$. Total cell lysis was performed by sonication for 30 min, pulses 2 s on 2 s off, 100 % amplitude and kept in cold condition using an ice bath. Polyethyleneimine (PEI) was then added to the solution at a final concentration of 0.44% (v/v) to precipitate bacterial DNA. Finally the released ELPs were purified by three successive steps of inverse transition cycling (ITC). Solutions were separated into 50 mL Eppendorf centrifugation vials, and insoluble debris were removed by centrifugation at $4\text{ }^{\circ}\text{C}$ at 8500 rpm for 30 minutes (“cold spin”). Pellets were discarded and few mLs of a 5 M ($290\text{ g}\cdot\text{L}^{-1}$) NaCl solution was added to the supernatants to precipitate the ELPs. Centrifugation was then carried at 25°C at 8500 rpm for 30 minutes (“hot spin”). The pellets were re-dispersed in PBS 1X buffer in an ice bath. These two centrifugation steps were reproduced two more times to purify the ELPs. The ELPs dispersed in PBS buffer were finally dialyzed three times for 12 h against 5 L of dionized water as a final step, before to be freeze-dried to evaluate the yields. 60 mg were obtained from the R118 strain; 170 mg were obtained from the R151 strain.

IONPs were synthesized by the co-precipitation pathway followed by a size-sorting process, as described in Chapter II. The S1S2 fraction was used for the bioconjugation with $(\text{VPGIG})_{20}$. 530 μL of AEAPTMS (2.4 mmol, representing an excess of 20 added molecules per nm^2 for S1S2) was grafted onto IONPs (420 mg, 5.25 mmol of Fe), in a mixture of solvents (10% water 90% ethanol) in acidic conditions (arising from the low pH of the ferrofluid) at first to hydrolyse the alkoxy silane into a hydroxysilane, followed by condensation with the Fe-OH moieties of iron oxide in neutral conditions for an hour, and boiling at reflux for another hour, a protocol adapted from Duguet and Mornet’s patent.[12] The sample was then washed multiple times with methanol by a precipitation-redispersion process before being redispersed in water with a pH corrected to a value of 3 with dilute HNO_3 .

Samples with different $(\text{VPGIG})_{20}$ grafting densities were prepared. For a grafting density of 0.1 chain of $(\text{VPGIG})_{20}$ per nm^2 , 2.12 mg of S1S2 were mixed in glycerol and dried overnight at $60\text{ }^{\circ}\text{C}$ at low pressure in an oven. They were then diluted in DMSO, 4.72 mg (36 μmol) of DIPEA, and 0.14 mg (0.41 μmol) of GMBS were added. The dispersion was sonicated for 30 min, pulses 1 s on 2 s off, 40 % amplitude and let to react for 2 h. Reactants were introduced as stock solutions in DMSO. 3.62 mg (0.41 μmol) of $(\text{VPGIG})_{20}$ was added and let to react overnight (12 h). The dispersion was sonicated for 30 min, pulses 1 s on 2 s off, 40 % amplitude. The sample was purified by centrifugation-redispersion, and redispersed in water.

3.2.2. Results and discussion

The ELP_{20} was produced by adapting a protocol that was already described elsewhere.[16] Harvested cells were lysed by sonication; PEI was added to the solution to separate cell debris as well

as insoluble proteins. The ELP₂₀ was recovered from the cell lysate by inverse transition cycling (ITC); a method based on the natural thermosensitive property of the ELP, avoiding time-consuming and expensive chromatography purification techniques. The bioproduction of ELP₂₀ led to few tens of mg of material, which purity could be assessed by sodium dodecyl sulfate polyacrylamide gel electrophoresis (SDS-PAGE).

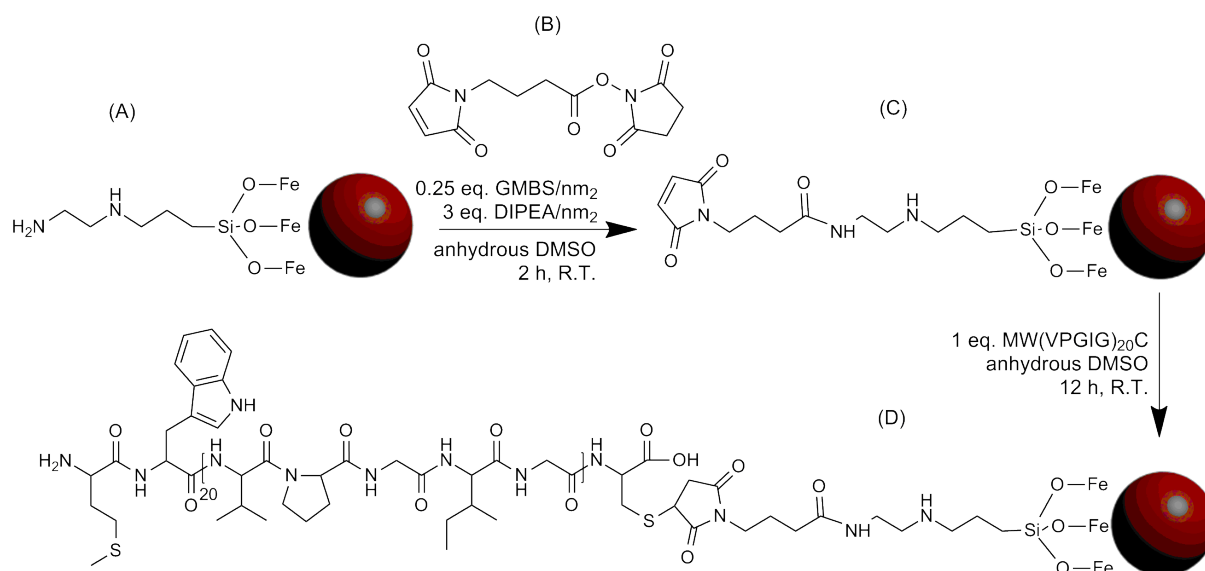


Figure 10 Synthetic scheme of the surface modification of IONPs with the ELP₂₀.

IONPs obtained by co-precipitation from the fraction S1S2, presenting spherical morphologies were used for the bioconjugation with ELP₂₀. The IONPs were grafted with the ELP₂₀ following a divergent strategy, by covalent assembly of a ligand and a heterofunctional linker before final attachment of the shell, as illustrated in **Figure 6**. The IONPs were first modified with AEAPTMS as described in the previous section, which acted as a ligand binding at one end onto the surface of the inorganic core of iron oxide, and presenting at the other end an amine moiety (**Figure 6 (A)**). A simplistic surface modification approach would have been to directly activate the C end of the ELP₂₀ using EDC and NHS. This would have led to the activation the carboxylic acid moiety with an NHS-ester, followed by a direct grafting onto the amines presented at the surface of the IONPs. Unfortunately, this would have led to a parasitic reaction of oligomerization, as the ELP₂₀ also presented a primary amine chemical moiety. It was therefore chosen to use a commercial heterofunctional linker GMBS (**Figure 6 (B)**) and carry the grafting reaction in two steps. The first step was the amide bond formation between the AEAPTMS-modified IONPs and the NHS-activated GMBS (**Figure 6 (C)**). The reaction was performed using DIPEA as a base to deprotonate the amine, and in anhydrous DMSO to prevent the hydrolysis of the NHS ester. The second step was the Michael-type addition of the thiol from the C terminated Cysteine residue of the ELP₂₀ on the maleimide functional group of GMBS. DMSO was a suitable solvent for this reaction, as it could solubilize ELP₂₀

at room temperature, and therefore made the thiol more accessible for the chemical modification. A hybrid core-shell organic-inorganic nanoparticle (**Figure 6 (D)**) was produced this way.

Table 1 Characteristics of the samples IONPs@ELP₂₀.

Sample n°	1	2	3	4	5	6	7
Expected grafting density (chain per nm ²)	0.01	0.025	0.04	0.055	0.07	0.085	0.1
Number of ELP ₂₀ per IONP	3.1	7.9	12.6	17.3	22.0	26.7	31.4
Reduced tethered density Σ	0.6	1.4	2.2	3.0	3.9	4.7	5.5

Several parameters of interest to describe the core-shell IONPs@ELP₂₀ nanoparticles are presented in **Table 1**. Different grafting densities were tried by varying the equivalents of reagents, to reach densities in a range of 0.01-0.1 chain per nm². This range of value corresponded to a number of ELP₂₀ tethered at the surface of the IONPs in a range of 3-31. These parameters were intuitively evaluated when preparing the reaction. A dimensionless number that was later discovered as useful to try and describe the state of the tethered chains at the surface of the IONPs was the reduced tethered density Σ . It allowed estimating the crowding of the surface of the IONPs with the ELP₂₀ chains. With ranges of values from 0.6 to 5.5, the chains were expected to be in the so-called mushroom-to-brush regime.

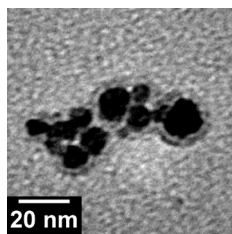


Figure 11 TEM micrograph of the core-shell structure of IONP@ELP₂₀.

IONPs functionalized with the ELP₂₀ were imaged by TEM. The micrograph evidenced core-shell structures as shown in **Figure 11**. Similarly to what was previously observed in the case of IONP@PDMAEMA, iron oxide cores showed a strong contrast due to their higher density in electrons coming from the dense nanocrystalline packing of iron ($Z_{Fe}=26$). The corona had a lighter shade of grey as it was mainly composed of carbon ($Z_C=6$) with moderately dense biopolymer brushes. The IONPs appeared regular in morphologies, with spherical morphologies and comparable diameters. As the sample was prepared by drying the material on the TEM grids, the corona imaged on the micrograph was dehydrated, which explained the observed thickness of few nanometers.

Thermogravimetric analysis (TGA) of the ELP₂₀ evidenced that the polypeptide degraded at 330 °C, which was similar to the temperature of degradation observed for IONPs functionalized with ELP₂₀ (**Figure 12 a-b**). This led to the estimation of a relative proportion of organic material of 15 %

w/w when reasoning in weight percentage. The relative volumic proportion of organic material could be estimated at 39 % v/v when taking into consideration the densities of the two materials (4.9 g/cm³ for maghemite γ -Fe₂O₃ and 1.35 g/cm³ for the ELP₂₀ as reported for proteins in the crystalline state)[17].

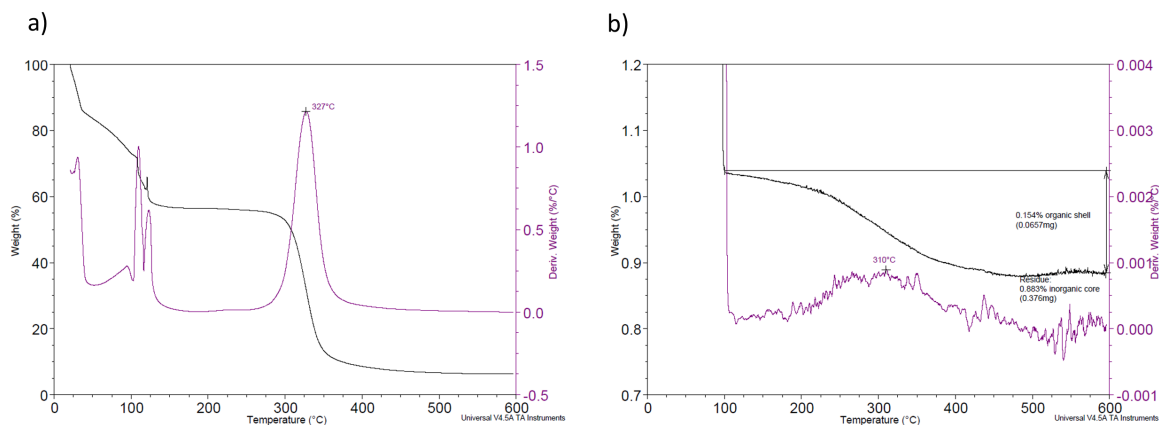


Figure 12 Thermogravimetric analyses of a) the ELP₂₀ and b) IONPs functionalized with the ELP₂₀.

These analyses allowed the determination of the number of ELP chains per nanoparticle, according to the following hypotheses: i) the IONPs were spherical, allowing the geometrical calculation of the total surface available for the grafting and therefore the determination of the grafting density calculated from the total surface and the total number of chains. ii) The IONPs had a homogeneous (neglectable roughness) surface and similar size, leading to the equal distribution of ELP chains among the IONPs, as they each present an equal surface. It was estimated on this example that the IONPs carried an average of 32 chains of (VPGIG)₂₀. Samples with different grafting densities were produced, and the influence of this parameter on the magnetic and thermosensitive properties of the IONPs is discussed in the next Chapter.

4. Convergent synthesis or “grafting to”

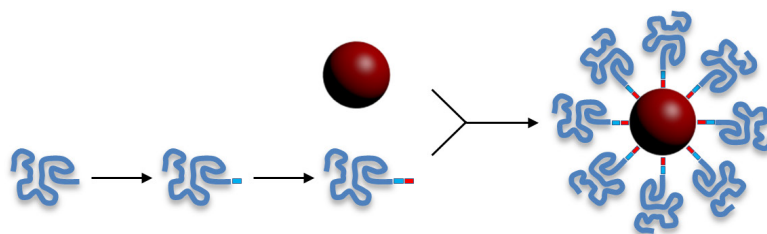


Figure 13 General principle of a convergent surface modification of IONPs.

The convergent surface modification of IONPs aimed to improve the efficiency of the multistep synthesis and the characterization of the final materials (**Figure 4**). Individual pieces of macromolecules to be grafted onto the cores were combined separately before grafting them at the surface of the IONPs in a single final step (**Figure 13**). Practically, this way to proceed enabled using common chemical characterization technics such as TLC or ¹H NMR (for the characterization of the

synthetic intermediates), which was not possible when starting the modification from the magnetic IONPs. This convergent strategy had the advantage of taking place in conditions suitable for the stability of the IONPs, enabling the modification of the whole surface available. The IONPs and molecules were simply stirred for a determined duration, before neutralizing the pH and purifying the IONPs by centrifugation-redispersion. The ratio of polymer to IONP was calculated to form a dense layer of tethered polymer chains, with a sufficient grafting density so that the molecular chains were extended. In this brush regime the IONPs were stabilized by steric repulsions between IONPs. In this strategy a phosphonic acid moiety was selected as it could not form oligomers in solution contrary to siloxanes.

4.1. Grafting of poly(ethylene glycol) and a fluorescent dye onto iron oxide nanoparticles

4.1.1. Materials and methods

1 equiv. (300 mg, 50 μmol) of poly(ethylene glycol) methyl ether thiol (mPEG-SH, average molar mass $M_n=6,000 \text{ g}\cdot\text{mol}^{-1}$, Sigma Aldrich) was reacted with 1 equiv. (14 mg, 50 μmol) of tris(2-carboxyethyl)phosphine hydrochloride (TCEP) (98%, ACROS Organics) in 50 mM phosphate buffer (PB) pH 7.4 for 24 h to reduce the disulphide bonds and (mPEG-S)₂ dimer content, thus leading to reactive free thiol groups. In parallel, 20 equiv. (125 mg, 1 mmol) of AEP was reacted with 5 equiv. (70 mg, 250 μmol) of *N*-succinimidyl 4-maleimidobutyrate (GMBS, TCI Europe) in PB for 24 h in an ice bath. Both solutions were then mixed and let to react for 24 h, and finally purified by dialysis against milliQ water for 72 h, using a 5 kDa membrane, and replacing 6 times with milliQ water. (The phosphonate-activated PEG was then referred to as PEG*) The final product was lyophilized and stored at -24 °C. The NHS-ester modified DY700 fluorescent probe (Dyomics, Germany) was reacted with 1.5 equiv. of 2-aminoethylphosphonic acid (AEP) (Sigma Aldrich) in DMSO for 24 h at room temperature and under orbital agitation, before long-term storage at -20 °C. The phosphonate activated DY700 (referred to as DY700*) was then grafted onto IONPs in water acidified to pH=2.5 with dilute nitric acid. After 1h, 30 % (16 %) w/w of PEG* was added to the dispersion of monocoresh or multicore IONPs. These proportions led to theoretical grafting densities of $\sigma = 1/D^2 = 0.64$ molecular chains per nm² or reduced tethered densities $\Sigma = \pi R_G^2/D^2 = 15$ according to our calculations, using scaling laws reported by Devanand ($R_G(\text{nm}) = 0.0215 \cdot M_n^{0.583}$)[18] or by Le Coeur *et al.* ($R_G(\text{nm}) = 0.066466 \cdot M_n^{0.45224}$)[19], which are different but both lead to the same value $R_G = 3.4 \text{ nm}$ for PEG of $M_n=6,000 \text{ g}\cdot\text{mol}^{-1}$. After 2 h of reaction, the pH was neutralised with Tris 50 mM and the solutions were purified from the excess of PEG* and DY700* by 3 cycles of centrifugation-redispersion (18,000 g, 1 h at 25 °C, 30 min at 1°C to increase viscosity and avoid pellet dispersion before removing the supernatant).

4.1.2. Results and discussion

The surface of IONPs was chemically modified by grafting poly(ethylene glycol) (PEG) in order to bring steric stability in physiological media. PEG was previously chemically modified in order to introduce a phosphonic acid anchor group, which was later used to tether the chain at the surface of the IONPs.

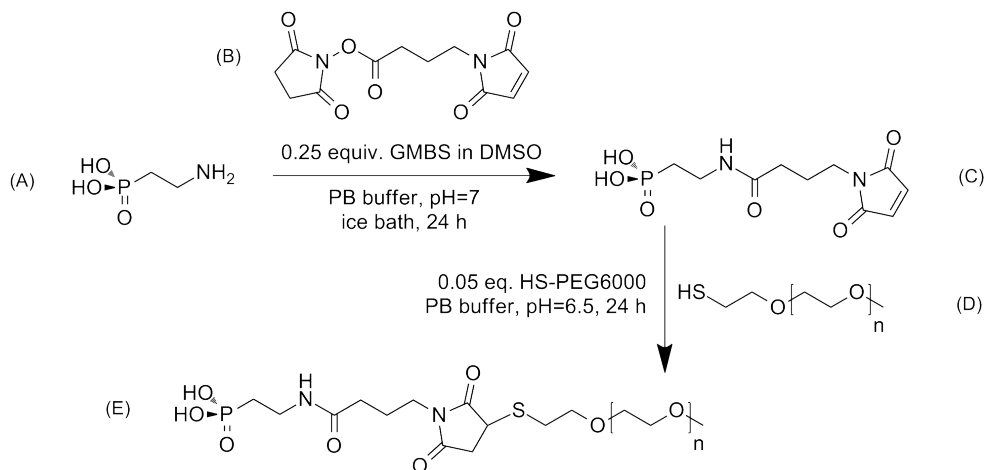


Figure 14 Chemical modification of PEG in order to introduce a phosphonic anchor group.

A thiol-terminated PEG was chemically modified to introduce a phosphonic anchor group at the chain end (**Figure 14**). 2-aminoethylphosphonic acid (AEP) (**Figure 14 (A)**) was reacted with GMBS (**Figure 14 (B)**) to produce a heterofunctional linker (**Figure 14 (C)**). Both solution temperature and pH were controlled in order to prevent a too fast hydrolysis of the NHS-activated ester. For this reason, the temperature of the solution was cooled using an ice bath and the pH was kept neutral using a phosphate buffer. Poly(ethylene glycol) methyl ether thiol (mPEG-SH, average molar mass $M_n=6,000 \text{ g}\cdot\text{mol}^{-1}$) (**Figure 14 (D)**) was reacted with the heterofunctional linker through a Michael-type addition. For the sake of simplicity, PEG chemically modified with a phosphonic anchor group was later referred to as PEG*.

^1H NMR was used to confirm the chemical modification of PEG* (**Figure 15**). Several pieces of information could be obtained from the integration of the peaks. The peak from PEG* served as a reference for the integration of other peaks, with its value fixed at 545 protons according to the average molar mass $M_n=6,000 \text{ g}\cdot\text{mol}^{-1}$ stated by the supplier, leading to an average degree of polymerization of $D_p=135$. The reaction was quantitative for the first reaction step leading to the formation of an amide bond between GMBS and AEP. The chemical yield was most probably improved by the excess of AEP, as well as by the pH and temperature of reaction leading to stable NHS-ester activated GMBS. The thiol-maleimide Michael addition of PEG and AEP-GMBS had a chemical yield of 80%, possibly due to the parasitic formation of disulfides.

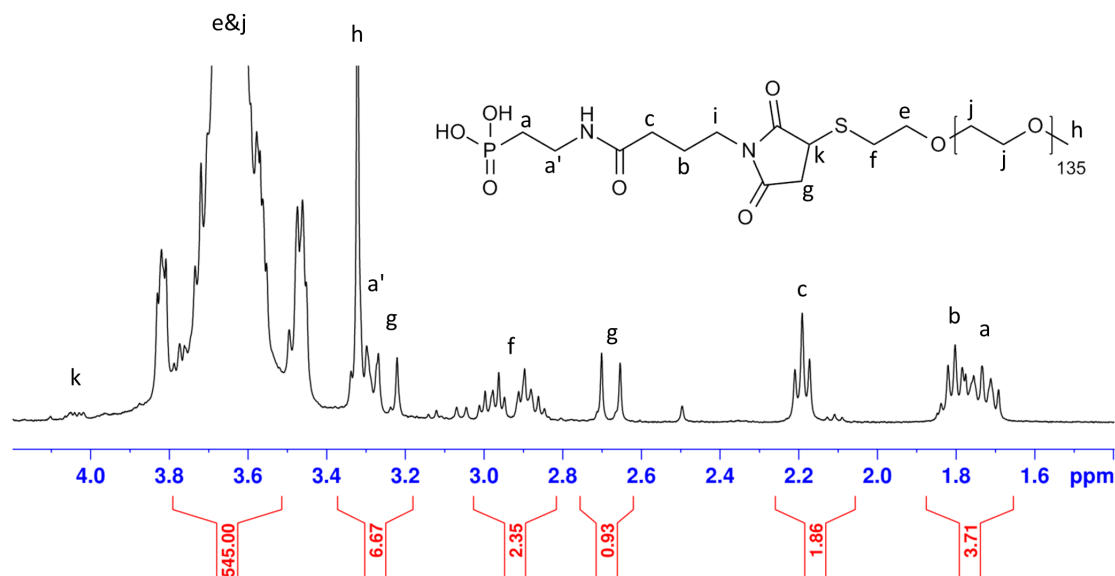


Figure 15 ^1H NMR spectrum of the chemically modified PEG* in water.

PEG* was then grafted onto IONPs in a single step. The reaction was carried out in acidic water, with IONPs being well-dispersed and the polymer solubilized. This allowed a better control over the grafting density, as the whole surface of iron oxide was available for modification as there was no aggregation effect. The IONPs grafted with PEG* were then purified by centrifugation-redispersion. The number of PEG* chains per IONP was varied and controlled to form a brush. The conformation of the PEG* chains grafted at the surface of the IONPs was studied. A convenient dimensionless parameter to represent the state of the grafted chains is the reduced tethered density Σ . It was introduced by Brittain *et al.* to describe the brush regime with a single adimensional parameter.[20] Σ represents “the number of chains that occupy an area that a free non-overlapping polymer chain would normally fill under the same experimental conditions”.

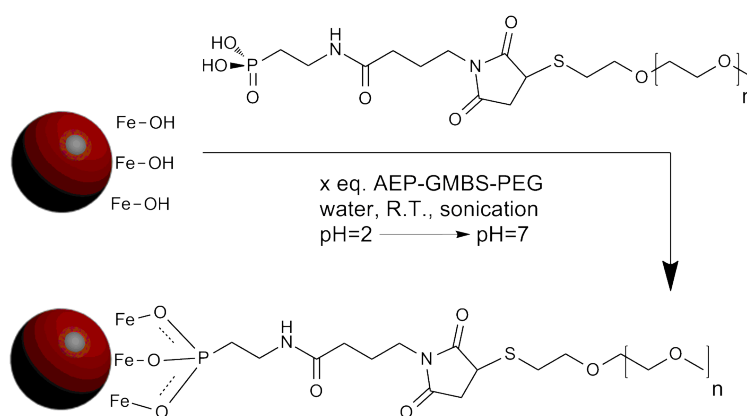


Figure 16 Grafting of IONPs with PEG*.

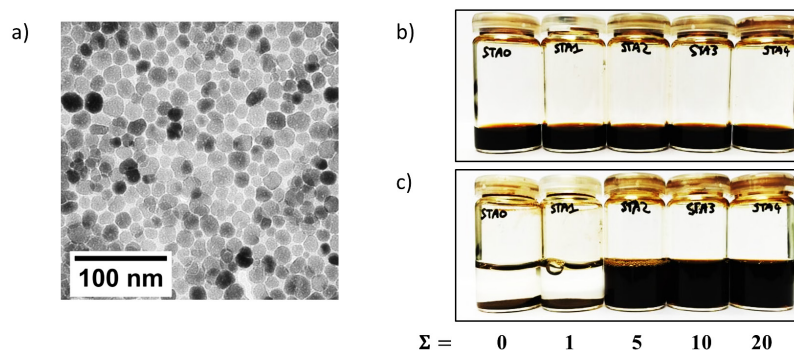


Figure 17 a) TEM micrograph of mono-core IONPs (batch 34ff). Stability test of 5 samples conjugated with PEG* at various reduced tethered densities Σ **b)** during grafting and **c)** after addition of Tris leading to a neutralization of the acidic solution.

Monocore IONPs from the polyol batch 34ff (**Figure 17 a)** were mixed with the correct quantities of PEG* in conditions previously described. All dispersions were deep black during the surface modification as IONPs were stabilized in acidic solution by both electrostatic and steric repulsions (**Figure 17 b)**. IONPs with $\Sigma > 5$ were stable in solution after neutralization of the pH with tris(hydroxymethyl)aminomethane (Tris) buffer (**Figure 17 c)**. The polymer chains grafted at their surface interacted and repelled the IONPs, while for $\Sigma < 5$ the magnetic dipolar moments of the IONPs made them attract to each other, aggregate and sediment.

Table 2 Characteristics of the samples IONPs@PEG* (monocore, batch 34ff).

Sample n°	STA0	STA1	STA2	STA3	STA4
Expected grafting density (chain per nm ²)	0	0.03	0.14	0.28	0.55
Number of PEG* per IONP	0	25	125	250	501
Reduced tethered density Σ	0	1	5	10	20

Several parameters of interest to describe the core-shell IONPs@PEG* nanoparticles are presented in **Table 2**. Different grafting densities were tried by varying the equivalents of reagents, to reach densities in a range from 0 to 0.55 chains per nm². This range of value corresponded to a number of PEG* tethered at the surface of the IONPs in a range from 0 to 501. The reduced tethered density Σ allowed estimating the crowding of grafted chains at the surface of the IONPs. With theoretical ranges of Σ from 0 to 20, the chains were expected to be in the mushroom, mushroom-to-brush, and brush regimes. Reduced tethered densities of up to 10 were estimated by TGA, the theoretical value of 20 was probably overestimated, and was meant to represent a saturation of the surface of the IONPs with PEG* chains.

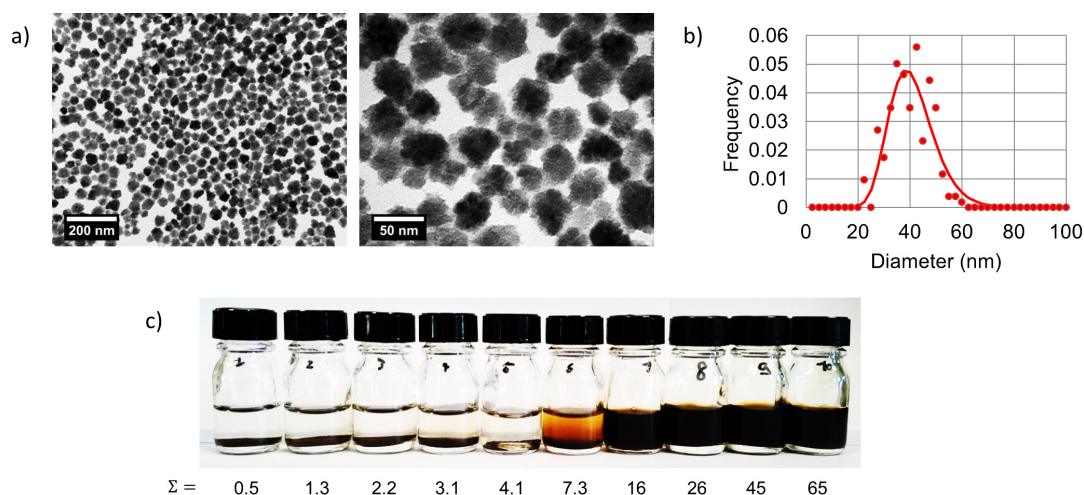


Figure 18 a) TEM micrographs of multi-core IONPs (batch 30FF) and b) their size-distribution as measured by TEM. c) Stability test of 10 samples conjugated with PEG* at various reduced tethered densities Σ .

A similar behavior was observed for multi-core IONPs from the polyol batch 30FF. Stable dispersions could be obtained at $\Sigma > 16$. The higher values of reduced tethered densities needed to stabilize the IONPs could be explained by their surface roughness. This led to an underestimate of their specific surfaces that could not be reasonably assessed by geometrical calculations. The Σ values were calculated in the hypothesis of spheres of radius of 40 nm, while the IONPs exhibited raspberry-like morphologies, leading to an underestimate of the total surface available for modification. Also the conformations of the grafted polymer chains were probably different compared to onto flat surfaces. The chains could not only interact sideways but also at narrower angles because of the rugosity of the surface.

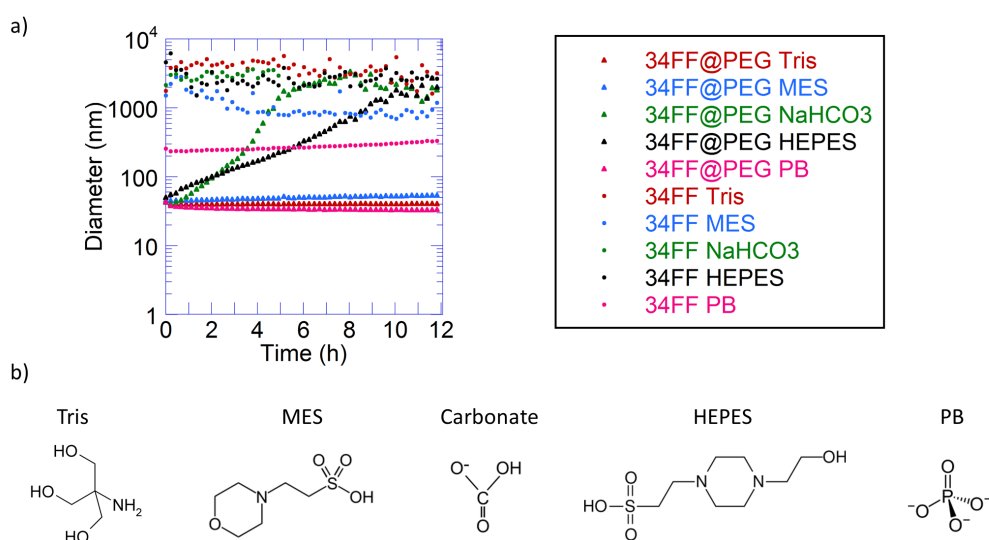


Figure 19 a) Stability study by DLS of IONPs (monocores, batch 34FF) grafted with PEG*. b) Structures of the molecules used to buffer the solutions.

The stability of mono-core IONPs from the polyol batch 34FF in different buffers was studied by DLS and compared with IONPs grafted with PEG* (**Figure 19 a**). The buffer selected were Tris,

MES (2-(*N*-morpholino)ethanesulfonic acid), carbonate, 4-(2-hydroxyethyl)-1-piperazineethanesulfonic acid (HEPES), and PB (**Figure 19 b**). All these molecules had a logarithmic acid dissociation constant pK_a that allowed obtaining buffers corrected at $pH=7$ with dilute nitric acid and/or sodium hydroxide, with a ionic strength of 50 mM. Among the 10 conditions studied, 3 samples were stable, and all of them were IONPs grafted with PEG*. This demonstrated the superior stability of IONPs stabilized by PEG* at physiological pH and saline conditions. Suitable buffers were Tris, phosphate, and MES. The explanation to this phenomenon was not unraveled.

A DY700 fluorescent dye was used to track the IONPs *in vitro* and *in vivo*. This dye is reportedly stable in biological conditions and has low cytotoxicity, which made it suitable for magnetic hyperthermia studies in biological conditions.[21] The DY700 was chemically modified to introduce a phosphonic moiety (referred to as DY700*) that served as an anchor group for the conjugation with the IONPs.

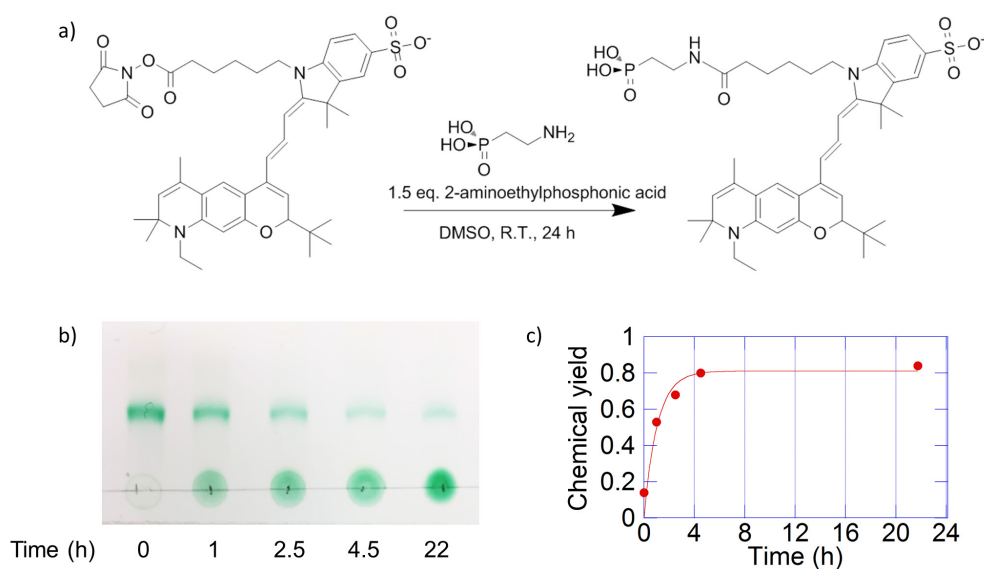


Figure 20 a) Chemical modification of the fluorescent dye DY700. **b)** Thin layer chromatography (TLC) of the product of reaction vs time. **c)** Chemical yield of the reaction vs time.

The NHS-activated DY700 fluorescent dye was reacted with AEP in DMSO (**Figure 20 a**). The reaction was monitored by depositing 1 μ l of the solution on a silica TLC plate at determined durations (**Figure 20 b**). Two spots were eluted: top spots corresponded to DY700, bottom spots corresponded to DY700* which phosphonic acid anchor group bound at the surface of silicon oxide. This binding effect on a metal oxide was later advantageously used to tag the surface of IONPs with the fluorophore. The intensities of the spots were quantified allowing the determination of the chemical yield as a function of time (**Figure 20 c**). For this experiment it was hypothesized that the intensity was proportional to the quantity of molecule. The intensities were quantified using the gel function in ImageJ, a method widely used by biologists for sodium dodecyl sulfate polyacrylamide gel electrophoresis (SDS-PAGE) analyses.

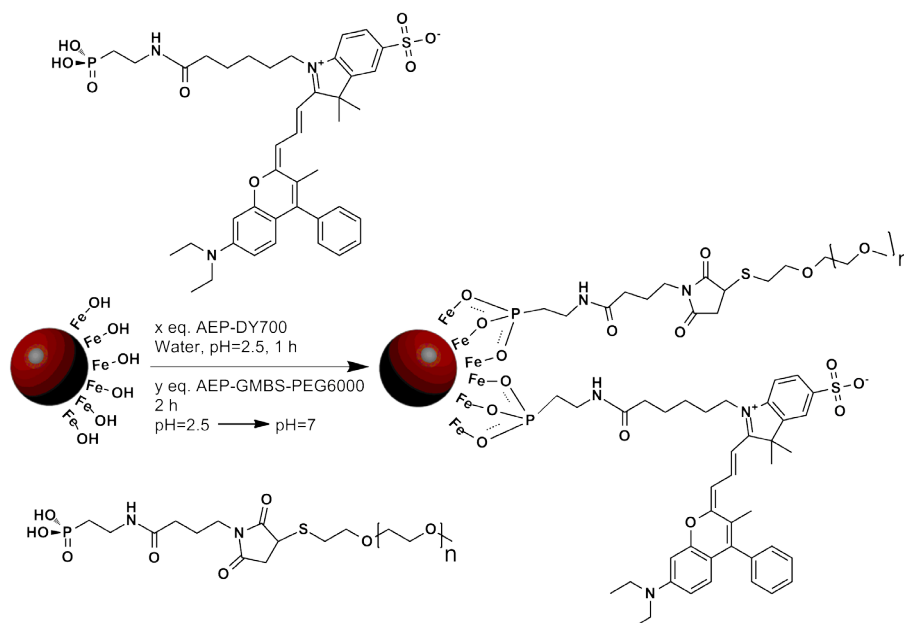


Figure 21 Grafting of the chemically modified fluorescent probe DY700* and PEG* onto the surface of an iron oxide nanoparticle in a simple one-step modification.

The NIR fluorescent probe DY700* was coupled directly onto the surface of IONPs resulting in a very likely shielding of the dye by the PEG* layer (**Figure 21**). The proximity of the fluorescent DY700* with the surface of the semi-conducting iron oxide was expected to lead to partial quenching of the fluorescence signal. This phenomenon may occur through two separate mechanisms: i) by IONP/fluorophore interaction[22] and/or ii) by fluorophore/fluorophore self-quenching due to a high local concentration of dye. The amount of dye to graft was therefore limited to 1 % w/w, to guaranty a sufficient fluorescence signal for detection as well as to avoid covering the IONPs surface with a hydrophobic molecule. Using a spacer to increase the distance between the IONPs surface and the dye as well as the distance between fluorophores was another option. However, we considered that the DY700* conjugation close to the IONPs surface would prevent undesirable hydrophobic interactions with the environment (biological fluids, cells, etc.). The DY700* characteristic wavelengths were respectively $\lambda_{exc}=650$ nm for excitation and $\lambda_{em}=700$ nm for emission. These values were in the NIR region of the electromagnetic spectrum, a range of minimum absorption of biological fluids and tissues, also far from the shorter wavelength radiations that were strongly absorbed by IONPs.

IONPs were cleaned from the excess of fluorophore and polymer by centrifugation-redispersion (). The volume of water could easily be reduced from 1500 μ L down to 50 μ L at each cycle without discarding significant quantities of IONPs. The purity of the final solution reached up to 99.99% after 3 cycles. This could be achieved in a non-time consuming manner; it was faster than dialysis, ultra-filtration, and centrifuge filtration. It was cost-effective, and it guaranteed a purity that could be quantitatively estimated. The purification process by centrifugation-redispersion is on-purpose presented in results and discussion. Though it was not a scientific advancement, it greatly helped cut efforts and time and allowed the project to be significantly pushed forward. The grafting

could be visually assessed as DY700* (**Figure 22 a**) and IONPs (**Figure 22 b**) were both colored. The supernatant of the first centrifugation was colorless (**Figure 22Error! Reference source not found. c**), evidencing that all IONPs were collected in the pellet, and that DY700* was bound to their surface. This binding behavior with iron oxide was similar to what was observed with silicon oxide TLC plates (**Figure 20 b**).

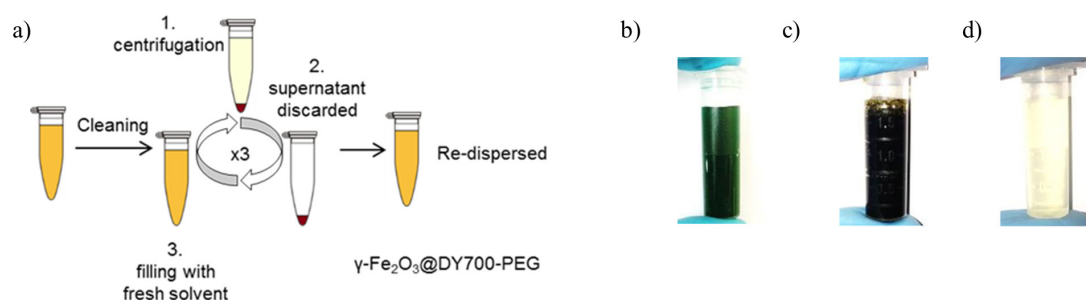


Figure 22 a) Scheme of the purification of IONPs from the excess of DY700* fluorophore and PEG* stabilizer. Color of the solution of DY700* **b)** before and **c)** after addition of IONPs and PEG*. **d)** Color of the supernatant of the first centrifugation-redispersion cycle.

4.2. Grafting of a thermosensitive diblock elastin-like polypeptide

4.2.1. Materials and methods

Preculture media were prepared by dissolving 55 g of terrific broth (TB) in 100 mL of deionized water and separated in two 250 mL erlenmeyers. Culture media were prepared by dissolving 220 g of TB broth in 4 L of deionized water and separated in four 5 L erlenmeyers. The solutions were sterilised at 110 °C at high pressure for 30 min in an autoclave. A single colony of bacteria cultivated in petri dishes was selected and used to inoculate preculture media, and a Kanamycin stock solution was added (20 µL, 45 mg·mL⁻¹). Bacteria were let to develop in an incubator at 180 rpm, 37 °C overnight. After approximately 14 h, precultures were harvested by centrifugation at 3200 rpm for 10 min at 4 °C. The supernatant was discarded; the pellet was stored at 4 °C for the rest of the day. The concentrated bacteria were redispersed in 4 mL of preculture media. 100 µL of the solution was diluted with 400 µL of preculture and 500 µL of glycerol 50 % in 2 mL Eppendorf tubes to store the selected bacteria colony at -80 °C for further productions. Approximately 1 mL of the concentrated preculture condition was added to each of the 1 L culture media along with 1 mL of Kanamycin solution, and let to develop in an incubator at 180 rpm, 37 °C overnight. Culture media were then transferred in 500 mL flasks, and centrifuged for 15 min at 30000 rpm, 4 °C. Supernatants were discarded and pellets were stored at - 80 °C, and then thawed. They were redispersed in PBS 1X (approximately 10 mL·g⁻¹ of pellet). Total cell lysis was performed by sonication for two times 3 min, pulses 10 s on 20 s off, 100 % amplitude and kept in cold condition using an ice bath (temperature not exceeding 10 °C). Then, polyethyleneimine (PEI) was added to the solution at a final concentration of 0.44% (v/v) to precipitate bacterial DNA. Finally the released ELPs

were purified by three successive steps of inverse transition cycling (ITC). Solutions were split into 50 mL Eppendorf centrifugation vials, and insoluble debris were removed by centrifugation at 4 °C at 8500 rpm for 30 minutes (“cold spin”). Pellets were discarded and few mLs of a 5 M (290 g·L⁻¹) NaCl solution was added to the supernatants to precipitate the ELPs. Centrifugation was then carried at 25°C at 8500 rpm for 30 minutes (“hot spin”). The pellets were re-dispersed in PBS 1X buffer in an ice bath. These two centrifugation steps were reproduced two more rounds to purify the ELPs. The ELPs dispersed in PBS buffer were finally dialyzed three times for 12 h against 5 L of dionized water as a final step, before to be freeze dried to evaluate the yields. Productions yielded 68 mg·L⁻¹ of ELP on average.

1 equiv. (147 mg, 3.6 μmol) of ELP_{40-60-Tat} ((VPGVG)₄₀-(VPG(A/G)G)₆₀) was reacted with 1 equiv. (1 mg, 3.6 μmol) of TCEP in 50 mM PB pH 7 for 24 h to reduce the disulphide bonds and dimer content, thus leading to reactive free thiol groups. In parallel, 20 equiv. (8.9 mg, 71 μmol) of AEP was reacted with 5 equiv. (5 mg, 18 μmol) of GMBS in 50 mM PB for 24 h in an ice bath. Both solutions were then mixed and let to react for 24 h, and finally purified by 3 ITC cycles and dialyzed three times for 12 h against 5 L of dionized water as a final step, before to be freeze dried.

Here is a description to produce IONPs grafted with the diblock ELP_{40-60-Tat}, that was used for biological experiments. 22ff IONPs (monocore, r=6.1 nm) were thoroughly washed with a solution of water and ethanol 20:80, 2 times in basic condition and 2 times in acidic conditions by precipitation-redispersion. Sonication was used at every step, with pulses 4 s on 1 s off, 30 % amplitude, 5 min. 70 mg of IONPs dispersed in aqueous solution at pH=2.5 were mixed with 450 μg of DY700* (stock solution at 1 g·L⁻¹, 450 μL, 200 molecules per IONP), and let to react for 1 h. 28 mg of diblock ELP_{40-60-Tat} was then added (stock solution at 10 g·L⁻¹, 2.8 mL, 28 chains per IONP, reduced tethered density of 15, grafting density of 0.06 chain per nm²). After 2 h, 4 mL of Tris was added, dilute ammonia was used to correct the pH to a neutral value (pH=6.5). The dispersions were stable and centrifuged in 2 mL Eppendorf tubes 1 h at 25 °C, 18000 g followed by 30 min at -1 °C, 18000 g to increase the viscosity of the solution and prevent the redispersion of the IONPs during deceleration. The supernatants were discarded and renewed with an arbitrary volume of fresh Tris solution. The process was repeated two times. The nanoparticles were finally sonicated pulses 1 s on 4 s off, 30 % amplitude, 5 min, yielding stable dispersions in 50 mM Tris solution.

4.2.2. Results and discussion

A thermoresponsive diblock ELP_{40-60-Tat} was grafted using the convergent strategy. The ELP_{40-60-Tat} was bio-synthesized using an *E. Coli*. strain, supplied by the research group of Pr. Ashutosh Chilkoti (Department of Biomedical Engineering, Duke University, North Carolina, US). The diblock ELP_{40-60-Tat} was designed to contain a thermosensitive block fused to a hydrophilic block. In a precedent work, these diblock ELPs were shown to form well defined nanometer-sized micelles above

their critical micellar temperature (CMT), whose core dehydrated and densified upon further temperature increase.[23]

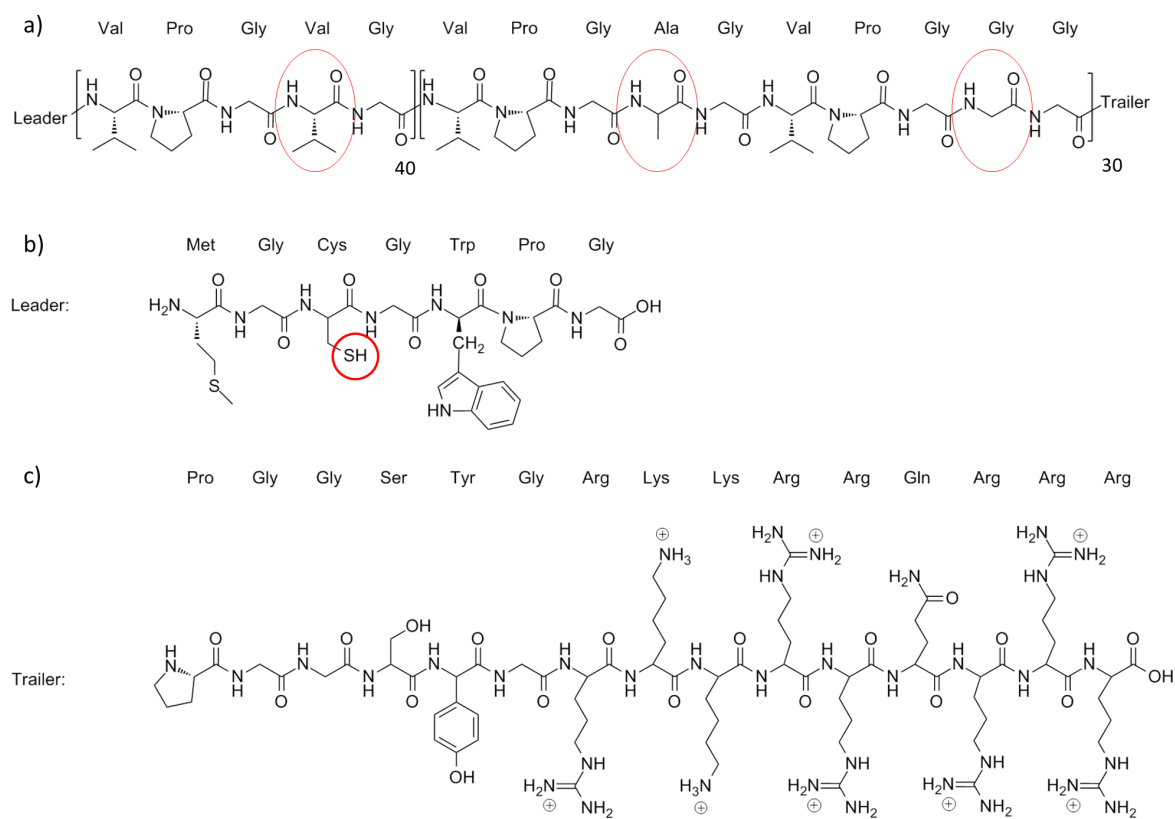


Figure 23 Primary sequence of the diblock ELP_{40-60-Tat} used. **a)** Sequence of the two fused ELP blocks. **b)** Sequence of the leader containing a thiol used for the bioconjugation strategy. **c)** Sequence of the trailer; an arginin-rich Tat cell-penetrating peptide.

The diblock ELP_{40-60-Tat} used in the current study was designed with a thermosensitive (VPGVG)₄₀ block undergoing a reversible phase transition in solution, followed by an hydrophilic (VPGXG)₆₀ (X=A,G 1:1) block. In this study the critical micellar temperature was of 42 °C, which was conveniently a few degrees above the human body temperature. This property could be exploited for drug delivery applications triggered by magnetic hyperthermia and complete biomedical applications envisioned for polypeptides.[24] The *N*-terminal end of this diblock ELP_{40-60-Tat} featured a seven aminoacid leader sequence containing a Cys residue, which was used for the convergent bioconjugation strategy with IONPs. The C-terminal end (trailer) contained a Tat peptide sequence, well-known for its cell penetrating properties thanks to its high density of positive charges at physiological pH.[25, 26] In this work, the diblock ELP_{40-60-Tat} was modified at the Cys resided leader peptide to introduce a phosphonic acid head group, and directly grafted onto the surface of IONPs.

In order to obtain IONPs with both magnetic and thermosensitive properties, a magnetic iron oxide core was first designed before further functionalization with the thermosensitive ELP_{40-60-Tat} (**Figure 24**). IONPs were synthesized by a polyol reaction as previously presented. Different morphologies were obtained, such as irreversible aggregates of nanoparticles so-called “nanoflowers”

with strong heating properties evidenced by SARs of several hundreds of W/g (up to 500). But for the sake of simplicity in the estimates of the grafting density, nanoparticles from polyol batches 23ff and 22ff were selected in the produced library showing good heating properties, but only with spheroidal shapes and satisfying size distribution (standard deviation inferior to 0.2). This ensured estimating correctly the surface of $\gamma\text{-Fe}_2\text{O}_3$ IONPs available for the grafting of macromolecules with basic geometrical formulas.

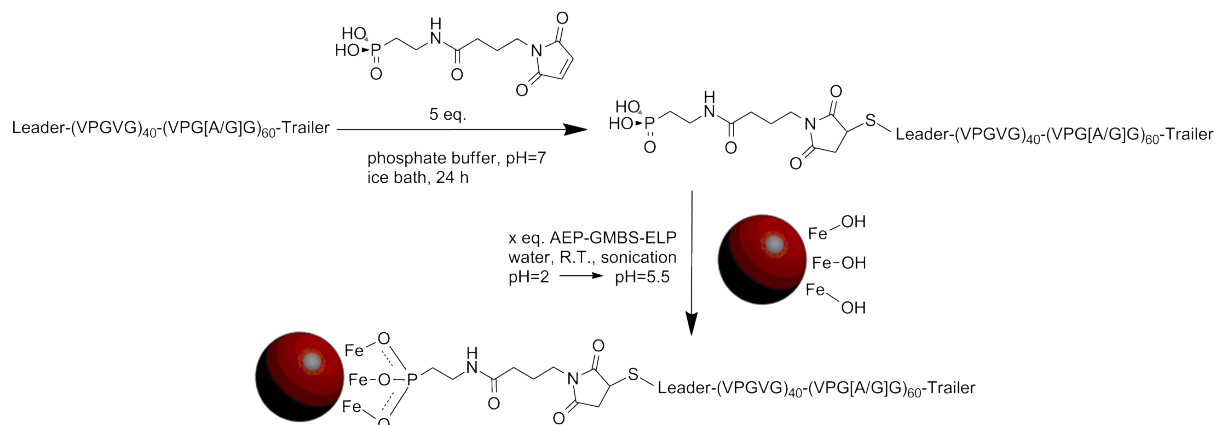


Figure 24 Synthetic scheme of the convergent grafting-to strategy of diblock $\text{ELP}_{40-60}\text{-Tat}$ post-modified with a phosphonic acid head group onto $\gamma\text{-Fe}_2\text{O}_3$ IONPs.

In order to achieve the grafting of diblock $\text{ELP}_{40-60}\text{-Tat}$ onto $\gamma\text{-Fe}_2\text{O}_3$ IONPs, an heterofunctional cross-linking agent 2-([4-(2,5-dioxo-2,5-dihydro-1H-pyrrol-1-yl)butanoyl]amino)ethyl)phosphonic acid (referred to as AEP-GMBS) presenting a thiol reactive maleimide group as well as a phosphonic acid head group was synthesized. This cross-linker was produced in one step by reacting 2-aminoethylphosphonic acid (AEP) with the commercial γ -maleimidobutyryloxysuccinimide ester (GMBS). This cross-linker was further reacted with the diblock $\text{ELP}_{40-60}\text{-Tat}$ through a Michael-type addition onto the Cys residue of the terminal end of the $\text{ELP}_{40-60}\text{-Tat}$. Diblock $\text{ELP}_{40-60}\text{-Tat}$ functionalized with the phosphonic acid anchor group were grafted onto the surface of IONPs in a single step. This bioconjugation was inspired by grafting strategies previously reported for grafting molecules with PEG side chains using mono- or bi-phosphonate anchoring groups.[27-29] At first, the colloidal stability of the un-grafted IONPs was preserved by keeping the nanoparticles in acidic conditions by addition of dilute nitric acid. The hydroxyls at the surface of the IONPs thus bore a positive charge preventing aggregation through electrostatic repulsions. After addition of the modified $\text{ELP}^*_{40-60}\text{-Tat}$, their phosphonic anchor group covalently bound to the surface of the IONPs. With such convergent strategy, an immediate stabilization of the dispersion at slightly acidic pH could be obtained where the $\text{ELP}^*_{40-60}\text{-Tat}$ were simply mixed with the IONPs.

Few characterization techniques were available to evaluate the chemical modification of the $\text{ELP}_{40-60}\text{-Tat}$ with the phosphonic acid anchor group. ATR-IR and NMR were tried but the signals from the aminoethylphosphonic acid and the heterofunctional linker (AEP-GMBS) could not be observed,

probably because of the too large difference of molecular weight between AEP-GMBS and the ELP. MALDI was then tried as it usually has a good sensitivity and a good resolution. The molecular weights were compared before (**Figure 25 a**) and after modification (**Figure 25 b**). Molecular weights of 41308 and 41511 g mol⁻¹ were obtained respectively. They both are different from the expected values (41273 and 41564 g mol⁻¹), with low relative errors of respectively 0.08 % and 0.12%. These errors were attributed to the resolutions of the measurements. As the molecular weights are extremely large, these relative errors reflect in absolute errors of 35 and 53 g mol⁻¹ respectively. Nevertheless, the chemical modification of the ELP_{40-60-Tat} was estimated to have taken place and the grafting was carried on the IONPs. The adhesion of the ELP_{40-60-Tat} was later observed and characterized.

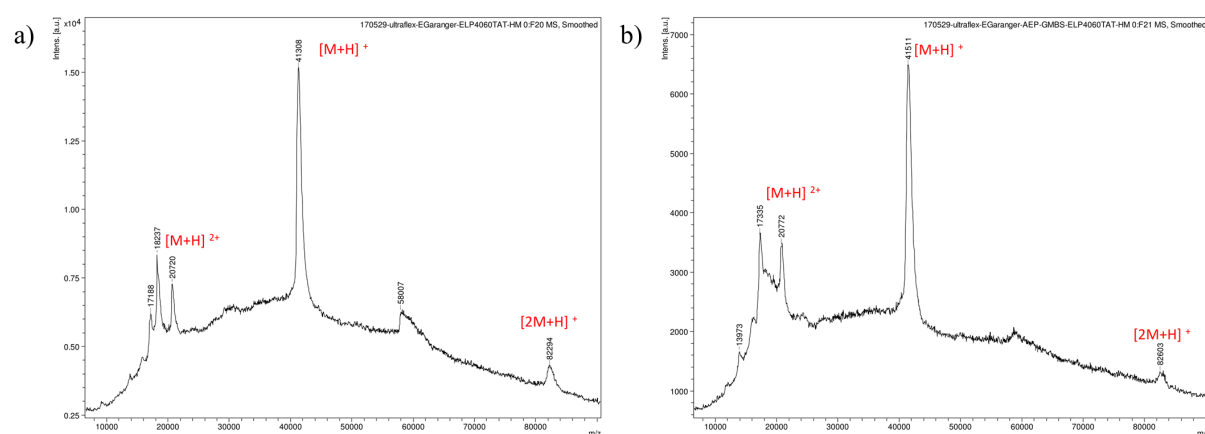


Figure 25 MALDI analysis of the ELP_{40-60-Tat} **a)** before and **b)** after chemical modification with the phosphonic acid anchor group.

The grafting density $\sigma = 1/d^2$ (with d being the distance between grafted (tethered) chains at the surface of the IONPs) was determined experimentally from thermogravimetric measurements. The amounts of ELP*_{40-60-Tat} grafted at the surface of the IONPs were calculated to reach the “mushroom to brush” and “true brush” regime of the ELP*_{40-60-Tat} coating as presented in the review by Brittain et al about polymers tethered to surfaces and colloids.[20] It was evidenced in a precedent work that ELPs in solution had chain conformations similar to that of polymers. The radius of gyration of free ELP in solution as a function of molecular weight could be described by a power law with an exponent value close to 0.5, which was characteristic of Gaussian coil conformation.[23] Calculating the reduced tethered density $\Sigma = \pi R_g^2/d^2$ helped representing the quantity of polypeptide grafted at the surface (with R_g the gyration radius of the ELP and d the distance between grafting points). Knowing the gyration radius of the ELP which was previously measured at 8.8 nm by small angle neutron scattering, the reduced tethered densities were either set in the range of $1 < \Sigma < 5$ for the “mushroom to brush” regime or $5 < \Sigma < 10$ for the “true brush” regime. These ranges respectively corresponded to interchain distances d (nm) of $16 < d < 7$ for the “mushroom to brush” regime or $7 < d < 5$ for the “true brush” regime, N chains per nanoparticle of $1 < N < 7$ for the “mushroom to brush” regime or $7 < N < 14$ for the “true brush” regime.

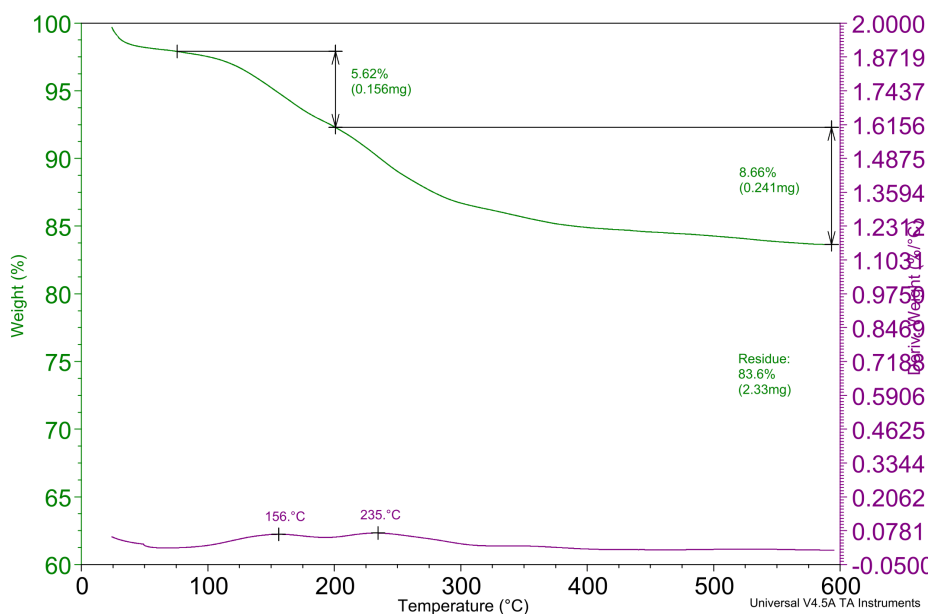


Figure 26 Thermogravimetric analysis of IONPs@ELP*_{40-60-Tat}.

Thermogravimetric analysis of IONPs@ELP*_{40-60-Tat} all evidenced two degradations. A first one at around 150 °C corresponding to the desorption of water bound at the surface of the nanoparticles, and a second one at 230-260 °C attributed to the degradation of the brush of ELP*_{40-60-Tat}. The residue is mainly composed of the iron oxide cores.

Table 3 Characteristics of the samples IONPs@ELP*_{40-60-Tat} (monocore, batch 34ff).

Sample n°	0	1	2	3
Grafting density (chain per nm ²)	0	0.016	0.024	0.041
Number of ELP* _{40-60-Tat} per IONP	0	5.2	8.0	13.5
Reduced tethered density Σ	0	3.9	6.0	10

Several parameters of interest to describe the core-shell IONPs@ELP*_{40-60-Tat} nanoparticles are presented in **Table 3**. Different grafting densities were tried by varying the equivalents of reagents, to reach densities in a range from 0 to 0.041 chains per nm². These values are relatively low, as the molecular weights of the ELP*_{40-60-Tat} is of 41564 g mol⁻¹, leading to a crowding of the surface at lower grafting densities. This range of value corresponded to an average number of ELP*_{40-60-Tat} tethered at the surface of the IONPs in a range from 0 to 13.5. The reduced tethered density Σ allowed estimating the crowding of grafted chains at the surface of the IONPs. With Σ values ranging from 0 to 10 as determined by TGA, the chains were expected to be in the mushroom-to-brush and brush regimes.

Infrared spectroscopy was carried out on the samples to assess the grafting of the ELPs on γ -Fe₂O₃ IONPs (**Figure 27**). The bare γ -Fe₂O₃ dried sample showed peaks in the 3000-3500 cm⁻¹ range corresponding to stretching vibrations of water. The peak at 1630 cm⁻¹ was ascribed to the bending vibration of water, and the large peak at 540 cm⁻¹ was attributed to the stretching vibration of the bond

between iron and oxygen. The same $\gamma\text{-Fe}_2\text{O}_3$ IONPs grafted with $\text{ELP}^*_{40-60\text{-Tat}}$ at different grafting densities showed additional peaks at 1660 cm^{-1} and 1550 cm^{-1} related to the amides of the proteins. Peaks in the range of 3200 to 2800 cm^{-1} were attributed to CH_2 , CH_3 and CH vibrations. The spectra were rescaled based on the intensity of the iron oxide peak at 540 cm^{-1} in order to compare the intensities of the peaks attributed to grafted proteins. As expected, the relative absorbance of the protein peaks increased along with the grafting density, as the quantity of proteins relative to IONPs increased.

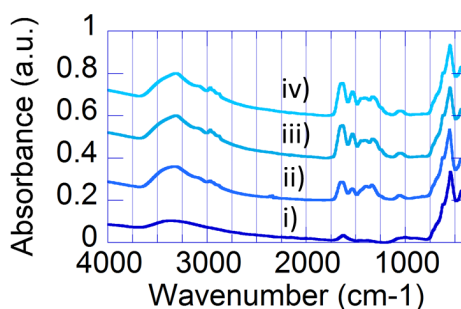


Figure 27 ATR-IR spectra of i) bare $\gamma\text{-Fe}_2\text{O}_3$ IONPs and core-shell IONPs@ $\text{ELP}^*_{40-60\text{-Tat}}$ at reduced tethered densities of ii) $\Sigma=3.9$, iii) $\Sigma=6.0$, and iv) $\Sigma=10$.

ELP brushes were grafted at different reduced tethered densities that were both evidenced by TGA and IR (**Table 3**, **Figure 26**, **Figure 27**). The influence of the grafting density over the thermoresponsive behavior of the IONPs is reported in **Chapter IV**. To the best of our knowledge, it is the first time that a core-shell structure of IONPs grafted with a thermosensitive ELP is reported.

5. Conclusion

Different anchor groups were tested for surface modifications, such as carboxylic acids, silanes, and phosphonic acids. They allowed grafting molecules of interest at the surface of IONPs, by bridging the gap between the inorganic core and the organic shell. Different molecules and macromolecules of interest were grafted, as a fluorescent probes (rhodamine123, DY700), a thermoresponsive polymer PDMAEMA, a stealth polymer PEG, a thermosensitive ELP_{20} and a thermosensitive diblock $\text{ELP}_{40-60\text{-Tat}}$ fused with a Tat cell-penetrating peptide. Two types of bioconjugation strategies of the IONPs with the organic shells were tried out: the divergent and the convergent grafting approaches. The divergent strategy was used in the first steps of the project, when developing surface modifications with silanes (grafting of PDMAEMA and ELP_{20}). It was not possible to do chemical modifications using silane anchor groups before final bioconjugation with the IONPs as silanes have a propensity to self-polymerize and form oligomers. For this reason, the silane terminated anchor groups had to be grafted first on the IONPs, and the final shell was constructed by successive covalent assembly of heterofunctional linkers and macromolecules. Switching to relatively chemically inert phosphonate anchor groups led to the possibility of using a convergent strategy, with a chemical modification of fluorescent probes, polymers and polypeptides beforehand, in a step prior

their bioconjugation with IONPs. This allowed characterizing the chemically modified (macro)molecules by classical means such as TLC, mass-spectrometry, NMR, and IR spectroscopies. The bioconjugation of the (macro)molecules with the IONPs was finally carried in a single one-pot step, in mild conditions of reaction, leading to readily stable dispersions of nanoparticles. Divergent grafting strategies followed by dialysis purification used to take weeks, with uncertain intermediate reaction steps. On the contrary, the convergent strategy coupled with a centrifugation-redispersion purification process helped cut time and effort. Core-shell nanoparticles could be produced in a single day with a good estimate on the purity of the final product. The newly formed hybrid core-shell structures presented new properties: magnetism due to their iron oxide core, and thermosensitive, cell-penetrating, stealth, fluorescent properties depending on the surface modification selected. This theoretically led to the equivalent of Swiss-knives multi-potent nano-objects for medical applications. Their properties are described in more details in **Chapters IV, V and VI**.

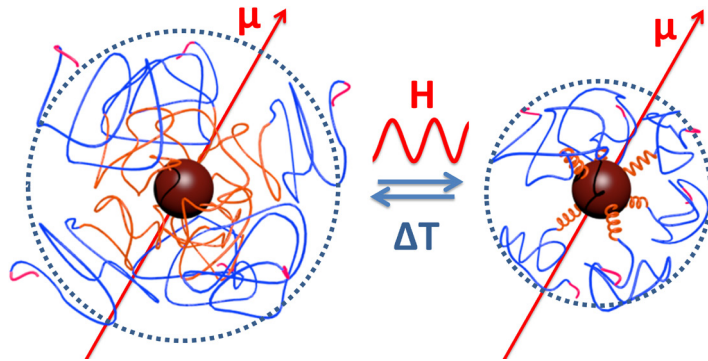
6. References

1. Parkinson, G.S., N. Mulakaluri, Y. Losovyj, P. Jacobson, R. Pentcheva, and U. Diebold, *Semiconductor-half metal transition at the Fe₃O₄(001) surface upon hydrogen adsorption*. *Physical Review B*, 2010. **82**(12): p. 125413.
2. Walter, A., A. Garofalo, P. Bonazza, F. Meyer, H. Martinez, S. Fleutot, C. Billotey, J. Taleb, D. Felder-Flesch, and S. Begin-Colin, *Effect of the Functionalization Process on the Colloidal, Magnetic Resonance Imaging, and Bioelimination Properties of Mono- or Bisphosphonate-Anchored Dendronized Iron Oxide Nanoparticles*. *ChemPlusChem*, 2017. **82**(4): p. 647-659.
3. Bee, A., R. Massart, and S. Neveu, *Synthesis of very fine maghemite particles*. *Journal of Magnetism and Magnetic Materials*, 1995. **149**(1–2): p. 6-9.
4. Molday, R.S., *Magnetic iron-dextran microspheres*. 1984, Google Patents.
5. Horák, D., M. Babič, P. Jendelová, V. Herynek, M. Trchová, Z. Pientka, E. Pollert, M. Hájek, and E. Syková, *d-Mannose-Modified Iron Oxide Nanoparticles for Stem Cell Labeling*. *Bioconjugate Chemistry*, 2007. **18**(3): p. 635-644.
6. Remya, N.S., S. Syama, A. Sabareeswaran, and P.V. Mohanan, *Toxicity, toxicokinetics and biodistribution of dextran stabilized Iron oxide Nanoparticles for biomedical applications*. *International Journal of Pharmaceutics*, 2016. **511**(1): p. 586-598.
7. Ha-Young, L., L. Sang-Hoon, X. Chenjie, X. Jin, L. Jin-Hyung, W. Bing, K. Ai Leen, W. Xiaoying, S. Robert, X.W. Shan, G.N. Dwight, B. Sandip, S. Shouheng, C. Sun Hang, and C. Xiaoyuan, *Synthesis and characterization of PVP-coated large core iron oxide nanoparticles as an MRI contrast agent*. *Nanotechnology*, 2008. **19**(16): p. 165101.
8. Ghobril, C., G. Popa, A. Parat, C. Billotey, J. Taleb, P. Bonazza, S. Begin-Colin, and D. Felder-Flesch, *A bisphosphonate tweezers and clickable PEGylated PAMAM dendrons for the preparation of functional iron oxide nanoparticles displaying renal and hepatobiliary elimination*. *Chemical Communications*, 2013. **49**(80): p. 9158-9160.
9. Fresnais, J., M. Yan, J. Courtois, T. Bostelmann, A. Bée, and J.F. Berret, *Poly(acrylic acid)-coated iron oxide nanoparticles: Quantitative evaluation of the coating properties and applications for the removal of a pollutant dye*. *Journal of Colloid and Interface Science*, 2013. **395**: p. 24-30.
10. Dao, T.P.T., M. Fauquignon, F. Fernandes, E. Ibarboure, A. Vax, M. Prieto, and J.F. Le Meins, *Membrane properties of giant polymer and lipid vesicles obtained by electroformation and pva gel-assisted hydration methods*. *Colloids and Surfaces A: Physicochemical and Engineering Aspects*, 2017. **533**: p. 347-353.
11. Swift, T., L. Swanson, M. Geoghegan, and S. Rimmer, *The pH-responsive behaviour of poly(acrylic acid) in aqueous solution is dependent on molar mass*. *Soft Matter*, 2016. **12**(9): p. 2542-2549.
12. Duguet, E., S. Mornet, and J. Portier, *Ferrofluids stable in neutral media and modified ferrofluids modifies obtained by modification of the surface of the particles of said ferrofluids*. 2004, PCT / WO2004107368 A2.
13. Srinivasan, R., L.P. Tan, H. Wu, P.-Y. Yang, K.A. Kalesh, and S.Q. Yao, *High-throughput synthesis of azide libraries suitable for direct "click" chemistry and in situ screening*. *Organic & Biomolecular Chemistry*, 2009. **7**(9): p. 1821-1828.
14. van de Wetering, P., E.E. Moret, N.M.E. Schuurmans-Nieuwenbroek, M.J. van Steenberg, and W.E. Hennink, *Structure–Activity Relationships of Water-Soluble Cationic Methacrylate/Methacrylamide Polymers for Nonviral Gene Delivery*. *Bioconjugate Chemistry*, 1999. **10**(4): p. 589-597.
15. Plamper, F.A., M. Ruppel, A. Schmalz, O. Borisov, M. Ballauff, and A.H.E. Müller, *Tuning the Thermoresponsive Properties of Weak Polyelectrolytes: Aqueous Solutions of Star-Shaped and Linear Poly(N,N-dimethylaminoethyl Methacrylate)*. *Macromolecules*, 2007. **40**(23): p. 8361-8366.
16. Bataille, L., W. Dieryck, A. Hocquellet, C. Cabanne, K. Bathany, S. Lecommandoux, B. Garbay, and E. Garanger, *Expression and purification of short hydrophobic elastin-like*

- polypeptides with maltose-binding protein as a solubility tag*. Protein Expression and Purification, 2015. **110**: p. 165-171.
17. Fischer, H., I. Polikarpov, and A.F. Craievich, *Average protein density is a molecular-weight-dependent function*. Protein Science, 2004. **13**(10): p. 2825-2828.
 18. Devanand, K. and J.C. Selser, *Asymptotic Behavior and Long-Range Interactions in Aqueous Solutions of Poly(ethylene oxide)*. Macromolecules, 1991. **24**: p. 5943-5947.
 19. Le Coeur, C., J. Teixeira, P. Busch, and S. Longeville, *Compression of random coils due to macromolecular crowding: Scaling effects*. Physical Review E, 2010. **81**(6): p. 061914.
 20. Brittain, W.J. and S. Minko, *A structural definition of polymer brushes*. Journal of Polymer Science Part A: Polymer Chemistry, 2007. **45**(16): p. 3505-3512.
 21. Pauli, J., T. Vag, R. Haag, M. Spieles, M. Wenzel, W.A. Kaiser, U. Resch-Genger, and I. Hilger, *An in vitro characterization study of new near infrared dyes for molecular imaging*. European Journal of Medicinal Chemistry, 2009. **44**(9): p. 3496-3503.
 22. Gilbert, B., J.E. Katz, N. Huse, X. Zhang, C. Frandsen, R.W. Falcone, and G.A. Waychunas, *Ultrafast electron and energy transfer in dye-sensitized iron oxide and oxyhydroxide nanoparticles*. Physical Chemistry Chemical Physics, 2013. **15**(40): p. 17303-17313.
 23. Garanger, E., S.R. MacEwan, O. Sandre, A. Brûlet, L. Bataille, A. Chilkoti, and S. Lecommandoux, *Structural Evolution of a Stimulus-Responsive Diblock Polypeptide Micelle by Temperature Tunable Compaction of its Core*. Macromolecules, 2015. **48**(18): p. 6617-6627.
 24. Duro-Castano, A., I. Conejos-Sánchez, and M. Vicent, *Peptide-Based Polymer Therapeutics*. Polymers, 2014. **6**(2): p. 515.
 25. Bechara, C. and S. Sagan, *Cell-penetrating peptides: 20 years later, where do we stand?* FEBS Letters, 2013. **587**(12): p. 1693-1702.
 26. Richard, J.P., K. Melikov, E. Vives, C. Ramos, B. Verbeure, M.J. Gait, L.V. Chernomordik, and B. Lebleu, *Cell-penetrating Peptides: A REEVALUATION OF THE MECHANISM OF CELLULAR UPTAKE*. Journal of Biological Chemistry, 2003. **278**(1): p. 585-590.
 27. Basly, B., D. Felder-Flesch, P. Perriat, C. Billotey, J. Taleb, G. Pourroy, and S. Begin-Colin, *Dendronized iron oxide nanoparticles as contrast agents for MRI*. Chemical Communications, 2010. **46**(6): p. 985-987.
 28. Garofalo, A., A. Parat, C. Bordeianu, C. Ghobril, M. Kueny-Stotz, A. Walter, J. Jouhannaud, S. Begin-Colin, and D. Felder-Flesch, *Efficient synthesis of small-sized phosphonated dendrons: potential organic coatings of iron oxide nanoparticles*. New Journal of Chemistry, 2014. **38**(11): p. 5226-5239.
 29. Blin, T., A. Kakinen, E.H. Pilkington, A. Ivask, F. Ding, J.F. Quinn, M.R. Whittaker, P.C. Ke, and T.P. Davis, *Synthesis and in vitro properties of iron oxide nanoparticles grafted with brushed phosphorylcholine and polyethylene glycol*. Polymer Chemistry, 2016. **7**(10): p. 1931-1944.

CHAPTER IV

A UNIQUE SET-UP TO MEASURE IN REAL TIME THE THERMOSENSITIVE PROPERTIES OF NANO- OBJECTS UNDER MAGNETIC HYPERTHERMIA



1. Introduction

Local increase of temperature in body tissues is envisioned as an attractive cancer therapy. Current approaches for local hyperthermia mainly involve focused ultrasound surgery (FUS),[1] visible or near-infrared plasmonic absorption by noble metal NPs,[2] and magnetic induction in the mega or giga-Hertz bandwidth.[3] Among these methods, magnetic hyperthermia is envisioned to become an efficient therapeutic treatment by oncologists to fight against incurable and hard to reach cancers such as glioblastoma; a type of brain cancer.[4] Magnetic hyperthermia has the major advantage to penetrate deeper tissues than what is possible with light or acoustic waves. Understanding the mechanism of how magnetic nanoparticles (MNPs) convert electromagnetic radiations into heat at the nanoscale and dissipate it into the surrounding environment is emerging as an intensive and debated research area.[5, 6] IONPs are prominent heating agent candidates due to their ease of synthesis, cost-effectiveness and magnetic properties.[7] Moreover, IONPs are highly biocompatible due to the homeostasis of iron.[8, 9] Tuning the morphology of the NPs has also been used to control their heating properties in cellular media under a radiofrequency magnetic field.[10] Different synthesis pathways were explored with the aim of providing IONPs with the highest heating properties, among which was selected the polyol pathway (discussed in **Chapter II**). This process has the advantage of providing IONPs readily dispersible in water, with well-controlled morphologies and satisfying heating properties.[11] The surface of these IONPs was frequently modified to bring stability in biological conditions or extra functionalities. Our group has previously reported the grafting of thermosensitive polymer chains exhibiting a temperature-dependent transition between swollen and dehydrated states onto IONPs. A commercial synthetic temperature-dependent statistical copolymer called Jeffamine™ was grafted onto IONPs to obtain thermosensitive contrast agents for magnetic resonance imaging (MRI).[12] We also reported a thermosensitive poly[2-(dimethylamino)ethyl methacrylate] (PDMAEMA) polymer chain synthesized by controlled radical polymerization and grafted onto IONPs using a copper assisted azide-alkyne cycloaddition reaction.[13] The hydrodynamic diameter variations of these thermosensitive and magnetic IONPs were measured *in situ* while applying a radiofrequency magnetic field by using an in-house designed dynamic backscattered light intensity setup combined with MH. With the aim of improving this method and applying it to cellular environments, a more biocompatible and biomimicking macromolecule coating was developed, based on thermoresponsive recombinant ELPs. Thanks to the collaboration with other laboratories, other systems were also investigated, as thermo-cleavable magnetic micelles made of self-immolative polymers loaded with IONPs. Thermo-sensitive and magnetic microgels or nanorattles were also studied. Their reversible change of conformation under

magnetic hyperthermia was evidenced *in situ* using our unique set-up. These structures provide promising strategies for drug delivery triggered externally by the application of a magnetic field.

2. Materials and methods

2.1. Presentation of magnetic hyperthermia coupled with DLS set-up

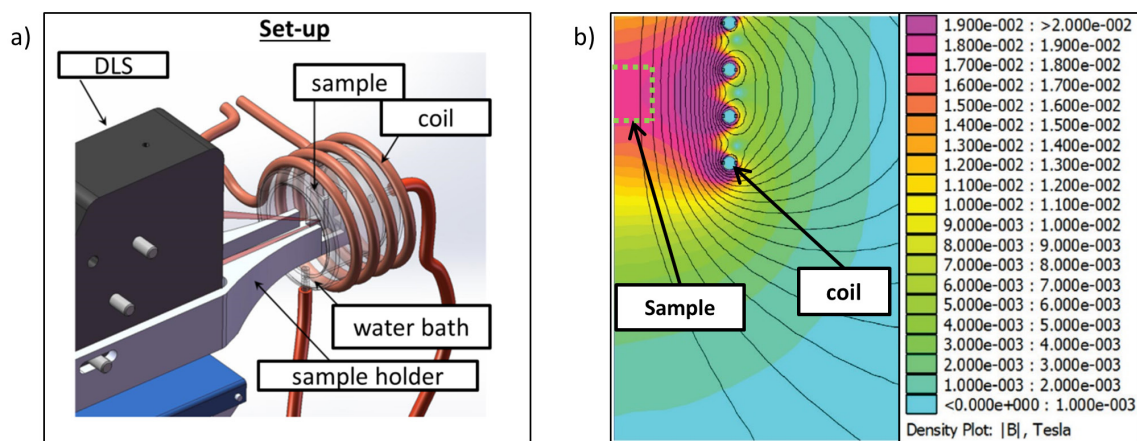


Figure 1 a) Illustration of set-up coupling a DLS instrument with an induction coil for magnetic hyperthermia experiments. **b)** Finite element model simulation for an AC current of 234 Amps. The position of the sample inside the coil is illustrated in a section plane.

A novel in-house set-up was developed in order to measure the thermo-sensitive properties of magnetic nano-objects in solution (**Figure 1 a**). This set-up allowed measuring the hydrodynamic diameters by dynamic light scattering (DLS) in solution while applying magnetic hyperthermia, and recording simultaneously the temperature of the solution with an optical probe. The remote head of the VASCO Flex™ backscattering setup was located ~ 8 cm from a cuvette placed in a glass water-jacket inside the 4-turn coil of 55 mm outer diameter. The stage maintained the optical path constant and held the cuvette inside the coil. It was made by 3D printing from a plastic material (insensitive to eddy currents). The radiofrequency power generator operating at $f=755$ kHz created a maximum induction $B_0=16.3$ mT as measured by a scout coil and as calculated by a finite element model simulation for an AC current of 234 Amps (**Figure 1 b**). For combined DLS/MH experiments, the magnetic induction was held at a maximum field strength $H_0=10.2$ $\text{kA}\cdot\text{m}^{-1}$. In situ measurements were acquired simultaneously during the magnetic field application using the VASCO Flex™ remote head DLS instrument developed by Cordouan Technologies. This commercial instrument was developed within the SNOW FP7NMP-2010-SME-4 European project dedicated to in situ characterization of nanoparticles in either harsh environments or combined with another technique (*e.g.* small angle x-ray scattering) for quality control of nanomaterials production. The principle is based on light scattering detected by fiber optics in backscattering conditions,[18] enabling measurements of concentrated samples (here around 1 $\text{g}\cdot\text{L}^{-1}$ of iron oxide). The scattering volume was defined at the intersection

between the incident measurement beam (horizontal) and the alignment beam (tilted at an angle) and the measurement distance was adjusted to 8 cm compared to the remote head. Kinetic DLS measurements were acquired with the NanoQ™2.5 software. The remote head was adjusted to locate the scattering volume approximately 2 mm behind the wall of the cuvette. The beam power was tuned to read a scattered intensity in the working range 1000–4000 kcps of the detector. After choosing the minimum decay time and number of channels of the correlator, the acquisitions were launched for an unlimited time with independent sub-runs of 30 s. The correlogram of each sub-run was analyzed on the fly by the 2nd order cumulant. The temperature was recorded by the Opsens conditioner (through RS-232 cable) and at a rate of 1 Hz by the NanoQ™2.5 software (through an analogous output, with a shielded cable to protect it from the electromagnetic perturbations when the radio frequency (RF) magnetic field was on). As any metallic part located too close to the solenoid would be heated through eddy currents generated by the electrical field component of the RF excitation, the magnetic field intensity in front of the coil (outside) was estimated to predict how it decayed with distance. A scout coil of diameter 1.75 cm (of surface $S=2.4 \text{ cm}^2$) was used to estimate the magnetic field strength, generating a root mean square (RMS) electromotive force $e_{RMS} = B_0 \times S \times 2\pi f$ when submitted to a RMS field induction B_0 , detected by an oscilloscope (Teledyne LeCroy Waveace™ 102). A magnetic induction $B_0=16.3 \text{ mT}$ was measured at a distance of 5 cm from the entry, $B_0=14.1 \text{ mT}$ at 15 cm, $B_0=1.28 \text{ mT}$ at 22 cm, and $B_0=0.44 \text{ mT}$ at 30 cm, in accordance with studies showing the field intensity decay vs. distance for such magnetic induction setups.[19] The field lines were also calculated using cylindrical axi-symmetry with the finite element simulation freeware FEMM (<http://www.femm.info>), which showed calculated field values close to the experimentally measured ones (**Figure 1. b**). For the control experiment under a static (DC) magnetic field, the sample holder was placed inside a solenoid with 1000 turns (8.75Ω) fed by a current from a DC generator (Française d'Instrumentation), the field intensity being measured with a Hall-effect probe (Lakeshore 425 gaussmeter).

2.2. Proton relaxometry

NMR tubes (7.5 mm outer diameter) were filled with 0.3 mL of each sample, and inserted in a Bruker™ mq60 relaxometer equipped with a 60 MHz / 1.41 Tesla magnet. Following recommended protocols in proton relaxometry,[14] longitudinal T_1 relaxation times were measured using an inversion-recovery sequence of first duration of $\sim 0.1 \times T_1$ and final duration of $\sim 3 \times T_1$ with a recycling delay (RD) of $\sim 5 \times T_1$ between two of the 10 acquisition points, 4 scans and an automatic RF receiver gain. Transverse T_2 relaxation times were measured using Car-Purcell-Meiboom-Gill (CPMG) sequence, with delay time τ of 0.04 ms between the 90° rotation to transverse plane and the 180°

focusing pulse, a duration time of $3 \times T_2$, RD of $5 \times T_1$, and automatic receiver gain. The number of acquisition points was set by dividing the duration time by the delay time τ .

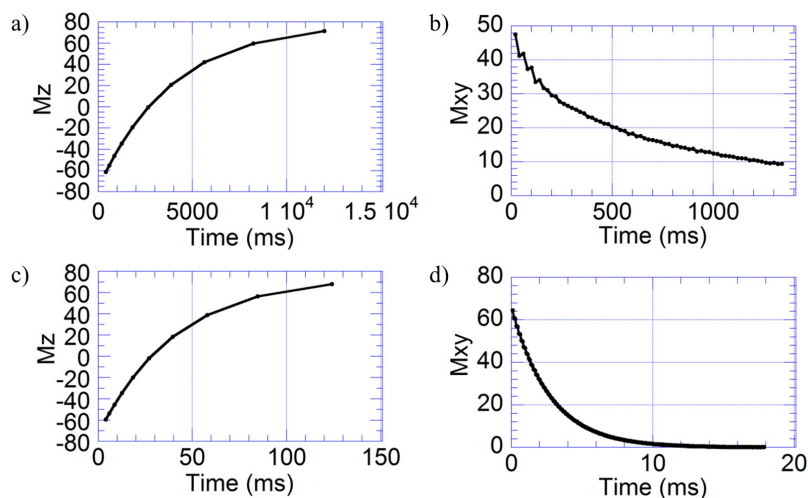


Figure 2 a) Longitudinal (Mz) and b) transverse (Mxy) relaxation times of protons of dionized water at 37 °C. c) Longitudinal (Mz) and d) transverse (Mxy) relaxation times of protons of dionized water containing superparamagnetic IONPs@PEG* nanoparticles at 37 °C.

Using the parameters of acquisition described above allowed measuring the longitudinal (Mz) and transverse (Mxy) relaxation times of the protons of water. The introduction of superparamagnetic IONPs@PEG* nanoparticles results in shortened relaxations times. This effect was later quantified as longitudinal (r_1) and transverse (r_2) relaxivities.

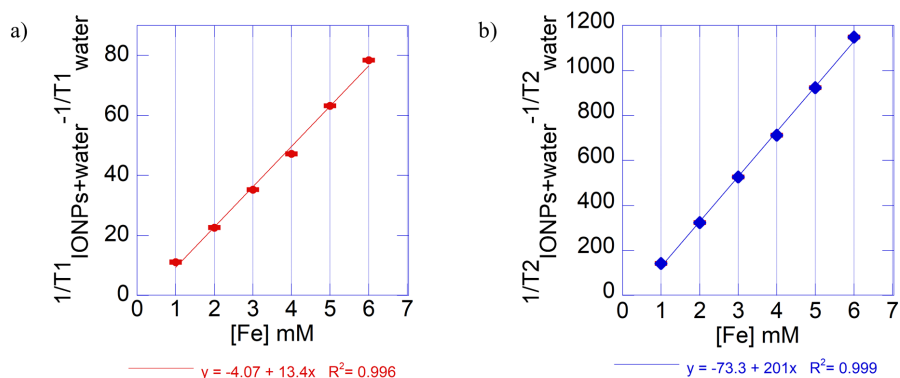


Figure 3 Investigation of the a) longitudinal and b) transverse relaxations of protons of water containing IONPs (34ff@PEG*) at different concentrations.

Samples were prepared at concentrations of iron from 1 to 6 mM_{Fe}. Transverse and longitudinal relaxations of the protons of water were measured, evidencing a linear dependence toward the concentration of IONPs@PEG* (**Figure 3 a-b**). All further measurements were performed in this range of concentration.

2.3. TEM measurements

TEM was performed on a Hitachi H7650 microscope operated at 80 kV on samples deposited at mass concentrations at around $1 \text{ g}\cdot\text{L}^{-1}$ onto copper grids by a lab-made spraying tool, and images were acquired on an ORIUS SC1000 11MPx Camera.

2.4. Transition Temperature Measurement

Transition temperatures (T_t), that are also often referred to as LCST, were determined by turbidity measurements at 350 nm between 20 and 80 °C at $1 \text{ }^\circ\text{C}\cdot\text{min}^{-1}$ scan rate of ELPs in aqueous solution at different concentrations. Data were collected on a Cary 300 Bio UV–visible spectrophotometer equipped with a multicell thermoelectric temperature controller (Varian, Palo Alto, CA).

3. Magnetic and thermo-sensitive magnetic micelles

3.1. Materials and methods

The surface of IONPs (21ff or 32ff) was modified as follow. 113 mg of Beycostat NE was deposited in a 50 mL beaker. 15.0 mL of water was added and the solution was stirred with a mechanical agitator. 2.5 mL of a ferrofluid with an iron oxide concentration of $18.0 \text{ g}\cdot\text{L}^{-1}$ (45 mg of IONPs) was added to the surfactant. Then 2.6 mL of a 69 % w/w HNO_3 solution was added to reach a final HNO_3 concentration of 2.0 M. The solution was heated to 60 °C for 30 min with a water bath. The nanoparticles were then sedimented over a permanent magnet and washed 3 times with 50 mL of methanol, before being dispersed in 45 mL of dichloromethane (DCM) or tetrahydrofuran (THF). The iron oxide content of this dispersion was estimated by dissolving 50.0 microliters of solution in 5.0 mL of 5.0 M HCl M with the help of a sonication bath. The absorption at 350 nm corresponding to the peak of the $[\text{Fe}(\text{Cl})_6]^{3-}$ complex was compared to a calibration curve. The final concentration was estimated at 6.0 g/L of Fe_2O_3 .

IONPs were loaded in polymer micelles as follow. 1.0 mg of PEtG-DA-PEG5000 or Micelle-control was dissolved in 0.2 mL of THF. Meanwhile, IONPs modified with Beycostat (dispersed in THF with a concentration of 6.0 mg/mL) were mixed at different feed weight ratios (FWR) as needed with the polymer solution. This mixture was then added dropwise to 1.8 mL water via a micro-syringe while magnetically stirring. THF was allowed to evaporate by leaving the vials open for 24 h.

Small angle neutron scattering (SANS) experiments were performed at the Orphée neutron facility of LLB-CEA (Saclay, France) on the PAXY spectrometer equipped with a 2D (anisotropic SANS) detector. Micelles were suspended at a concentration of $0.6 \text{ mg}\cdot\text{mL}^{-1}$ in pure D_2O , of neutron scattering length density $\text{SLD}(\text{D}_2\text{O})=6.40\times 10^{-6} \text{ \AA}^{-2}$. The calculated SLD of iron oxide and ethyl glyoxylate monomer are $\text{SLD}(\gamma\text{-Fe}_2\text{O}_3)=6.98\times 10^{-6} \text{ \AA}^{-2}$ and $\text{SLD}(\text{EtG})=1.31\times 10^{-6} \text{ \AA}^{-2}$, respectively. The

neutron scattering contrast of the micelles in heavy water thus arises almost exclusively from the hydrophobic Poly(EtG) block of the polymer, the hydrophilic PEG block being highly hydrated, thus having negligible contribution to the neutron scattering contrast. Three beamline configurations were used to cover overlapping scattering vector (q) ranges of $1.92 \times 10^{-3} - 2.84 \times 10^{-2}$, $1.05 \times 10^{-2} - 0.154$, and $3.19 \times 10^{-2} - 0.427 \text{ \AA}^{-1}$, with the following values of sample-to-detector distance D and neutron wavelength λ : $D=7 \text{ m}$ and $\lambda=15 \text{ \AA}$, $D=3 \text{ m}$ and $\lambda=6 \text{ \AA}$, $D=1 \text{ m}$ and $\lambda=6 \text{ \AA}$. The scattering intensity curves were divided by the transmission factor and subtracted from the incoherent background, before normalizing by the flat signal of a cuvette filled with light water to correct the detector efficiency, yielding the absolute intensity in cm^{-1} .

3.2. Results and discussion

A thermosensitive polymer of poly(ethylene oxide)-co-poly(ethyl glyoxylate)-co-poly(ethylene oxide) (PEG5k-PEtG50k-PEG5k) was received from the team of Elizabeth R. Gillies (Western University, Department of Chemistry, London, Canada). Their group already reported self-immolative polymers based on PEtG, and studied their properties for drug-delivery applications.[15-18] The idea was to form magnetic polymersomes by incorporating hydrophobic iron oxide nanoparticles to the PEtG part of polymersomes' membranes. Degradations from de-polymerization of such objects were assessed using the DLS/MH set-up.

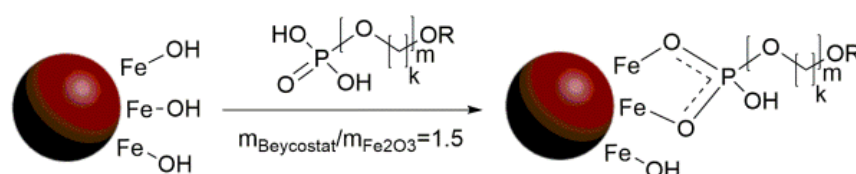


Figure 4 Surface modification of IONPs (21ff or 32ff) with a hydrophobic coating of Beycostat. The chemical structure is represented from information available on the patent of the provider (CECA chemicals, France).

Next, magnetic and thermo-responsive micelles were formed by incorporating magnetic IONPs to the polymer. IONPs were synthesized following the so-called polyol pathway, leading to nanoparticles with well-defined morphologies and magnetic properties. The IONPs were produced with a spherical morphology and an average diameter of $11.2 \pm 1.9 \text{ nm}$ (21ff) or $14.5 \pm 3.4 \text{ nm}$ (32ff). They were well-suitable for magnetic hyperthermia (MH), with a specific absorption rate of $84 \text{ W} \cdot \text{g}^{-1}$ (or respectively $134 \text{ W} \cdot \text{g}^{-1}$) with our set-up ($10.2 \text{ kA} \cdot \text{m}^{-1}$, 755 kHz). The commercial Beycostat NE (NB09, CECA chemicals, France) was used to modify the surface of the nanoparticles and make them hydrophobic, in order to incorporate them with the polymers. Beycostat was grafted through its phosphonic acid anchor group in acidic conditions (2 M HNO_3). Solutions of polymer and suspensions of IONPs were stored in at $-24 \text{ }^\circ\text{C}$ to prevent the evaporation of the solvents, to avoid changing the

concentrations, and to prevent the polymer from degrading. DCM, DMSO and THF were tested to evaluate the best conditions of nano-precipitation. DCM was poorly miscible with water leading to two separate phases and no nano-precipitation. DMSO was miscible with water but had to be removed by dialysis. A screening of different parameters was carried out to determine the best conditions for the nano-precipitation and co-assembly of IONPs and amphiphilic copolymers. The optimized results were obtained by following these conditions: IONPs were dispersed in THF and mixed at different feed weight ratios (FWR) with the polymer also solubilized in THF (**Figure 5 a**).

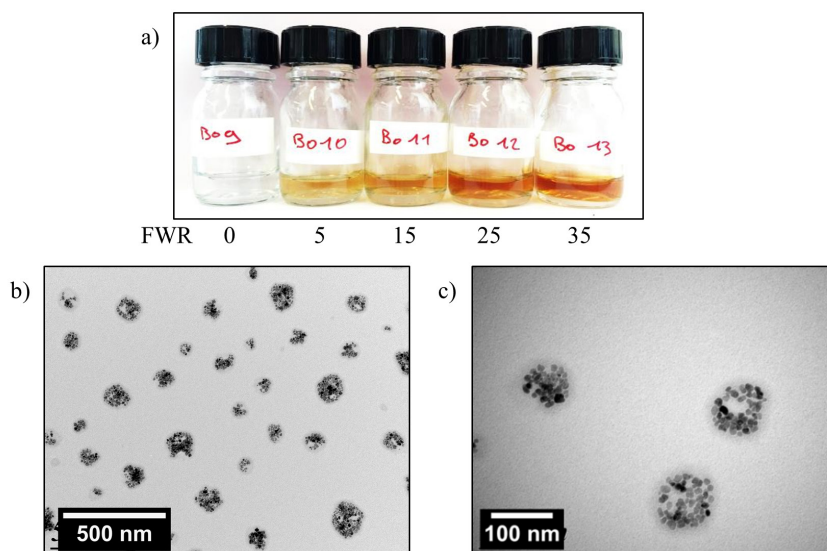


Figure 5 a) Picture of the dispersions after nano-precipitation showing the variation of color along with the FWR of IONPs. **b,c)** TEM micrographs of the magnetic micelles.

This mixture was added dropwise to a volume of water with a micro-syringe while magnetically stirring. In all cases the final fraction of water was of 90 % and the polymer was at a final concentration of $0.5 \text{ g}\cdot\text{L}^{-1}$. THF was allowed to evaporate by using a vacuum pump. Samples were considered stable in the range of FWR from 0 to 35 %. Dispersions could be stored for several days in a fridge without visible aggregation. Samples were deposited on TEM grids with a thin Holey carbon film from Pacific GridsTM in order to produce the largest electron contrast without using a stain. Spherical objects with dimensions in the order of 100 nm were observed, spread homogeneously on the surface of the grid (**Figure 5 b,c**). The polymer was visible, forming a diffuse grey area in the periphery of the objects. Considering the morphology and the dimensions of the nano-objects, they were most probably micelles.

Samples with the highest FWR of 35 %, theoretically able to produce larger increases of temperature, were studied by DLS/MH (**Figure 6**). The measurements were carried as follow: the temperatures of the samples were allowed to slowly adjust to the temperature of the water bath for an hour. Then magnetic fields at maximum amplitudes of $10.2 \text{ kA}\cdot\text{m}^{-1}$ with a frequency of 755 kHz were

applied. The heat generated by the sample led to a slight increase of temperature in the range of 2 °C. The stimulation of the IONPs in the magnetic micelles by the magnetic field was lower than in the case of IONPs freely suspended in the solution. This could be interpreted by their strong interactions with the polymers, leading to a blocked state of their magnetic moments. They could relax only by the Néel and not by the Brownian mechanism. Nevertheless, the magnetic stimulus had an effect on the morphology of the magnetic micelles, leading to an increase of diameter in the case of the thermo-sensitive polymer, probably through an aggregation phenomenon.

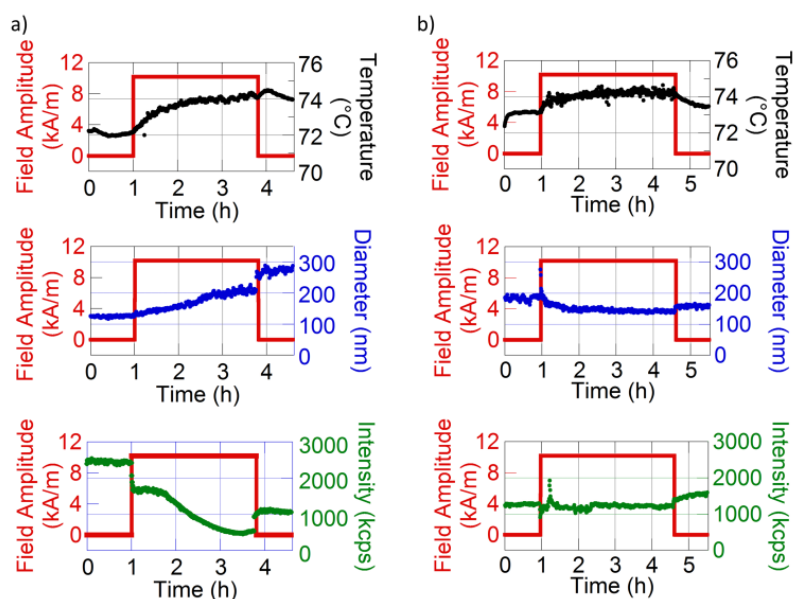


Figure 6 DLS coupled with MH experiment in the case of **a)** the thermosensitive polymer, and **b)** the light-sensitive polymer. Baseline temperature of 72 °C.

The scattered intensity also underwent a sharp variation upon application of MH. As the diameter increased the intensity was expected to increase, but we observed the contrary. Based on the experiments carried on non-magnetic micelles, we hypothesized that upon application of MH, the polymer degraded, leading to an overall reduction of the concentration of scattering species. Then the un-stabilized hydrophobic IONPs aggregated. This would explain both the behavior of hydrodynamic diameter and scattered intensity. In the case of the control non-thermosensitive sample, a similar elevation of temperature was recorded, but diameters and intensities remained relatively flat.

The thermal degradation of the thermosensitive micelles was also investigated by SANS (**Figure 7**). Micelles loaded with IONPs were prepared as previously described, with few changes to adapt to this other characterization technique. The IONPs ($d_{\text{TEM}}=10.5$ nm) and the polymer were mixed in deuterated THF, and nano-precipitated in deuterated water to improve the contrast between the micelles and their solvent. Thermosensitive micelles (BO14) or magnetically loaded thermosensitive micelles (BO15, 35 wt. % iron oxide relatively to polymer) were prepared this way, at

a concentration of $0.6 \text{ mg}\cdot\text{mL}^{-1}$. The effect of long heating on the structure of the micelles was evidenced by comparing the SANS curves before and after heating at $80 \text{ }^\circ\text{C}$ in an oven for 30 min.

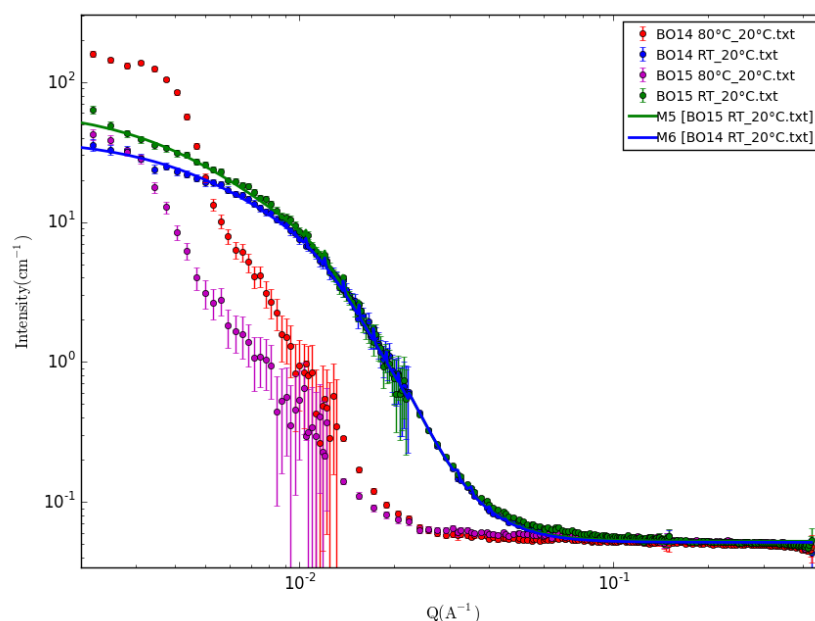


Figure 7 Small-angle neutron scattering of pure (BO14) or IONPs loaded (BO15) thermosensitive micelles, before or after heat treatment at $80 \text{ }^\circ\text{C}$.

The curves of the heat-treated micelles were not fitted by a model shape. Nonetheless, they can be interpreted by a drastic reduction of the volume fraction of suspended copolymer micelles, together with an increase of the size of the remaining objects (as ascribed to aggregation). This SANS experiment thus brings another evidence of the thermosensitivity of PEG5k-PEtG50k-PEG5k copolymer micelles that did not disappear when embedding IONPs in their core.

4. Magnetic and thermo-sensitive nanorattles

Nanorattles were received from the team of Markus Gallei (Technische Universität Darmstadt, Ernst-Berl-Institute for Chemical Engineering and Macromolecular Science, Darmstadt, Germany). They were synthesized from ferrocene-containing polymer precursors using semi-continuous emulsion polymerization and Stöber process protocols followed by thermal treatment.[19] This bottom-up strategy led to original structures for advanced ceramics with potential applications within fields of sensing.

Nano-rattles composed of hollow capsules of silica containing iron oxide and covered by a layer of poly(*N*-isopropylacrylamide) (PNIPAM) were received (**Figure 8 a**). The particles dispersed in water were analyzed by DLS using a Malvern NanoZS. The size versus temperature was measured

from 20 to 60 °C with steps of 0.5 °C, each measurement consisting of 10 runs of 30 s. The graph obtained showed a decrease of hydrodynamic diameter along increasing temperature (**Figure 8 b**).

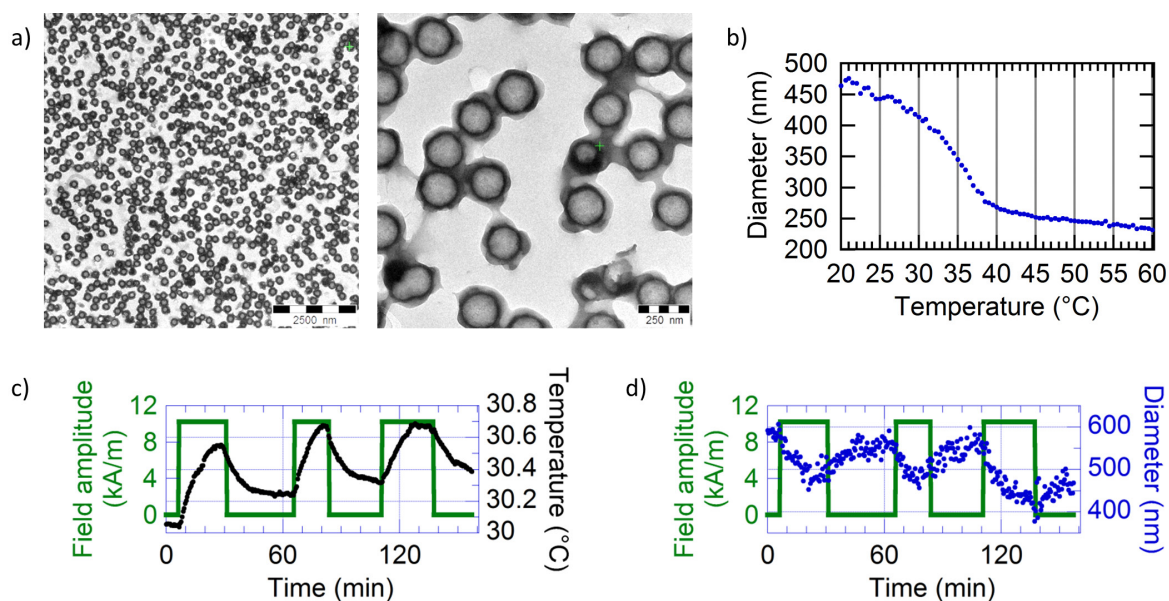


Figure 8 a) TEM micrograph of the magnetic nano-rattles. b) Diameter of the nano-rattles versus temperature observed by DLS. c) Temperature of the sample vs. amplitude of magnetic field measured by an optical fibre during magnetic hyperthermia. d) Diameter of the sample vs. amplitude of magnetic field measured by DLS during magnetic hyperthermia.

The plotted curve had a sigmoidal shape presenting an inflexion point at around 35 °C. This confirmed the thermosensitive property of these particles, with a maximum variation of diameter from 30 to 37 °C. The sample dispersed in water at 0.2 wt% was concentrated by a factor 10 using centrifugation to generate sufficient variations of temperature when applying a radiofrequency magnetic field. The temperature of the bath was set at 30 °C to thermalize the sample at this baseline temperature. The sample was thermally insulated with bubble wrap to prevent the strong noise observed due to small variations of temperature over long times coupled with parasitic effects coming from the set-up. When the sample was thermalized, magnetic fields were applied for 20 min, followed by no magnetic fields for 30 min. This was repeated thrice to put in evidence the reproducibility of the experiment. The particles were stimulated by the magnetic field and generate heat, rising the temperature of the sample up to 30.6 °C as measured with an optical fiber probe (**Figure 8 c**). The temperature of the sample gradually lowered to 30 °C, the value set by the glass water-jacket, when no magnetic field was applied. Variations of diameters along temperature were observed, the higher the temperature, the lower the diameter ((**Figure 8 d**)). This was consistent with the DLS Malvern experiment. It is worth noting that the variations of diameter were reversible. Larger variations under magnetic hyperthermia would be required to produce a stronger response of the thermosensitive PNIPAM shell. Two options would be possible: concentrating the sample or improving its heating

properties. IONPs synthesized by the polyol pathway and presenting strong SARs (as presented in the **Chapter II**) were sent for chemical modification.

5. Magnetic and thermo-sensitive microgels

A collaboration with the team of Pr. Laurent Billon (Université de Pau et des Pays de L'Adour, Equipe de Physique et Chimie des Polymères, Pau, France) led to the measurement of magnetic and thermosensitive microgels. Smart oligo(ethylene glycol)-based microgels loaded with magnetic IONPs were received.[20, 21] They were analyzed with the DLF/MH set-up to observe their thermosensitive response under magnetic hyperthermia. As for the precedent section, the sample had to be concentrated in order to produce larger variations of temperature under MH.

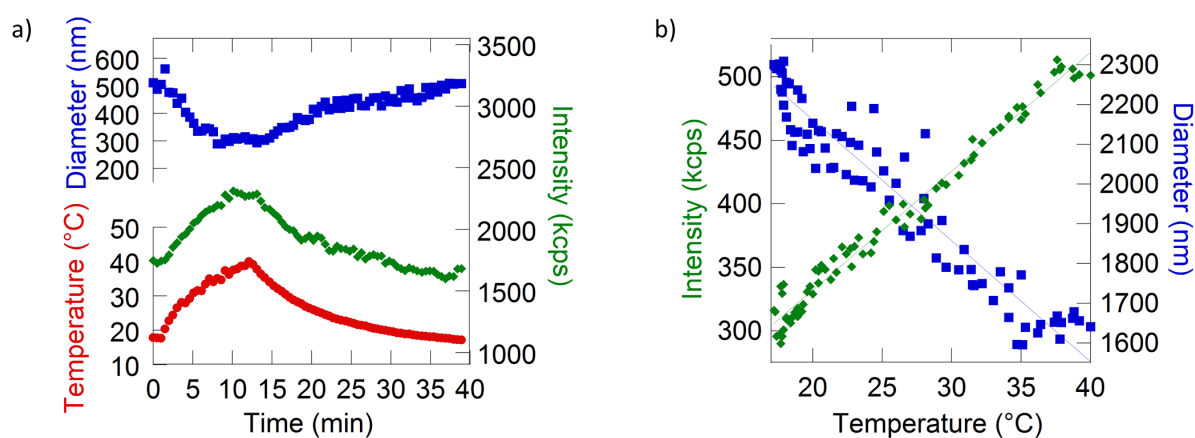


Figure 9 *in situ* DLS/MH results obtained for the MB106 sample with an IONP feed weight ratio of 20% relatively to copolymer. Hydrodynamic diameters measured by 2nd order cumulant analysis (blue squares), backscattered light intensity on the photodetector (green diamonds) and temperature (red circles) measured by the optic fiber probe were recorded and plotted vs. time (a). Hydrodynamic diameter (blue squares) and backscattered intensity (green diamonds) plotted vs. temperature (b). Iron oxide concentration was 9.0 g·L⁻¹, with a pH value of 6.1.

When the radiofrequency magnetic field was applied, heat was generated by the magnetic IONPs, resulting in an increase in temperature first in their direct vicinity, and then following diffusion of heat into the bulk solution, measured by the optical fiber (**Figure 9 a**). The magnetic microgels exhibited a volume transition as shown by the variations of their hydrodynamic diameter. This system exhibited a high level of reversibility: when the radiofrequency magnetic field was switched off, the hydrodynamic diameter returned back to its initial value around 500 nm. Concomitantly, a reversible variation of backscattered intensity was observed. Another way to represent the results of this experiment consists in eliminating the time variable that is plotting the diameter and intensity vs. temperature measured by the optical fiber.

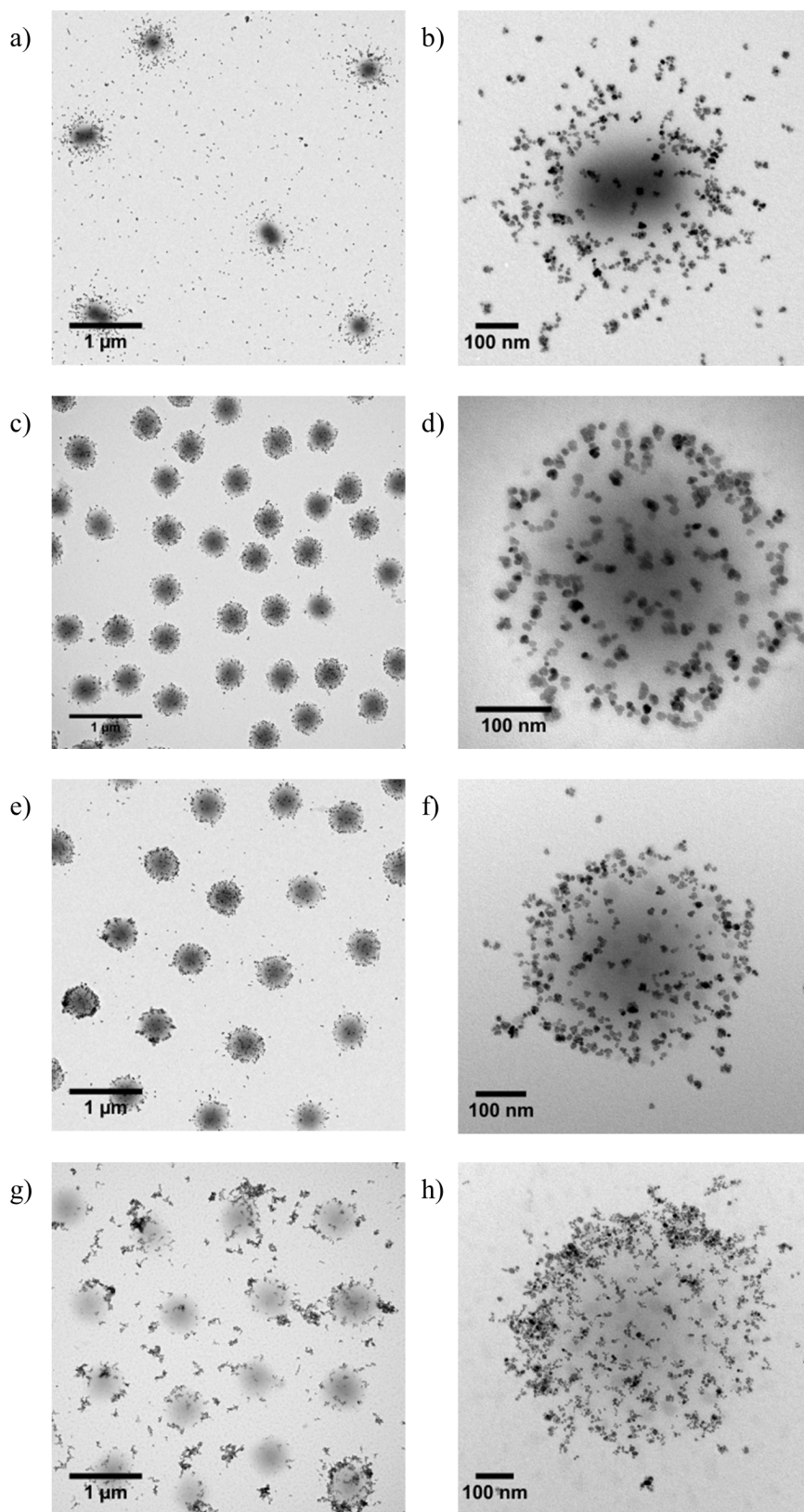


Figure 10 TEM micrographs of microgels loaded with IONPs. **a,b)** MB87, **c,d)** MB100, **e,f)** MB108, **g,h)** MBMBA.

As shown on **Figure 9 b**, both the hydrodynamic diameter and the backscattered intensity were directly correlated to the macroscopic temperature measured by the optical fiber probe. The SAR of the microgels was estimated to be of $37 \text{ W}\cdot\text{g}^{-1}$ of iron oxide or $7 \text{ W}\cdot\text{g}^{-1}$ when considering the whole mass of material (polymer comprised).

Following this encouraging experiment empty microgels were received. They were obtained by precipitation copolymerization of oligo(ethylene glycol) methyl ether methacrylate, di(ethylene glycol) methyl ether methacrylate, oligo(ethylene glycol)diacrylate and methacrylic acid. They were loaded with IONPs produced by the polyol pathway (as presented in **Chapter II**) in order to improve the heating properties of the microgels under magnetic hyperthermia and their thermal response. To do so, IONPs with a SAR of $170 \text{ W}\cdot\text{g}^{-1}$ and a diameter of 10 nm and microgels were simply mixed overnight. The magnetic microgels were imaged by TEM, and noticeable differences between samples could be observed (**Figure 10**). The IONPs were well visible and co-localized on the grid with the microgels. They were located on the periphery of the microgels, as they hardly diffuse through the cross-reticulated material. These images brought information about the density of the gels. A dense material resulted in a darker area of the image. Some micro-gels exhibited a gradient of density, with a dense core and a lighter periphery, while others exhibited homogeneous grey shades. These morphologies were clearly dependent on the polymers used for their precipitation polymerization. These samples were measured by small angle neutron scattering coupled with magnetic hyperthermia to provide complementary information to the DLS coupled with magnetic hyperthermia. The samples were prepared in deuterated water to ensure a good contrast with the polymers of the microgels. They were heated by magnetic hyperthermia using similar amplitude and frequency as for the previous DLS experiment. Their neutron scattering patterns were analyzed, evidencing a change of conformation of the microgels under application of a magnetic field. This project is still ongoing as the data were extremely difficult to analyze and necessitated models to interpret the variations of scattering distances in the material, the density of cross-reticulation, the gradient of loading of IONPs, and gradient of density of the microgels. To the best of our knowledge, it is the first time that scientists coupled SANS with MH, making it a world premiere.

6. Iron oxide nanoparticles grafted with PDMAEMA

Superparamagnetic IONPs were prepared by the co-precipitation of ferrous and ferric salts, as described in the **Chapter II**. They were functionalized with an aminosilane using a sol-gel route, followed by addition of a hetero-crosslinker containing an azide. Finally the thermo-sensitive poly[2-(dimethylamino)ethyl methacrylate] (PDMAEMA) terminated with an alkyne was conjugated with the IONPs with an azide-alkyne cycloaddition reaction in a click-chemistry strategy.

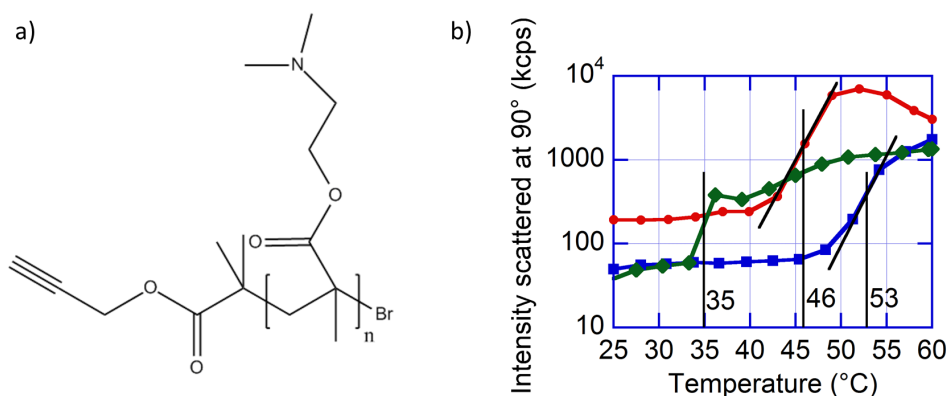


Figure 11 a) Molecular structure of PDMAEMA. **b)** Determination of the cloud point of PDMAEMA by DLS at 90° in solutions at 35°C at a concentration of $3\text{ mg}\cdot\text{mL}^{-1}$ at pH 5 (diamonds), near 53°C for $10\text{ mg}\cdot\text{mL}^{-1}$ at pH 7 (squares), and 46°C for $20\text{ mg}\cdot\text{mL}^{-1}$ at pH 7 (circles). The decrease in scattered light intensity for temperatures above 50°C for $20\text{ mg}\cdot\text{mL}^{-1}$ at pH 7 denotes a macroscopic phase-separation (coacervation) and sedimentation.

The solution behavior of PDMAEMA chains in water is known to be both thermo- and pH-sensitive. Tertiary amines of the PDMAEMA chains (**Figure 11 a**) were characterized by their respective value of the logarithmic constant of dissociation (pKa). From the Henderson-Hasselbalch equation, it was possible to plot the relative percentages of both species, depending on solution pH. At pH lower than their pKa, amines were protonated, whereas they were un-protonated and un-charged at pH higher than the pKa of 9.5, as determined in **Chapter III**. This pKa value appeared relatively lower than usual for amines, but the proximity of charges along a polymer backbone was not thermodynamically favorable, and lowered the apparent pKa of PDMAEMA. It is also known from its Flory-Huggins phase diagram that PDMAEMA chains become insoluble in water above their cloud point and that this cloud point becomes lower when the polymer concentration increases, tending towards a limit called the “lower consolute transition temperature” or “lower critical solution temperature” (LCST). In the case of PDMAEMA, the cloud point critically depended not only on concentration but also on pH[22] and on the polymer length and architecture (linear vs. branched chains).[23] The **Figure 11 b** illustrates this variation of the cloud point at different values of concentration and pH, either below (pH 5) or near (pH 7) the pKa of the amines.

Figure 12 a shows the variation of the derived count rate of scattered light and of the Z-average diameter of polymer-grafted IONPs over varying temperatures. Like PDMAEMA chains in solution, the shell of the grafted IONPs, mainly composed of this polymer, dehydrated at elevated temperature, resulting in a variation of both their scattered light intensity and hydrodynamic diameter. However, unlike polymer chains in solution, which usually exhibit an abrupt transition over a narrow range of temperatures (defined as the “cloud point”), for these thermo-sensitive nano-objects the variation appeared continuous and spanned a broader range of temperatures. Nevertheless, a transition

temperature could still be deduced from the inflection point of the scattered light intensity vs. temperature curve.

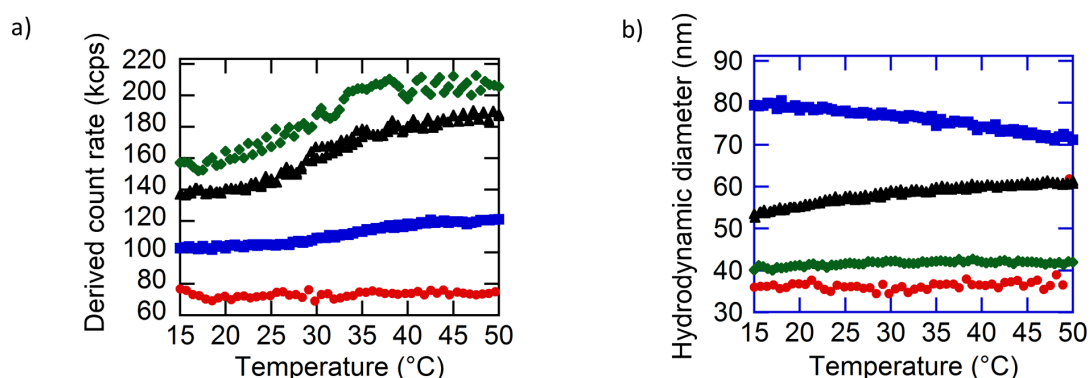


Figure 12 Off-line DLS results on bare acidic IONPs (circles), and on three batches of IONPs@AEAPTMS-AZ-PDMAEMA differing by the inorganic core sizes ($\sim 0.1 \text{ g L}^{-1}$ iron oxide): S1S2 (squares), C1C2 (diamonds) and C1S2 (triangles). **a)** The scattered intensity and **b)** the Z-average diameter are plotted vs. temperature. The pH was adjusted to 5.3 (below pKa of PDMAEMA) to maintain the IONPs well dispersed while still exhibiting a LCST behaviour.

This inflection point was located between 30 and 35 °C for the three grafted IONPs, which was close to the cloud point determined at 35 °C on a solution of PDMAEMA chains at $3 \text{ mg}\cdot\text{mL}^{-1}$ in pH 5 buffer (**Figure 11 b**). It was also close to the value of 38 °C reported in literature[22] for chains PDMAEMA of similar length ($DP=85$) at $1 \text{ mg}\cdot\text{mL}^{-1}$ but above the pKa (pH=11). Therefore it can be concluded that the thermal transition of the chains grafted at the iron oxide surface have a direct influence on the colloidal state of the core-shell IONPs. Usually an increase in derived count rate accompanies an increase of hydrodynamic diameter, the scattered intensity being proportional to the sixth power of the size of the IONPs (or aggregates) in the Rayleigh approximation. However, the present samples did not show any sign of aggregation and the evolution of hydrodynamic diameter with temperature was different depending on the iron oxide core sizes. It decreased by $\sim 10 \text{ nm}$ for S1S2 between 15 and 50 °C, increased by $\sim 10 \text{ nm}$ for C1S2, and remained almost constant for C1C2. In comparison, the bare S1S2 cores without the thermosensitive shell exhibited both constant scattered intensity and hydrodynamic diameter over the whole temperature range. The increase in derived count rate for all the polymer-grafted IONPs was tentatively explained by the dehydration of the outer shell, resulting in stronger light scattering contrast and a higher intensity collected at either 90° or 173° from the incident laser beam.

In order to fully demonstrate that IONPs with a magnetic core and a thermosensitive PDMAEMA corona were required in order to obtain a variation of hydrodynamic size under a RF magnetic field, complementary experiments of in situ DLS under an applied RF magnetic field were carried on with non-thermosensitive and non-magnetic polystyrene latexes (**Figure 13**). For these

particles, no increase of temperature was observed under an applied RF magnetic field, suggesting that no parasitic heating ascribed to Joule or eddy current effects occurred in the experimental system in the absence of magnetic IONPs. Apart from experimental noise, the recorded diameters and intensities were also constant over time for the application of different magnetic field intensities.

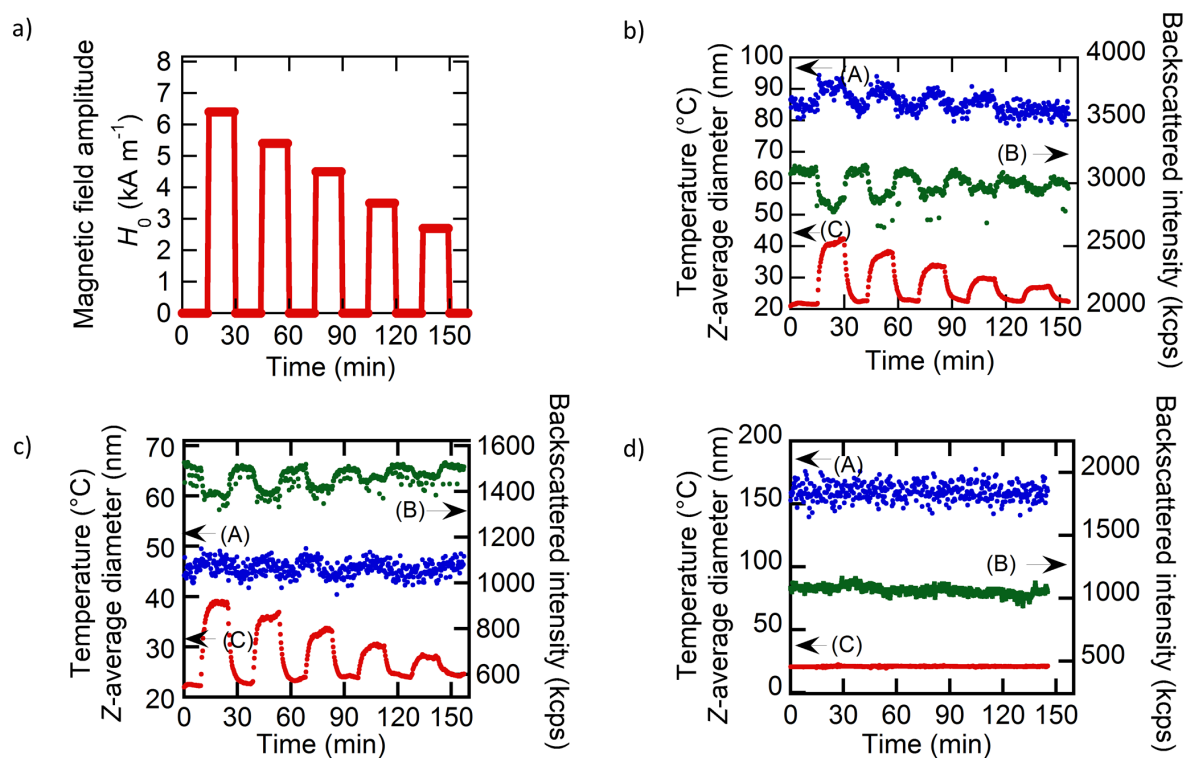


Figure 13 a) Magnetic field intensity vs. time profile (at 755 kHz radiofrequency) applied to the sample and controls. In situ DLS/MH results (at $\sim 1 \text{ g L}^{-1}$ iron oxide) obtained for: **b)** the C1C2@AEPTMS-AZ-PDMAEMA coated sample, **c)** the uncoated non-thermosensitive C1C2@AEPTMS control (both sample and control had a pH adjusted to 5.3-5.4), and **d)** polystyrene latexes as a non-magnetic non-thermosensitive control. The arrows indicate which axis to consider as ordinate for: the Z-average hydrodynamic diameter as measured by 2nd order cumulant analysis (A); the scattered light intensity on the photodetector (kcps) (B) and the temperature ($^{\circ}\text{C}$) measured by the fibre optic probe versus time (C).

The comparison of the results of in situ DLS under RF magnetic field of C1C2@AEPTMS-AZ-PDMAEMA magnetic and thermo-sensitive IONPs, of C1C2@AEPTMS, magnetic but not thermo-sensitive IONPs, and of non-magnetic and non-thermosensitive polystyrene latexes highlighted that the variations of hydrodynamic diameters observed in the first case were specific to the thermo-sensitivity of the polymer shell and to the magnetic field-induced hyperthermia. Regarding the variations of backscattered intensity observed for magnetic IONPs (without polymer) but not for non-magnetic latexes, this phenomenon could be ascribed to the magnetic dichroism (also called ‘Faraday rotation’) inherent of magnetic IONPs. Due to a direct coupling between the magnetic moments of the IONPs aligned by the magnetic field and their optical anisotropy axis when a longitudinal magnetic field was applied (i.e. oriented parallel to the incident beam), the polarization of

light rotated by an angle θ_F as measured in transmission through the sample or in reflection. This angle proportional to the field intensity could be as high as 15° cm^{-1} at 633 nm at high magnetic field (saturated moments) and changed in sign with the field direction.[28] Although we cannot exclude such direct influence of the magnetic field on the optical detection during in situ DLS measurement under RF magnetic field, we did not observe a variation of the backscattered intensity on any of the IONPs used under a static magnetic field.

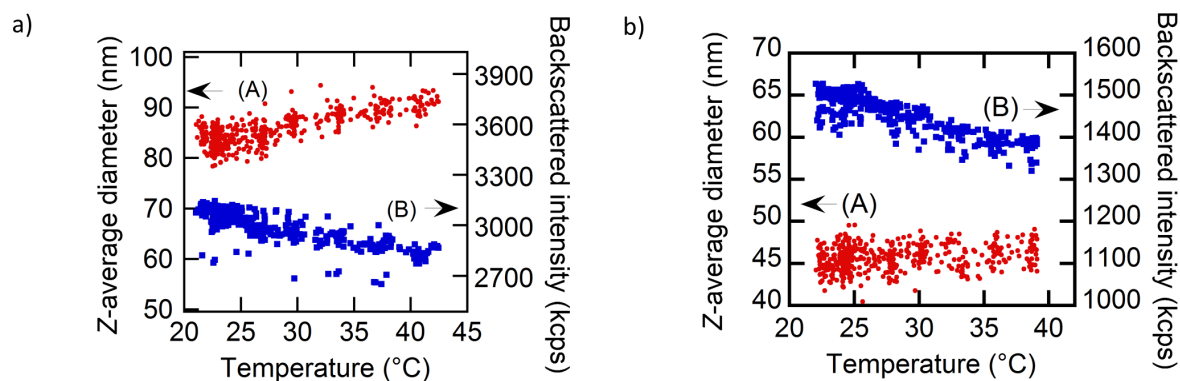


Figure 14 (A) Hydrodynamic diameter and (B) backscattered intensity plotted vs. temperature for **a)** the thermosensitive sample C1C2@AEAPTMS-AZ-PDMAEMA and **b)** the C1C2@AEAPTMS control, under an alternating magnetic field of intensity $H_0=6.4 \text{ kA}\cdot\text{m}^{-1}$ and frequency $f=755 \text{ kHz}$. Iron oxide concentrations were $\sim 1 \text{ g}\cdot\text{L}^{-1}$ and pH adjusted to 5.3-5.4.

Another way to represent the results of these experiments involved the elimination of the time variable and the plotting of diameter and intensity vs. temperature measured by the fiber optic, for the PDMAEMA-coated and uncoated IONPs (**Figure 14**). This showed that both the hydrodynamic diameter (**Figure 14 a**) (A)) and the backscattered intensity (**Figure 14 a**) (B)) were directly correlated to the *macroscopic temperature* for the thermo-sensitive IONPs but only the intensity (**Figure 14 b**) (B)), not the diameter (**Figure 14 b**) (A)), for the control uncoated IONPs. With the PDMAEMA shell undergoing a transition from a hydrophilic to a hydrophobic state, the IONPs exhibited transient variations of their hydrodynamic diameter directly correlated with the applied field intensity. This thermal sensitivity was particularly high around 30°C , *i.e.* near the thermal transition of PDMAEMA. The system demonstrated a high level of reversibility; when the radiofrequency magnetic field was switched off, the hydrodynamic diameter returned back to its initial value around 82 nm. Concomitantly, a reversible variation of intensity was also observed, with a short characteristic time ($\sim 1.5 \text{ min}$). However, the backscattered intensity surprisingly decreased when the field was applied, which was contrary to what was expected from the off-line DLS curve vs. temperature (**Figure 12 a**). Usually a destabilization of a colloidal dispersion induced large aggregates that scattered incoming laser light more intensely, because the scattered light intensity is proportional to the sixth-power of the diameter (in Rayleigh's approximation). Here the colloidal stability was ensured by electro-steric

repulsion. Therefore the diameter increased (by 10 nm at most) could more likely be attributed to a decrease in the entropic component (present only when chains are swollen by water) and the IONPs remained stable due to electrostatic repulsions. The formed aggregates must also have been very loose; otherwise the scattered intensity would have increased. Interestingly, the backscattered intensity showed rapid variations with applied magnetic field intensity, meaning that the intensity curve (B) had a characteristic time of ~ 1.5 min comparable to the temperature curve (C) and was lower than the curve of diameter (A) showing few minutes of inertia.

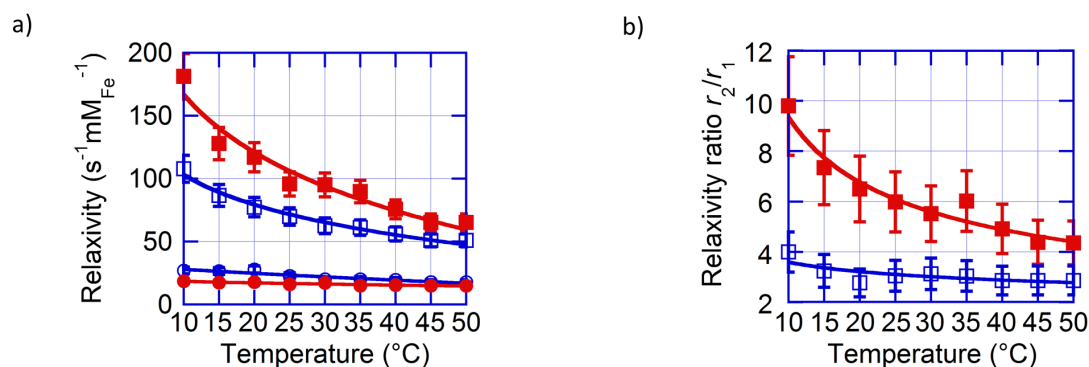


Figure 15 a) Longitudinal r_1 (circles) and transverse r_2 (squares) relaxivities of protons for uncoated S1S2 control-IONPs (empty markers) and thermosensitive S1S2@AEAPTMS-AZ-PDMAEMA coated-NPs (filled markers). **b)** r_2/r_1 relaxivity ratios for S1S2 control-IONPs (empty squares) and S1S2@AEAPTMS-AZ-PDMAEMA coated-NPs (filled squares). The solid lines are power law fits not based on a physical model.

Water proton relaxivity measurements were performed at different temperatures from 10 to 50 $^{\circ}C$ for samples containing uncoated S1S2 superparamagnetic IONPs and S1S2@AEAPTMS-AZ-PDMAEMA coated-IONPs. **(Figure 15)** showed a comparison of the results and the effect of the thermosensitive polymer shell. First, it was observed that the relaxivities obtained were similar to the ones exhibited at the clinical field of 0.47 T (frequency of 20 MHz) and physiological temperature by commercial superparamagnetic MRI contrast agents such as Ferridex[®] ($r_2=98 s^{-1}mM_{Fe}^{-1}$ and $r_1=24 s^{-1}mM_{Fe}^{-1}$, $r_2/r_1=4$) or Resovist[®] ($r_2=151 s^{-1}mM_{Fe}^{-1}$ and $r_1=25 s^{-1}mM_{Fe}^{-1}$, $r_2/r_1=6$).[24] It is generally described in MRI textbooks that the r_2/r_1 ratio determines whether superparamagnetic IONPs are best suited as positive contrast agents (with T_1 -weighted imaging sequences) or negative contrast agents (with T_2 -weighted imaging sequences). The solutions of the Bloch equations for the relaxation of the longitudinal (M_z) and transverse (M_{xy}) magnetization components to their equilibrium state indeed lead to a MRI signal that is proportional to the proton density of the solutions or tissues and to the product $(1 - e^{-TR/T_1}) \cdot e^{-TE/T_2}$, where TR is the repetition or read-out time of the sequence, and TE the inter-echo time. Thus, the sample signal becomes brighter than pure water when T_1 relaxation is accelerated while the T_2 -effect is not already dominant (since the MRI signal is detected by an antenna in the transverse plane). Here, the uncoated magnetic IONPs with a relatively low ratio $r_2/r_1=3$ could be used

as positive (T_1 -type) contrast agents, while the PDMAEMA-coated contrast agents presented a T_2 -type behavior at low temperature ($r_2/r_1=6$ at 25°C) that decreased above the LCST ($r_2/r_1=4$ at 50°C) (**Figure 15 b**). It is noteworthy that the r_2/r_1 ratio remained relatively constant over the whole tested temperature range for the control uncoated IONPs, as both r_1 and r_2 decreased with temperature, but their thermal behavior was dictated solely by the variation of water diffusivity with temperature.[12] On the contrary, the r_2/r_1 ratio varied by a factor greater than 2 for the PDMAEMA-coated IONPs, which proved that the temperature responsiveness of the shell was dominant. A similar two-fold decrease of the relaxometric ratio over an even more narrow temperature range (15°C) with liposomes encapsulating a paramagnetic compound was proposed by Terreno et al. to obtain an MRI response independent of concentration but dependent on pH or temperature.[25] In the studied case, the PDMAEMA shell was hydrated at low temperature and shrunk at higher temperature, particularly above the LCST. While the two samples were very different at 10°C (the coated and uncoated IONPs behaving respectively as negative and positive contrast agents), they became more similar at 50°C . Several studies have proven that partial aggregation of superparamagnetic IONPs is a means to increase their T_2 -type behavior. The fact that during the multiple steps of synthesis the colloidal stability of the IONPs was disturbed could explain this difference. For the thermal behavior, a simple explanation can be given in the context of the so called “outer sphere” mechanism. For superparamagnetic MRI contrast agents, r_2 is determined by three parameters only:[26] the specific magnetization M_v , the internal magnetic volume fraction in the IONP, and the “relaxometric size”, defined as the minimum approach distance between water protons and the surface of the MNP. In the case of the magnetic core-shell PDMAEMA-coated IONPs, these parameters were almost the same as for the uncoated particles when the polymer brush was swollen by water. However, when the polymer brush became dehydrated and collapsed at the surface of the iron oxide core, it formed a layer impermeable to water molecules, which at the same time lowered the average magnetization of the particle (since the polymer layer is not magnetic) and increased the relaxometric size, thereby lowering the transverse relaxivity r_2 in a greater extent than r_1 . To conclude, these iron oxide cores were wrapped by a PDMAEMA shell that was highly hydrated below the LCST and impermeable to water molecules above it, and behaved exactly like other thermosensitive MRI contrast agents recently described by Hannecart et al., with PDMAEMA instead of JeffamineTM as a grafted thermosensitive brush.[12]

In this section, the synthesis of magnetic IONPs comprising an iron oxide core and thermosensitive polymer shell exhibiting reversible size variation when subjected either to macroscopic heating or magnetic heating induced by a radiofrequency magnetic field was described. These PDMAEMA coated magnetic IONPs could be used as MRI contrast agents, with a transition from a purely negative (T_2 -type) contrast at low temperature to a less efficient T_2 -type contrast at high

temperature but also potentially positive (T1-type), due to a lower r_2/r_1 relaxivity ratio. An experiment that enabled in situ DLS under RF magnetic heating by placing a fibre-based backscattering remote-head DLS as close as possible to the inductor coil of the MH generator was specially designed. The hydrodynamic diameters and the backscattered intensity of coated magnetic IONPs and of uncoated (control) IONPs were monitored on-line during the treatment with the RF magnetic field. It was found that the hydrodynamic diameter and the backscattered intensity correlated well with the macroscopic temperature changes measured independently by standard fiber optic thermometry. These results are promising as they show for the first time that the size variation of IONPs can be measured without switching off the magnetic field, which is important as the swelling/collapsing response time of a polymer brush has very fast kinetics. In the next work (**Section 7**), the RF magnetic field application was extended to higher powers via the replacement of metallic parts in the remote head of the DLS setup. This may enable further insights into the mechanisms of heat generation and dissipation by magnetic IONPs at the scale of the polymer shell, less than 10 nm. The temperature profile in the close vicinity of IONPs is an intensively debated question in view of the standardization and optimization of medical magnetic hyperthermia and magnetic-field triggered drug delivery. In addition, the same in situ DLS methodology can be applied to study other kinds of thermogenic NPs such as plasmonic NPs under visible or near-infrared illumination.

7. Iron oxide nanoparticles grafted with a single block (VPGIG)₂₀ elastin-like polypeptide

The (VPGIG)₂₀ (referred to as ELP₂₀) was the first ELP to be grafted onto IONPs during this project. Grafting conditions were then later improved for the grafting of the diblock ELP.

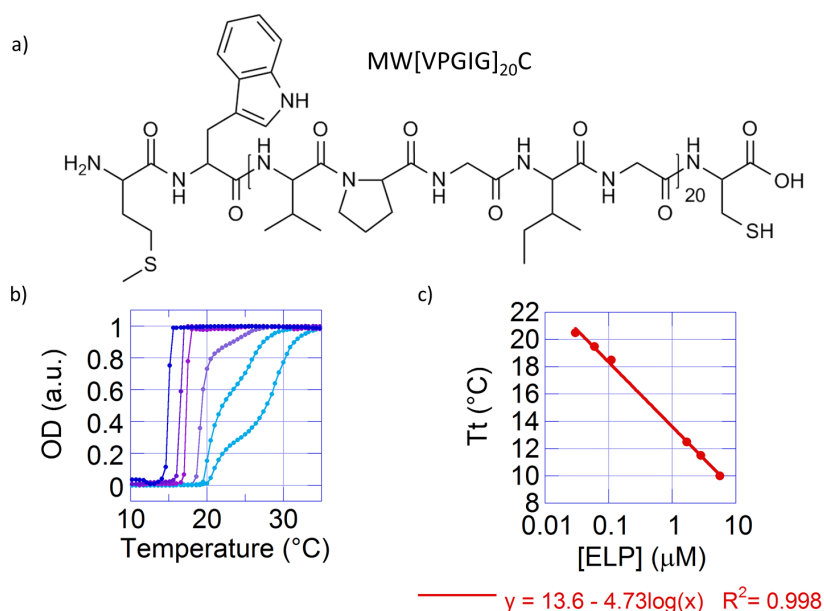


Figure 16 a) Molecular structure of the single block ELP₂₀, exhibiting a cysteine amino acid at its C-terminal end. **b)** Turbidity measurement of the ELP₂₀ dispersed in PB as a function of concentration. **c)** Onset of the temperature transition versus ELP₂₀ concentration.

The ELP (VPGIG)₂₀ is a relatively short ELP, with a molecular weight of 8.9 kg mol⁻¹ (**Figure 16 a**), which would normally guarantee a transition temperature (Tt) above room temperature. However, because of the highly hydrophobic isoleucine guest residue, the hydrophilicity of the overall bio-macromolecule was rather poor. This observation was in accordance with the pioneer work of Urry.[27] The (VPGIG)₂₀ Tt vs. concentration in PB was determined by measuring the optical density of the solutions at 350 nm using temperature trends. The results were normalized and plotted on a single graph (**Figure 16 b**). The cloud point was determined by the temperature at the onset of the curves. Tt values were reported as a function of concentration (**Figure 16 c**), and the experimental curve was perfectly fitted with the empirical equation established by Chilkoti *et al.*: [28]

T_t transition temperature

$T_{t,c}$ transition temperature at the critical point

k constant

L chain length in pentapeptide units

C_c concentration at the critical point

C concentration

$$T_t = T_{t,c} + \frac{k}{L} \cdot \ln \frac{C_c}{C}$$

The parameters k , C_c and T_c could have been accessible by multivariate regression of a library of ELPs (VPGIG)_L with different chain lengths L . It was not the purpose of this study. The ELP₂₀ was grafted onto IONPs with different grafting densities, as described in **Chapter III Section III**. The magnetic and thermosensitive properties of the resulting core-shell nanoparticles were then evaluated. The very low T_t of the ELP₂₀ unfortunately impeded the characterization by DLS coupled with magnetic hyperthermia. The nanoparticles were thus only analyzed using a DLS Malvern instrument, meaning that the solutions were macroscopically heated thanks to an external heating/cooling system (Peltier).

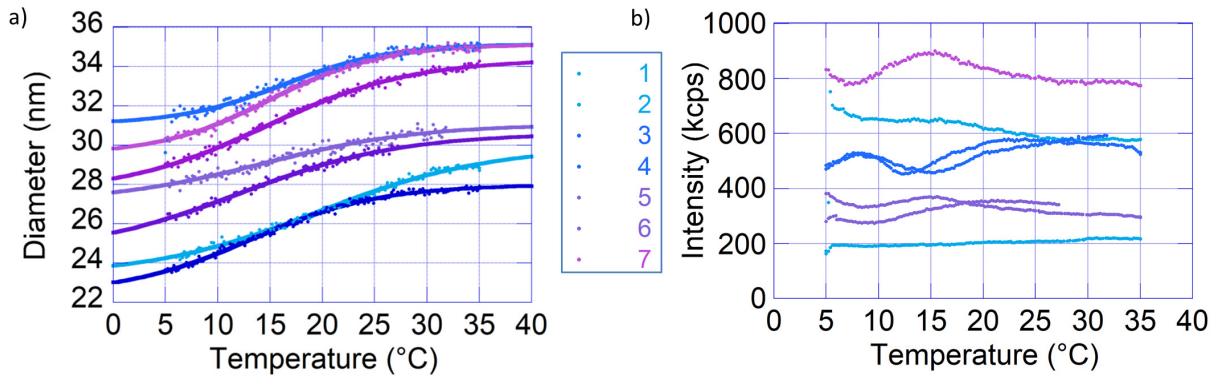


Figure 17 a) Diameter and b) intensity versus temperature of IONPs grafted with different densities of ELP (VPGIG)₂₀.

Measurements were carried from 5 to 35 °C in order to observe a variation over a large enough range of temperature (**Figure 17**). The resulting measurement of diameter versus temperature was quite surprising. On a simplistic point of view, the nanoparticles were expected to diminish in size as the brush of ELP was supposed to dehydrate over the T_t . Here the contrary was observed when increasing the temperature. Several hypotheses could be made to describe this phenomenon: the nanoparticles were stabilized only by steric repulsions, when the shell dehydrated, the brush collapsed, resulting in a loss of stability. Said differently, the ELPs underwent a change from swollen to dehydrated, meaning that the surfaces of the nanoparticles became hydrophobic. This loss of affinity

toward the solvent resulted in a loss of stability, as the attractive forces (magnetic dipolar attraction, Van der Waals forces) overbalanced the repulsive forces (nearly non-existent electrostatic forces, steric stabilization). The increase of diameter would then not be attributed to the direct variation of the conformation of the brush which was collapsing but to its consequence: the aggregation of nanoparticles. The curves of diameter versus temperature had sigmoidal shapes. In general this system proved to be difficult to work with. The starting temperature of measurement of 5 °C was the lowest guaranteed by the manufacturer of the DLS instrument. A flow of gaseous nitrogen had to be used to fill the sample holder and prevent a condensation of water on the quartz cuvette. Samples rapidly proved to be unstable when stored at room temperature and had to be kept in the fridge or in an ice bath when transported. The chemistry was over-complicated and relying on a multi-step modification of the surface of the IONPs. The characterization was tedious, and the application uncertain. This first experience with ELPs helped develop a new convergent chemistry approach. New ELPs were tried out with di-block morphologies, allowing one block to undergo a conformation change while the other block kept stabilizing the IONPs. Also the T_t was selected to be more relevant for biomedical applications, at least superior to room temperature. These results are described in **Section 8**.

8. Iron oxide nanoparticles grafted with diblock ELPs

We next grafted diblock ELPs with the aim of obtaining IONPs for cellular internalization and cell death by MH.

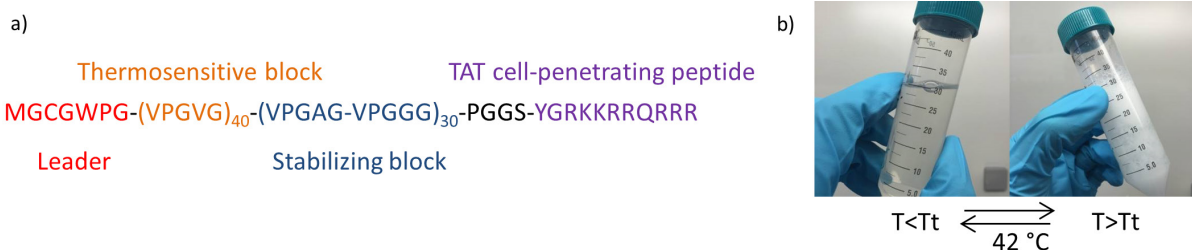


Figure 18 a) Diblock structure of the ELP grafted on the IONPs. **b)** Solubility transition of the diblock ELP upon heating and cooling of the solution.

The ELP diblock used for this work was designed to contain a thermosensitive block (VPGVG)₄₀ (represented in orange) undergoing a de-swelling transition at a critical temperature around 42 °C in solution (**Figure 18 b**), and a hydrophilic block (VPG(A/G)G)₆₀ (represented in blue) to provide colloidal stability to the resulting IONPs@ELP_{40-60-Tat} core-shell nanoparticles (**Figure 18 a**). The ELP sequence was preceded by a leader sequence (represented in red) featuring a cysteine residue that was used for the covalent conjugation onto IONPs. This ELP_{40-60-Tat} was also side terminated with a cell-penetrating (CPP) Tat peptide (represented in purple) to help the internalization of the IONPs in cells (results presented in **Chapter IV**). This CPP was derived from the transactivator

of transcription (Tat) of human immunodeficiency virus (HIV).[29] IONPs used in this study were obtained following a polyol synthesis, leading to well-defined moncore morphologies and strong heating properties under an alternating magnetic field (AMF). The biofunctionalization of the magnetic IONPs cores with the diblock ELPs was achieved *via* a convergent strategy through the strong coordination bonding of a phosphonate group introduced near the N-terminus of the diblock ELP.

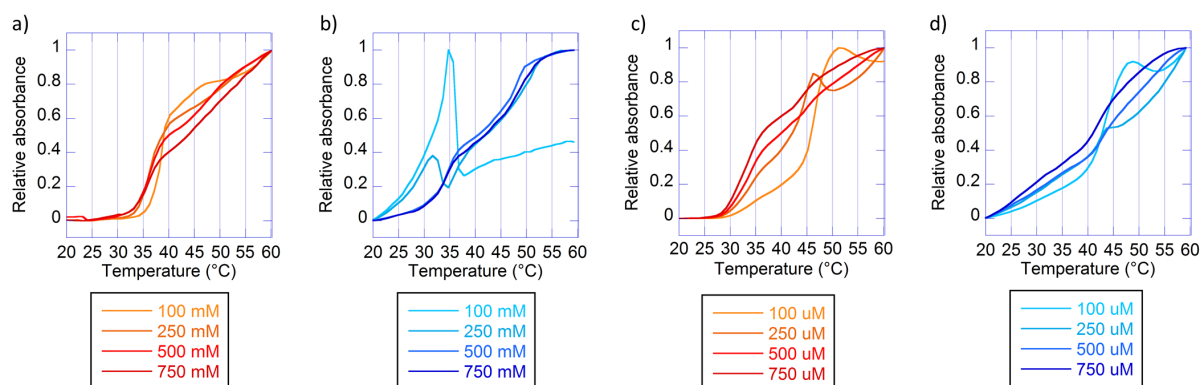


Figure 19 a) Turbidity measurement when heating and b) cooling a solution of the diblock ELP_{40-60-Tat} and when c) heating and d) cooling a solution of the phosphonate group-containing diblock ELP*_{40-60-Tat}.

The critical micellar temperatures (CMT) vs. concentration in PB of the ELP_{40-60-Tat} and ELP*_{40-60-Tat} were determined by measuring the optical density of the solutions at 350 nm using temperature trends. The results were normalized and compiled in **Figure 19**. Transition temperatures of single-block ELPs from soluble unimers to insoluble coacervates are usually measured using the maximum of the first derivative of the turbidity versus temperature curve.[28] Here, as the variations of turbidity correspond to the self-assembly of diblock ELPs into micelles.[30] We used the onset of the curves as the minimum temperature required to induce a change of solubility of the (VPGVG)₄₀ hydrophobic block during heating experiments. Contrary to what was previously observed during Tt measurements of the (VPGIG)₂₀ mono-block ELP (**Figure 16 b-c**), the ELP and phosphonate modified ELP*_{40-60-Tat} had a CMT that was independent on concentration (**Figure 19 a**). Moreover, contrary to the sharp transitions that were observed with ELP₂₀, the variations of turbidity of ELP_{40-60-Tat} and ELP*_{40-60-Tat} were spread over large ranges of temperature from 30 to 60 °C. The CMT of the ELP_{40-60-Tat} was determined to be at 33 °C, while the CMT of the ELP*_{40-60-Tat} was estimated to be at 30 °C, slightly shifted towards lower temperatures (**Figure 19 c**). This result was unexpected as the phosphonate anchor group was predicted to bring more hydrophilicity to the (VPGVG)₄₀ hydrophobic block. The cooling of ELP*_{40-60-Tat} gave a far more regular re-solvation (**Figure 19 d**) as opposed to what was observed with the bare ELP_{40-60-Tat}. This behavior of free chains in solution helped

anticipating the behavior of chains tethered at the surface of IONPs, with expected variations of diameter of the core-shell structure spread over a large range of temperature.

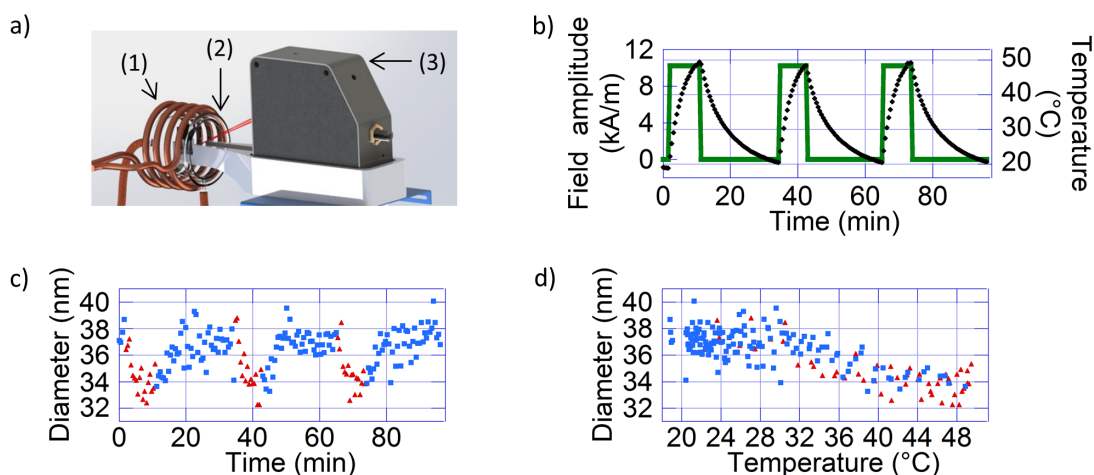


Figure 20 a) Illustration of the simultaneous DLS/MH experiment: the sample (IONP@ELP*_{40-60-Tat} dispersed in water) contained in a cuvette was placed in a 4-turn coil (1), and thermalized with a glass water-jacket (2) while DLS measurements were carried out with a remote head collecting the scattered intensity at a 165° angle (backscattering) (3). **b)** The temperature of the sample (black diamonds) was measured while magnetic field intensity profiles were applied (green circles). **c)** Variations of the hydrodynamic diameters (intensity averaged) were measured when the magnetic field was either on (red triangles) or off (blue squares). **d)** Hydrodynamic diameters were plotted against temperature when the magnetic field was either on (red triangles) or off (blue squares).

A radiofrequency power generator was connected to the induction coil (**Figure 20 a**). This generated a radiofrequency magnetic fields at a frequency $f=755$ kHz with a maximum field value of $10.2 \text{ kA}\cdot\text{m}^{-1}$. Superparamagnetic IONPs were stimulated when radiofrequency magnetic fields were applied, and generated heat, rising the temperature of the sample from 20 °C up to 50 °C as measured with an optical fiber probe (**Figure 20 b**). The temperature of the sample could be controlled by adjusting the application time of magnetic fields, although the increase of temperature was limited by heat diffusion after few minutes (typically 5-10 min). This phenomenon was due to the non-adiabatic conditions of measurement. When no radiofrequency magnetic fields were applied, the temperature of the sample stabilized back to 20 °C, which was the value set by the thermalizing glass water-jacket. Hydrodynamic diameters of IONPs in suspension were measured by DLS with a Vasco FlexTM backscattering remote head set-up. Variations of hydrodynamic diameters were observed during the experiment (**Figure 20 c-d**). They were ascribed to the thermosensitive property of the ELP*_{40-60-Tat} grafted on the surface of the IONPs. The heat produced by the IONPs under an AMF stimulus increased the temperature at the surface of the nanoparticles, and the shell dehydrated leading to a decrease of hydrodynamic diameters down to 34 nm. The hydrodynamic diameter slowly recovered to a baseline value of 37 nm along with temperature when no magnetic field was applied. Three cycles of measurement were successively performed to evidence the full-reversibility of this phenomenon.

Plotting these variations of hydrodynamic diameter vs. temperature removed the time-dependence of the data (**Figure 20 d**). These variations could be plotted against temperature (**Figure 20 d**), highlighting 3 different regimes. There was a first plateau of diameter at around 37 nm from 20 °C to approximately 30 °C. Then, the diameters gradually decreased in the range of temperature from 30 to 40 °C. A second plateau of diameter at around 34 nm was reached above 40 °C. Measurement of hydrodynamic diameters versus magnetic field application was then carried out in the same conditions on samples at different grafting densities. With expected differences of variation of diameter depending on the stretching of the chains tethered at the surface of the IONPs.

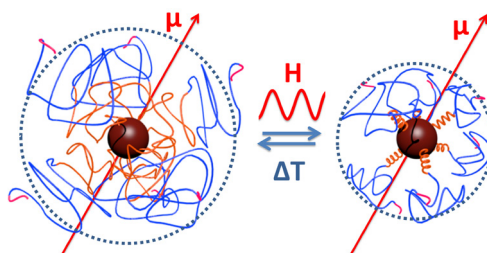


Figure 21 Reversible variations of the thickness of the ELP*_{40-60-Tat} shell under magnetic hyperthermia.

Variations of hydrodynamic diameters observed during DLS/MH experiments were ascribed to the thermosensitive property of the ELP*_{40-60-Tat} grafted onto the surface of the IONPs. During the DLS coupled with hyperthermia experiment, only the thermosensitive part of the ELP*_{40-60-Tat} dehydrated, the hydrophilic part being still swollen by water giving them steric stability at higher temperatures (**Figure 21**).

The magnetic hyperthermia coupled with DLS measurement was performed on samples at different reduced tethered densities Σ (**Figure 23 a-d**). These variations are reported in (**Figure 23 e**), which was constructed by averaging the diameters corresponding to the 10 lowest and 10 highest temperatures measured for each sample (**Figure 22**) and reporting these values as a function of Σ . The diameters at low and high temperature increase with the reduced tethered density, in accordance with the polymer physics model.[31-33] Indeed, as ELP*_{40-60-Tat} chains were tethered at higher grafting densities, the chains stretched, and the grafted layers changed from the mushroom to brush regime. Higher amplitudes of variation of diameters were also observed at higher Σ .

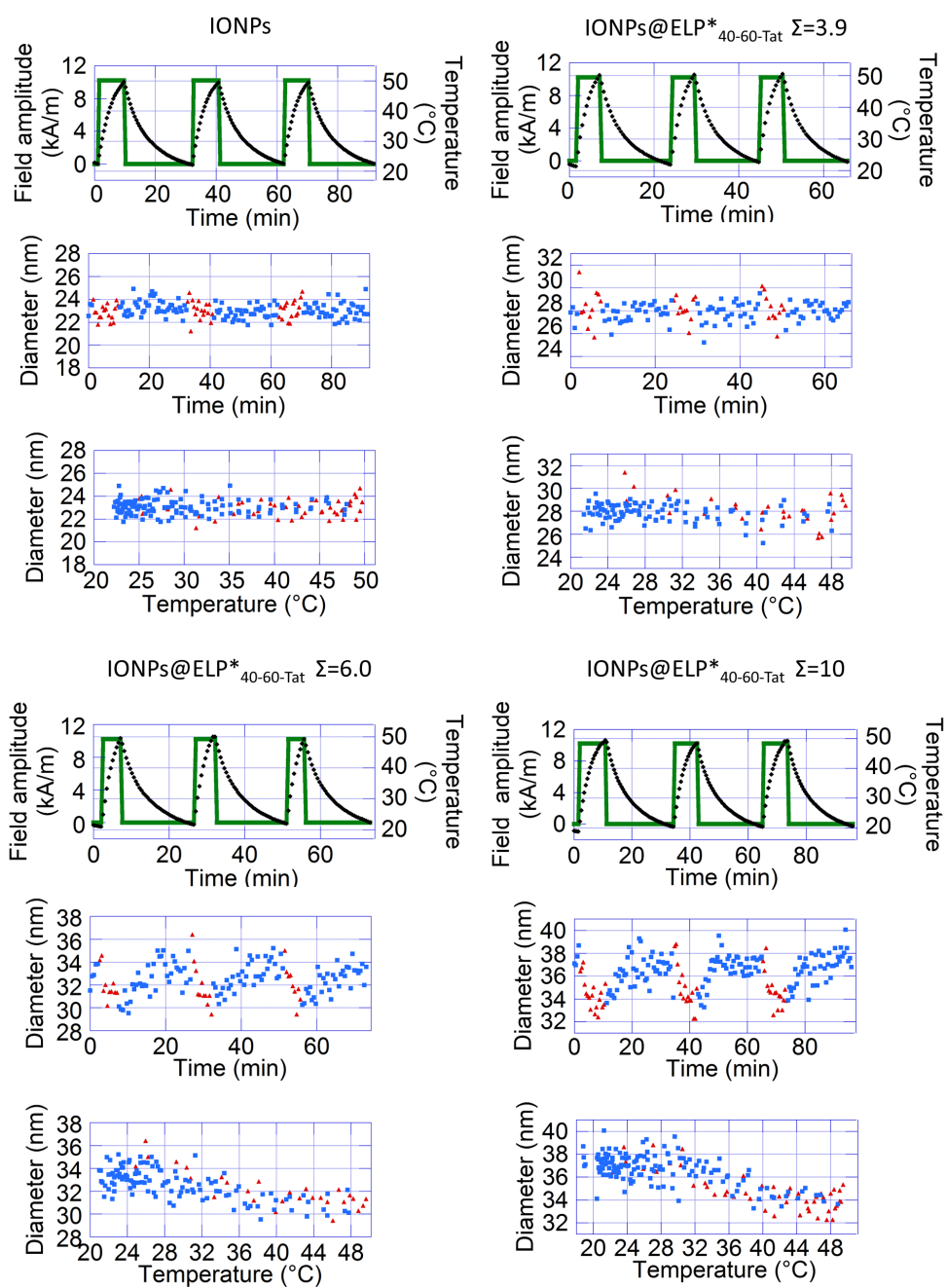


Figure 22 The Z-average hydrodynamic diameters of bare IONPs and grafted IONPs@ELP*_{40-60-TAT} ($\Sigma=3.9$, $\Sigma=6.0$, $\Sigma=10$) are plotted against temperature when the magnetic field is either on (red triangles) or off (blue squares).

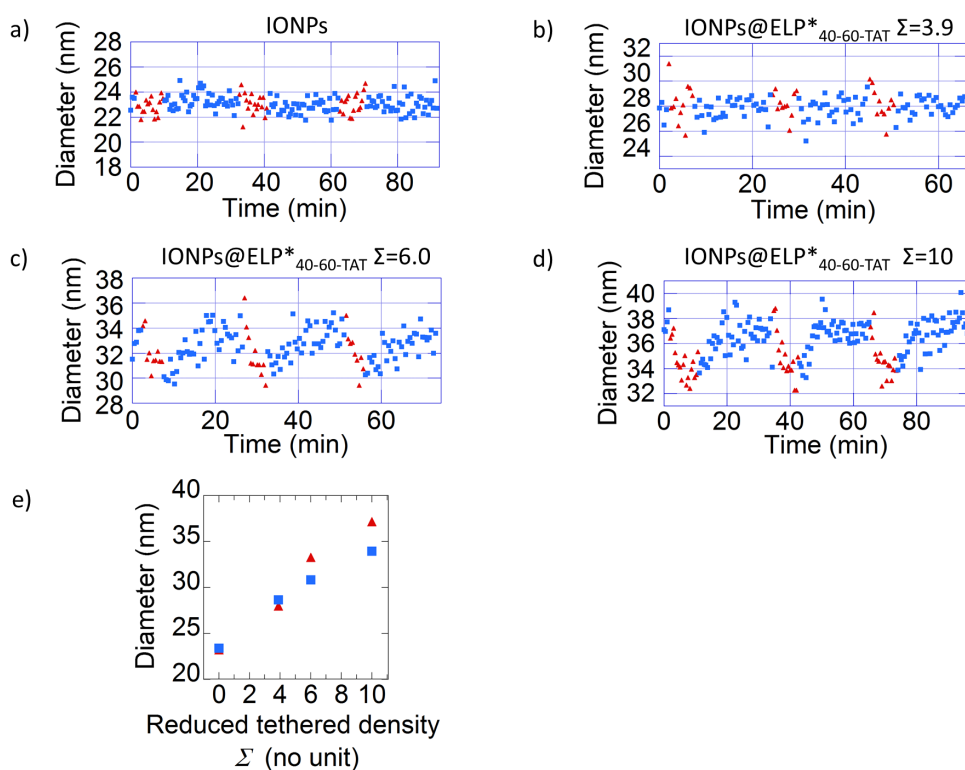


Figure 23 The average hydrodynamic diameters (in Intensity) of **a)** bare IONPs and grafted IONPs@ELP*_{40-60-Tat} at reduced densities **b)** $\Sigma=3.9$, **c)** $\Sigma=6.0$, **d)** $\Sigma=10$ are plotted against temperature when the magnetic field is either on (red triangles) or off (blue squares). **e)** The amplitudes of variations of diameter are plotted as a function of reduced density.

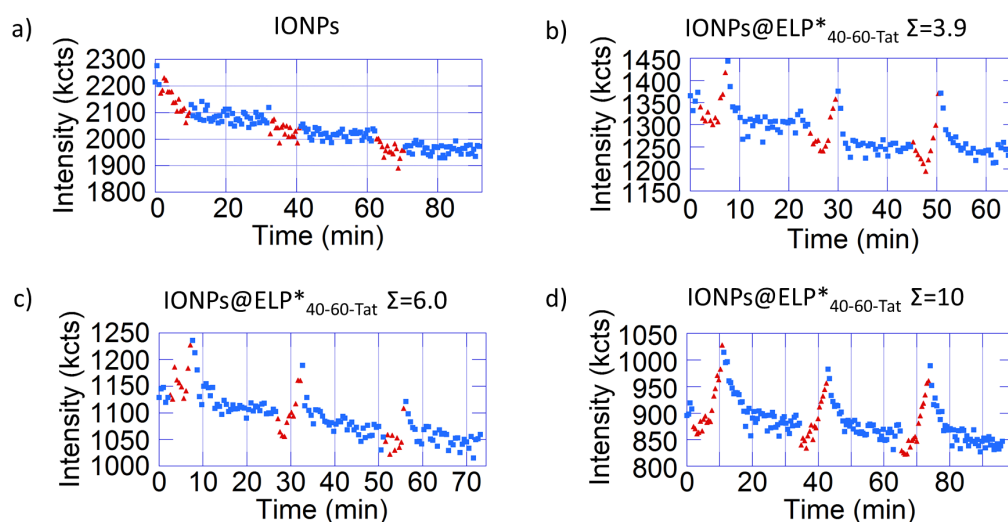


Figure 24 The backscattered intensities of **a)** bare IONPs and grafted IONPs@ELP*_{40-60-Tat} at reduced tethered densities **b)** $\Sigma=3.9$, **c)** $\Sigma=6.0$, **d)** $\Sigma=10$ are plotted against temperature when the magnetic field is either on (red triangles) or off (blue squares).

Intensities were also measured depending on the application of AMF. No noticeable variations of intensity were observed for the bare $\gamma\text{-Fe}_2\text{O}_3$ IONPs at field on (**Figure 24 a**), but for the grafted IONPs@ELP*_{40-60-Tat} intensities increased when applying a field (**Figure 24 b-d**). This increase could not be ascribed to an aggregation phenomenon because the diameters of the samples diminished upon application of an AMF. Another interpretation would be that when heated, part of the ELP*_{40-60-Tat} brushes dehydrated, leading to densification of the shells. This increase of contrast with the solvent explained the increase of backscattered light.

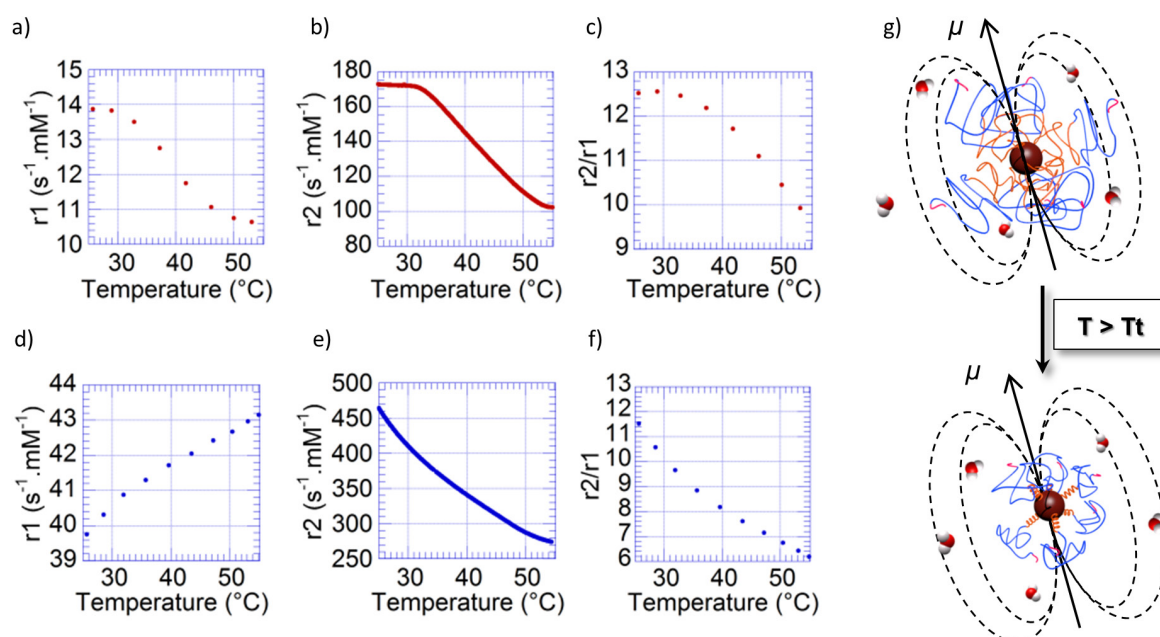


Figure 25 Proton nuclear magnetic relaxometry of water containing IONPs@ELP*_{40-60-Tat} ($\Sigma=10$). **a)** longitudinal and **b)** transverse relaxation of a thermosensitive sample, along with **c)** the ratio of relaxivities. **d)** longitudinal and **e)** transverse relaxation of a non-thermosensitive sample, along with **f)** the ratio of relaxivities. **g)** Scheme of the diffusion of protons at the surface of a thermosensitive IONPs as a function of temperature.

The proton relaxation measurement of water containing IONPs@ELP*_{40-60-Tat} ($\Sigma=10$) varied as a function of temperature. In the case of ELP*_{40-60-Tat} grafted IONPs, the longitudinal relaxation decreased with temperature (**Figure 25 a**), contrary to what was observed for non-modified IONPs (**Figure 25 d**). The value of relaxation was also lower, as the diffusion of protons toward the surface of the nanoparticle was hindered by the presence of a brush. A similar observation was made in the case of the transverse relaxation (respectively **Figure 25 b** and **Figure 25 e**). Both longitudinal and transverse relaxations of the thermosensitive ELP*_{40-60-Tat} grafted IONPs had a sigmoidal shape, with a regime of transition that was equivalent to the one observed during DLS/MH. These phenomena could be ascribed to the differences of diffusion of protons of water at the surface of the magnetic IONPs (**Figure 25 g**). The variations of conformation of the brush and its interactions with the molecules of solvents could be evidenced and confirmed using two different techniques. These variations of

magnetic signal as a function of temperature could be used to produce thermosensitive nanoprobe for MRI. This would allow a 3D mapping of temperature in tissues of interest, which would help monitor the generation of heat by magnetic hyperthermia, either in a sequential mode, or simultaneously.

According to literature, this was the first time that a core-shell structure of IONPs grafted with a thermosensitive ELP was reported. The resulting core-shell structure presented both magnetic and thermosensitive properties, which were evidenced by heating the dispersions under MH and measuring the variations of temperature with an optical probe and observing the variations of hydrodynamic diameters *in situ* with a DLS set-up. Such equipment provides a promising platform for estimating the response of magnetic IONPs to application of a radiofrequency magnetic field or for understanding the behavior of other types of thermogenic NPs. The quantity of macromolecules added at the surface of the IONPs was controlled in order to tune the grafting density and thickness of the brushes. Amplitudes of variations of diameters observed by DLS/MH were directly correlated to the thicknesses of the brushes. This system was further investigated as a drug delivery agent by encapsulation of hydrophobic drugs in the shell and release under magnetic stimulus.

9. Study of iron oxide nanoparticles grafted with a diblock ELP as drug delivery agents

We previously showed that brushes of IONPs@ELP*_{40-60-Tat} underwent swelling/deswelling transitions triggered by magnetic hyperthermia. With the aim of benefiting from this phenomenon, we encapsulated a drug to study the potential application of the IONPs@ELP*_{40-60-Tat} as drug carriers.

9.1. Materials and methods

60 μL of a $0.1 \text{ mg}\cdot\text{mL}^{-1}$ stock solution of Dox in Tris (corresponding to $6\mu\text{g}$) was added in a 1.5 mL Eppendorf centrifuge tube. Various volumes of a $15.2 \text{ } 0.1 \text{ mg}\cdot\text{mL}^{-1}$ stock solution of IONPs@ELP*_{40-60-Tat} were added, from 0 to $40 \mu\text{L}$, corresponding to a range of 0 to $600 \mu\text{g}$, equivalent to a range of feed weight ratios of Dox from 0 to 10 %. Dox was let to incubate for 2 h at $20 \text{ }^\circ\text{C}$, 1000 rpm in a ThermoMixer© (Eppendorf). Volumes were finally completed to 1 mL with Tris, and dispersions were centrifuged at $20 \text{ }^\circ\text{C}$ for 30 min at 18000 g. The fluorescence of supernatants ($100 \mu\text{L}$) were then measured ($\lambda_{\text{exc}}=485 \text{ nm}$, $\lambda_{\text{cut-off}}=515 \text{ nm}$, $\lambda_{\text{em}}=590 \text{ nm}$) and compared to standard curves.

5 mg of IONPs@ELP*_{40-60-Tat} were incubated with 0.04 mg of Dox (FWR=0.8 %) and collected in conditions previously described. They were redispersed in 1 mL of Tris, added in a dialysis tube with a MWCO of 20 kDa, and immersed in a 50 mL Flacon tube filled with 20 mL of Tris. The solutions were then thermalized with a water bath and/or magnetic hyperthermia was applied. $100 \mu\text{L}$ of

solutions were taken at regular time intervals for fluorescence measurement, while 100 μL of Tris were added to keep a constant volume.

9.2. Results and discussion

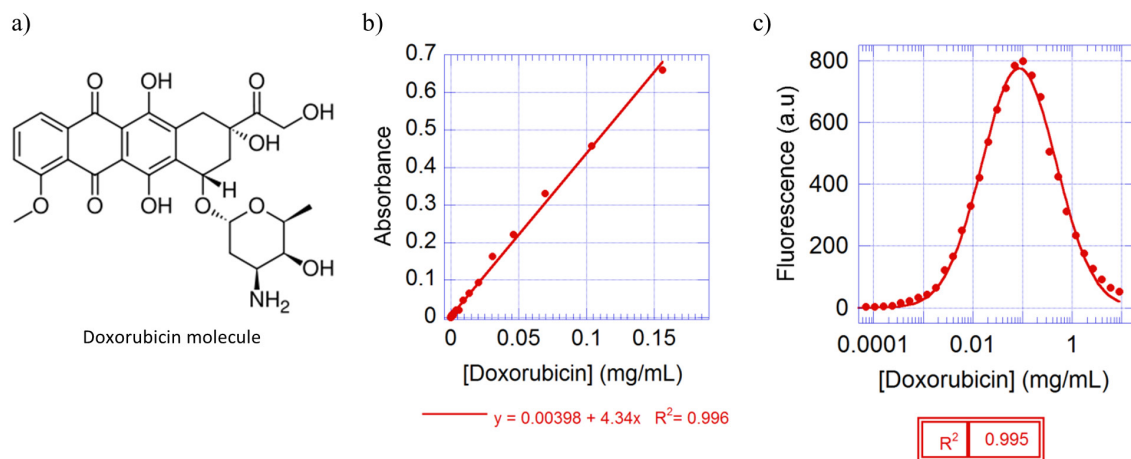


Figure 26 a) Chemical structure of Doxorubicin. b) Absorbance and c) fluorescence standard curves determined and used for the titration of doxorubicin solutions.

Doxorubicin is a chemotherapy medication used to treat cancer (**Figure 26 a**).^[34] It works in part by interfering with the function of DNA. We used it as a model to test the loading of a drug in the brush of IONPs@ELP*_{40-60-Tat} nanoparticles and its release triggered by magnetic hyperthermia. Doxorubicin (referred to as Dox) is conveniently fluorescent, allowing a detection at low ($\mu\text{g}\cdot\text{mL}^{-1}$) concentrations. It was handled with care due to its high toxicity.^[35] Standard curves were built and used to later quantify the loading and release of Dox (**Figure 26 b,c**). Interestingly, the fluorescence standard curve is well-fitted with a log-normal distribution, and Dox presents a quenching effect at concentrations superior to $0.1 \text{ mg}\cdot\text{mL}^{-1}$.

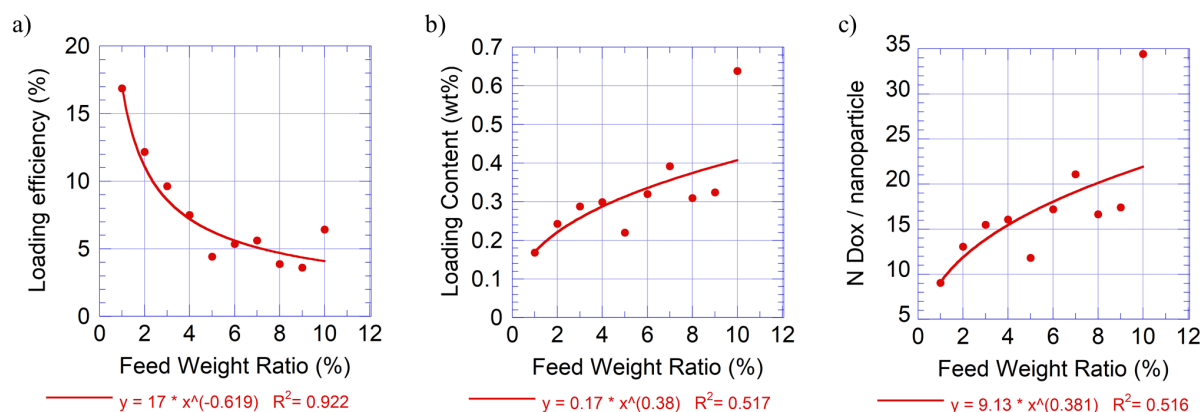


Figure 27 a) Loading efficiency, b) loading content and c) number of doxorubicin molecule per IONP@ELP*_{40-60-Tat} nanoparticle. (Power law curves serve as visual guides).

IONPs@ELP*_{40-60-Tat} and Dox were incubated in Tris buffer. Different feed weight ratios (FWR) were obtained by keeping the concentration of Dox constant while varying amounts of added IONPs@ELP*_{40-60-Tat}. The suspensions were pelleted by centrifugation, and the fluorescence of the supernatants was measured, allowing an indirect titration of the loaded Dox. Quantification of Dox loading was given through the loading efficiency (LE), and the loading content (LC). These features were calculated according to the following equations:

$$\text{FWR (\%)} = \frac{w_2}{w_3} \times 100$$

$$\text{LE (\%)} = \frac{w_1}{w_2} \times 100$$

$$\text{LC (\%)} = \frac{w_1}{w_1 + w_3} \times 100$$

Where w_1 was the amount of entrapped Dox in IONPs@ELP*_{40-60-Tat} nanoparticles, w_2 and w_3 were the respective amounts of Dox and IONPs@ELP*_{40-60-Tat} in the initial dispersion. The LE vs FWR (Figure 27 a) was globally decreasing, possibly because of the limited amount of Dox that could be encapsulated in IONPs@ELP*_{40-60-Tat}. A higher FWR led to an excess of Dox. The LC vs FWR (Figure 27 b) was slightly increasing, which was attributed to a saturation of the brush of ELP*_{40-60-Tat}. The LC was later converted into a number of Dox molecules per IONP@ELP*_{40-60-Tat} nanoparticle for a better representation of the system (Figure 27 c). We calculated that 10 to 20 Dox molecules could be adsorbed in the brush of the nanoparticles in the range of FWR explored. To put things into perspective, considering a Dox density of 1600 kg·m⁻³ and a molecular weight of 0.543 kg·mol⁻¹ returned a molecular volume of 0.6 nm⁻³, which is well in the dimensions of the IONP core and the ELP*_{40-60-Tat} brush.

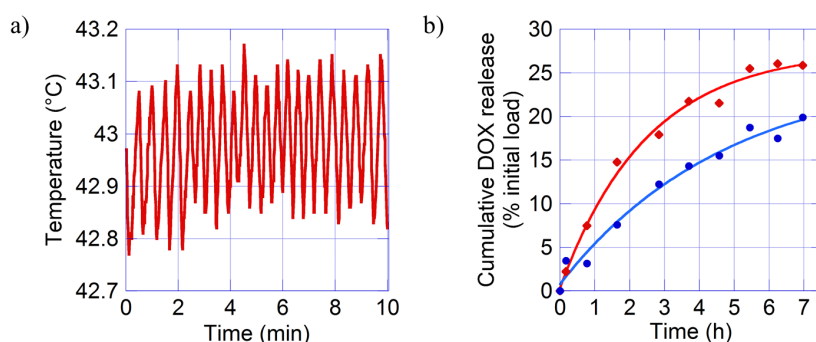


Figure 28 a) Solution temperature vs. time regulated by sequential application of magnetic hyperthermia to reach a setpoint value of 43 °C. **b)** Cumulative Dox release at 43 °C during magnetic hyperthermia (red diamonds) or in a water bath thermostated at 43 °C (blue circles).

The cumulative Dox release was assessed in “sink boundary conditions”, [36] meaning that the volume of solution containing Dox encapsulated in IONPs@ELP*_{40-60-Tat} was negligible compared to

the volume of the solvent in which Dox was released. The temperature of the sample was regulated by sequential application of magnetic hyperthermia, with a setpoint value of 43 °C (**Figure 28 a**). Cumulative Dox release profiles from a sample that underwent magnetic hyperthermia and a sample that was thermalized in a water bath were compared (**Figure 28 b**). A first observation is that the kinetics of release was slow; several hours were needed to see an inflection of the curves. This limitation probably came from the method selected to measure the release by dynamic dialysis using a semi-permeable membrane. This system is the most common method for the determination of release kinetics from nanoparticle drug delivery systems.[37] However, it cannot represent fast release kinetics because of the process of diffusion of Dox through the volume of solvent and the transport issue of Dox across the dialysis membrane. Nonetheless, at equal temperatures, MH induced a faster release profile, and larger cumulative releases. Also, it could be worth adding a second control temperature at 37 °C to gain more insight on the benefits of MH in the scope of drug release applications.

10. Conclusion

Magnetic and thermosensitive nano-objects find interesting applications as drug delivery agents. Different strategies were used to make and/or study these objects, thanks to collaborations with other laboratories. Magnetic and thermosensitive micelles were successfully obtained by nanoprecipitation of IONPs and cleavable PEG5k-PEtG50k-PEG5k. Their degradation was studied with a prototype DLS/MH apparatus. Magnetic and thermosensitive nanorattles of IONPs, silica and PNIPAM were received and proved to undergo a well-reversible variation of swelling/dehydration under application of a magnetic field. Thermosensitive microgels were loaded with IONPs and their volume transition was evidenced. Thermosensitive ELP*_{40-60-Tat} and PDMAEMA were grafted at the surface of the IONPs leading to core-shell structures. The shell of these structures exhibited changes of conformation, so that the most advanced systems could be studied both by NMR and DLS/MH. All these systems differed in terms of chemical composition, synthesis and structure. They were representative of the variety of existing strategies to produce micelles, microgels, or core-shell structures. They were all relying on the application of a magnetic field as an external stimulus to trigger their thermosensitive properties, with a prospective application as drug carriers. According to literature, this is the first time that a brush of recombinant ELPs grafted onto magnetic IONPs was studied. High temperature variations of the sample (up to 30 °C) could be obtained in few minutes by applying an AMF. Fast size changes of the thermosensitive and magnetic IONPs@ELP*_{40-60-Tat} were measured *in situ* by DLS when rising the temperature of the sample, with highly reproducible results. The hydrodynamic sizes corresponded to the ones calculated in a model of an iron oxide hard core grafted with a swollen or dehydrated brush shell. The potential application of IONPs@ELP*_{40-60-Tat} as

drug nano-carriers was studied. They could moderately load up to 20 doxorubicin anti-cancerous agent molecules per nanoparticle and released them under magnetic hyperthermia. This biocompatible system provided an interesting coupling of magnetic and thermosensitive properties that could find applications in magnetic hyperthermia cancer treatment, drug delivery therapies and as MRI contrast agents.

11. References

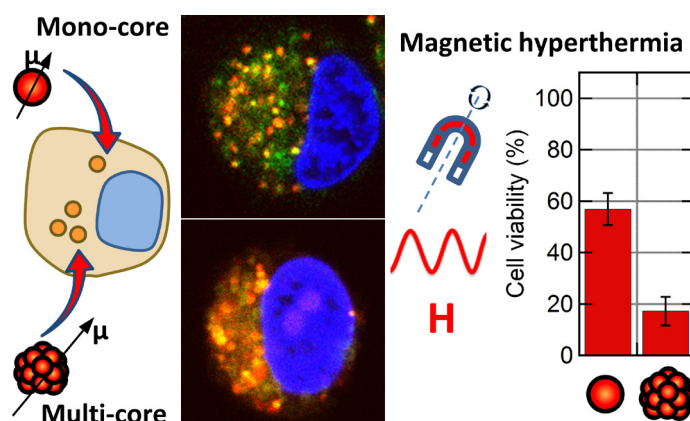
1. Chae, S.Y., Y.-s. Kim, M.J. Park, J. Yang, H. Park, M.-S. Namgung, H. Rhim, and H.K. Lim, *High-Intensity Focused Ultrasound-Induced, Localized Mild Hyperthermia to Enhance Anti-cancer Efficacy of Systemic Doxorubicin: An Experimental Study*. *Ultrasound in Medicine & Biology*, 2014. **40**(7): p. 1554-1563.
2. Huang, X., I.H. El-Sayed, W. Qian, and M.A. El-Sayed, *Cancer Cell Imaging and Photothermal Therapy in the Near-Infrared Region by Using Gold Nanorods*. *Journal of the American Chemical Society*, 2006. **128**(6): p. 2115-2120.
3. Garaio, E., J.M. Collantes, J.A. Garcia, F. Plazaola, S. Mornet, F. Couillaud, and O. Sandre, *A wide-frequency range AC magnetometer to measure the specific absorption rate in nanoparticles for magnetic hyperthermia*. *Journal of Magnetism and Magnetic Materials*, 2014. **368**: p. 432-437.
4. Maier-Hauff, K., F. Ulrich, D. Nestler, H. Niehoff, P. Wust, B. Thiesen, H. Orawa, V. Budach, and A. Jordan, *Efficacy and safety of intratumoral thermotherapy using magnetic iron-oxide nanoparticles combined with external beam radiotherapy on patients with recurrent glioblastoma multiforme*. *Journal of Neuro-Oncology*, 2011. **103**(2): p. 317-324.
5. Dong, J. and J.I. Zink, *Taking the Temperature of the Interiors of Magnetically Heated Nanoparticles*. *ACS Nano*, 2014. **8**(5): p. 5199-5207.
6. Keblinski, P., D.G. Cahill, A. Bodapati, C.R. Sullivan, and T.A. Taton, *Limits of localized heating by electromagnetically excited nanoparticles*. *Journal of Applied Physics*, 2006. **100**(5): p. 054305.
7. Périgo, E.A., G. Hemery, O. Sandre, D. Ortega, E. Garaio, F. Plazaola, and F.J. Teran, *Fundamentals and advances in magnetic hyperthermia*. *Applied Physics Reviews*, 2015. **2**(4): p. 041302.
8. Berkovitch, M., A. Livne, G. Lushkov, M. Segal, C. Talmor, Y. Bentur, J. Klein, and G. Koren, *The efficacy of oral deferiprone in acute iron poisoning*. *The American Journal of Emergency Medicine*, 2000. **18**(1): p. 36-40.
9. Mazuel, F., A. Espinosa, N. Luciani, M. Reffay, R. Le Borgne, L. Motte, K. Desboeufs, A. Michel, T. Pellegrino, Y. Lalatonne, and C. Wilhelm, *Massive Intracellular Biodegradation of Iron Oxide Nanoparticles Evidenced Magnetically at Single-Endosome and Tissue Levels*. *ACS Nano*, 2016. **10**(8): p. 7627-7638.
10. Di Corato, R., A. Espinosa, L. Lartigue, M. Tharaud, S. Chat, T. Pellegrino, C. Ménager, F. Gazeau, and C. Wilhelm, *Magnetic hyperthermia efficiency in the cellular environment for different nanoparticle designs*. *Biomaterials*, 2014. **35**(24): p. 6400-6411.
11. Caruntu, D., Y. Remond, N.H. Chou, M.-J. Jun, G. Caruntu, J. He, G. Goloverda, C. O'Connor, and V. Kolesnichenko, *Reactivity of 3d Transition Metal Cations in Diethylene Glycol Solutions. Synthesis of Transition Metal Ferrites with the Structure of Discrete Nanoparticles Complexed with Long-Chain Carboxylate Anions*. *Inorganic Chemistry*, 2002. **41**(23): p. 6137-6146.
12. Hannecart, A., D. Stanicki, L. Vander Elst, R.N. Muller, S. Lecommandoux, J. Thevenot, C. Bonduelle, A. Trotier, P. Massot, S. Miraux, O. Sandre, and S. Laurent, *Nano-thermometers with thermo-sensitive polymer grafted USPIOs behaving as positive contrast agents in low-field MRI*. *Nanoscale*, 2015. **7**(8): p. 3754-3767.
13. Hemery, G., E. Garanger, S. Lecommandoux, A.D. Wong, E.R. Gillies, B. Pedrono, T. Bayle, D. Jacob, and O. Sandre, *Thermosensitive polymer-grafted iron oxide nanoparticles studied by in situ dynamic light backscattering under magnetic hyperthermia*. *Journal of Physics D: Applied Physics*, 2015. **48**(49): p. 494001.
14. Henoumont, C., S. Laurent, and L. Vander Elst, *How to perform accurate and reliable measurements of longitudinal and transverse relaxation times of MRI contrast media in aqueous solutions*. *Contrast Media & Molecular Imaging*, 2009. **4**(6): p. 312-321.

15. Fan, B., J.F. Trant, A.D. Wong, and E.R. Gillies, *Polyglyoxylates: A Versatile Class of Triggerable Self-Immolative Polymers from Readily Accessible Monomers*. Journal of the American Chemical Society, 2014. **136**(28): p. 10116-10123.
16. Fan, B. and E.R. Gillies, *Poly(ethyl glyoxylate)-Poly(ethylene oxide) Nanoparticles: Stimuli-Responsive Drug Release via End-to-End Polyglyoxylate Depolymerization*. Molecular Pharmaceutics, 2017. **14**(8): p. 2548-2559.
17. Fan, B., J.F. Trant, and E.R. Gillies, *End-Capping Strategies for Triggering End-to-End Depolymerization of Polyglyoxylates*. Macromolecules, 2016. **49**(24): p. 9309-9319.
18. Fan, B., J.F. Trant, R.E. Yardley, A.J. Pickering, F. Lagugné-Labarhet, and E.R. Gillies, *Photocontrolled Degradation of Stimuli-Responsive Poly(ethyl glyoxylate): Differentiating Features and Traceless Ambient Depolymerization*. Macromolecules, 2016. **49**(19): p. 7196-7203.
19. Scheid, D., G. Cherkashinin, E. Ionescu, and M. Gallei, *Single-Source Magnetic Nanorattles By Using Convenient Emulsion Polymerization Protocols*. Langmuir, 2014. **30**(5): p. 1204-1209.
20. Boularas, M., E. Gombart, J.-F. Tranchant, L. Billon, and M. Save, *Design of Smart Oligo(ethylene glycol)-Based Biocompatible Hybrid Microgels Loaded with Magnetic Nanoparticles*. Macromolecular Rapid Communications, 2015. **36**(1): p. 79-83.
21. Boularas, M., E. Deniau-Lejeune, V. Alard, J.-F. Tranchant, L. Billon, and M. Save, *Dual stimuli-responsive oligo(ethylene glycol)-based microgels: insight into the role of internal structure in volume phase transitions and loading of magnetic nanoparticles to design stable thermoresponsive hybrid microgels*. Polymer Chemistry, 2016. **7**(2): p. 350-363.
22. Agut, W., A. Brûlet, C. Schatz, D. Taton, and S. Lecommandoux, *pH and Temperature Responsive Polymeric Micelles and Polymersomes by Self-Assembly of Poly[2-(dimethylamino)ethyl methacrylate]-b-Poly(glutamic acid) Double Hydrophilic Block Copolymers*. Langmuir, 2010. **26**(13): p. 10546-10554.
23. Plamper, F.A., M. Ruppel, A. Schmalz, O. Borisov, M. Ballauff, and A.H.E. Müller, *Tuning the Thermoresponsive Properties of Weak Polyelectrolytes: Aqueous Solutions of Star-Shaped and Linear Poly(N,N-dimethylaminoethyl Methacrylate)*. Macromolecules, 2007. **40**(23): p. 8361-8366.
24. Wang, Y.-X.J., *Superparamagnetic iron oxide based MRI contrast agents: Current status of clinical application*. Quantitative Imaging in Medicine and Surgery, 2011. **1**(1): p. 35-40.
25. Terreno, E., D. Delli Castelli, C. Cabella, W. Dastrù, A. Sanino, J. Stancanella, L. Tei, and S. Aime, *Paramagnetic Liposomes as Innovative Contrast Agents for Magnetic Resonance (MR) Molecular Imaging Applications*. Chemistry & Biodiversity, 2008. **5**(10): p. 1901-1912.
26. Vuong, Q.L., J.-F. Berret, J. Fresnais, Y. Gossuin, and O. Sandre, *A Universal Scaling Law to Predict the Efficiency of Magnetic Nanoparticles as MRI T2-Contrast Agents*. Advanced Healthcare Materials, 2012. **1**(4): p. 502-512.
27. Urry, D.W., *Physical Chemistry of Biological Free Energy Transduction As Demonstrated by Elastic Protein-Based Polymers*. The Journal of Physical Chemistry B, 1997. **101**(51): p. 11007-11028.
28. Meyer, D.E. and A. Chilkoti, *Quantification of the Effects of Chain Length and Concentration on the Thermal Behavior of Elastin-like Polypeptides*. Biomacromolecules, 2004. **5**(3): p. 846-851.
29. Debaisieux, S., F. Rayne, H. Yezid, and B. Beaumelle, *The Ins and Outs of HIV-1 Tat*. Traffic, 2012. **13**(3): p. 355-363.
30. Garanger, E., S.R. MacEwan, O. Sandre, A. Brûlet, L. Bataille, A. Chilkoti, and S. Lecommandoux, *Structural Evolution of a Stimulus-Responsive Diblock Polypeptide Micelle by Temperature Tunable Compaction of its Core*. Macromolecules, 2015. **48**(18): p. 6617-6627.
31. Sevick, E.M., *Shear Swelling of Polymer Brushes Grafted onto Convex and Concave Surfaces*. Macromolecules, 1996. **29**(21): p. 6952-6958.

32. Vogiatzis, G.G. and D.N. Theodorou, *Structure of Polymer Layers Grafted to Nanoparticles in Silica–Polystyrene Nanocomposites*. *Macromolecules*, 2013. **46**(11): p. 4670-4683.
33. Brittain, W.J. and S. Minko, *A structural definition of polymer brushes*. *Journal of Polymer Science Part A: Polymer Chemistry*, 2007. **45**(16): p. 3505-3512.
34. De Angelis, A., K. Urbanek, D. Cappetta, E. Piegari, L.P. Ciuffreda, A. Rivellino, R. Russo, G. Esposito, F. Rossi, and L. Berrino, *Doxorubicin cardiotoxicity and target cells: a broader perspective*. *Cardio-Oncology*, 2016. **2**(1): p. 2.
35. Tacar, O., P. Sriamornsak, and C.R. Dass, *Doxorubicin: an update on anticancer molecular action, toxicity and novel drug delivery systems*. *Journal of Pharmacy and Pharmacology*, 2013. **65**(2): p. 157-170.
36. Mertz, D., O. Sandre, and S. Bégin-Colin, *Drug releasing nanoplatforms activated by alternating magnetic fields*. *Biochimica et Biophysica Acta (BBA) - General Subjects*, 2017. **1861**(6): p. 1617-1641.
37. Modi, S. and B.D. Anderson, *Determination of Drug Release Kinetics from Nanoparticles: Overcoming Pitfalls of the Dynamic Dialysis Method*. *Molecular Pharmaceutics*, 2013. **10**(8): p. 3076-3089.

CHAPTER V

GLIOBLASTOMA CELL DEATH INDUCED BY MAGNETIC HYPERTHERMIA: MONOCORE VS. MULTICORE NANOPARTICLES



1. Introduction

Cancer is a major cause of death in developed countries and the second cause of death in Europe and USA.[1] Among the different types and locations of cancer, malignant brain tumors show lower incidence as compared to the more common breast, prostate or liver cancers. The annual global age-standardised incidence of brain cancers are 2.6 and 3.7 per 100,000 individuals, for females and males respectively.[2] However, brain tumors of high grade (glioblastoma) are aggressive and have very poor prognosis. They are exceedingly complicated to treat due to their deep implantation in the cranial cavity, limiting the ease of treatment, and to the vital role of the brain limiting tumour resection by surgery. Patients suffering from glioblastoma have a median survival of 14 months,[3] with survival chance depending on various parameters, such as size and location of the tumour, patient age, and administrated treatment.[4] Standard existing solutions to treat cancers by resection, radiotherapy and chemotherapy have to be combined into a multi-modal treatment with generally poor prognosis, and marginal benefits.[3, 4]

In search for a more efficient cure, magnetic hyperthermia (MH) coupled with conventional radiotherapy proved to be a promising alternative, which is well-tolerated by the patients, and with little to no side effects.[5] In a phase 3 clinical trial, these combined methods of thermal ablation and X-rays were able to prolong the median survivability from 14.6 months to 23.2 months.[6] They have therefore been authorized in the clinics. In parallel, different pre-clinical models were developed to test the conditions of MH application *in vitro* on different cell lines or *in vivo* on small animals (mostly rodents). Emphasis was placed in particular on the type of magnetic nanoparticles used to generate heat and on the characteristics of the alternating magnetic field (AMF).[7] Magnetic iron oxide nanoparticles (IONPs) are in this sense promising internal heating agents for magnetic hyperthermia, due to their inherent biocompatibility and because they can reach sufficiently high values of specific absorption rates (SAR) to elevate temperature up to 51.2 °C in glioblastomas by intra-tumour injection.[6]

The present study aims at comparing the efficacy of two morphologies of IONPs (monocore *vs* multicore) for treating human glioblastoma cells *in vitro*. Among the different synthesis pathways yielding IONPs (alkaline co-precipitation, hydrothermal treatment, thermal decomposition etc.),[8] we chose in this study the polyol route introduced by Caruntu *et al.*[9] as this synthesis is robust, up-scalable and enables producing either monocore or multicore IONPs: the latter are among the synthetic IONPs with the highest reported SAR values, of $\sim 1 \text{ kW}\cdot\text{g}^{-1}$ or more,[10-12] yet at moderate AMF conditions out-passing the “Brezovich criterion” on the product of AMF frequency and intensity by a factor ~ 10 only ($f \times H < 5 \cdot 10^9 \text{ A}\cdot\text{m}^{-1}\cdot\text{s}^{-1}$), as proposed by Dutz and Hergt.[13] The surfaces of these two types of IONPs were functionalized with a dense polymer brush of poly(ethylene glycol) (PEG) as a stabilizer for bringing longer blood circulation lifetime *in vivo*. In the present study, the

near infrared (NIR) fluorescent dye DY700 that is stable under *in vitro* conditions and has low cytotoxicity[14] was also grafted using the phosphonate pre-functionalisation strategy in order to easily track the IONPs incubated with cells.

Monocore and multicore nanoparticles were studied *in vitro* using a U87 human glioblastoma cell line, genetically modified to overexpress the bioluminescent reporter gene firefly luciferase (Fluc). The bioluminescence property of the cells was used to provide a convenient way to monitor the time course of cell viability by bioluminescence imaging (BLI) and to quantify the IONPs' performances in terms of magnetically-induced toxicity.[15, 16] The internalization pathway was studied both by transmission electron microscopy (TEM) of cell microtomes and by confocal laser scanning microscopy (CLSM) of living cells, evidencing that the IONPs were internalized inside intracellular compartments, more precisely in lysosomes. The quantities of IONPs internalized inside the cells for several conditions of incubation were determined by flow cytometry and fluorescence imaging, showing good correlation with IONP concentration during incubation. Their efficiency to induce U87 glioblastoma cell death by MH was assessed by bioluminescence imaging (BLI), as luciferase expression is ATP-dependent and thus serves as a quantitative and direct read-out of cell viability.[17] We evidenced noticeable differences between monocore and multicore IONPs, regarding their internalization and the magnetically-induced cytotoxicity effects.

2. Materials and methods

2.1. Surface modification of monocore and multicore iron oxide nanoparticles

Magnetic iron oxide nanoparticles were synthesized by the polyol route, adapting the reaction conditions reported by Caruntu *et al.*, i.e. by adding controlled fractions of water in the polyol reaction medium to drive the morphology of the IONPs obtained, as reported recently by our group.[12] Monocore IONPs from the polyol batch 32ff and multicore IONPs from the polyol batch 35ff were selected for this study. NHS-ester modified DY700 fluorescent probe (Dyomics, Germany) was reacted with 1.5 eq. of 2-aminoethylphosphonic acid (AEP) (Sigma Aldrich) in DMSO for 24 h at room temperature and under orbital agitation, before long-term storage at -20 °C (later referred to as DY700*). Poly(ethylene glycol) methyl ether thiol (mPEG-SH, average molar mass $M_n=6000 \text{ g}\cdot\text{mol}^{-1}$, Sigma Aldrich) was reacted with 1 eq. of tris(2-carboxyethyl)phosphine hydrochloride (TCEP) (98%, ACROS Organics) in 50 mM phosphate buffer (PB) pH 7.4 for 24 h to reduce the disulfide bonds between (mPEG-S)₂ dimers, leading to reactive thiols. In parallel, 5 eq. AEP was reacted with 1 eq. *N*-succinimidyl 4-maleimidobutyrate (GMBS, TCI Europe) in PB for 24 h in an ice bath. Both solutions were then mixed and let to react for 24 h, and finally purified by dialysis against milliQ water for 72 h, using a 5 kDa membrane, and replacing 6 times with milliQ water (later referred to as PEG*). 1 % w/w equivalents of DY700* were then grafted onto IONPs in water acidified to pH=2.5 with dilute nitric acid. After 1 h, 30 % (16 %) w/w of PEG* was added to the dispersion of mono-core (multi-

core) IONPs. These proportions lead to theoretical grafting densities of $\sigma = 1/D^2 = 0.64$ molecular chains per nm^2 or reduced tethered densities $\Sigma = \pi R_G^2/D^2 = 15$ according to our calculations, using scaling laws reported by Devanand[18] ($R_G(\text{nm}) = 0.0215 \cdot M_n^{0.583}$) or by Le Coeur *et al.*[19] ($R_G(\text{nm}) = 0.066466 \cdot M_n^{0.45224}$), which are different but both lead to the same value $R_G = 3.4$ nm for PEG 6,000 $\text{g}\cdot\text{mol}^{-1}$. After 2 h of reaction, the pH was neutralized by Tris 50 mM and the solutions were purified from the excess of PEG* and DY700* by 3 cycles of centrifugation-redispersion (18,000 g, 1 h at 25°C, 30 min at 1°C to increase viscosity and avoid pellet dispersion before removing the supernatant).

2.2. Cell line generation and culture

U87 human glioma cell line was procured by the American Tissue Culture Collection (ATCC, Manassas, Virginia). The bioluminescent U87-CMV-lucF cell line generation was previously reported.[16] Cells were cultivated in Dulbecco's modified Eagle's medium (DMEM, Invitrogen, Carlsbad, California) supplemented with 10% foetal bovine serum (FBS, Invitrogen), 1% antimycotic-antibiotic mix (PSA, Invitrogen), 1% nonessential amino acid (MEM NEAA, Invitrogen) and 50 $\mu\text{g}\cdot\text{mL}^{-1}$ Hygromycin B (Euromedex, Souffelweyersheim, France). Cell line was maintained in a humidified 5% CO_2 incubator at 37°C.

2.3. Incubation of cells with iron oxide nanoparticles

Cells (5000 cells per well) were plated in 16-well Nunc™ Lab-Tek® microscopy chambers (Thermo Fisher) 24 h before experiments. They were then incubated with 100 μL of determined concentrations of IONPs (0, 100, 200, 300, 400 or 500 $\mu\text{g}\cdot\text{mL}^{-1}$) in supplemented DMEM for 24 h. They were finally washed with 2 times 100 μL of PBS and 100 μL of fresh supplemented DMEM.

2.4. Laser scanning confocal microscopy

Cells (22,500 cells per well) were plated in 24-well plates 24 h before experiments and then incubated with IONPs conjugated to the NIR fluorescent probe DY700 (Dyomics GmbH) for 24 h at 100 $\mu\text{g}\cdot\text{mL}^{-1}$. They were washed with PBS, and their nucleus was stained with the blue fluorescent probe Hoechst 33342 (Thermo Fisher Scientific) at a concentration of 2 $\mu\text{g}\cdot\text{mL}^{-1}$ for 5 min at 37 °C. Finally, the lysosomes were specifically tagged with the green fluorescent probe LysoTracker™ at a concentration of 100 nM for 1 min at RT. The cells were harvested with trypsin for 5 min at RT, suspended in PBS and centrifuged for 5 min at 300 g. They were re-suspended in 200 μL of PBS-EDTA 2 mM supplemented with 0.5 % of FBS, and kept on ice to prevent adhesion, before visualization. Laser scanning confocal microscopy images were acquired on an inverted Leica TCS SP5 microscope equipped with an HCX PL APO 63× NA 1.4 oil immersion objective in fluorescence mode. Samples (≈ 15 μL) were injected in a homemade chamber that was sealed to prevent evaporation. The laser outputs are controlled via the acousto-optical tunable filter and the three

collection windows using the acousto-optical beam splitter and photomultiplier detectors as follows: Blue Hoechst 33342 was excited with a laser diode at 405 nm (3%) and measured with emission setting at 410-510 nm, green LysoTracker™ was excited with a DPSS diode at 561 nm (50%) using a window at 570-650 nm and red DY700 was excited with a Helium-Neon laser at 633 nm (80%) using a window at 640-770nm. LSCM images were collected using the microscope in sequential mode to avoid overlapping of the emissions between the channels with a line average of 4 and a format of 1024×1024 pixels. The transmission mode images were provided from the Helium-Neon laser at 633 nm (10%). PMT gain and offset configurations were set up on control cells so as to correct images from green and red auto-fluorescence.

2.5. Flow cytometry

Cells (22,500 cells per well) were plated in 24-well plates 24 h before experiments and then incubated with 450 µL of determined concentrations of IONPs@PEG* (0, 100, 200, 300, 400 or 500 µg·mL⁻¹). After 24h incubation, the cells were washed 2 times with PBS, harvested with trypsin and washed with PBS. Cells were re-suspended in 200 µL of PBS-EDTA 2 mM supplemented with 0.5 % of FBS and analysed by flow cytometry using a BD FACS Canto™ setup (BD Biosciences). Samples were analysed using an excitation laser at 633 nm, absorption with the APC-Cy7 canals at 680 nm, the forward scatter channel (FSC) voltage being fixed at 160 V and the side scatter channel (SSC) voltage fixed at 160 V.

2.6. Fluorescence and bioluminescence imaging

Fluorescence and bioluminescence imaging (BLI) was performed at Vivoptic (UMS 3767 – Univ. Bordeaux) by using a Lumina LT instrument (Perkin Elmer Inc., Boston, MA, USA). For BLI, the cells were incubated for 5 min with a 0.6 mM solution of D-luciferin in PBS (Promega, Madison, WI, USA). Bioluminescence images (1 min, 4×4 binning) and photographs (100 ms) were acquired successively. Fluorescence reflectance images (FRI) (1 s, excitation at 640 nm, 695-770 nm filter emission, 4×4 binning) and photographs (100 ms) were acquired successively. Images were analyzed using Living Image software.

2.7. Transmission electron microscopy

Glial U87 cells were cultivated on 16-well optical glass supports (Nunc™ 178599 Lab-Tek® Chamber Slide™ System, Glass, Volume: 0.1-0.2 mL, Culture Area: 0.4 cm²/well). After incubation (24 h) with the IONPs@PEG*, cells were washed two times with PBS, fixed with 1.6 % (v/v) paraformaldehyde 2 % (v/v) glutaraldehyde in 0.08 M cacodylate buffer (pH 7.4) during 30 min minimum at room temperature (RT), washed in 0.1 M cacodylate buffer (pH 7.4) and then post-fixed in a mix of 1% osmium tetroxide (v/v) / 1 % potassium ferricyanide K₃Fe(CN)₆ (p/v) in 0.1 M cacodylate buffer during 2 hours on ice in the dark. After washing in water, samples were stained in block in 0.5 % (p/v) aqueous uranyl acetate solution during 30 min, in the dark, at RT. Subsequently,

cells were washed in water then dehydrated through a series of graded ethanol and embedded in a mixture of pure ethanol and epoxy resin (Epon 812; Delta Microscopies, Toulouse, France) 50/50 (v/v) during 2 h and then in 100 % resin overnight at RT. The polymerization of the resin was carried out over a period between 24-48 h at 60 °C. Samples were then sectioned using a diamond knife (Diatome, Biel-Bienne, Switzerland) on an ultramicrotome (EM UCT, Leica Microsystems, Vienna, Austria). Ultrathin sections (65 nm) were picked up on copper grids and then stained with Uranylless (Delta Microscopies, Toulouse, France) and lead citrate. Grids were examined with a Transmission Electron Microscope (H7650, Hitachi, Tokyo, Japan) at 80 kV in High Contrast Mode.

2.8. Magnetic hyperthermia

The applied radiofrequency AMF was generated using a DM3 applicator for *in vivo* magnetic hyperthermia (nB nanoScale Biomagnetics, Zaragoza, Spain). Cells were thermalized at 37.5 °C using a water bath connected to a water tubing jacket. The temperature of the sample was monitored using a fibre optic sensor (OTG-M420, Opsens™, Québec city, Canada). The alternating magnetic field was set on a frequency of 473 kHz, 12 kA·m⁻¹ of amplitude, and applied for 30 min. The cells were put back in the incubator at 37 °C / 5 % CO₂ and observed by bioluminescence and fluorescence imaging 24 h later.

3. Results and discussion

3.1. Monocore and multicore nanoparticles modified with a brush of poly(ethylene glycol) and a fluorescent probe

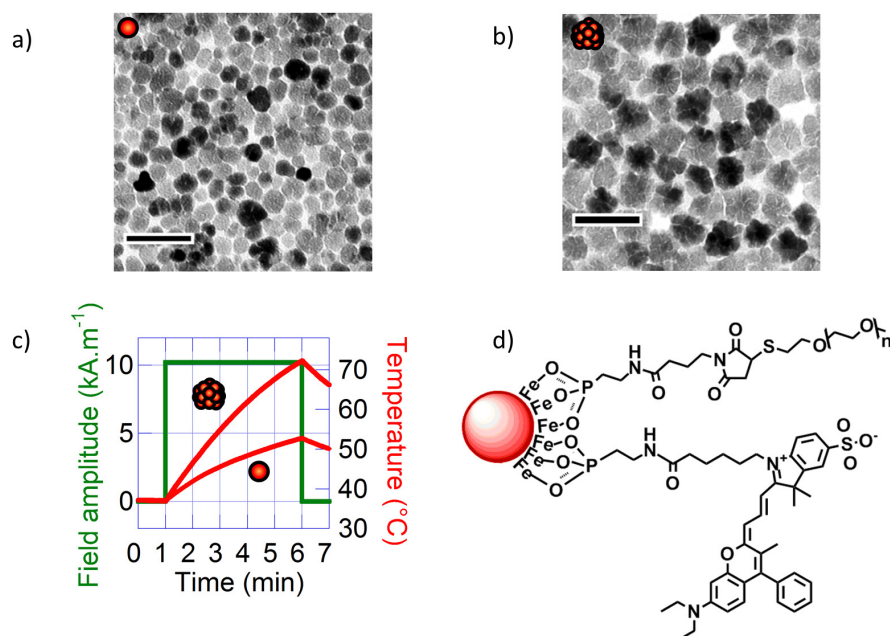


Figure 1 TEM micrographs of **a)** monocore (batch 32ff) and **b)** multicore (batch 35ff) IONPs of diameters respectively 14.5±3.4 and 29.1±4.4 nm. The scale bar length is 50 nm. **c)** Core-shell structure of an IONP grafted with a DY700* fluorescent probe and PEG*.

Monocore and multicore IONPs were synthesized by the forced hydrolysis route in a mixture of polyol and poly(hydroxy)amine with controlled addition of water during the reaction, as previously described in **Chapter II**.^[12] The batches of monocore (**Figure 1 a**) and multicore (**Figure 1 b**) IONPs selected for this study presented specific SAR of 134 and 265 W·g⁻¹, respectively, in the AMF conditions used (755 kHz, 10.2 kA·m⁻¹) (**Figure 1 c**). Their surface was chemically modified by grafting 6,000 MW PEG chains in order to provide steric repulsion and ensure colloidal stability in physiological media (**Figure 1 d**). The PEG was primarily modified at one end by introducing a phosphonic acid anchor group, which was subsequently used to tether the chains at the surface of IONPs in a single reaction step. The number of PEG* chains per IONP was adjusted to form a dense repulsive brush. A NIR fluorescent probe (DY700, Dyomics GmbH, Jena) was simultaneously grafted at the IONP surface using a similar strategy. The ratio of PEG* to IONP was calculated to form a dense layer. In order to obtain a grafting density sufficient to reach the “brush regime” so that the tethered chains were neither too far from each other (“mushroom regime”) nor too extended, we used the criterion established by Brittain and Minko^[20] comparing the chain-to-chain distance D between the grafting points to the gyration radius R_G of the free chains in solution through the reduced grafting density $\Sigma = \pi R_G^2 / D^2$. In this dense brush regime defined by $\Sigma > 5$,^[20] the IONPs were stabilized by maximal steric repulsions.

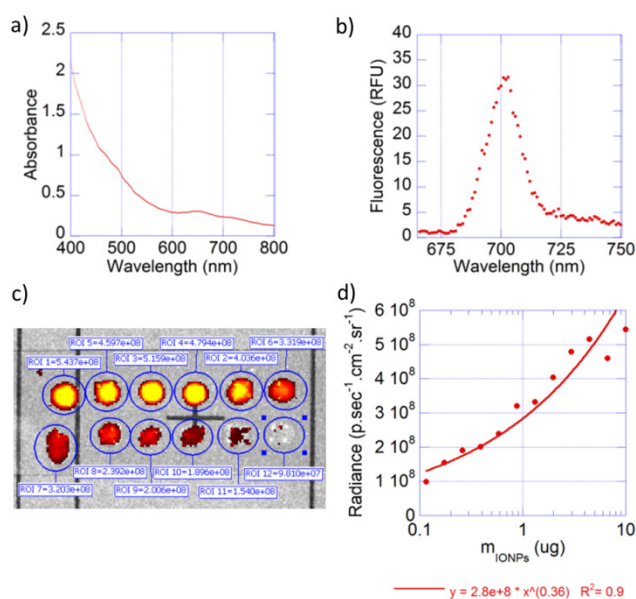


Figure 2 a) Absorbance of multicore IONPs grafted with DY700* and PEG*. **b)** Fluorescence of the IONPs. **c)** Fluorescence of drops of IONPs@PEG* dispersed in solution, as observed with the Lumina instrument. **d)** Standard curve of fluorescence as a function of quantity of IONPs@PEG*.

The NIR fluorescent probe DY700* was coupled directly onto the surface of IONPs resulting in a very likely shielding of the dye by the PEG* layer. The proximity of the DY700* with the surface of the semi-conducting iron oxide led to a partial quenching of the fluorescent signal. This

phenomenon possibly occurred through two mechanisms; by nanoparticle/fluorophore interaction[21] or by fluorophore/fluorophore self-quenching due to a local high concentration. For this reason, the amount of dye to be grafted at the surface of the IONPs was carefully evaluated and the optimum quantity was used, both to guaranty sufficient fluorescent signal for detection and to keep the surface hydrophilic by not covering it too much with a hydrophobic molecule. Using a spacer to increase the distance between the surface of the IONPs and the fluorophore and the distance between fluorophores could have been another option. On the other hand, the DY700* conjugation very close to the surface prevented its interaction with the environment of the IONPs@PEG* when studying their interaction with cells. The maxima were respectively at $\lambda_{exc}=650$ nm for excitation and $\lambda_{em}=700$ nm for emission (**Figure 2 a-b**). These values of absorption and emission were in the near-infrared (NIR) spectrum, which was in the range of minimum absorption of both the biological environment and of the IONPs that strongly absorbed the shorter wavelengths. The fluorescence signal as a function of quantity of IONPs@PEG* could be quantified to build a standard curve (**Figure 2 c-d**).

3.2. Interaction of nanoparticles with U87 glioblastoma cancer cells

3.2.1. Observation of nanoparticles-cells interactions by fluorescence imaging

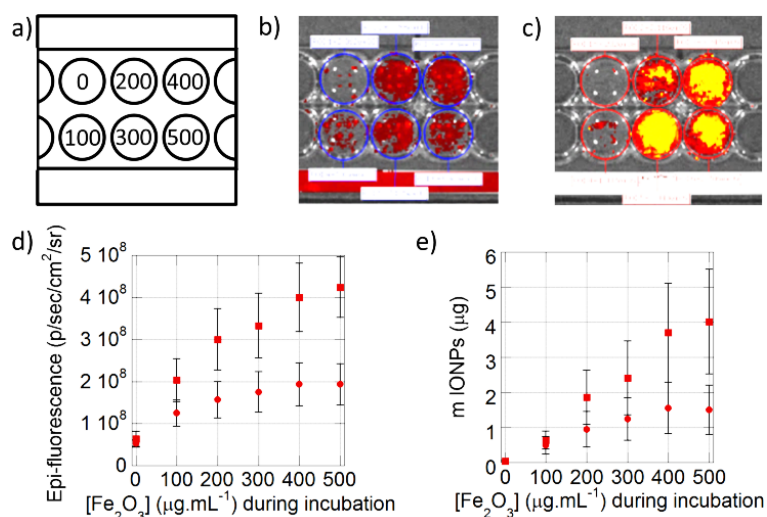


Figure 3 a) Scheme representing the concentration of IONPs@PEG* ($\mu\text{g}\cdot\text{mL}^{-1}$) in the wells during cell incubation. Fluorescence measurement of **b)** monocore and **c)** multicore IONPs@PEG* internalized in U87 cells 24 hours after incubation. **d)** Epi-fluorescence of the cells for monocore (circles) and multicore (square) IONPs@PEG*. **e)** Quantity of monocore (circles) and multicore (square) IONPs@PEG* internalised in the cells deduced by prior fluorescence calibration with known amounts.

The fluorescence of the DY700-labelled IONPs@PEG* uptaken by the cells was also detected directly on the culture plates by the non-destructive fluorescence reflectance imaging (FRI) technique that is complementary to flow cytometry and corresponds to a spatial visualization of the fluorescence signal on a camera. As for flow cytometry, 6 different conditions of incubation during 24 h at increasing IONPs@PEG* concentrations were experimented (**Figure 3 a**). The fluorescence signal in each well was relatively homogeneous, as the cells were spread over the whole surface available.

Visually, the fluorescence intensity of cells incubated with multicores was higher (**Figure 3 c**) than with monocoresh IONPs@PEG* (**Figure 3 b**). The average fluorescence signal for each incubation condition was quantified by using a region of interest (ROI) selection tool. This plot showed (**Figure 3 d**) a signal initially proportional to the IONPs@PEG* concentration during incubation before plateauing. Like in flow cytometry results, the multicores (squares) exhibited higher cellular internalization as compared to the monocoresh ones (circles). This intensity of FRI signal could be correlated to the quantity of IONPs@PEG* internalized in the cells using calibration curves: These are reported in **Figure 2** for multicore morphologies, the intensity of signal being fitted by a power law of the quantity of IONPs@PEG* expressed in μg per well. In both flow cytometry (**Figure 4 j**) and FRI (**Figure 3 d**), fluorescence signals reached a plateau which would indicate a saturation of the cells with IONPs@PEG*. However, when plotting the total quantity of IONPs@PEG* up-taken by cells in each well versus the concentration during incubation (**Figure 3 e**), a more linear relationship was obtained than expected from the raw fluorescence levels, after taking into account the calibration curves well-fitted by power laws for both morphologies. The plateaus observed in the fluorescence levels measured by the two methods were therefore more likely ascribed to signal self-quenching rather than to saturation of the cells with IONPs@PEG*. Considering the constant number of 5000 cells per well, the IONPs@PEG* mass up-taken per U87 cell after 24 h incubation at $500 \mu\text{g}\cdot\text{mL}^{-1}$ corresponded respectively to $\sim 300 \text{ pg/cell}$ for monocoresh and $\sim 800 \text{ pg/cell}$ for multicoresh, which was larger than the 40 pg/cell value reported in the pioneering work by Wilhelm *et al.* on IONP endocytosis in the HeLa cell line.[22] However, when taking into account the difference of IONP diameters (8.7 nm for the work of Wilhelm *et al.*, 14.5 nm for the monocoresh and 29.1 nm for the multicoresh here, the calculated up-taken numbers were approximately the same: 23, 38 and 12 million of IONPs@PEG* per cell, respectively.

3.2.2. Observation of nanoparticles-cells interactions by bright field microscopy and flow cytometry

The cells incubated with monocoresh or multicore IONPs@PEG* were detached from the surface of the culture plate for flow cytometry analysis. Under optical bright field microscopy, the cell membrane, nuclei membrane and nucleolus were visible for the control U87 cell, along with smaller un-resolved structures in the cytoplasm (**Figure 4 a**). Spherical structures with high contrast appeared when the cells were incubated with either monocoresh (**Figure 4 b**) or multicoresh (**Figure 4 c**). These structures are most probably lysosomes encapsulating the IONPs@PEG*, leading to dark-colored objects.

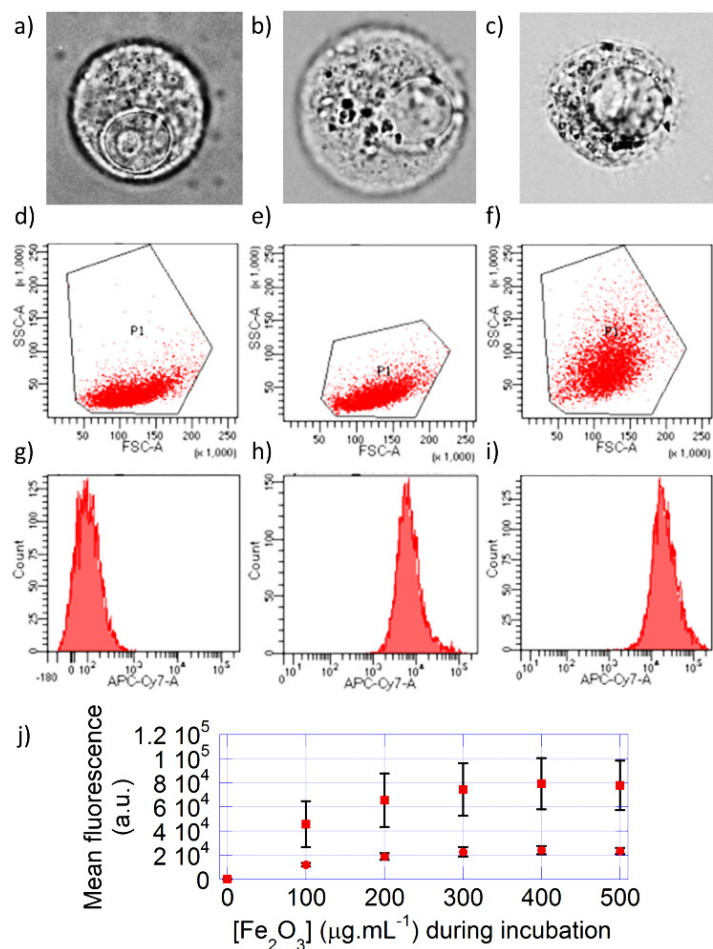


Figure 4 Bright field microscopy images of **a)** control U87 cells, and U87 cells incubated with either **b)** monocore or **c)** multicore IONPs@PEG*. Flow cytometry 2D plots of **d)** U87 cells, U87 cells incubated with **e)** monocore and **f)** multicore IONPs@PEG*. Fluorescence histograms of **g)** U87 cells, U87 cells incubated with **h)** monocore and **i)** multicore IONPs@PEG*. **j)** Mean fluorescence of cells as a function of IONPs@PEG* concentration during incubation for monocore (circles) and multicore (squares) IONPs@PEG*. Error bars represent statistical scatter.

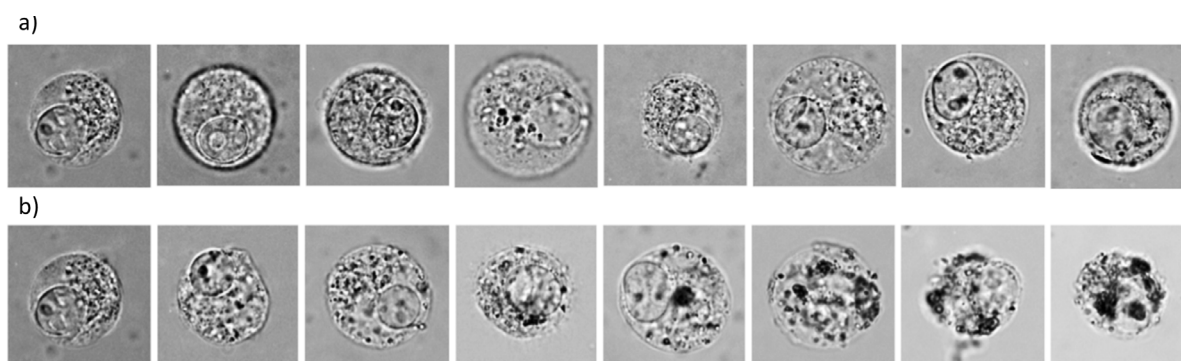


Figure 5 Bright field microscopy images of U87 cells incubated with IONPs@PEG* at concentrations of (from left to right) 0, 10, 50, 100, 200, 300, 400, 500 μg/mL. The morphologies of the IONPs@PEG* are **a)** monocore and **b)** multicore.

The observation of these microscopic structures was complemented by flow cytometry that analyses large numbers of cells and reports the results in a statistical manner. The 2D multi-parametric plot represents both the forward scatter channel (FSC) which is proportional to the cell size, and the side scatter channel (SSC) representing the granularity and structural complexity inside the cells. Control U87 cells (**Figure 4 d**) and U87 cells incubated with monocore IONPs@PEG* (**Figure 4 e**) exhibited similar 2D dot plots, while U87 cells incubated with multicore IONPs@PEG* (**Figure 4 f**) had a broader and larger distribution of SSC values. This means that in all three cases the size of the cells was relatively identical, as confirmed by bright field microscopy, while the internal granularity of the U87 cells incubated with multicores was more complex, leading to a stronger side scattering of the laser light. Comparison of flow cytometry 2D plots indicated a higher internalization of multicores as compared to monocoresh, with possibly a higher density of lysosomes. The total fluorescence intensity of each of the cell cultures was defined by using polygon gate selections on the 2D plots, measuring the signal of each individual cell and reporting the counts on single-parameter histograms (**Figure 4 g-i**). Finally the plot of the integrated fluorescence signal *versus* the IONPs@PEG* concentration evidenced that the U87 cells exhibited low auto-fluorescence level and behave as a single homogeneous population on the selected polygon gates. U87 cells incubated with increasing concentrations of IONPs@PEG*s exhibited a strong fluorescence signal. In addition, the histogram representing single populations hinted that the internalization happened in small fractions, and that all the cells incubated with IONPs@PEG* have internalized them as they were all fluorescent. The integrated fluorescence levels of samples at different IONPs@PEG* concentrations during incubation (**Figure 4 j**) showed a linear behavior, until reaching a plateau value. Larger quantities of nanoparticles were internalized by cells at higher incubation concentration. This plot also evidenced around four-fold higher internalization of the multicores as compared to monocoresh at a given concentration during incubation. The same ratio was found between the plateaus of IONPs@PEG* mass internalized per cell, for both types of morphologies.

3.2.3. Observation of nanoparticles-cells interactions by confocal microscopy

The interactions between cells and IONPs@PEG* were investigated, using a U87 human glioblastoma cell line, genetically modified to overexpress a bioluminescent reporter gene (Fluc) under the transcriptional control of constitutive CMV promoter. The luciferase expressed by cells is an enzyme which catalyzes D-luciferin oxidation to produce photons. Emitted light is correlated with the dioxygen- and ATP-dependant activity of luciferase which is itself correlated with cell viability (O₂ and ATP content) and cell numbers (luciferase amount) in the samples.[17] Following addition of D-luciferin in the culture medium, light emission was monitored non-invasively, by bioluminescence imaging. This property was later used as a viability assay when evaluating the effect of IONPs@PEG* on cells under magnetic field hyperthermia. The treated cells were incubated with nanoparticles for

24h. The blue fluorescent signal of the Hoechst dye was specifically located in the nuclei, revealing the position of the cells in the sample (**Figure 6** and **Figure 7**).

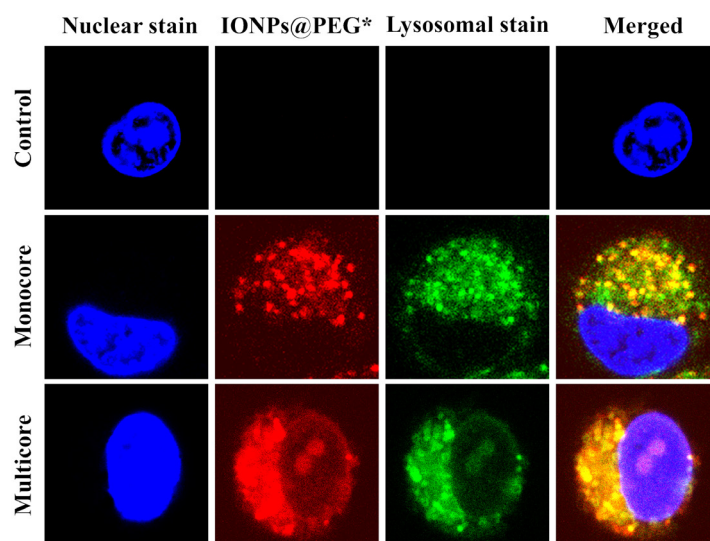


Figure 6 Intracellular distribution of IONPs in U87 glioblastoma cells. Cells were incubated with IONPs conjugated to DY700 (red) for 24 h at $100 \mu\text{g}\cdot\text{mL}^{-1}$. They were visualised by fluorescence confocal microscopy at $63\times$ magnification. The nucleus (blue) was stained with Hoechst 33342 ($2 \mu\text{g}\cdot\text{mL}^{-1}$), the lysosomes (green) with LysoTracker™ green (100 nM).

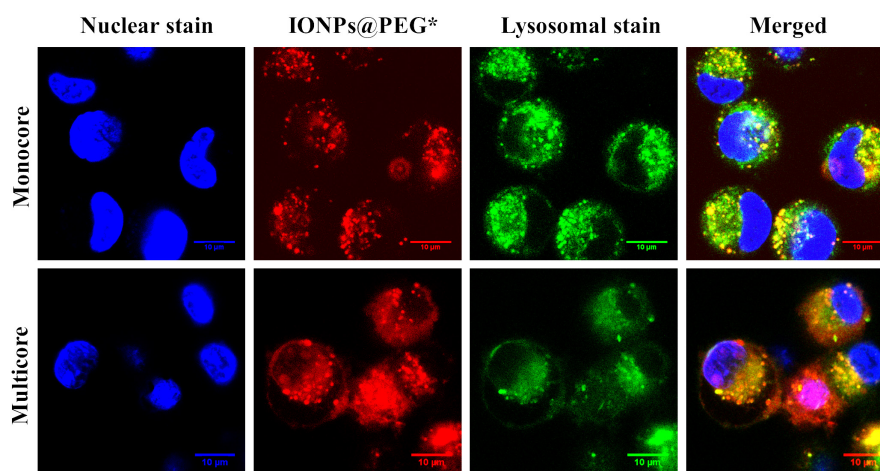


Figure 7 Intracellular distribution of IONPs@PEG* in U87 Glioblastoma cells. Cells were incubated with IONPs@PEG* conjugated to DY700* (red) for 24 h at $100 \mu\text{g}/\text{mL}$. They were visualized by fluorescence confocal microscopy at $60\times$ magnification. The nucleus (blue) was stained with Hoechst 33342 ($2 \mu\text{g}/\text{mL}$), the lysosomes (green) with LysoTracker green (100 nM).

A strong red fluorescent signal ascribed to DY700* was detected, evidencing the presence of the IONPs@PEG*. Images captured at different confocal section planes assessed that they were located inside the cytoplasm and located in the vicinity of the nucleus. This aspect and range of sizes of fluorescent spots suggested an endocytosis pathway, and most likely corresponded to lysosomes. Therefore the green fluorescent LysoTracker™ dye was used as confirmation, as its signal was observed in cells that were incubated with the IONPs@PEG*, while for the control cells, no

lysosomes were visible. The red fluorescence spots of IONPs@PEG* were exclusively co-localized with the green fluorescent signal from lysosomes resulting in yellow fluorescent spots, a co-localization technique used by Connord *et al.* to prove the utmost important role played by lysosomes in intracellular MH.[23] This further suggested that the degradative enzymes contained within the lysosomes were unable to alter the fluorescence signal of the DY700* probes.

3.2.4. Observation of nanoparticles-cells interactions by transmission electron microscopy

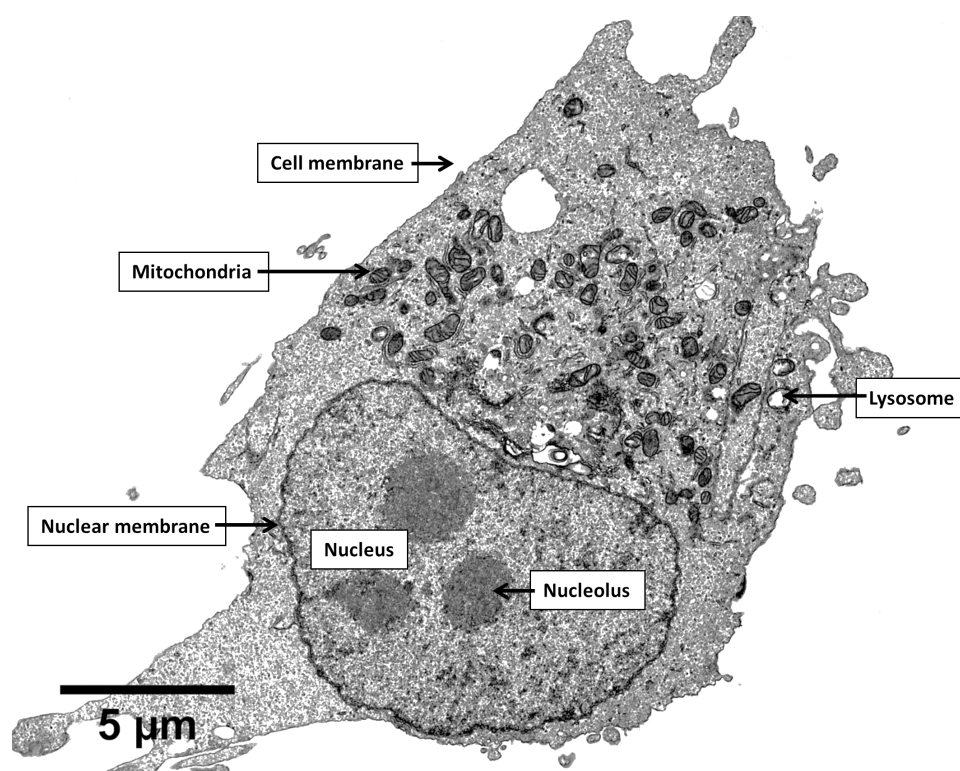


Figure 8 TEM micrograph of an U87 cell incubated with IONPs@PEG*.

The U87 cells were also analyzed by transmission electron microscopy (TEM) to observe the sub-cellular localization of the IONPs@PEG*, giving histological cross-sections at much higher resolution than confocal microscopy (**Figure 8**). The microstructure of the cells was well observable thanks to the small thickness of the sample section (65 nm) and staining with an osmium complex to enhance the contrast. Compartmentalization being the main feature of eukaryotes, various membrane-bound organelles were revealed inside the cytoplasm. The cell-membrane, the mitochondria, the nuclear membrane, nucleus and nucleolus were easily recognizable from their specific morphologies and localization. The structure of the cell was bipolar, with a nucleus on one side and the organelles on the other side, while large portions of cytoplasm were left without apparent content. U87 cells incubated with monocoresh (Figure 9 a-c) or multicore IONPs@PEG* (Figure 9 d-f) were imaged after microtome preparation.

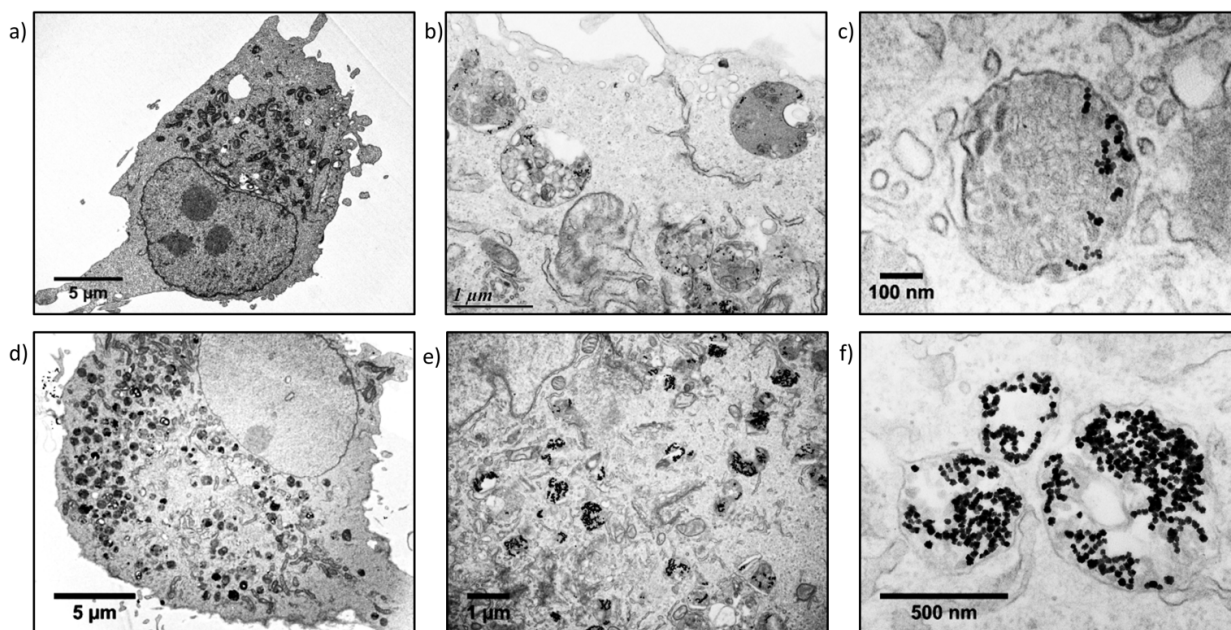


Figure 9 TEM micrograph of U87 cells incubated with **a-c)** monocore or **d-f)** multicore IONPs@PEG*.

The lysosomes were recognizable by their spherical morphology and diameter of the order of 1 μm . They were also located on one side of the nucleus, which was in agreement with what was observed by confocal microscopy, where blue nuclei and red lysosomes formed dipolar structures. The electron scattering contrast of the lysosomes depended on the quantity of IONPs contained inside, and on the age of the lysosome. Early endocytic compartments had a clear shade of grey while later ones were darker due to the fusion with other endocytic structures. Lysosomes were in greater numbers and encapsulated larger quantities of IONPs in the case of cells incubated with multicore IONPs@PEG*. This observation by TEM correlated well with the data obtained by flow cytometry: in both cases the sizes of the cells were similar, only the granularity and the complexity of the microstructures inside of the cells appeared differently.

The internalization pathway could be observed on three micrographs (**Figure 10 a-d**). They offered a glimpse of the different stages when IONPs@PEG* entered inside the cells. Several IONPs@PEG* were found outside of the cells, whereas the preparation of the sample for TEM required several washes, and IONPs@PEG* outside of cells were visible only in the close vicinity of the cells. This suggested that there was already an interaction between the cell surface and the IONPs@PEG*, likely *via* decoration by the IONPs@PEG* of polysaccharide chains linked to the plasma membrane (glycocalix). The morphology adopted by the plasma membrane was similar to the macropinocytosis or phagocytosis pathways described in most popular reviews or textbooks,[24] with the membrane maximizing its contact with the IONPs outside of the cells by deforming itself and reaching out of the cell boundaries to engulf the nanoparticles together with a volume of the outer aqueous medium.[22, 25] This explained also why clear spherical structures having the same electron

contrast as the outer medium of the cells were observed close to the inside of the membrane, while darker ones were observed closer to the nucleus, suggesting that the endocytic compartments traveled from the boundaries of the cell towards its centre, becoming more and more dense along the process.[26] In each case, the morphology and size of the IONPs@PEG* were not modified inside the cells, meaning that the reported mechanisms of IONP degradation and iron metabolising did not start to occur within the 24 hour incubation period.[27]

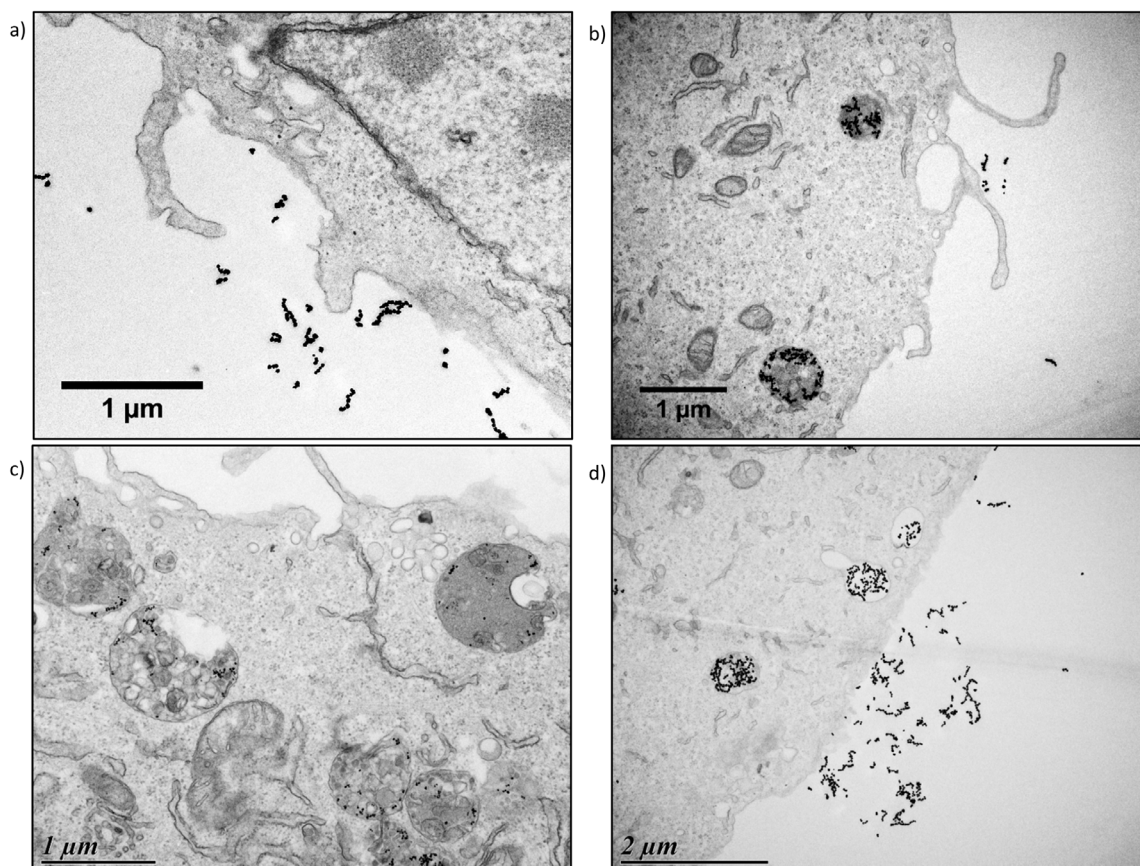


Figure 10 TEM micrograph of U87 cells evidencing the internalization pathway of IONPs@PEG* inside the cells. **a-b)** Cell membrane deformation in morphologies typical of macropinocytosis. **c-d)** Endocytic compartments at different stages.

3.3. Effect of magnetic hyperthermia over the cells' viabilities

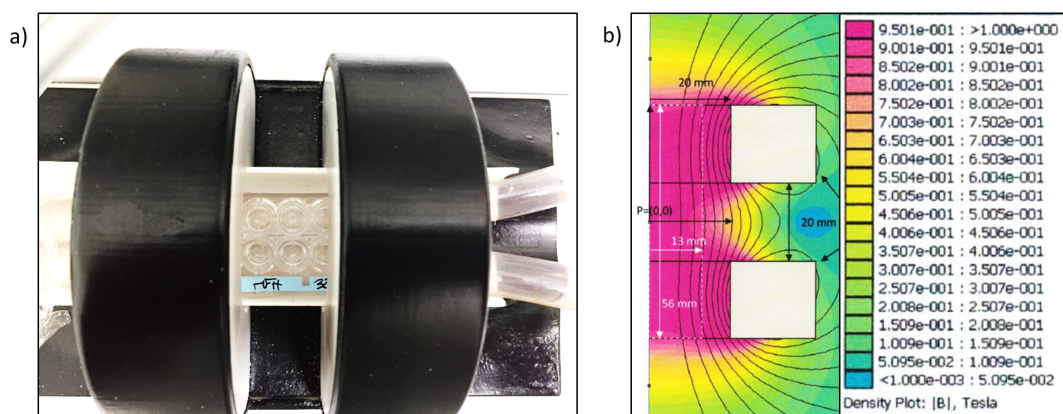


Figure 11 a) Set-up used for magnetic hyperthermia on the U87 glioblastoma cells. The Nunc™ Lab-Tek® chamber was placed in the central region between the two coils. **b)** Finite element model simulation of the magnetic field intensity generated in the two-coils set-up. Six wells could fit in the homogeneous field zone.

After studying extensively the internalization of IONPs@PEG* in U87 glioblastoma cells, we focused on treating them by applying an alternating magnetic field (AMF), with a generator (DM100) and 2-coil inductor (DM3) from the nanoscale Biomagnetics (nB) company (Zaragoza, Spain), specially designed for biological *in vivo* experimentation (**Figure 11 a**). The sample (16-well microscopy glass slide) was placed inside of a Helmholtz-like induction coil pair, thermalized at 37.5 °C using a water jacket. The 2-coil configuration of the inductor helped observing the wells containing the cells while performing magnetic hyperthermia during 30 min. The wells were placed in the region of maximum and homogeneous field intensity (**Figure 11 b**).

The viability of the U87 cells was assayed by BLI readout based on luciferase activity,[17] enabling to test the cytotoxicity of IONPs@PEG*, either happening during IONPs@PEG* internalization or after applying an external AMF to perform magnetic hyperthermia. Circular regions of interests (ROIs) were integrated on BLI images of U87 cells taken 24 hours after AMF treatment to quantify the bioluminescence signal, for monocore (**Figure 12 a**) or multicore (**Figure 12 c**) IONPs@PEG*. The cell viability was compared at varying concentrations during incubation, before (blue) or after (red) the AMF application for 30 min, for either monocore (**Figure 12 b**) or multicore (**Figure 12 d**) IONPs@PEG*. For both morphologies, the cytotoxicity without the AMF application remained at a low level on all the range of incubation concentrations explored. On the opposite, the magnetic hyperthermia treatment caused a significant decrease of cell viability, with a death after 24 h of approximately 40 % of the cells with monocores, whatever the concentration incubated. In the case of multicores, cytotoxicity determined 24 h after magnetic hyperthermia was even far more pronounced, leading to the death of the majority (80-90 %) of the cells. Looking at these results, the multicores appeared more efficient compared to monocores for the same conditions in a strategy of treatment of glioblastoma cells by magnetic hyperthermia. This result could be explained by several

reasons. The first reason was the higher internalized quantity of the multicore IONPs@PEG*, as observed by TEM, confocal microscopy, fluorescence imaging, and flow cytometry. Such higher mass of internalized heating agents led theoretically to higher elevation of temperature, although a real temperature increase inside the cells induced by MH is still a subject of debate in the community, due to their too small size for the heating power to compensate the dominant thermal losses into the surrounding environment.[28] Non-thermal effects were also hypothesized to contribute to the cytotoxicity in cellular MH, like for example a direct mechanical destabilization of the cell membranes (the plasma membrane during IONP internalization and later the lysosome membrane): Also called “nanoflowers” as ascribed to their morphology, multicore IONPs@PEG* exhibited a pronounced surface roughness that might have caused membrane deformation and tearing, when comparing the high magnification TEM view of lysosomes loaded with multicores (**Figure 9 f**) to the micrograph of a lysosome filled with monocoers (**Figure 9 c**).

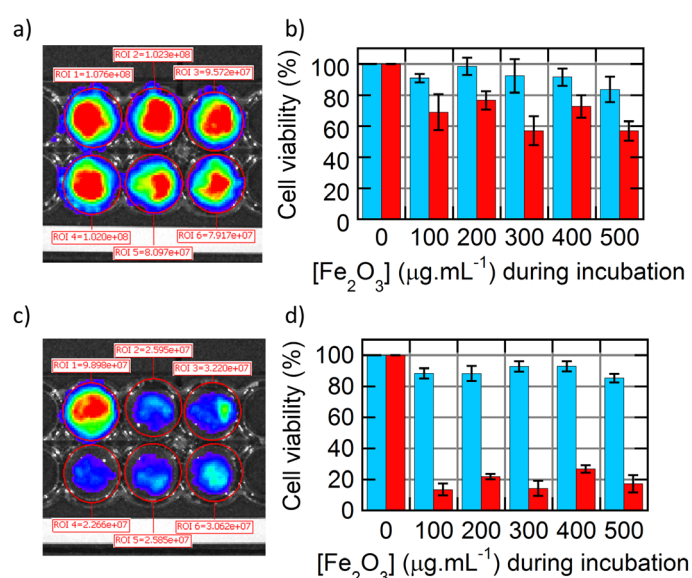


Figure 12 a) Bioluminescence imaging of U87 cells incubated at different concentrations of monocore IONPs@PEG* after AMF application, and b) viability assay obtained from the BLI signal integrated in the ROIs (circles) before (blue) and after AMF application (red). c) BLI of U87 cells incubated at different concentrations of multicore IONPs@PEG* after AMF application, and d) viability assay before (blue) and after AMF application (red).

Another often reported non-thermal effect is the Fenton reaction by which residual Fe²⁺ cations on the iron oxide surface can produce reactive oxygen species (ROS) oxidizing phospholipids and causing the lysosome membrane rupture, as shown in several recent articles to be the main cause of intra-cellular MH.[29-31] Multicore IONPs having a specific surface area typically 60 % higher than smooth spherical IONPs,[12] such non-thermal oxidative contribution to MH would also be larger. The second reason was the highest SAR of the multi-core IONPs (expressed in W.g⁻¹), meaning that they induced higher heating power efficiencies at equal iron oxide concentration compared to monocore spherical IONPs. Taking into account the two effects – SAR and internalized concentration

of $265 \text{ W}\cdot\text{g}^{-1}$ and 800 pg/cell for multicore IONPs as compared respectively to $134 \text{ W}\cdot\text{g}^{-1}$ and 300 pg/cell for monocore IONPs) – the heating power was more than five times higher for multicore compared to monocore IONPs. The higher cytotoxicity at 24 h after 30 min treatment under an AMF with multi-cores (80-90 % compared to 40 %) could be directly correlated to their more efficient heating power, maybe also combined with a mechanical disruption of the plasma and lysosomal membranes induced by their surface roughness.

4. Conclusion

In this chapter, we reported the surface modification of IONPs of two sizes and morphologies (14.5 nm monocores or 29.1 nm multicores) with two molecules: a NIR fluorescent probe (DY700) to allow tracking of the nanoparticles in cells, and a PEG stabilizing brush. This molecular design was completed through a one-pot convergent strategy, in aqueous conditions, and on stable, *i.e.* individually dispersed IONPs. The modified IONPs@PEG* obtained were readily dispersed in water, and could be purified by a simple centrifugation-redispersion process. The interaction of these IONPs@PEG* with cancerous cells was investigated using a bioluminescent human glioblastoma cell line, genetically modified to express the luciferase enzyme as a convenient read-out of cell viability. IONPs@PEG* accumulated in lysosomes, as firstly observed by confocal microscopy, using the LysoTracker™ green dye. There was a direct correlation between the quantity of IONPs@PEG* internalized and the concentration of IONPs@PEG* during incubation, as evidenced by flow cytometry and fluorescence imaging. The number of nanoparticles internalized in 24 h in each cell was evaluated around a few tens of million, in agreement with literature. With much higher resolution, TEM images showed that the morphology of the IONPs was conserved after incubation, even after 24 h, meaning that the IONPs were fairly insensitive of the mechanisms of degradation occurring inside of the lysosomes and keep their heating efficiencies, at least at this time scale. This ability of these IONPs@PEG* to kill cells by magnetic field hyperthermia was studied using a commercial DM3 set-up (nB) by applying an AMF amplitude, frequency, and duration of application suitable for medical applications. The cell viability was assessed quantitatively based on the bioluminescence signal of cells 24 h after the AMF application. The higher efficiency of the multicore IONPs compared to the monocore IONPs was evidenced by an increased cytotoxicity that appeared also to be independent of the iron oxide dose. Therefore multicore IONPs are particularly suitable agents for magnetic hyperthermia treatment of cancerous cells, and a lot of research is currently on-going in our group and others to design molecular coatings providing further functionalities such as cancer cell targeting,[32] or anticancer drug delivery activated by the AMF application.[33]

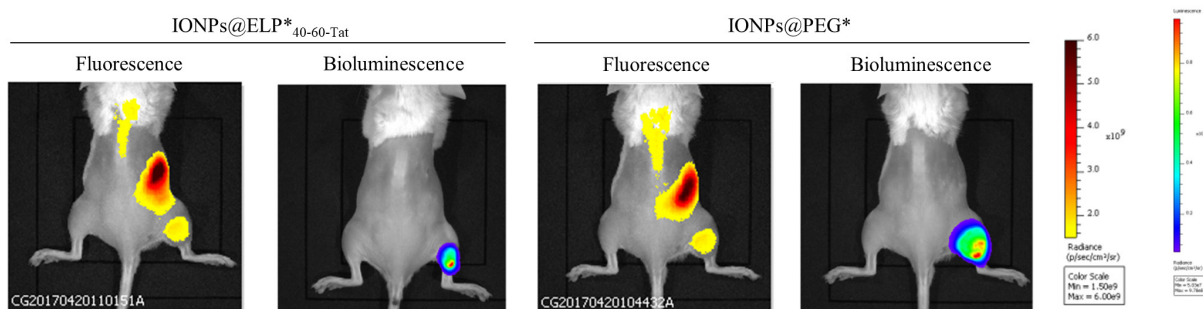
5. References

1. Siegel, R.L., K.D. Miller, and A. Jemal, *Cancer statistics, 2017*. CA: A Cancer Journal for Clinicians, 2017. **67**(1): p. 7-30.
2. Parkin, D., S. Whelan, J. Ferlay, L. Teppo, and D. Thomas, *Cancer in Five Continents Vol. VIII*. 2002, Lyon, France: IARC Scientific Publications.
3. Adamson, C., O.O. Kanu, A.I. Mehta, C. Di, N. Lin, A.K. Mattox, and D.D. Bigner, *Glioblastoma multiforme: a review of where we have been and where we are going*. Expert Opinion on Investigational Drugs, 2009. **18**(8): p. 1061-1083.
4. Walid, M.S., *Prognostic Factors for Long-Term Survival after Glioblastoma*. The Permanente Journal, 2008. **12**(4): p. 45-48.
5. Maier-Hauff, K., R. Rothe, R. Scholz, U. Gneveckow, P. Wust, B. Thiesen, A. Feussner, A. von Deimling, N. Waldoefner, R. Felix, and A. Jordan, *Intracranial ThermoTherapy using Magnetic Nanoparticles Combined with External Beam Radiotherapy: Results of a Feasibility Study on Patients with Glioblastoma Multiforme*. Journal of Neuro-Oncology, 2007. **81**(1): p. 53-60.
6. Maier-Hauff, K., F. Ulrich, D. Nestler, H. Niehoff, P. Wust, B. Thiesen, H. Orawa, V. Budach, and A. Jordan, *Efficacy and safety of intratumoral thermoTherapy using magnetic iron-oxide nanoparticles combined with external beam radiotherapy on patients with recurrent glioblastoma multiforme*. Journal of Neuro-Oncology, 2011. **103**(2): p. 317-324.
7. Silva, A.C., T.R. Oliveira, J.B. Mamani, S.M.F. Malheiros, L. Malavolta, L.F. Pavon, T.T. Sibov, E. Amaro, A. Tannús, E.L.G. Vidoto, M.J. Martins, R.S. Santos, and L.F. Gamarra, *Application of hyperthermia induced by superparamagnetic iron oxide nanoparticles in glioma treatment*. International Journal of Nanomedicine, 2011. **6**: p. 591-603.
8. Périgo, E.A., G. Hemery, O. Sandre, D. Ortega, E. Garaio, F. Plazaola, and F.J. Teran, *Fundamentals and advances in magnetic hyperthermia*. Applied Physics Reviews, 2015. **2**(4): p. 041302.
9. Caruntu, D., G. Caruntu, Y. Chen, C.J. O'Connor, G. Goloverda, and V.L. Kolesnichenko, *Synthesis of Variable-Sized Nanocrystals of Fe₃O₄ with High Surface Reactivity*. Chemistry of Materials, 2004. **16**(25): p. 5527-5534.
10. Lartigue, L., P. Hugounenq, D. Alloyeau, S.P. Clarke, M. Lévy, J.-C. Bacri, R. Bazzi, D.F. Brougham, C. Wilhelm, and F. Gazeau, *Cooperative Organization in Iron Oxide Multi-Core Nanoparticles Potentiates Their Efficiency as Heating Mediators and MRI Contrast Agents*. ACS Nano, 2012. **6**(12): p. 10935-10949.
11. Hugounenq, P., M. Levy, D. Alloyeau, L. Lartigue, E. Dubois, V. Cabuil, C. Ricolleau, S. Roux, C. Wilhelm, F. Gazeau, and R. Bazzi, *Iron Oxide Monocrystalline Nanoflowers for Highly Efficient Magnetic Hyperthermia*. J. Phys. Chem. C, 2012. **116**(29): p. 15702-15712.
12. Hemery, G., A. Keyes Jr., C., E. Garaio, I. Rodrigo, J.A. Garcia, F. Plazaola, E. Garanger, and O. Sandre, *Tuning sizes, morphologies, and magnetic properties of monocoresh versus multicore iron oxide nanoparticles through the controlled addition of water in the polyol synthesis*. Inorganic Chemistry, 2017. **56**(14): p. 8232-8243.
13. Hergt, R. and S. Dutz, *Magnetic particle hyperthermia—biophysical limitations of a visionary tumour therapy*. Journal of Magnetism and Magnetic Materials, 2007. **311**(1): p. 187-192.
14. Pauli, J., T. Vag, R. Haag, M. Spieles, M. Wenzel, W.A. Kaiser, U. Resch-Genger, and I. Hilger, *An in vitro characterization study of new near infrared dyes for molecular imaging*. European Journal of Medicinal Chemistry, 2009. **44**(9): p. 3496-3503.
15. Germain-Genevois, C., O. Garandeau, and F. Couillaud, *Detection of Brain Tumors and Systemic Metastases Using NanoLuc and Fluc for Dual Reporter Imaging*. Molecular Imaging and Biology, 2016. **18**(1): p. 62-69.
16. Fortin, P.-Y., C. Genevois, A. Koenig, E. Heinrich, I. Texier, and F. Couillaud, *Detection of brain tumors using fluorescence diffuse optical tomography and nanoparticles as contrast agents*. Journal of Biomedical Optics, 2012. **17**(12): p. 126004-126004.
17. Rome, C., H. Loiseau, J. Arsaut, V. Roullot, and F. Couillaud, *Diversity of Contactin mRNA in Human Brain Tumors*. Molecular Carcinogenesis, 2006. **45**: p. 774-785.

18. Devanand, K. and J.C. Selser, *Asymptotic Behavior and Long-Range Interactions in Aqueous Solutions of Poly(ethylene oxide)*. *Macromolecules*, 1991. **24**: p. 5943-5947.
19. Le Coeur, C., J. Teixeira, P. Busch, and S. Longeville, *Compression of random coils due to macromolecular crowding: Scaling effects*. *Physical Review E*, 2010. **81**(6): p. 061914.
20. Brittain, W.J. and S. Minko, *A structural definition of polymer brushes*. *Journal of Polymer Science Part A: Polymer Chemistry*, 2007. **45**(16): p. 3505-3512.
21. Gilbert, B., J.E. Katz, N. Huse, X. Zhang, C. Frandsen, R.W. Falcone, and G.A. Waychunas, *Ultrafast electron and energy transfer in dye-sensitized iron oxide and oxyhydroxide nanoparticles*. *Physical Chemistry Chemical Physics*, 2013. **15**(40): p. 17303-17313.
22. Wilhelm, C., F. Gazeau, J. Roger, J.-N. Pons, and J.-C. Bacri, *Interaction of Anionic Superparamagnetic Nanoparticles with Cells: Kinetic Analyses of Membrane Adsorption and Subsequent Internalization*. *Langmuir*, 2002. **18**: p. 8148-8155.
23. Connord, V., P. Clerc, N. Hallali, D. El Hajj Diab, D. Fourmy, V. Gigoux, and J. Carrey, *Real-Time Analysis of Magnetic Hyperthermia Experiments on Living Cells under a Confocal Microscope*. *Small*, 2015. **11**(20): p. 2437-2445.
24. Hillaireau, H. and P. Couvreur, *Nanocarriers' entry into the cell: relevance to drug delivery*. *Cell. Mol. Life Sci.*, 2009. **66**: p. 2873-2896.
25. Kann, B., H.L. Offerhaus, M. Windbergs, and C. Otto, *Raman microscopy for cellular investigations — From single cell imaging to drug carrier uptake visualization*. *Advanced Drug Delivery Reviews*, 2015. **89**: p. 71-90.
26. Oh, N. and J.-H. Park, *Endocytosis and exocytosis of nanoparticles in mammalian cells*. *International Journal of Nanomedicine*, 2014. **9**(Suppl 1): p. 51-63.
27. Levy, M., N. Luciani, D. Alloyeau, D. Elgrabli, V. Deveaux, C. Pechoux, S. Chat, G. Wang, N. Vats, F. Gendron, S.L. Cécile Factor, A. Luciani, C. Wilhelm, and F. Gazeau, *Long term in vivo biotransformation of iron oxide nanoparticles*. *Biomaterials*, 2011. **32**: p. 3988-3999.
28. Baffou, G., H. Rigneault, D. Marguet, and L. Jullien, *A critique of methods for temperature imaging in single cells*. *Nat Meth*, 2014. **11**(9): p. 899-901.
29. Domenech, M., I. Marrero-Berrios, M. Torres-Lugo, and C. Rinaldi, *Lysosomal Membrane Permeabilization by Targeted Magnetic Nanoparticles in Alternating Magnetic Fields*. *ACS Nano*, 2013. **7**(6): p. 5091-5101.
30. Sanchez, C., D. El Hajj Diab, V. Connord, P. Clerc, E. Meunier, B. Pipy, B. Payré, R.P. Tan, M. Gougeon, J. Carrey, V. Gigoux, and D. Fourmy, *Targeting a G-Protein-Coupled Receptor Overexpressed in Endocrine Tumors by Magnetic Nanoparticles To Induce Cell Death*. *ACS Nano*, 2014. **8**(2): p. 1350-1363.
31. Wydra, R.J., P.G. Rychahou, B.M. Evers, K.W. Anderson, T.D. Dziubla, and J.Z. Hilt, *The role of ROS generation from magnetic nanoparticles in an alternating magnetic field on cytotoxicity*. *Acta Biomaterialia*, 2015. **25**: p. 284-290.
32. Ulbrich, K., K. Holá, V. Šubr, A. Bakandritsos, J. Tuček, and R. Zbořil, *Targeted Drug Delivery with Polymers and Magnetic Nanoparticles: Covalent and Noncovalent Approaches, Release Control, and Clinical Studies*. *Chemical Reviews*, 2016. **116**(9): p. 5338-5431.
33. Mertz, D., O. Sandre, and S. Bégin-Colin, *Drug releasing nanoplatfoms activated by alternating magnetic fields*. *Biochimica et Biophysica Acta (BBA) - General Subjects*, 2017. **1861**(6): p. 1617-1641.

CHAPTER VI

MAGNETIC IRON OXIDE NANOPARTICLES GRAFTED WITH A THERMOSENSITIVE ELASTIN-LIKE POLYPEPTIDE AND A CELL PENETRATING PEPTIDE: AN *IN VITRO* AND *IN VIVO* STUDY



1. Introduction

Cancer is to day one of the leading causes of death in developed countries, among which glioblastoma brain tumors leads to poor prognosis.[1] Different therapies exist, as surgical resection[2] followed by radiotherapy and/or chemotherapy[3]. This combination of therapies to improve the patient's prognosis has also been tried out with magnetic hyperthermia coupled with X-ray radiotherapy. This recent use of magnetic iron oxide nanoparticles to treat glioblastoma has shown promising results, doubling the life expectancy of patients.[4] This article focuses on magnetic hyperthermia possibly associated with chemotherapy. With the aim to select the best strategy to couple these two treatments, we developed a nanovector able either to deposit a thermal dose internally or to release a drug under application of an alternating magnetic field (AMF). Multiple designs of drug-carrier nanoparticles have been reported in the literature to improve the targeting efficiency and solve the poor solubility issue of a vast percentage of drug molecules developed by the pharmaceutical industry.[5-8] The best candidates for the magnetic mediator part are still iron oxide nanoparticles, thanks to their biocompatibility, large surface to volume ratio and outstanding performances as heating mediators. Vectors combining both magnetic and thermosensitive properties can theoretically treat any part of the body as radiofrequency alternating magnetic fields (AMF) are able to penetrate deeply in tissues. The concepts of drug releasing by AMF have been presented in different reviews.[9, 10] The designs typically rely on the destabilization of membranes,[11] a lower critical solubility transition (LCST) properties,[12, 13] or cleavable bonds sensitive to temperature or pH.[14]

Though the internalization pathway of nanoparticles in cells is well-described,[15, 16] the cells death mechanism under magnetic hyperthermia is still actively studied. For magnetic hyperthermia alone, cytotoxicity is tentatively explained by the so called "cold hyperthermia" or intra-lysosomal hyperthermia conditions, through generation of reactive oxygen species (ROS) causing lipid oxidation and lysosome membrane permeation[17, 18]. On the other hand, IONPs were also shown to cause anti-inflammatory effect *in vivo* by lowering the pro-inflammatory cell markers and ROS levels.[19] For magnetic hyperthermia coupled with drug delivery, a strategy sometimes called "magneto-chemotherapy"[11] or "thermo-chemotherapy"[20], the mechanism is more complex and relies on the molecular design. But the mechanism of drug release under magnetic hyperthermia after cell internalization and entrapment of the nanovector in endocytic compartments is still a debated topic. Depending on the strategy of release, the liberation of the drug may start in endocytic compartments by passive (enzymatic degradation, pH degradation) or active means (thermoreponsive systems). [21-23] At this stage, the drug is liberated from the nanocarrier but is still trapped inside of the endocytic compartments. The liberation of the drug needs to occur were it is active, either in the cytosol of the cells or in organelles (e.g. nucleus for DNA intercalating agents). Alternatively, a limited number of nanoparticles (NPs) such as gold NPs with an arginine coating were shown to escape the endocytosis pathway and to translocate through the plasma membrane, enabling direct delivery of proteins to

cytoplasm.[24] In the case of IONPs, the leakage of lysosomes was proved by the activity of enzymes in the cytosol,[25] but the synergistic activity of drug delivery coupled with magnetic hyperthermia is still to be unraveled.

In this chapter, we studied the accumulation of IONPs of two different coatings in the cells for long durations (superior to 24 h). This allowed following the whole internalization pathway of the nanoparticles inside the cells, and monitoring the aging of the endocytic compartments. The influence of the nanoparticles on the cells' life cycle was also studied through a bioluminescence-based assay, dependent both on the proliferation of cells and their viability. To understand the magnetic hyperthermia effect on biological cells, especially on their microstructure of the lysosome and on the liberation of the lysosomes' content, we designed a nano-platform with multiple functionalities, by grafting magnetic iron oxide nanoparticles with an elastin-like polypeptide (ELP) and a fluorescent probe, leading to a core-shell structure which has both magnetic, thermosensitive, cell-penetrating and fluorescent capabilities. The cellular uptake of those peptide-coated IONPs was compared to control IONPs made from the same magnetic cores coated by a repulsive PEG layer. Complementary to *in vitro* experiments, these two types of IONPs were administered to mice both by intravenous (systemic) or intra-tumoral (local) injection. Their fate was followed using fluorescence imaging, and their use for magnetic hyperthermia treatment was evaluated by bioluminescence imaging (BLI) and quantification of tumor activities.

2. Materials and methods

2.1. IONP synthesis

Magnetic iron oxide nanoparticles were produced by the polyol route by adapting the conditions of reaction previously reported by Caruntu *et al.* Controlled fractions of water were injected in the polyol medium to drive the morphology of the IONPs (*i.e.* moncore or multicore), as reported recently by our group.[26] 1.5 eq. of 2-aminoethylphosphonic acid (AEP) (Sigma Aldrich) were reacted with 1 eq. of NHS-ester modified DY700 fluorescent probe (Dyomics, Germany) in DMSO for 24 h at room temperature under agitation. The phosphonate modified DY700 was later referred to as DY700*. 1 eq. of tris(2-carboxyethyl)phosphine hydrochloride (TCEP) (98%, ACROS Organics) was dissolved with 1 eq. of poly(ethylene glycol) methyl ether thiol (mPEG-SH, average molar mass $M_n=6000 \text{ g}\cdot\text{mol}^{-1}$, Sigma Aldrich) in 50 mM phosphate buffer (PB) at pH 7.4 for 24 h. This step allowed the reduction of the disulfide bonds between (mPEG-S)₂ dimers, providing reactive thiols. Separately, the heterofunctional cross-linker was produced by reacting 5 eq. of AEP with 1 eq. of N-succinimidyl-4-maleimidobutyrate (GMBS, TCI Europe) in PB for 24 h in cold conditions with an ice bath, to prevent the too fast hydrolysis of the NHS ester. The two solutions were mixed after 24 h and let to react for another 24 h. The product later referred to as PEG* was purified by dialysis against milliQ water for 3 consecutive days, using a 5 kDa membrane, and renewing 6 times the dialysis bath. The ELP_{40-60-Tat} was modified using the same protocol, with a first step of reduction and a second step

of chemical modification with the heterofunctional cross-linker. The purification was done by inverse transition cycling; a fast and efficient process based on the thermosensitive properties of the ELP*_{40-60-Tat}.

0.6 % w/w eq. of DY700* (corresponding to 20 molecules per nanoparticle) were then grafted onto IONPs in water acidified to pH=2.5 with dilute nitric acid. After 1 h, 28 % w/w of ELP*_{40-60-Tat} (28 % w/w for PEG*) was added to the dispersion of IONPs. These proportions lead to theoretical grafting densities of $\sigma = 1/D^2 = 0.06$ molecular chains per nm² (0.4 nm⁻² for PEG*) or reduced tethered densities $\Sigma = \pi R_G^2/D^2 = 15$ in both cases. The reduced tethered density of PEG* was calculated with the radius of gyration estimated using scaling laws reported by Devanand[27] ($R_G(\text{nm}) = 0.0215 \cdot M_n^{0.583}$) or by Le Coeur *et al.*[28] ($R_G(\text{nm}) = 0.066466 \cdot M_n^{0.45224}$). Even though the equations are different (respectively good and Theta solvents), they both provide radii of gyration of $R_G = 3.4$ nm for PEG with a molar weight of 6,000 g·mol⁻¹. The scaling law reported by Garanger *et al.*[29] ($R_G(\text{nm}) = 0.505 \cdot M_n^{0.486}$) was used to estimate the radius of gyration of the ELP*_{40-60-Tat} chains in solution, with a value of $R_G = 8.8$ nm. After 2 h of reaction, the pH was corrected from acidic to neutral using Tris 50 mM. The solutions were purified from the excess of DY700*, PEG*, and ELP*_{40-60-Tat} by 3 cycles of centrifugation-redispersion at 18,000 g, 1 h at 25°C, directly followed by 30 min at 1 °C to increase the viscosity of the solvent and avoid pellet dispersion during the deceleration phase. The supernatant was renewed between the cycles of centrifugation-redispersion. Following our calculations, up to 99.9 % of the original solvent was removed this way.

2.2. Transmission electron microscopy on nanoparticles

A Hitachi™ H7650 microscope was used at an acceleration voltage of 80 kV. Images were acquired with an ORIUS™ SC1000 large format (11 MPx) camera. The sample was prepared by nebulizing the IONP dispersion at a concentration of 1 g·L⁻¹ on Formvar™ carbon-coated 200 mesh copper grids from Agar Scientific™ followed by a drying step at room temperature. The IONP size distribution was obtained by measuring 100 nanoparticles with the ImageJ freeware (<https://imagej.nih.gov/ij/>). The size-histogram was fitted to a log-normal distribution law of diameters $P(d)$ with optimized values of median diameter α and non-dimensioned width β :

$$P(d) = \frac{1}{d \cdot \beta \sqrt{2\pi}} \cdot \exp\left(\frac{-(\ln(d) - \ln(\alpha))^2}{2\beta^2}\right)$$

The mean size $d_0 = \langle d \rangle$ (number-average) and standard deviation $\sigma = \langle (d - \langle d \rangle)^2 \rangle^{1/2}$ were calculated with the classical Gaussian statistics formulas.

2.3. Dynamic light scattering

Z-average hydrodynamic diameters (D_h) and polydispersity indexes (PDI) were acquired on a Nanosizer™ Nano ZS90 instrument (Malvern™, UK). DLS data was converted into size distributions using a 2nd order Cumulant fit. The PDI were defined as the ratio of the 2nd order coefficient to the square of the 1st order one in the series.[30]

2.4. TGA

TGA analyses were carried on a Q500 apparatus from TA instruments. A temperature ramp of 10 °C·min⁻¹ from RT to 600 °C was applied, with an oxygen flow. The data was analyzed using the software Universal Analyses.

2.5. ATR-IR

ATR-IR spectroscopy was carried on a GladiATR™ device from Pike Technologies mounted on a Bruker Vertex™ 70 FT-IR spectrometer. Typically a drop of sample was dried on the diamond prism using a hair blower followed by a 64 scans measurement. Spectra were analyzed with the Opus™ software.

2.6. Cell line generation and culture

U87 human glioma cell line was obtained from the American Tissue Culture Collection (ATCC, Manassas, Virginia). The bioluminescent U87-CMV-lucF cell line was generated as previously reported.[31] Cells were cultivated in Dulbecco's modified Eagle's medium (DMEM, Invitrogen, Carlsbad, California) supplemented with 10% foetal bovine serum (FBS, Invitrogen), 1% nonessential amino acid (MEM NEAA, Invitrogen), 1% antimycotic-antibiotic mix (PSA, Invitrogen), and 50 µg·mL⁻¹ Hygromycin B (Euromedex, Souffelweyersheim, France). Cell line was maintained in a humidified 5% CO₂ incubator at 37°C.

2.7. Incubation of cells with IONPs

5000 cells per well were plated in 16-well microscopy chambers (Nunc™ Lab-Tek®, Thermo Fisher) 24 h before experiments. Determined concentrations of IONPs dispersed in supplemented DMEM (0, 100, 200, 300, 400 or 500 µg·mL⁻¹) were added to the cells for 24 h of incubation. They were then washed 2 times with 100 µL of PBS before addition of 100 µL of fresh supplemented DMEM.

2.8. Laser scanning confocal microscopy (LSCM)

22,500 cells per well were plated in 24-well plates 24 h before experiments and then incubated with IONPs conjugated to the NIR fluorescent probe DY700* (Dyomics GmbH) for 24 h at 100 µg·mL⁻¹. They were washed with PBS before fluorescent staining. The blue fluorescent probe Hoechst 33342 (Thermo Fisher Scientific) was used at a concentration of 2 µg·mL⁻¹ in PBS for 5 min at 37 °C to stain the nuclei. The green fluorescent probe LysoTracker™ was used at a concentration of 100 nM in PBS for 1 min at RT to stain the lysosomes. The cells were then harvested with trypsin for 5 min at RT, suspended in PBS and centrifuged for 5 min at 300 g. They were re-suspended in 200 µL of PBS supplemented with 0.5 % of FBS and 2 mM of EDTA. They were preserved on ice to prevent adhesion, before observation. Samples cells were imaged on an inverted confocal microscope Leica TCS SP5 equipped with an Acousto-Optical Beam Splitter (AOBS) and using a 63× lens (Leica HCX PL APO lambda blue 63.0 × 1.40 oil UV) in fluorescence mode. Confocal images were acquired using the Leica TCS software in sequential mode to avoid the overlapped emission as follows: Blue Hoechst

33342 was excited with a laser diode at 405 nm (6%) and measured with emission setting at 410-510 nm, green LysoTracker™ was excited with a DPSS diode at 561 nm (53%) using a window at 570-650 nm and red DY700 was excited with a Helium-Neon laser at 633 nm (90%) using a window at 640-770nm. LCSM images were collected at 400 Hz scan rates with a line average of 4 and a format of 1024×1024 pixels. The transmission mode images were acquired using the Helium-Neon laser at 633 nm (15%). A Z-stack of 50 frames covering a depth of 25 µm was carried out for assessment of label distribution across the cell using the sequential mode. PMT gain and offset configurations were set up on control cells so as to correct images from green and red auto-fluorescence.

2.9. Fluorescence and bioluminescence imaging

A Lumina LT instrument (Perkin Elmer Inc., Boston, MA, USA) was used for fluorescence and bioluminescence imaging (BLI) at Vivoptic (UMS 3767 – Univ. Bordeaux). For BLI, the cells were incubated for 5 min at RT with a 0.6 mM solution of D-luciferin in PBS (Promega, Madison, WI, USA). Bioluminescence images (1 min acquisition, 4×4 binning) and photographs (100 ms) were acquired successively. Fluorescence images (1 s acquisition, excitation at 640 nm, 695-770 nm filter emission, 4×4 binning) and photographs (100 ms) were also acquired successively. The Living Image software was used to analyze the images.

2.10. Transmission electron microscopy on cells

Glial U87 cells were cultivated on 16-well optical glass supports (Nunc™ 178599 Lab-Tek® Chamber Slide™ System, Glass, Volume: 0.1-0.2 mL, Culture Area: 0.4 cm²/well). After incubation (24 h) with the IONPs, cells were washed two times with PBS, fixed with 1.6 % (v/v) paraformaldehyde 2 % (v/v) glutaraldehyde in 0.08 M cacodylate buffer (pH 7.4) during 30 min minimum at room temperature (RT), washed in 0.1 M cacodylate buffer (pH 7.4) and then post-fixed in a mix of 1% osmium tetroxide (v/v) / 1 % potassium ferricyanide K₃Fe(CN)₆ (p/v) in 0.1 M cacodylate buffer during 2 hours on ice in the dark. After washing in water, samples were stained in block in 0.5 % (v/v) aqueous uranyl acetate solution during 30 min, in the dark, at RT. Subsequently, cells were washed in water then dehydrated through a series of graded ethanol and embedded in a mixture of pure ethanol and epoxy resin (Epon 812; Delta Microscopies, Toulouse, France) 50/50 (v/v) during 2 h and then in 100 % resin overnight at RT. The polymerization of the resin was carried out over a period between 24-48 h at 60 °C. Samples were then sectioned using a diamond knife (Diatome, Biel-Bienne, Switzerland) on an ultramicrotome (EM UCT, Leica Microsystems, Vienna, Austria). Ultrathin sections (65 nm) were picked up on copper grids and then stained with Uranyless (Delta Microscopies, Toulouse, France) and lead citrate. Grids were examined with a Transmission Electron Microscope (H7650, Hitachi, Tokyo, Japan) at 80 kV in High Contrast Mode.

2.11. Magnetic hyperthermia

The applied radiofrequency AMF was generated using a DM3 applicator for *in vivo* MFH (nB nanoScale Biomagnetics, Zaragoza, Spain). Cells (5000 cells per well) were plated in 16-well Nunc™

Lab-Tek[®] microscopy chambers (Thermo Fisher) 24 h before experiments. They were then incubated with 100 μL of IONPs at 100 $\mu\text{g}\cdot\text{mL}^{-1}$ in supplemented DMEM for 24 h. They were finally washed with 2 times 100 μL of PBS and 100 μL of fresh supplemented DMEM. The Nunc[™] Lab-Tek[®] microscopy chamber was placed in the space between the two coils of the DM3 applicator (**Figure 11** in previous chapter). Cells were thermalized at 37.5 $^{\circ}\text{C}$ using a water bath connected to a water tubing jacket. The temperature of the sample was monitored using a fiber optic sensor (Neoptix[™], Québec city, Canada). The alternating magnetic field was set at a frequency of 473 kHz, 12 $\text{kA}\cdot\text{m}^{-1}$ of amplitude, and applied for 30 min. The cells were put back in the incubator at 37 $^{\circ}\text{C}$ / 5 % CO_2 and observed by bioluminescence and fluorescence imaging 24 h later.

3. Results and discussion

3.1. Synthesis strategy of the thermosensitive, cell-penetrating, fluorescent and magnetic nanoparticles

Iron oxide nanoparticles (IONPs) were produced by the forced hydrolysis pathway in a mixture of polyol and poly(hydroxy) amine. A spherical monocoresh morphology was selected by the controlled addition of water to the solvent and no-stirring condition during the synthesis, as previously reported elsewhere.[32] A diblock elastin-like polypeptide (ELP) terminated by a Tat sequence MGCGWPG-(VPGVG)₄₀-(VPGAG-VPGGG)₃₀-PGGS-YGRKKRRQRRR was used to modify the surface of the IONPs. The leader polypeptide block MGCGWPG was chemically modified with a heterofunctional cross-linker AEP-GMBS containing a maleimide group at one end and a phosphonic acid moiety at the other end. The maleimide was reacted with the thiol of the cysteine in a Mikael-type addition. The second block (VPGVG)₄₀ of the ELP_{40-60-Tat} is thermosensitive, with a cloud point at 42 $^{\circ}\text{C}$. The third block (VPG(A/G)G)₆₀ is hydrophilic and was later used to stabilize the IONPs in aqueous conditions. The arginine rich YGRKKRRQRRR trailer block is a derivative of the trans-activator of transcription (Tat) sequence of the HIV-1 capsid, and was later used to enhance the cell-penetrating properties of the IONPs. A poly(ethylene glycol) (PEG) terminated at one end with a thiol (mPEG-SH) was also chemically modified with the AEP-GMBS linker previously described to introduce a phosphonic acid anchor group. The near infrared (NIR) fluorescent dye DY700 was also grafted using the phosphonic acid functionalization strategy to track the IONPs in cells and in mice (**Figure 1 a**). In this study, IONPs were modified with DY700* and either with the ELP*_{40-60-Tat} or the PEG*, allowing comparing the properties brought from the surface modification of the nanoparticles for the same iron oxide cores.

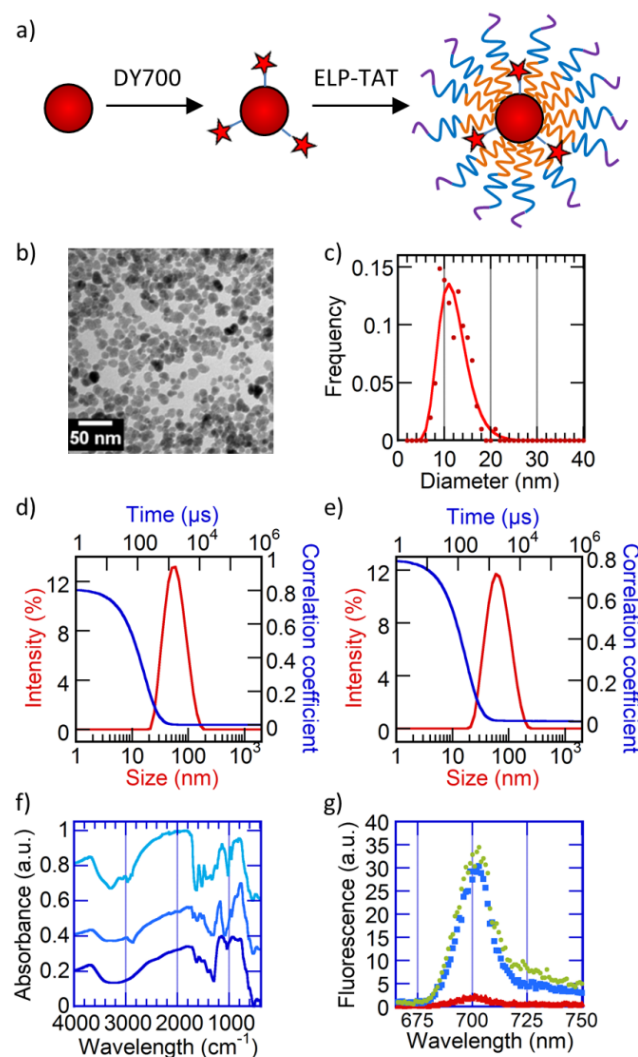


Figure 1 a) Schematic illustration of the functionalization of IONPs with the DY700 fluorescent probe and the ELP*_{40-60-Tat} cell-penetrating and thermosensitive peptide b) TEM micrograph of the iron oxide nanoparticles. c) Histogram of the diameters measured from TEM (11.7 ± 3.1 nm) fitted by a Log-normal size-distribution. DLS diagrams of d) IONPs grafted with PEG and e) IONPs grafted with ELP*_{40-60-Tat}. f) ATR-IR absorbance spectra of the bare and modified IONPs. From top to bottom: IONPs@ELP*_{40-60-Tat}, IONPs@PEG* and bare IONPs. g) Fluorescence measurement of the IONPs modified with a fluorescent probe and PEG* (blue squares), ELP*_{40-60-Tat} (green dots) or bare IONPs (red triangles).

The IONPs selected for this chemical modification were imaged by TEM and their diameters were measured, leading to an average diameter of 11.7 nm, and a standard deviation of 3.1 nm (**Figure 1 b-c**). The phosphonic acid functionality introduced on the polymer chain-ends was used for the conjugation of the ELP*_{40-60-Tat} or PEG* with the IONPs. The IONPs and peptide or polymer chains were conjugated by mixing in weakly acidic aqueous conditions, in a one-pot single step. During the surface modification, the IONPs always formed a stable suspension, possibly improving the grafting efficiency. The resulting core-shell nanoparticles were then purified by cycles of centrifugation-redispersion, yielding nanoparticles stable at physiological pH, as measured by DLS in Tris 50 mM buffer (**Figure 1 d-e**). The bare IONP sample was measured in water acidified at pH=2.5 with HNO₃

to have a stable sample. The hydrodynamic diameters measured by DLS are reported in the following table:

Table 1 Hydrodynamic diameters and polydispersity indexes of bare iron oxide nanoparticles, and nanoparticles grafted with PEG* or with the ELP*_{40-60-Tat}.

	D _h (nm)	PDI
IONPs	43.9	0.22
IONPs@PEG*	53.7	0.17
IONPs@ELP* _{40-60-Tat}	60.0	0.22

DLS evidenced that stable dispersions were obtained, with low polydispersity index, *i.e.* PDI~0.2. The increased diameters confirmed the surface modifications of the IONPs, as additional shell layers were grafted. The small curvature radius of the IONPs (5.9 nm), as calculated from TEM micrographs, was taken into account to estimate the molecular conformation of the tethered polymer chains through the Daoud-Cotton[33] or Birhstein-Zhulina[34] model, revised by Lin and Gast who introduced pre-factors.[35] The grafting yield was estimated by thermogravimetric analyses (TGA) in order to describe the surface state.

Table 2 Characteristics of the iron oxide nanoparticles grafted with either ELP*_{40-60-Tat} or PEG*, calculated from thermo-gravimetric analyses.

	IONPs@ELP* _{40-60-Tat}	IONPs@PEG*
w/w % of organic material	21	13
Chains per nanoparticle	19	63
Grafting density (chain per nm ²)	0.04	0.15
Reduced tethered density Σ	10	5.3

Weight ratios of organic to inorganic material were obtained. For the determination of the parameters described above, the following hypotheses were made: *i*) the nanoparticles were considered to be spherical, and *ii*) the surface of the spheres had a negligible roughness. The average number of chains per nanoparticle was determined from the molecular weights of the ELP_{40-60-Tat} and PEG (respectively 41,260 and 6,000 g·mol⁻¹). The grafting densities were estimated by taking into account the total surface that was available for the grafting and the total number of chains of ELP*_{40-60-TAT} and PEG*. As there were less ELP*_{40-60-Tat} chains compared to PEG*, the distance *D* between two anchoring sites was larger, leading to larger surface areas covered by a single chain. Finally, the reduced tethered densities Σ were estimated:

$$\Sigma = \frac{\pi \cdot R_g^2}{D^2} \quad \begin{array}{l} R_g \text{ is the radius of gyration of chains in solution} \\ D \text{ is the distance between grafting points} \end{array}$$

This a-dimensional number gives an estimate on the state of the chains at the surface, from “mushroom” to “brush” conformations[36]. The values of Σ represent the ratio of the projected surface

area of a free non-overlapping single chain normally filled under the same solvent conditions by the surface area occupied by a chain grafted on the surface. With values of $\Sigma=10$ for the ELP*_{40-60-Tat} and $\Sigma=5.3$ for PEG*, the chains were in both cases strongly overlapping and interacting, leading to brushes protruding into solvent and providing steric stability to the grafted IONPs. The higher value of Σ for a lower number of ELP*_{40-60-Tat} chains compared to PEG* came from their difference of molecular weight and therefore their difference of radius of gyration (8.8 nm against 3.4 nm). The hydrated shell thickness could be estimated using formulas introduced by Birshtein and Zhulina to describe the curvature of a polymer brush around a spherical particle for the Theta solvent regime[34] (the Daoud-Cotton model being derived in the good solvent case) that could be approximated by $H = R_g \cdot (R/D)^{0.5}$. The brush height was estimated to be 23.3 nm for the ELP*_{40-60-Tat}, leading to an overall diameter of 58.6 nm as compared to 60 nm measured by DLS. The same calculation was made for PEG* grafted IONPs: the brush height was estimated to be 6.7 nm, which would have led to an overall diameter of 25.5 nm much lower than the 54 nm measured by DLS. In general, the diameter measured by DLS is overestimated as polydispersity and the presence of clusters shift the intensity average diameter toward larger values. For bare uncoated IONPs, the diameter measured by TEM was of 11.7 nm, while DLS provided a value of 44 nm in aqueous solution acidified at pH2 with HNO₃ contrary to the coated samples buffered at pH7 with 50 mM Tris. The theoretical brush height and the one reported by DLS were compared with caution, but in both cases, the surface modifications with PEG* and ELP*_{40-60-Tat} led to a consequent increase of hydrodynamic diameter (**Table 1**).

Aside from DLS and TGA, the surface modification was assessed by attenuated total reflection infrared (ATR-IR) spectroscopy (**Figure 1 f**). Bare IONPs presented a broad peak in the 3000-3500 cm⁻¹ range corresponding to stretching vibrations of surface hydroxyls Fe–OH and Fe–H₂O⁺. The peak at 1650 cm⁻¹ corresponded to their bending vibrations. The strong peak starting at 540 cm⁻¹ corresponded to the stretching vibration of the Fe–O bond in the matrix. IONPs modified with PEG showed an ether stretch at 1000-1300 cm⁻¹ and an alkyl C-H stretch in the range of 2950 – 2850 cm⁻¹. This alkyl stretch was also present for the ELP*_{40-60-Tat} modified IONPs, with additional peaks corresponding to amide C=O stretch at 1690 – 1630 cm⁻¹, and amide N-H stretch at 3700 – 3500 cm⁻¹. These observations were in agreement with the surface modification of the IONPs with respectively PEG* and the ELP*_{40-60-Tat}. The grafting of the fluorescent probe DY700* was assessed by measuring the fluorescence of the nanoparticles (**Figure 1. g**). An excitation at $\lambda_{exc}=650$ nm led to a maximum of emission at $\lambda_{em}=700$ nm.

3.2. Nanoparticles interactions with U87 glioblastoma cells

The IONPs were incubated with a U87 glioblastoma cancerous cell line to investigate their interactions and the cell-penetrating properties of the ELP*_{40-60-Tat} modified nanoparticles. Interaction between PEG-grafted monocoresh and multicore IONPs were previously investigated, showing enhanced internalization with multi-core IONPs (see **Chapter V**). Here we report the effect of surface modification on the internalization efficiency and cytotoxicity under magnetic hyperthermia, while

keeping identical core morphology and size. The cell line was genetically modified to introduce a bioluminescent reporter (Fluc) under the transcriptional control of constitutive CMV promoter. The cells expressed luciferase, an enzyme which catalyzes chemiluminescent oxidation of the D-luciferin substrate, yielding photons. The intensity of emitted light is directly correlated with the cell viability and cell number, and could therefore be used as a physical read-out of cell viability and replace another assay like MTT reagent reduction into Formazan probing the mitochondrial activity of cells.

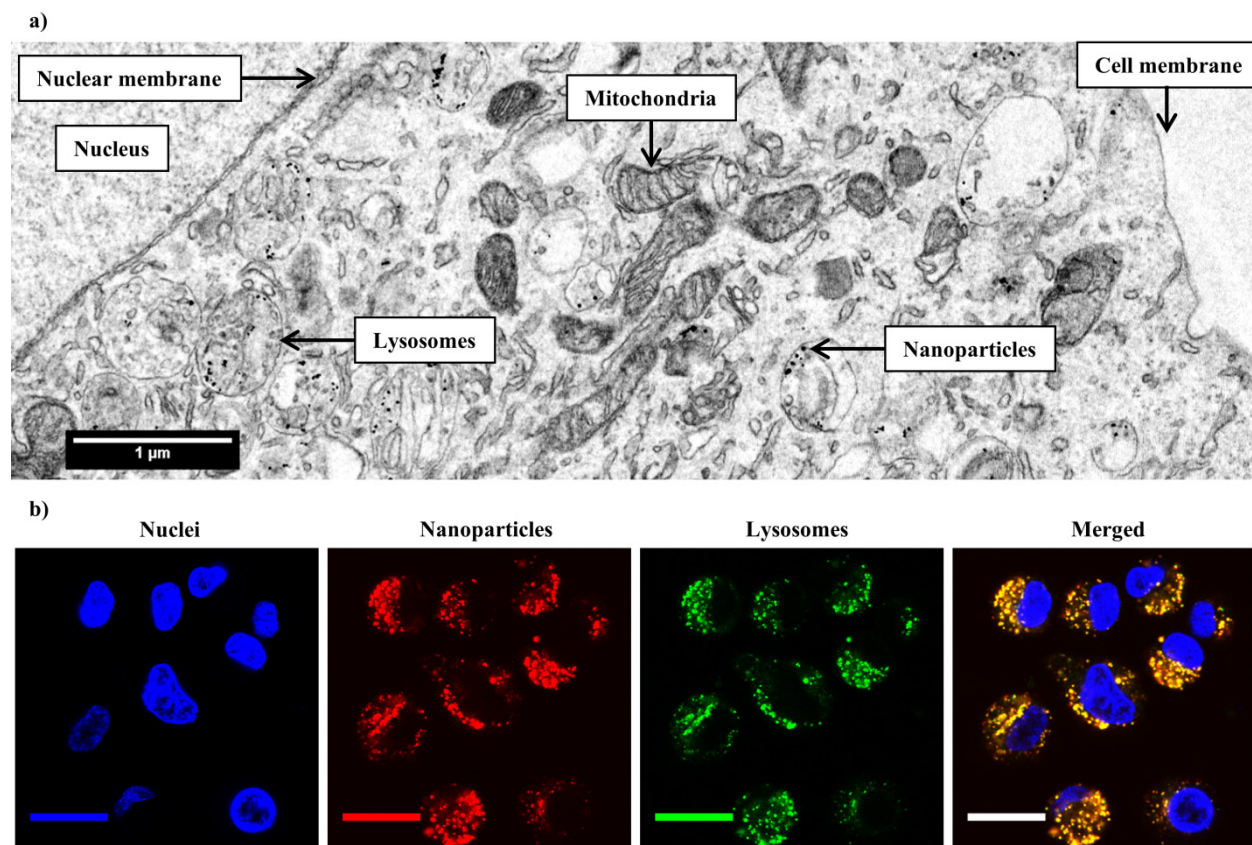


Figure 2 Glioblastoma cells incubated with magnetic iron oxide nanoparticles grafted with the ELP*_{40-60-Tat} observed by a) TEM and b) confocal microscopy. For confocal microscopy, cells were incubated with IONPs@ELP*_{40-60-Tat} conjugated to DY700* (red) for 24 h at 100 $\mu\text{g}\cdot\text{mL}^{-1}$. They were visualized by fluorescence confocal microscopy at 63 \times magnification. Hoechst 33342 (2 $\mu\text{g}\cdot\text{mL}^{-1}$) was used to stain the nucleus in blue. LysoTrackerTM (100 nM) was used to stain the lysosomes in green. Scale bars are 20 μm wide.

The glioblastoma cells were incubated with concentrations of IONPs at a concentration of 100 $\mu\text{g}\cdot\text{mL}^{-1}$ for 24 h. After fixation, staining and microtome, ultrathin sections of 65 nm were imaged by TEM. The cell membrane, mitochondria, nucleus and nuclear membrane were recognizable from their specific morphologies and locations inside the cell. Spherical structures encapsulating IONPs@ELP*_{40-60-Tat}, suspected to be lysosomes, were also imaged and observed in great numbers. More than a dozen of these structures were visible on **Figure 2 a**, in different locations inside the cell. Their dimensions were in the order of 500 nm, with a sample thickness of 65 nm. They presented different nuances of grey, with contrasts equivalents to that of the exterior of the cell for the ones close to the cell membrane, while the ones closer to the nucleus appeared more frequently darker. Later endocytic compartments also present other smaller spherical structures inside their membrane, resulting from the

fusion with other compartments involved in the endocytosis pathway. As reported by Collinet *et al.*, there is a strong correlation between the endosome distance from the nucleus, their number inside the cells, and their size.[37] This reflects a progression from small peripheral to larger and less numerous perinuclear endosomes. The cells were also imaged by laser scanning confocal microscopy to determine whether the IONPs were encapsulated inside lysosomes or in earlier stage endosomes (**Figure 2 b**). The cells were incubated with the blue Hoechst fluorescent dye to specifically tag the genetic material, and with the Green LysoTracker™ in dilute conditions to specifically identify the lysosomes, which are late stage of endosomes. They were then detached from the surface of the wells with trypsin and re-suspended in PB buffer supplemented with FBS and EDTA to prevent further adhesion. The sample was then imaged by LSCM. The position of the cells was revealed by the strong blue fluorescent signal of their nuclei. Cells incubated with ELP*_{40-60-Tat} modified IONPs presented a red signal arising from the nanoparticles, evidencing their internalization inside the cells. The green fluorescence signal of the lysosomes could also be detected. The LysoTracker™ molecule presents a weak base amine moiety, and has a tropism for cellular compartments with low pH, which is one of the key characteristics of lysosomes. The green fluorescent lysosomes were found to have a strong co-localization with the red IONPs. On merged images, the lysosomes and IONPs fluorescent signals overlap, leading to bright concentrated yellow spots.

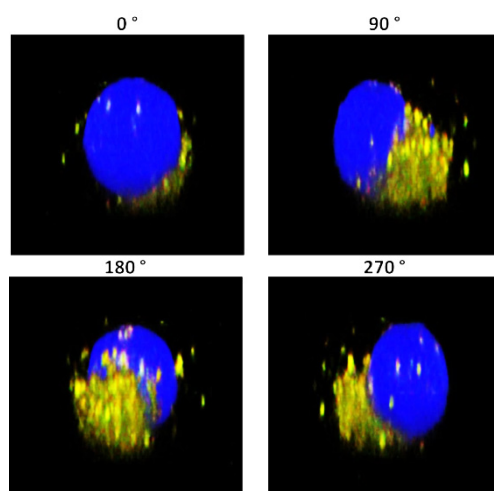


Figure 3 3D stacks of U87 cells incubated with ELP*_{40-60-Tat} grafted nanoparticles. The image was rotated at 4 different angles, which helped visualizing the repartition of the nanoparticles contained in the lysosomes.

A 3D stack of a cell incubated with ELP*_{40-60-Tat} grafted IONPs was acquired to better understand their microstructure (**Figure 3**). The three fluorescent signals were merged to compose these images: the blue color of the nucleus, the red of the IONPs@ELP*_{40-60-Tat} and the green of the lysosomes. As previously observed in **Figure 2**, lysosomes and IONPs were strongly co-localized leading to yellow spots. Although for a few cells the lysosomes were localized all around the nucleus, most frequently the lysosomes were found only on one side of the cell and the nucleus on the other side. This anisotropic perinuclear localization was already reported in the case of Tat-peptide functionalized quantum dots.[38] With a multivalence of 19 Tat peptides per nanoparticle, the ELP*₄₀₋

$^{60}\text{-Tat}$ modified IONPs were well internalized inside the cells. Zhao *et al.* reported non-linear enhanced intracellular accumulation with Tat modified IONPs, with multivalences in the range of 10 to 15.[39] They obtained intracellular accumulations non-linear with the valence, with uptakes up to 100-fold superior for valences larger than 10. Usually attachment of a cargo to Tat sequence decreases or even annihilates its cell membrane translocation property, except if it is compensated by a large multivalence effect, as demonstrated on cancer cells by MacEwan *et al.* with diblock ELP micelles[40] and by Drappier *et al.*[22] with synthetic polymer micelles conjugated with a high density of Tat end-groups. Such cell-penetrating effect is later presented here in more detail, by comparing the internalization of IONPs@PEG* and IONPs@ELP* $_{40-60}\text{-Tat}$ nanoparticles, both for *in vitro* and *in vivo* conditions.

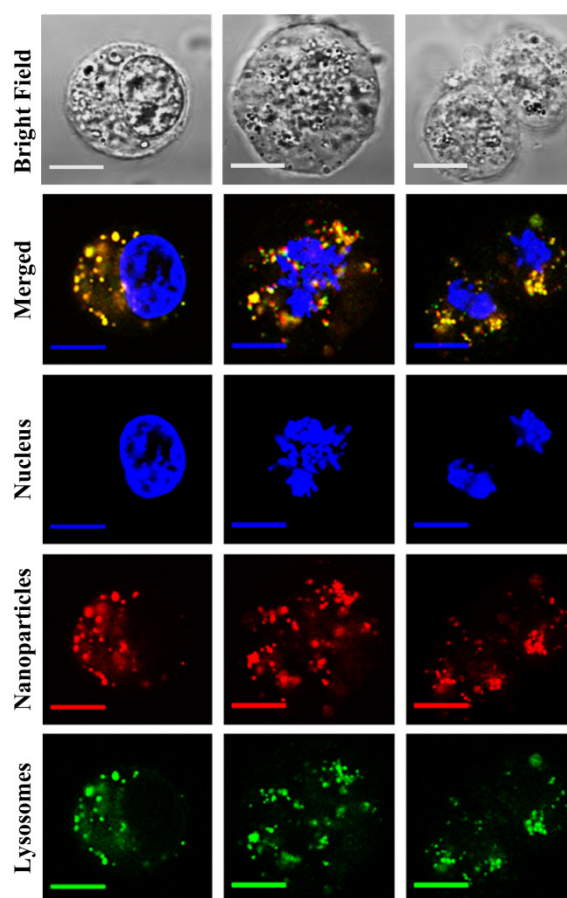


Figure 4 Cell divisions at different stages, observed by confocal imaging.

As images were taken on live cells, different stages of cell mitosis were observed and reported on **Figure 4**. The cell on the left column had the most common type of morphologies observed, with a bright nucleus of irregular coloration, and a strong coloration on the periphery. The cell in the middle column was dividing, with visible chromosomes that had already duplicated and condensed, forming these specific elongated spindle-shape structures. The membrane around the nucleus had dissolved, releasing away the chromosomes. A single cell membrane was observed by pseudo bright-field illumination. The cell on the right column had already divided, leading to the splitting of the

organelles, cell membrane and cytoplasm into two new daughter cells, with a roughly equal share of the cellular components. The nuclear membranes had not yet reformed. This observation shows that at every cell division, the nanoparticles contained within the lysosomes were shared between the two resulting daughter cells. This potentially allows the treatment of several generations of cells after incubation, and/or successive applications of magnetic hyperthermia on time scales superior to the cell life cycles. The incubation of ELP*_{40-60-Tat} modified IONPs appears to have low impact on the cell viability, as they retain their microstructures, morphologies and activities such as mitosis. Different articles presented the potential (unwanted) toxicity of IONPs. This toxicity can be manifested by membrane leakage, apoptotic bodies or chromatin condensation.[41] The vast majority of the cells observed by bright field or confocal microscopy were clear from these symptoms. The toxicity effect leading to chromatin condensation results in a coloration only in the periphery of the nuclei.[42] In the images reported here, the condensed chromosomes are characteristic of live cells undergoing cellular division.

3.3. Effect of magnetic hyperthermia on cells

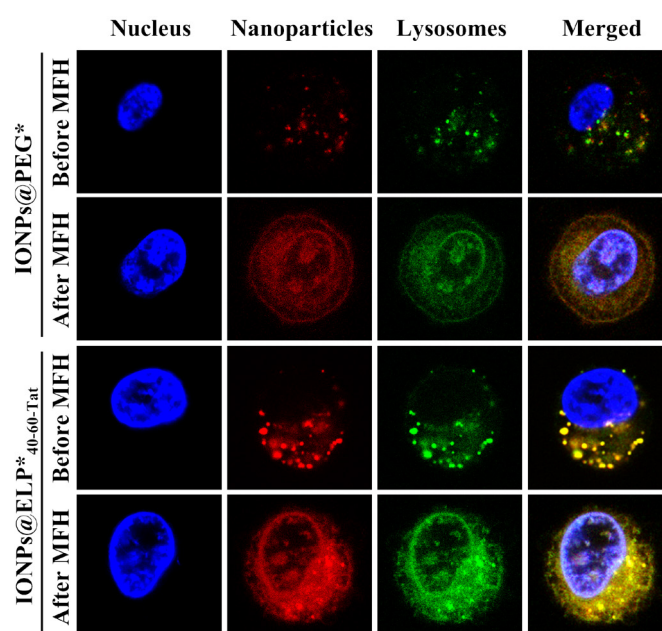


Figure 5 Intracellular distribution and internalization efficiency of nanoparticles in U87 glioblastoma cells. The effect of the nature of surface modification of IONPs grafted with either PEG* or ELP*_{40-60-Tat} was evidenced on both their internalization and on their sensitivity to magnetic hyperthermia. The size of the pictures is 30×30 μm.

After fluorescence staining and preparation, half of the cell suspension was preserved in cold conditions (approximately 4 °C) to inhibit the cell activity and to retain their morphologies before imaging. An alternating magnetic field (AMF) was applied on the other half using a frequency of 473 kHz and amplitude of 12 kA·m⁻¹ for 30 min. The internalization efficiency of ELP*_{40-60-Tat} and PEG* modified IONPs can be directly compared on **Figure 5** Intracellular distribution and internalization efficiency of nanoparticles in U87 glioblastoma cells. The effect of the nature of surface modification of IONPs grafted with either PEG* or ELP*_{40-60-Tat} was evidenced on both their internalization and on

their sensitivity to magnetic hyperthermia. The size of the pictures is $30 \times 30 \mu\text{m}$. In both cases, cells were incubated with IONPs at $100 \mu\text{g}\cdot\text{mL}^{-1}$ concentration for 24 h. For ELP*_{40-60-Tat} modified IONPs, the red fluorescent spots of the nanoparticles were brighter, which evidences larger internalization compared to PEG modified IONPs. The lysosomes were also larger and in greater quantities. For the two types of surface modifications, the application of an AMF for 30 min led to the disruption of the lysosomes. This was evidenced by the escape of the Lysotracker™ dye into the cytosol, as well as the diffusion of the IONPs inside the cells. The red and green dyes diffused as clouds inside the cytosol, and seemed to concentrate in the cellular and nuclear membranes, as well as in what appeared to be other organelles. These results proved that magnetic nanoparticles were capable of disrupting the lysosome membranes and liberate their content. In drug delivery strategies, this would allow the escape of the trapped drug by an external trigger, answering to the issue of drug liberation. Cells not incubated with IONPs did not show the specific red signal of the nanoparticles, and were also generally free of the green fluorescence signal of the lysosomes, at the same gain of the PMT adjusted to detect the signal of the green channel.

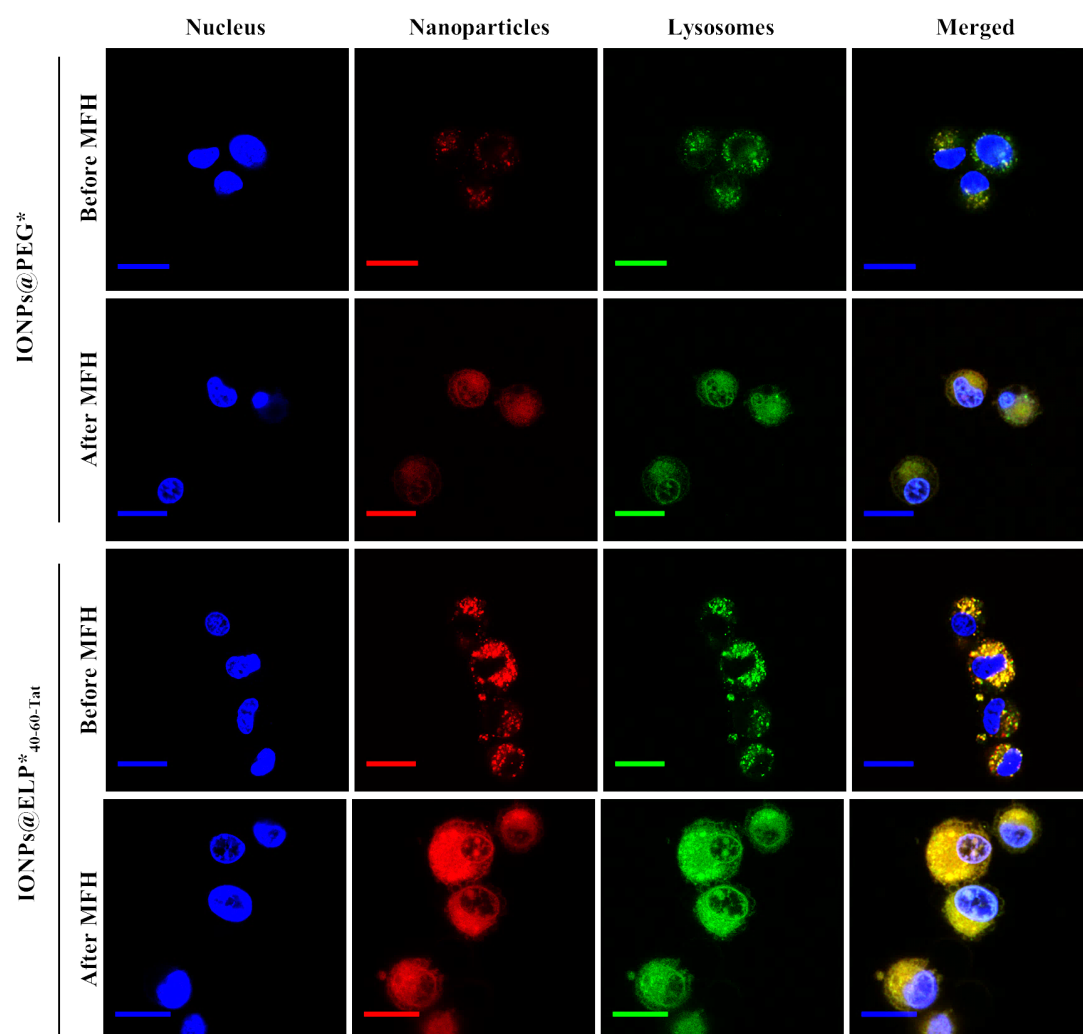


Figure 6 Intracellular distribution and internalization efficiency of nanoparticles in U87 glioblastoma cells. The effect of surface modification of IONPs grafted with either PEG* or ELP*_{40-60-Tat} was evidenced on both their internalization and on their sensitivity to magnetic hyperthermia. The scale bars are $50 \mu\text{m}$ wide.

The rupture of the lysosomes upon application of an external AMF detected on **Figure 5** Intracellular distribution and internalization efficiency of nanoparticles in U87 glioblastoma cells. The effect of the nature of surface modification of IONPs grafted with either PEG* or ELP*_{40-60-Tat} was evidenced on both their internalization and on their sensitivity to magnetic hyperthermia. The size of the pictures is 30×30 μm. was observed in every cell of the samples, as also seen on **Figure 6** Intracellular distribution and internalization efficiency of nanoparticles in U87 glioblastoma cells. The effect of surface modification of IONPs grafted with either PEG* or ELP*_{40-60-Tat} was evidenced on both their internalization and on their sensitivity to magnetic hyperthermia. The scale bars are 50 μm wide.. The effect was nevertheless stronger in the case of U87 glioblastoma cells incubated with IONPs@ ELP*_{40-60-Tat} nanoparticles compared to IONPs@PEG* ones.

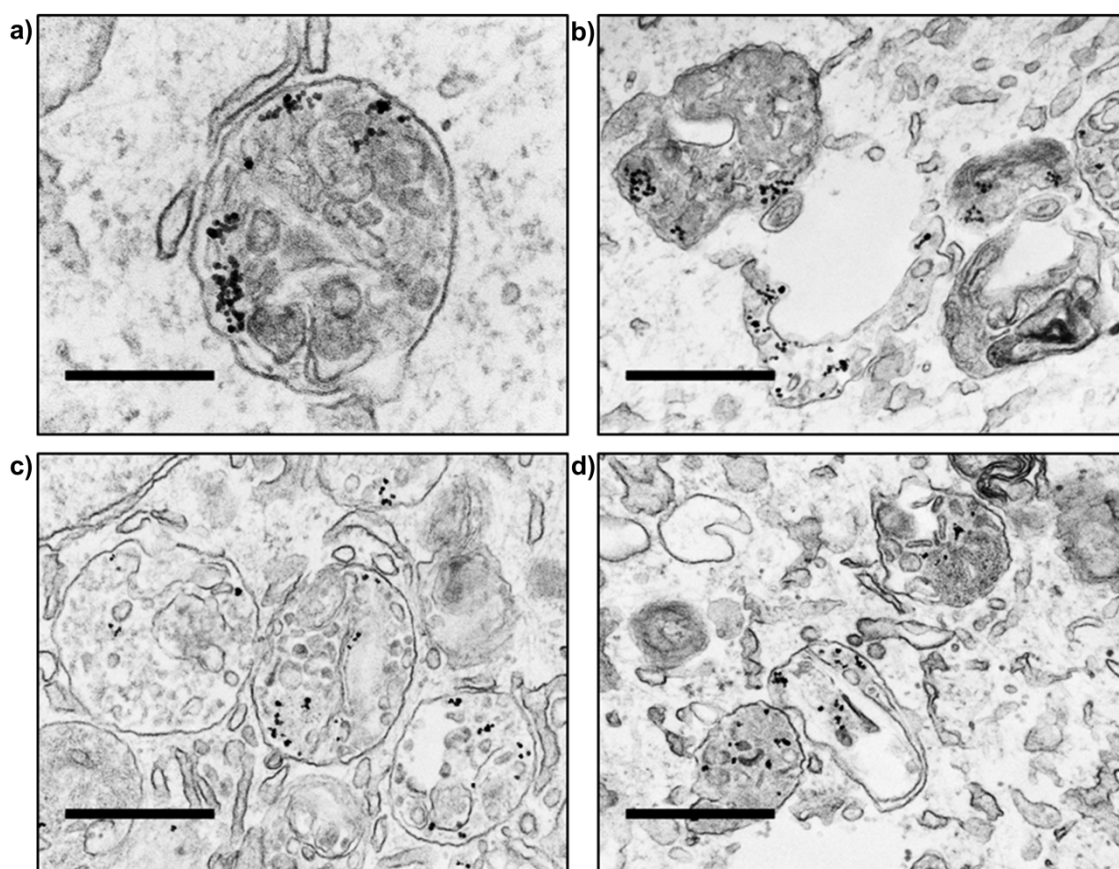


Figure 7 TEM micrographs of lysosomes containing IONPs@PEG* **a)** before and **b)** after application of magnetic hyperthermia. TEM micrographs of lysosomes containing IONPs@ ELP*_{40-60-Tat} **c)** before and **d)** after application of magnetic hyperthermia. Scale bar lengths are for **a)** 250 nm and for **b-d)** 500 nm. Arrows indicate localization of large pores in lysosomal membranes.

In order to study the cell microstructure at higher (nanoscale) resolution, the effect of AMF application on the U87 cells was also observed on TEM microtomes. For untreated cells, the lysosome shapes varied from ellipsoidal to spherical, with relatively tensed membranes, for both PEG and ELP*_{40-60-Tat} modified IONPs (**Figure 7 a** and **c**). The lysosomes were clearly disrupted after application of magnetic hyperthermia, leading to a significant reduction of their volume (**Figure 7 b** and **d**). This observation was in agreement with the confocal images presented in **Figure 5**. TEM

micrographs reporting the deformation of endosomes encapsulating magnetic nanoparticles under a static magnetic field was previously reported,[43] but to the best of our knowledge, it is the first time that the effect of an alternating magnetic field alone is reported, showing direct images of the disruption of the lysosomal membrane and leakage of their interior into the cytosol. In a very recent article, a group from Zaragoza and Lausanne has published similar TEM analysis of ruptured lysosomes,[44] but in their case there was a macroscopic temperature increase (up to 46°C). In their case, the cells were detached and pelleted at a very high concentrations (9 million in 150 μL) before applying the AMF or heating in a water bath. The same strategy had been used in an older work by Fortin *et al.*,[45] since a macroscopic cell pellet had a sufficient heating power (compared to the thermal losses) to reach a macroscopic increase of temperature. In our case, the cells were still adherent on the glass substrate and their concentration was low (5,000 in 100 μL DMEM) so that “cold” or “intra lysosomal” hyperthermia treatment was applied instead, *i.e.* no macroscopic heating occurred.

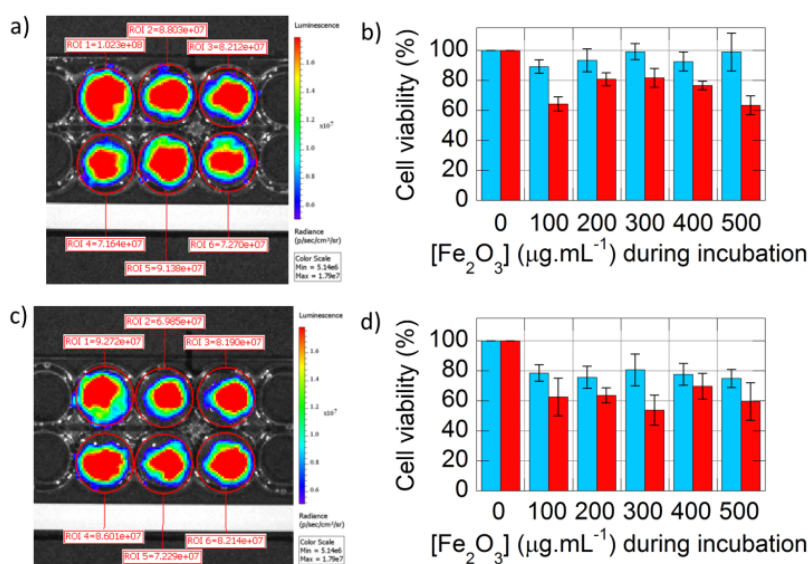


Figure 8 Bioluminescence imaging of CMV Luciferase modified U87 glioblastoma cells incubated at different concentrations of magnetic iron oxide nanoparticles (from top to bottom and left to right: wells with 0, 100, 200, 300, 400 and 500 $\mu\text{g}\cdot\text{mL}^{-1}$), 24 h after AMF application. **a)** BLI image of the microscopy chamber with cells incubated with IONPs@PEG*; **b)** corresponding cell viability measurements before (blue) and after (red) application of the treatment. **c)** BLI image of the microscopy chamber with cells incubated with IONPs@ELP*_{40-60-Tat}; **d)** corresponding cell viability measurements before (blue) and after (red) application of the AMF treatment (at 24 h delay).

After studying the internalization of the magnetic IONPs and their effect on the cell microstructures under AMF application, we studied the cytotoxic effect. The cytotoxicity effect of IONPs, occurring during IONP internalization or after applying an external alternative magnetic field (AMF) was assayed by bioluminescence imaging (BLI) readout based on luciferase activity inside the cells.[46] Circular regions of interests (ROIs) were integrated on BLI images of U87 cells taken 24 hours after AMF treatment to quantify the bioluminescence intensity, either in the case of PEG*

(**Figure 8 a**) or ELP*_{40-60-Tat} (**Figure 8 c**) modified IONPs. The cell viability was compared at varying IONP concentrations during incubation, before (blue) or after (red) the AMF application for 30 min, for either PEG* (**Figure 8 b**) or ELP*_{40-60-Tat} (**Figure 8 d**) modified IONPs. For both surface modifications, AMF treatment induced a decrease in cell viability compared to untreated cells. The effect was stronger for ELP*_{40-60-Tat} modified IONPs, as ascribed to their larger internalization.

3.4. Biodistribution of intravenously administered nanoparticles in mice

IONPs@ELP*_{40-60-Tat} and IONPs@PEG* nanoparticles were administered to mice by tail vein injection (750 µg in around 100 µL bolus). The biodistribution of the nanoparticles as a function of time was followed by *in vivo* fluorescence imaging thanks to the dye emission at 700 nm, *i.e.* in the near infrared (NIR) transparent window of tissues.

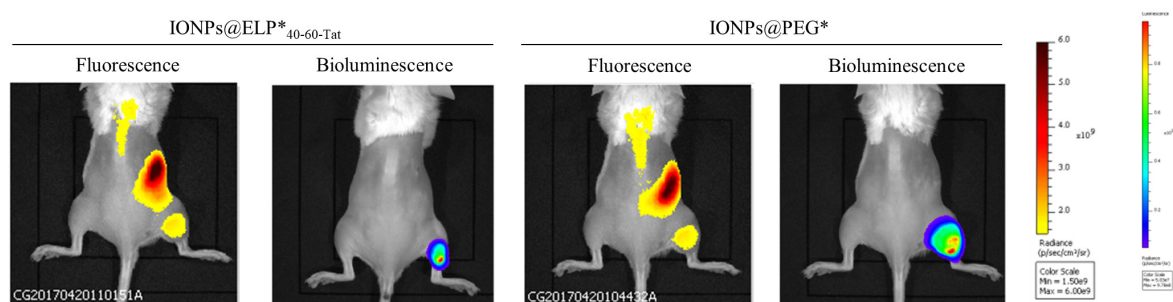


Figure 9 Comparison between the fluorescence signal of IONPs@ELP*_{40-60-Tat} and IONPs@PEG* nanoparticles (30 min after intravenous injection), and of the bioluminescence signal of the tumors (before injection).

Both IONPs@PEG* and IONPs@ELP*_{40-60-Tat} modified nanoparticles were up-taken in the liver, as well as in the tumor located on the mouse leg (**Figure 10** and **Figure 11**). There was also perfect overlap of the fluorescence signal from the nanoparticles and of the bioluminescence signal from the tumor (**Figure 9**). As there was no active targeting for both nanoparticles designs, the tropisms of the IONPs toward the tumors were ascribed to the enhanced permeability and retention (EPR) effect. The signal of the IONPs in tumors was still strong after an hour but faded away after several hours, indicating a draining effect. Similarly, the fraction of IONPs that was up-taken by the liver seemed to be eliminated through the hepatobiliary pathway as suggested by fluorescence images taken on mice in dorsal *decubitus* position showing transfer – of at least the dye molecules – from the liver to the intestinal track.[47]

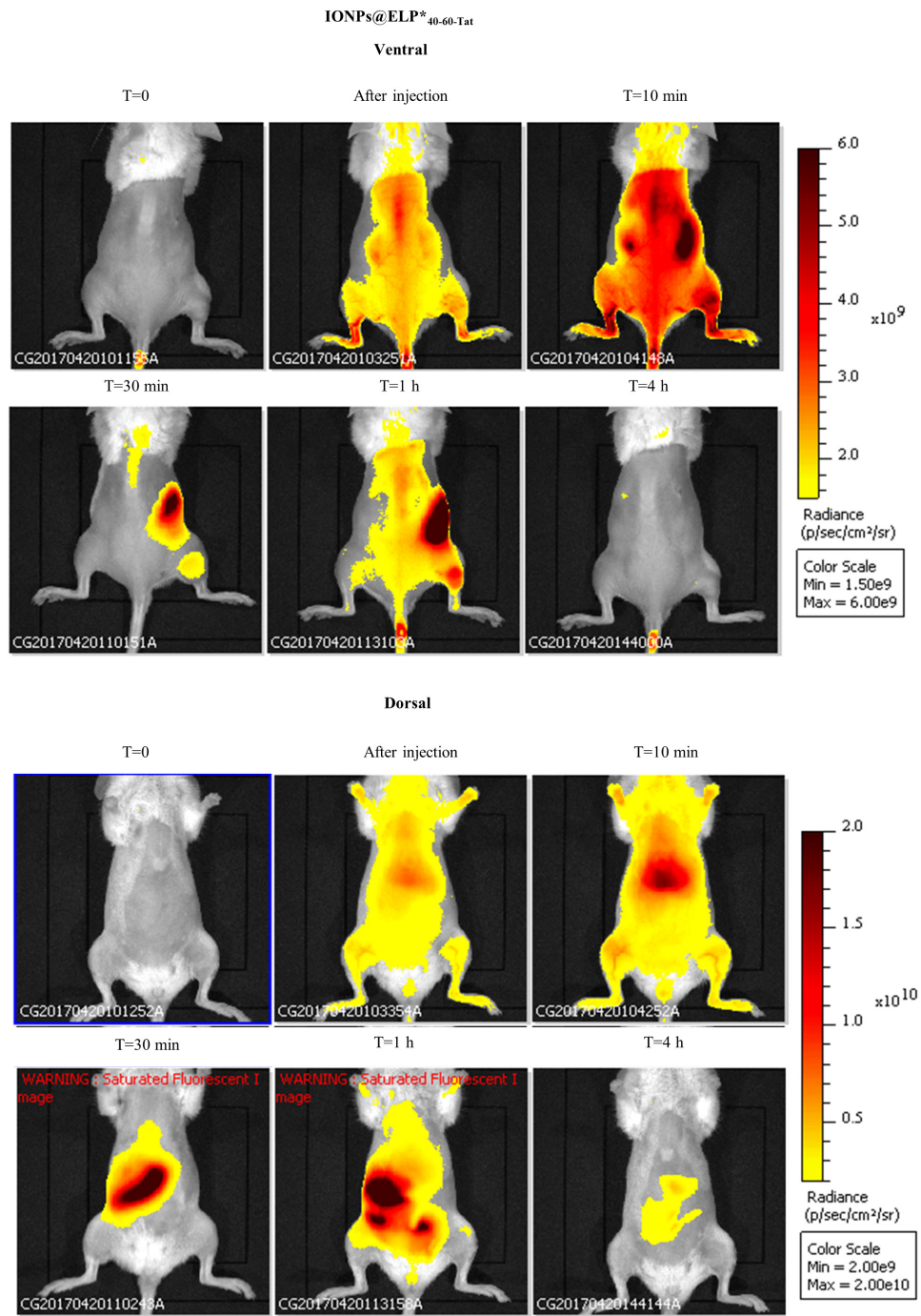


Figure 10 Biodistribution in a mouse of 11.7 nm diameter spherical, magnetic, fluorescent thermosensitive and cell-penetrating IONPs@ELP*_{40-60-Tat} nanoparticles (750 μ g in around 100 μ L PBS injected intravenously). Xenograft U87 glioblastoma tumors were implanted and grown on the mouse until maturation (in 6-7 weeks). The animal was anaesthetized by breathing isoflurane gas (Belamont, Nicholas Piramal Ltd, London, UK, 2% in air).

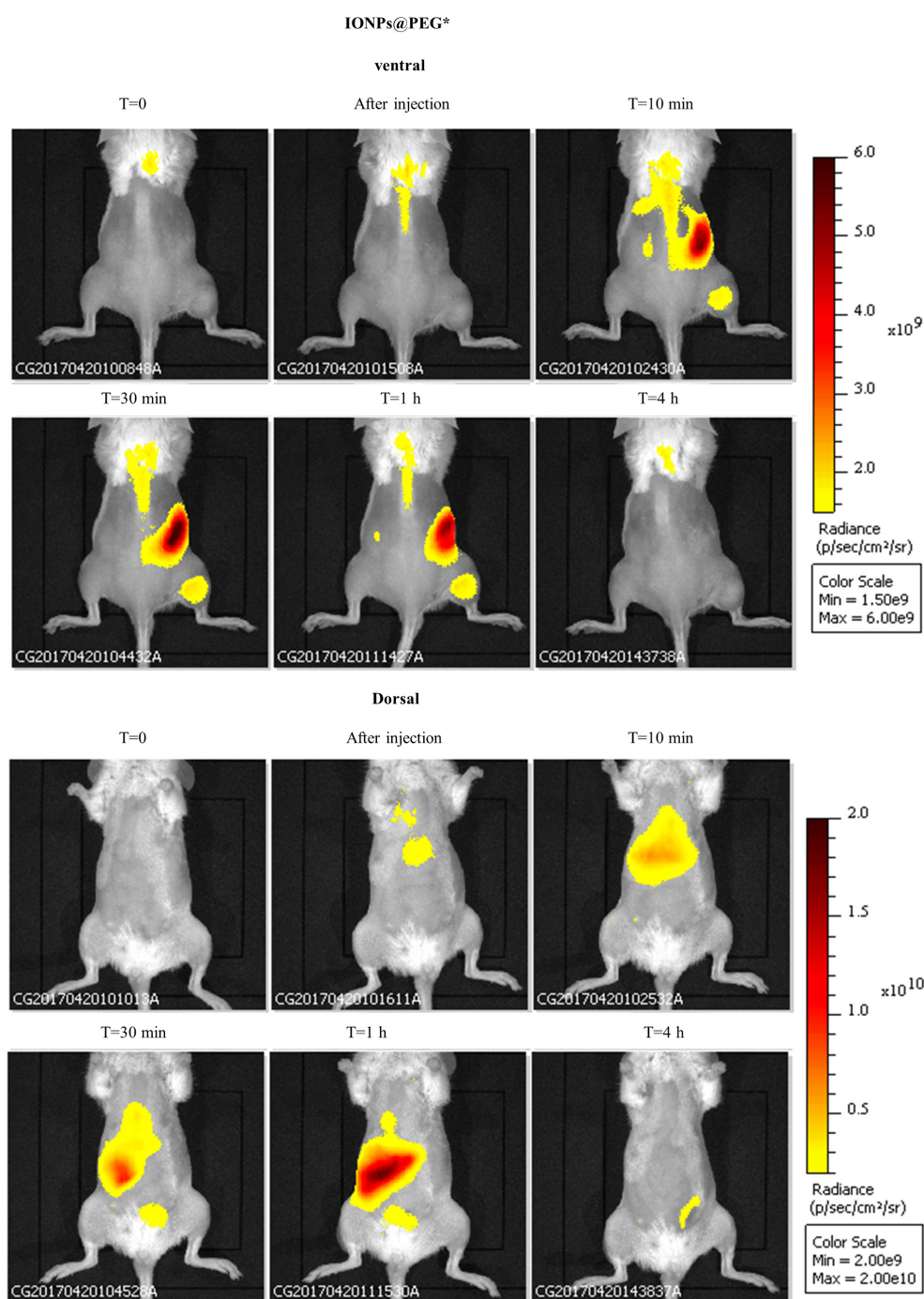


Figure 11 Biodistribution in a mouse of 11.7 nm diameter spherical, magnetic and fluorescent IONPs@PEG* nanoparticles (750 μg in around 100 μL PBS injected intravenously). Xenograft U87 glioblastoma tumors were implanted and grown on the mouse until maturation (in 6-7 weeks). The animal was anaesthetized by breathing isoflurane gas (Belamont, Nicholas Piramal Ltd, London, UK, 2% in air).

Mice were sacrificed 10 h after injection of IONPs@ELP*_{40-60-Tat} and IONPs@PEG* nanoparticles, and livers and tumors were removed (**Figure 12 a,b**). Fluorescence imaging showed a signal from the nanoparticles in tumors, and no signal in livers. It appeared that the fluorescence of the tumors came from the liquid at their exterior surface. Confocal imaging on microtomes of livers and tumors showed a red fluorescence signal from the IONPs. For IONPs@PEG*, the nanoparticles were partially retained in the liver, but no signal was observed inside the tumor. For IONPs@ELP*_{40-60-Tat}

nanoparticles, a signal could be observed in both the liver and inside the tumor. This suggests that during the circulation of IONPs in the mice blood, a fraction of IONPs@ELP*_{40-60-Tat} nanoparticles entered the extra-tumoral environment through the EPR effect and internalized inside the cancerous cells. The difference between PEG* and ELP*_{40-60-Tat} surface modifications on cell internalization *in vitro* studies was also observed *in vivo*. The Tat peptide segment had positive influence on the uptake of nanoparticles in cells cultivated *in vitro* or in tumors: The multivalent Tat presentation that restored cargo translocation through cell membranes demonstrated by MacEwan and Chilkoti with diblock ELP-Tat micelles above CMT[40] was thus also present when peptides constituted a shell around IONPs.

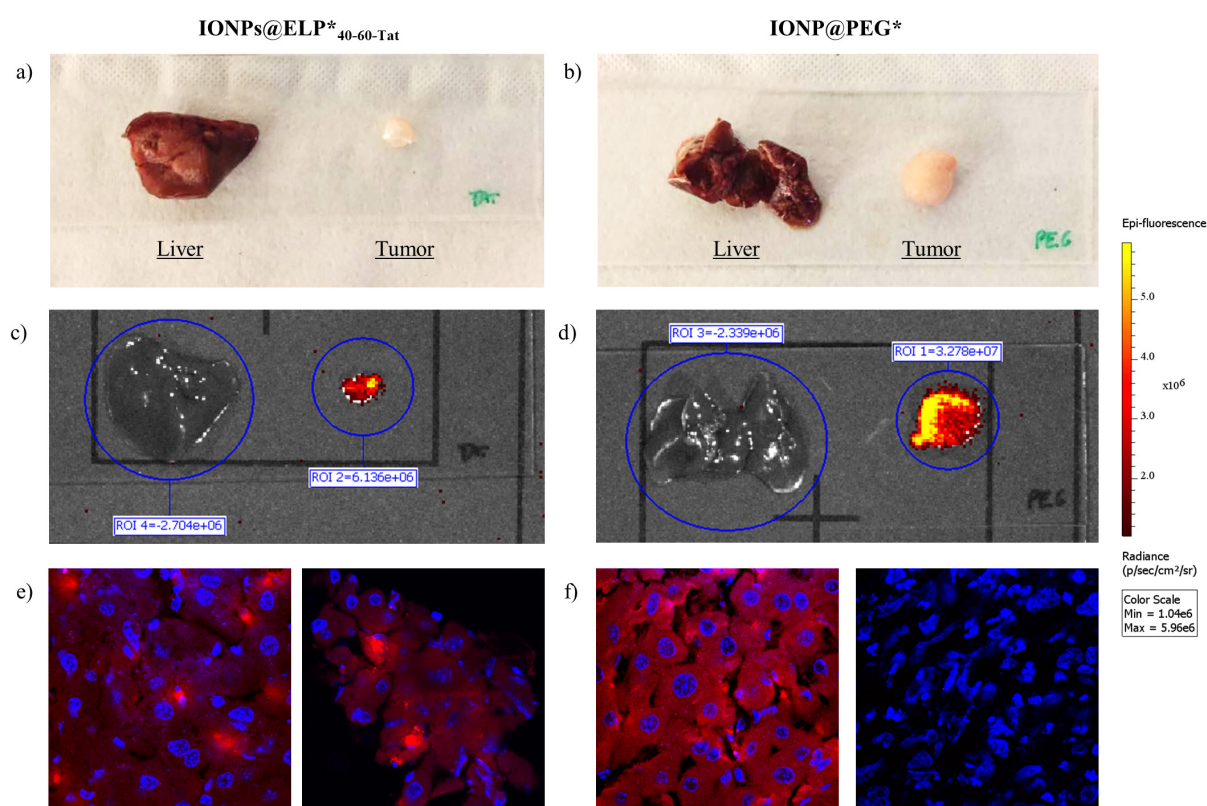


Figure 12 Photographs of livers and tumors extracted from mice 10 h after injection of **a)** IONPs@ELP*_{40-60-Tat} and **b)** IONPs@PEG* nanoparticles. **c,d)** Respective photographs and fluorescence merged images. Confocal imaging of liver (left) and tumor (right) microtomes of mice injected with **e)** IONPs@ELP*_{40-60-Tat} and **f)** IONPs@PEG* nanoparticles. Nuclei from microtomes were stained using ProLong[®] Gold Antifade Mountant containing DAPI, after fixation with paraformaldehyde (PFA).

3.5. Treatment by intravenous (systemic) administration

Larger doses of 1 mg were injected intravenously (100 μL bolus in caudal vein). AMF treatment was applied 30 min after injection (15 min, 473 kHz, 12 $\text{kA}\cdot\text{m}^{-1}$). The tumors on the mice leg were positioned inside the 2-coil inductor in the region of homogeneous field intensity (**Figure 13 a**), while keeping the liver in a small circular region of lowest field intensity, *i.e.* less than 5% of the nominal field intensity (as determined by finite element modelling, see **Figure 11 b** in previous chapter). This strategy to concentrate the application of AMF on tumors and to limit the anticipated side-effect heating of liver by positioning the animal perpendicularly to the coil axis instead of parallel was proposed in a work by Rodrigues *et al.* with their lab-made 2 coil applicator.[48] The temperature of the mice was monitored by IR thermometry (**Figure 13 b,c**). No significant macroscopic heating was observed, with the surface temperature of the tumors remaining surprisingly lower than that of the rest of the body, presumably due to an artefact of thermal imaging due to the tilt angle of the camera view[48] and to the smaller surface of the leg compared to the back of the animal. These results show that although IR thermal imaging is widely used for *in vivo* magnetic hyperthermia experiments, this method is unable to assess the exact intra-tumor temperature and should rather be used for relative assessments, for instance by comparing a test tumor on one side to a control tumor on the other one.[49] Moreover, the skin temperature decreased from 34 to 32 $^{\circ}\text{C}$, as the mice went into hypothermia which is a well-known effect of anesthesia.

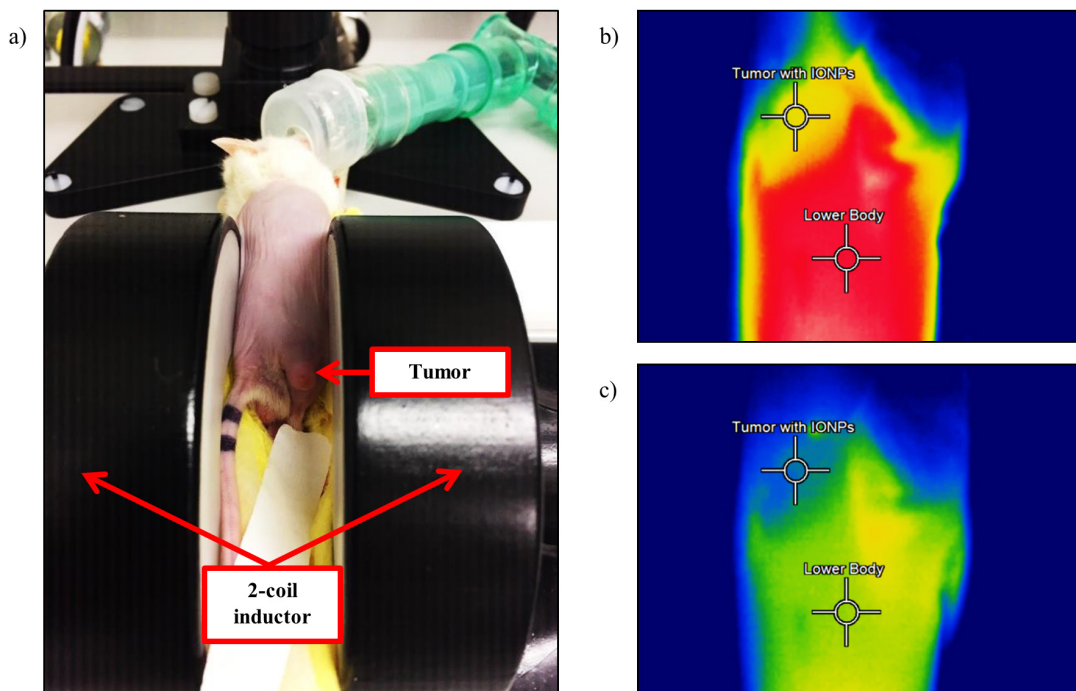


Figure 13 a) Position of the tumor inside the 2-coil inductor for magnetic hyperthermia treatment. Infrared thermal imaging **b)** before and **c)** after treatment (15 min, 473 kHz, 12 $\text{kA}\cdot\text{m}^{-1}$, 1 h after injection).

The progression of tumor growth after application of magnetic hyperthermia was quantified by LucF enzyme activity (**Figure 14 a**). The development of implanted U87 glioblastoma cells was

relatively slow, with tumors reaching full maturity in time scales of commonly 6 to 7 weeks after xenograft implantation. The tumors continued to grow after application of the treatment, with an average increase of relative LucF activity of a factor 2.6 for IONPs@ELP*_{40-60-Tat} and 3.1 for IONPs@PEG* after 72 h (**Figure 14 b**). Using 3 mice for each condition (instead of 2 only) and adding a pool with untreated tumors would have allowed a statistical comparison of the efficiency of the two treatments. Nevertheless, several conclusions can be made out of these preliminary collected data. The administration of IONPs@ELP*_{40-60-Tat} nanoparticles was apparently more efficient at reducing tumor growth compared to IONP@PEG nanoparticles. This can be interpreted again by their higher internalization efficiency in cells; this claim is supported both by *in vitro* (**Figure 5, Figure 6**) and *in vivo* (**Figure 12**) experiments. The AMF treatment did not lead to a macroscopic heating, so the hypothetical mechanism of action is a cold hyperthermia effect. In this scenario, cells death was provoked by generation of reactive oxygen species (ROS) and most-probably loss of integrity of the cells (rupture of lysosomal membranes). Finally, in both cases, the treatment was not effective enough to induce a decrease of LucF activity. These observations are representative of the intravenous administration of nanomedicine. The systemic biodistribution led to a fraction of material being directed to the region of interest, by EPR effect. Specific ligands could improve the tumor targeting, although reviews on the subject evidence that the fraction of material effectively reaching their target still remains low, typically around only 1% of the dose at best.[50]

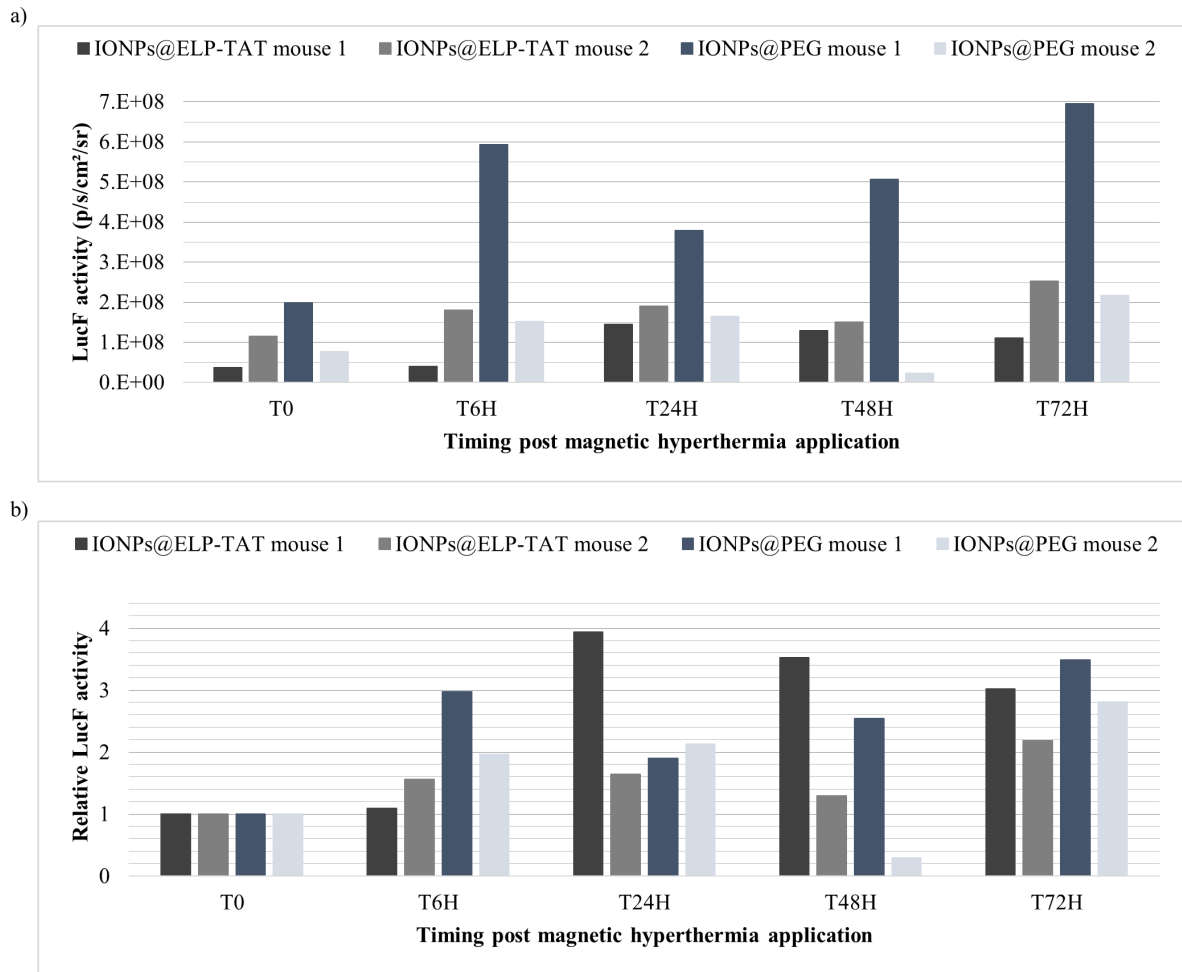


Figure 14 a) Bioluminescence activity of the LucF enzyme contained in the tumors at 0, 6, 24, 48 and 72h after AMF application. b) Relative bioluminescence activity of the LucF enzyme contained in the tumors compared to initial time. Two animals were studied for each coating (ELP*_{40-60-Tat} and PEG*) of the IONPs.

As IONPs@ELP*_{40-60-Tat} nanoparticles have cell-penetrating but no active targeting properties, they were also administered by intra-tumoral injection.

3.6. Treatment by intra-tumoral administration

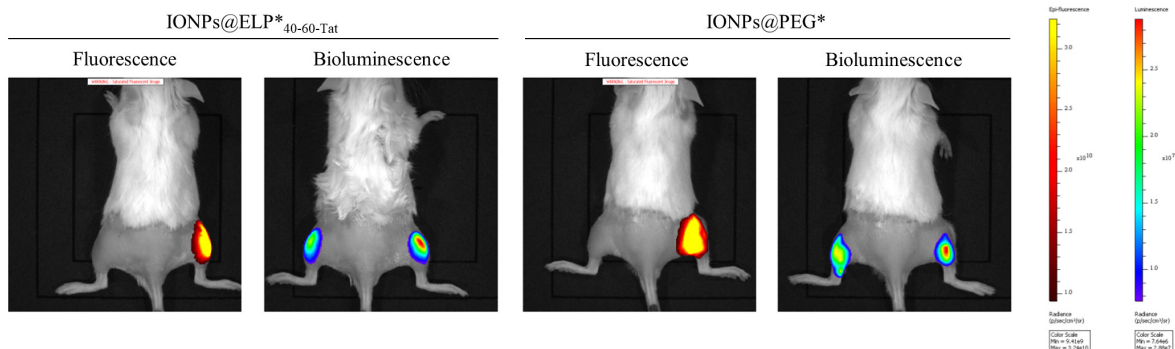


Figure 15 Fluorescence signal of IONPs@ELP*_{40-60-Tat} and IONP@PEG* nanoparticles (intra-tumoral injection, immediately after administration), and bioluminescence signal of the tumors (prior administration).

In the previous experiments by intravenous administration, the EPR effect allowed targeting tumors passively, but the main fraction of nanomedicines did not reach their target and were collected by the liver. The nanoparticles were therefore directly injected in the tumors to improve the quantity of material retained in the area of interest. The cells implanted were changed from U87 glioblastoma to RM1 prostate in order to reduce the maturation time of the model tumors. The RM1 tumors used in this study were more aggressive and developed faster, in a few days only. For very practical reasons, this allowed injecting cancerous cells on a Friday and administrating the nanoparticles the next Monday, to cut down experimentation times. For these experiments, doses of around 1.3-1.5 mg of IONPs@ELP*_{40-60-Tat} or IONPs@PEG* were administered in 6 μL injections. As the sizes of the tumors were relatively small (dimensions of few millimeters) and the inflammation significant, the locations of the tumors were preliminary determined by bioluminescence imaging (**Figure 15**). The correctness of these administrations was confirmed by fluorescence imaging of the nanoparticles.

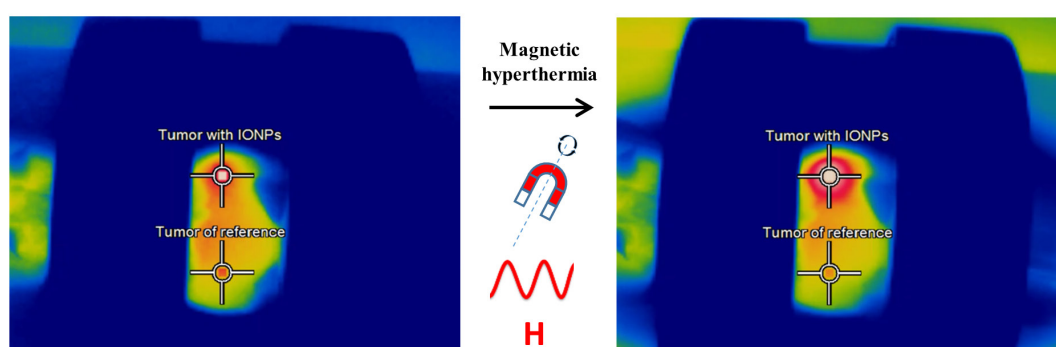


Figure 16 IR thermal imaging of a mouse at $t=0$ (left) and $t=15$ min (right) during magnetic hyperthermia treatment (15 min, 473 kHz, $12 \text{ kA}\cdot\text{m}^{-1}$) after intra-tumoral administration.

The absence of nanoparticles in the liver allowed the positioning of the mice along the axis of symmetry of the set-up. The tumor injected with nanoparticles and the control one were both positioned in areas with equal magnetic field intensities. IR thermal imaging allowed measuring the surface temperature of the skin while applying magnetic hyperthermia. The two legs of a mouse were visible inside the 2-coil inductor in **Figure 16**, along with the head on the left side of the set-up.

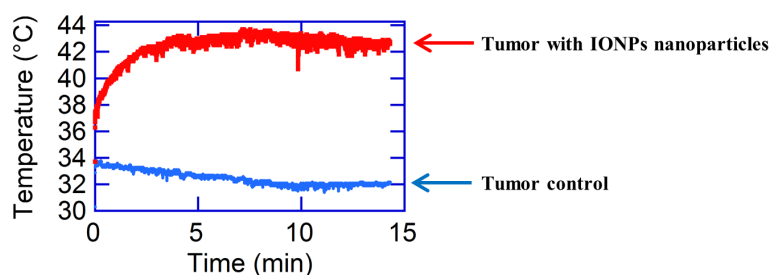


Figure 17 Surface temperature of the tumors as a function of time

The surface temperatures were recorded during the treatment. Typically, the temperatures of the tumors without nanoparticles were slightly decreasing of a few $^{\circ}\text{C}$ due to anesthesia, while the temperatures of the tumors injected with nanoparticles were significantly increasing until reaching a

plateau value (**Figure 17**). The shapes of the curves were typical of magnetic hyperthermia experiments, with an increase of temperature until reaching the compensation of heat generation and heat loss. The mice regulated their temperature and their body acted as heat sinks. Surface temperature gaps of up to 10 °C between the two tumors were recorded at equilibrium. As the IR thermography was mapping the surface of the skin, the temperature of deeper tissues was underestimated. This most likely explains the value of 32 °C for the control tumor, while the rectal temperature of a mouse is typically of 37 °C, leading to a bias of typically 5 °C. By correcting the temperature of the tumor injected with nanoparticles by 5 °C, as suggested by reported simulations of tumor phantoms at different depths,[51, 52] the plateau temperature could be as high as 48 °C (while a more rigorous estimate would consist in simulating the diffusion profile of heat generated in the center of the tumor by the so-called “bio-heat equation”). This would mean that the temperature in the center of the tumor is high enough to induce the apoptosis of cells, or even necrosis.

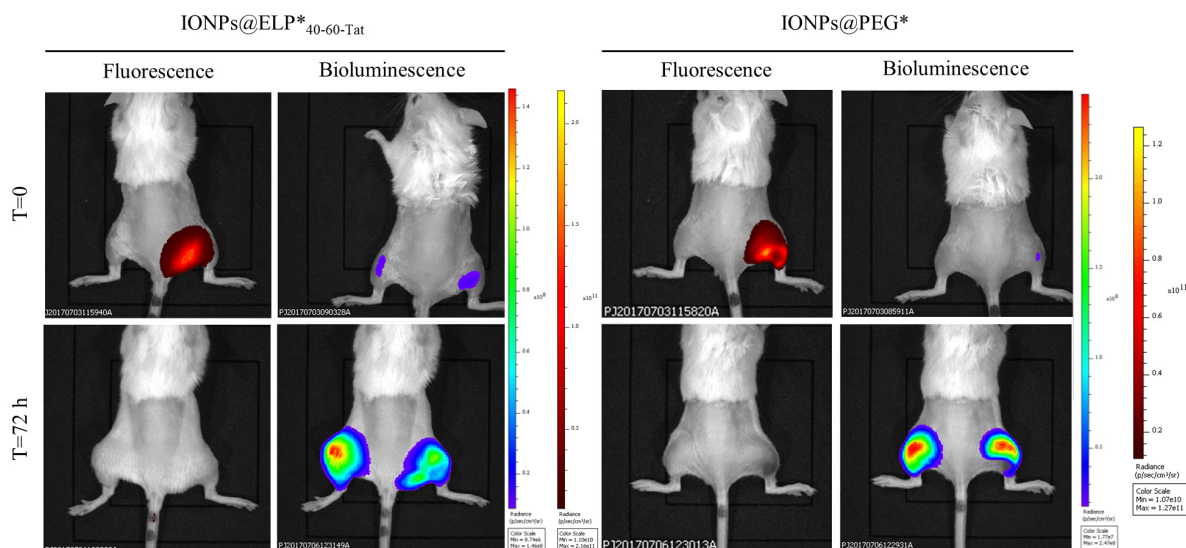


Figure 18 Fluorescence imaging of IONPs@ELP*_{40-60-Tat} and IONPs@PEG* nanoparticles, and bioluminescence imaging of the tumors. Top pictures were taken after IONP administration (t=0). Bottom pictures were taken at t+72 h, after successive applications of MH at t+4, t+8, t+24, and t+48 h.

Fluorescence and bioluminescence imaging allowed keeping track of the nanoparticles and follow the growth of the tumors on a time-scale of 72 h (**Figure 18**). The magnetic hyperthermia treatment was applied four times in a row, at 4, 8, 24 and 48 hours after administration of IONPs@ELP*_{40-60-Tat} and IONPs@PEG* nanoparticles. During the duration of the repetitive treatment, the nanoparticles were progressively eliminated while the tumors significantly developed as shown from the decrease of the fluorescence signal. The fluorescence signals of the nanoparticles were stable during the first 24 h after their administration, and declined steeply during the following days. The application of magnetic hyperthermia had little effect on the kinetics of elimination, as similar relative evolutions were observed in both cases, for the two types of nanoparticles. The signal measured on this experiment arised from the DY700* fluorophore chemically bound to the nanoparticles. We hypothesized that the fluorescence signal was directly proportional to the quantity

of nanoparticles inside the tumors. This hypothesis surely holds for small durations, but the fluorophore might be de-grafted from the nanoparticles and eliminated following an alternative pathway at the scale of several days. In future experiments, inductively coupled plasma mass spectrometry (ICP-MS) could be used as a complementary measurement to quantify the iron content inside the tumors at the end of the experiment, and compare with the injected dose at the beginning of the experiment.

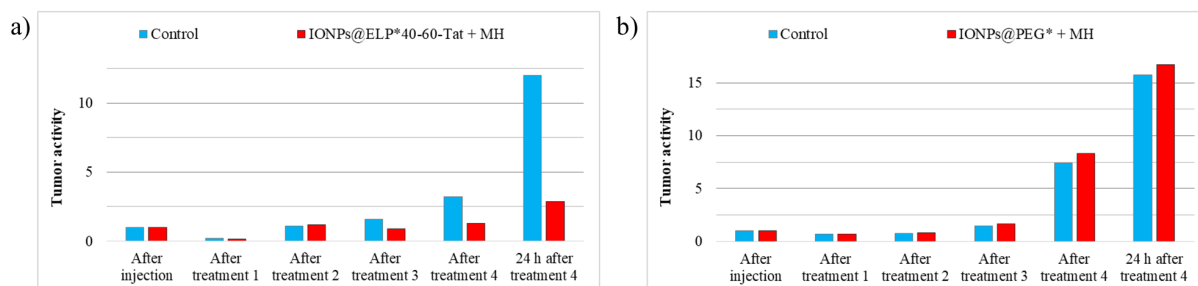


Figure 19 Quantification of the bioluminescence signal of tumors administered with **a)** IONPs@ELP*_{40-60-Tat} and **b)** IONPs@PEG* nanoparticles by intra-tumoral injection and after successive applications of MH at t+4 (treatment 1), t+8 (treatment 2), t+24 (treatment 3), and t+48 h (treatment 4).

As the normalization of bioluminescence was done shortly after injection, a large quantity of iron oxide material was present inside and in the vicinity of the tumors. This led to a well-observable deep black coloration of these areas under the mice skin, absorbing the bioluminescence signal during its imaging and leading to a bias of tumor activity measurement. As the nanoparticles were removed through time, two effects were added: the natural tumor growth and the removal of the bioluminescence absorption by the nanoparticles. This phenomenon was not observed for IONPs@ELP*_{40-60-Tat} nanoparticles. Upon injection, they significantly remained located inside the tumors, possibly through an improved cell penetration effect arising from the Tat peptide or from a gelling effect of the ELP. The ELPs are known to undergo a transition from soluble unimers to coacervates when heated and in saline conditions, which is the case in physiological conditions. As nanoparticles were injected at high concentrations (6 μL at $220 \text{ mg}\cdot\text{mL}^{-1}$), they probably interacted with the extracellular matrix when located in the environment of the tumors. After injection, IONPs@PEG* nanoparticles diffused in the area of inflammation, while IONPs@ELP*_{40-60-Tat} nanoparticles probably stayed trapped inside the tumors. The administration of IONPs@PEG* followed by successive applications of MH did not show a significant effect on tumor activity (in this example). IONPs@ELP*_{40-60-Tat} reduced the tumor activity by a factor 4, evidencing the benefit of the ELP*_{40-60-Tat} surface modification (in this example). These experiments must be carried on a greater number of mice to obtain a statistically significant result. Nonetheless, the benefit of the repeated MH applications, the use of nanoparticles specifically engineered for the treatment of tumors, the bioluminescent tumor models, the 2-coil inductor set-up coupled with an IR camera, and the advantage of using fluorescent nanoparticles were evidenced by these preliminary results of magnetic hyperthermia *in vivo* assays.

4. Conclusion

IONPs were synthesized by the polyol pathway leading to controlled morphologies and magnetic properties. Their heating performance under application of an external alternating magnetic field makes them suitable agents for magnetic hyperthermia cancer treatment. The optimized polyol synthesis strategy allowed producing smooth spherical nanoparticles, around 12 nm in diameter and with narrow size-distribution. The surface of the nanoparticles was grafted with molecules of interest using a convergent strategy, meaning that molecules were chemically modified with a phosphonic anchor group beforehand. A DY700 fluorescent probe, a PEG* polymer and an ELP*_{40-60-Tat} were modified using this strategy, to respectively bring new functionalities to the IONPs: fluorescent, stealth, thermosensitive and cell penetrating properties. A single one-pot step in mild-acidic conditions was used to graft these molecules of interest onto the IONPs, followed by a fast and efficient centrifugation-redispersion process to isolate the grafted IONPs from residual un-grafted species. U87 glioblastoma cells were used as a model to study the nanoparticle internalization pathway. The IONPs were shown to end-up in lysosomes, with relatively no incidence on the cells' life cycle. The glioblastoma cells were viable, as quantified using their bioluminescence signal. The application of AMF resulted in the rupture of the lysosome, even in absence of macroscopic heating, as characterized by the leakage of their content observed by confocal microscopy. Their change of morphology was also evidenced by transmission electron microscopy, with originally spherical structures being distorted and deflated. The loss of microstructure integrity resulted in a cytotoxic effect, with a statistically significant drop of cell viability assessed by the BLI assay. These observations help highlighting the crucial role of lysosome rupture in the still debated mechanism of cell death under "cold" magnetic hyperthermia. Integrating magnetic nanoparticles in an anticancer drug delivery strategy is clearly relevant as an external magnetic field trigger can be used to release the drug trapped inside lysosomes, and push forward the cytotoxic effect. We also showed that the lysosomes and encapsulated IONPs are passed on to next generations of cells. The lysosomes keep their integrity during the cell division, still isolating the cytosol of the cells from the content of the lysosomes. This allows a possible delay between incubation and application of a magnetic field, with a time range superior to the cells' life cycle one. The thermosensitive property of the ELP*_{40-60-Tat} modified IONPs will be studied as outlook of this work in a near future in a drug-delivery strategy triggered by AMF application. *In vivo* experiments were carried to complement the *in vitro* observations and to study the effect of surface modification of the nanoparticles in relation with their application: the treatment of tumors. IONPs@ELP*_{40-60-Tat} and IONPs@PEG* nanoparticles were shown to accumulate in tumors when administered intravenously. As the surface of the nanoparticles was not decorated with active targeting ligand, the tropism toward the tumors was ascribed to a passive targeting, the canonical enhanced permeability and retention effect. Significant differences between the two surface modifications were observed by confocal imaging on microtomes of livers and tumors.

IONPs@ELP*_{40-60-Tat} nanoparticles were shown to be internalized deep inside the tumors as they exhibited cell-penetrating properties. Nevertheless, the application of an AMF led to no significant reduction of the tumor activities, as the fractions of administered nanomedicines effectively reaching the tumors were not sufficient to lead to a macroscopic heating during treatment. On the opposite, intra-tumoral administration led to significant elevations of temperature during the AMF treatment, of up to 10 °C compared to control tumors. Then successive applications of magnetic hyperthermia led to an effective reduction of tumor growth, also not leading to regression in the case of this very aggressive RM1 tumor model. Outlooks of this work would consist in repeating the *in vivo* experiments on a larger number of animals, and in the case of IV administration to possibly reach the threshold IONP concentration inside the tumor for thermal ablation by grafting efficient active targeting ligands to their surfaces.

5. References

1. Siegel, R.L., K.D. Miller, and A. Jemal, *Cancer statistics, 2017*. CA: A Cancer Journal for Clinicians, 2017. **67**(1): p. 7-30.
2. Trifiletti, D.M., C. Alonso, S. Grover, C.E. Fadul, J.P. Sheehan, and T.N. Showalter, *Prognostic Implications of Extent of Resection in Glioblastoma: Analysis from a Large Database*. World Neurosurgery, 2017. **103**: p. 330-340.
3. Stupp, R., M.E. Hegi, W.P. Mason, M.J. van den Bent, M.J.B. Taphoorn, R.C. Janzer, S.K. Ludwin, A. Allgeier, B. Fisher, K. Belanger, P. Hau, A.A. Brandes, J. Gijtenbeek, C. Marosi, C.J. Vecht, K. Mokhtari, P. Wesseling, S. Villa, E. Eisenhauer, T. Gorlia, M. Weller, D. Lacombe, J.G. Cairncross, and R.-O. Mirimanoff, *Effects of radiotherapy with concomitant and adjuvant temozolomide versus radiotherapy alone on survival in glioblastoma in a randomised phase III study: 5-year analysis of the EORTC-NCIC trial*. The Lancet Oncology, 2009. **10**(5): p. 459-466.
4. Maier-Hauff, K., F. Ulrich, D. Nestler, H. Niehoff, P. Wust, B. Thiesen, H. Orawa, V. Budach, and A. Jordan, *Efficacy and safety of intratumoral thermotherapy using magnetic iron-oxide nanoparticles combined with external beam radiotherapy on patients with recurrent glioblastoma multiforme*. Journal of Neuro-Oncology, 2011. **103**(2): p. 317-324.
5. Hu, J., K.P. Johnston, and R.O. Williams, *Nanoparticle Engineering Processes for Enhancing the Dissolution Rates of Poorly Water Soluble Drugs*. Drug Development and Industrial Pharmacy, 2004. **30**(3): p. 233-245.
6. Allen, T.M. and P.R. Cullis, *Liposomal drug delivery systems: From concept to clinical applications*. Advanced Drug Delivery Reviews, 2013. **65**(1): p. 36-48.
7. Masood, F., *Polymeric nanoparticles for targeted drug delivery system for cancer therapy*. Materials Science and Engineering: C, 2016. **60**: p. 569-578.
8. Kumari, A., S.K. Yadav, and S.C. Yadav, *Biodegradable polymeric nanoparticles based drug delivery systems*. Colloids and Surfaces B: Biointerfaces, 2010. **75**(1): p. 1-18.
9. Mertz, D., O. Sandre, and S. Bégin-Colin, *Drug releasing nanoplatforms activated by alternating magnetic fields*. Biochimica et Biophysica Acta (BBA) - General Subjects, 2017. **1861**(6): p. 1617-1641.
10. Ulbrich, K., K. Holá, V. Šubr, A. Bakandritsos, J. Tuček, and R. Zbořil, *Targeted Drug Delivery with Polymers and Magnetic Nanoparticles: Covalent and Noncovalent Approaches, Release Control, and Clinical Studies*. Chemical Reviews, 2016. **116**(9): p. 5338-5431.
11. Sanson, C., O. Diou, J. Thévenot, E. Ibarboure, A. Soum, A. Brûlet, S. Miraux, E. Thiaudière, S. Tan, A. Brisson, V. Dupuis, O. Sandre, and S. Lecommandoux, *Doxorubicin Loaded Magnetic Polymersomes: Theranostic Nanocarriers for MR Imaging and Magneto-Chemotherapy*. ACS Nano, 2011. **5**(2): p. 1122-1140.
12. Sun, P., Y. Zhang, L. Shi, and Z. Gan, *Thermosensitive Nanoparticles Self-Assembled from PCL-b-PEO-b-PNIPAAm Triblock Copolymers and their Potential for Controlled Drug Release*. Macromolecular Bioscience, 2010. **10**(6): p. 621-631.
13. Liu, T.-Y., S.-H. Hu, K.-H. Liu, R.-S. Shaiu, D.-M. Liu, and S.-Y. Chen, *Instantaneous Drug Delivery of Magnetic/Thermally Sensitive Nanospheres by a High-Frequency Magnetic Field*. Langmuir, 2008. **24**(23): p. 13306-13311.
14. Kievit, F.M., F.Y. Wang, C. Fang, H. Mok, K. Wang, J.R. Silber, R.G. Ellenbogen, and M. Zhang, *Doxorubicin loaded iron oxide nanoparticles overcome multidrug resistance in cancer in vitro*. Journal of Controlled Release, 2011. **152**(1): p. 76-83.
15. Oh, N. and J.-H. Park, *Endocytosis and exocytosis of nanoparticles in mammalian cells*. International Journal of Nanomedicine, 2014. **9**(Suppl 1): p. 51-63.
16. Hillaireau, H. and P. Couvreur, *Nanocarriers' entry into the cell: relevance to drug delivery*. Cell. Mol. Life Sci., 2009. **66**: p. 2873-2896.
17. Sanchez, C., D. El Hajj Diab, V. Connord, P. Clerc, E. Meunier, B. Pipy, B. Payré, R.P. Tan, M. Gougeon, J. Carrey, V. Gigoux, and D. Fourmy, *Targeting a G-Protein-Coupled Receptor Overexpressed in Endocrine Tumors by Magnetic Nanoparticles To Induce Cell Death*. ACS Nano, 2014. **8**(2): p. 1350-1363.

18. Wydra, R.J., P.G. Rychahou, B.M. Evers, K.W. Anderson, T.D. Dziubla, and J.Z. Hilt, *The role of ROS generation from magnetic nanoparticles in an alternating magnetic field on cytotoxicity*. Acta Biomaterialia, 2015. **25**: p. 284-290.
19. Wu, P.-C., H.-T. Hsiao, Y.-C. Lin, D.-B. Shieh, and Y.-C. Liu, *The analgesia efficiency of ultrasmall magnetic iron oxide nanoparticles in mice chronic inflammatory pain model*. Nanomedicine: Nanotechnology, Biology and Medicine, 2017. **13**(6): p. 1975-1981.
20. Hervault, A. and N.T.K. Thanh, *Magnetic nanoparticle-based therapeutic agents for thermo-chemotherapy treatment of cancer*. Nanoscale, 2014. **6**(20): p. 11553-11573.
21. de la Rica, R., D. Aili, and M.M. Stevens, *Enzyme-responsive nanoparticles for drug release and diagnostics*. Advanced Drug Delivery Reviews, 2012. **64**(11): p. 967-978.
22. Drappier, C., H. Oliveira, O. Sandre, E. Ibarboure, S. Combet, E. Garanger, and S. Lecommandoux, *Self-assembled core-shell micelles from peptide-b-polymer molecular chimeras towards structure-activity relationships*. Faraday Discussions, 2013. **166**(0): p. 83-100.
23. Mura, S., J. Nicolas, and P. Couvreur, *Stimuli-responsive nanocarriers for drug delivery*. Nat Mater, 2013. **12**(11): p. 991-1003.
24. Mout, R., M. Ray, G. Yesilbag Tonga, Y.-W. Lee, T. Tay, K. Sasaki, and V.M. Rotello, *Direct Cytosolic Delivery of CRISPR/Cas9-Ribonucleoprotein for Efficient Gene Editing*. ACS Nano, 2017. **11**(3): p. 2452-2458.
25. Domenech, M., I. Marrero-Berrios, M. Torres-Lugo, and C. Rinaldi, *Lysosomal Membrane Permeabilization by Targeted Magnetic Nanoparticles in Alternating Magnetic Fields*. ACS Nano, 2013. **7**(6): p. 5091-5101.
26. Hemery, G., A. Keyes Jr., C., E. Garaio, I. Rodrigo, J.A. Garcia, F. Plazaola, E. Garanger, and O. Sandre, *Tuning sizes, morphologies, and magnetic properties of monocoreshell versus multicore iron oxide nanoparticles through the controlled addition of water in the polyol synthesis*. Inorganic Chemistry, 2017. **56**(14): p. 8232-8243.
27. Devanand, K. and J.C. Selser, *Asymptotic Behavior and Long-Range Interactions in Aqueous Solutions of Poly(ethylene oxide)*. Macromolecules, 1991. **24**: p. 5943-5947.
28. Le Coeur, C., J. Teixeira, P. Busch, and S. Longeville, *Compression of random coils due to macromolecular crowding: Scaling effects*. Physical Review E, 2010. **81**(6): p. 061914.
29. Garanger, E., S.R. MacEwan, O. Sandre, A. Brûlet, L. Bataille, A. Chilkoti, and S. Lecommandoux, *Structural Evolution of a Stimulus-Responsive Diblock Polypeptide Micelle by Temperature Tunable Compaction of its Core*. Macromolecules, 2015. **48**(18): p. 6617-6627.
30. Koppel, D.E., *Analysis of Macromolecular Polydispersity in Intensity Correlation Spectroscopy: The Method of Cumulants*. The Journal of Chemical Physics, 1972. **57**(11): p. 4814-4820.
31. Fortin, P.-Y., C. Genevois, A. Koenig, E. Heinrich, I. Texier, and F. Couillaud, *Detection of brain tumors using fluorescence diffuse optical tomography and nanoparticles as contrast agents*. Journal of Biomedical Optics, 2012. **17**(12): p. 126004-126004.
32. Hemery, G., A.C. Keyes, E. Garaio, I. Rodrigo, J.A. Garcia, F. Plazaola, E. Garanger, and O. Sandre, *Tuning Sizes, Morphologies, and Magnetic Properties of Monocoreshell Versus Multicoreshell Iron Oxide Nanoparticles through the Controlled Addition of Water in the Polyol Synthesis*. Inorganic Chemistry, 2017. **56**(14): p. 8232-8243.
33. Daoud, M. and J.P. Cotton, *Star shaped polymers : a model for the conformation and its concentration dependence*. J. Phys. France, 1982. **43**(3): p. 531-538.
34. Birshtein, T.M. and E.B. Zhulina, *Conformations of star-branched macromolecules*. Polymer, 1984. **25**(10): p. 1453-1461.
35. Lin, E.K. and A.P. Gast, *Self Consistent Field Calculations of Interactions between Chains Tethered to Spherical Interfaces*. Macromolecules, 1996. **29**(1): p. 390-397.
36. Brittain, W.J. and S. Minko, *A structural definition of polymer brushes*. Journal of Polymer Science Part A: Polymer Chemistry, 2007. **45**(16): p. 3505-3512.
37. Collinet, C., M. Stoter, C.R. Bradshaw, N. Samusik, J.C. Rink, D. Kenski, B. Habermann, F. Buchholz, R. Henschel, M.S. Mueller, W.E. Nagel, E. Fava, Y. Kalaidzidis, and M. Zerial,

- Systems survey of endocytosis by multiparametric image analysis*. Nature, 2010. **464**(7286): p. 243-249.
38. Simnick, A.J., C.A. Valencia, R. Liu, and A. Chilkoti, *Morphing Low-Affinity Ligands into High-Avidity Nanoparticles by Thermally Triggered Self-Assembly of a Genetically Encoded Polymer*. ACS Nano, 2010. **4**(4): p. 2217-2227.
 39. Zhao, M., M.F. Kircher, L. Josephson, and R. Weissleder, *Differential Conjugation of Tat Peptide to Superparamagnetic Nanoparticles and Its Effect on Cellular Uptake*. Bioconjugate Chemistry, 2002. **13**(4): p. 840-844.
 40. MacEwan, S.R. and A. Chilkoti, *Digital Switching of Local Arginine Density in a Genetically Encoded Self-Assembled Polypeptide Nanoparticle Controls Cellular Uptake*. Nano Letters, 2012. **12**(6): p. 3322-3328.
 41. Singh, N., G.J.S. Jenkins, R. Asadi, and S.H. Doak, *Potential toxicity of superparamagnetic iron oxide nanoparticles (SPION)*. Nano Reviews, 2010. **1**: p. 10.3402/nano.v1i0.5358.
 42. Häfeli, U.O., J.S. Riffle, L. Harris-Shekhawat, A. Carmichael-Baranauskas, F. Mark, J.P. Dailey, and D. Bardenstein, *Cell Uptake and in Vitro Toxicity of Magnetic Nanoparticles Suitable for Drug Delivery*. Molecular Pharmaceutics, 2009. **6**(5): p. 1417-1428.
 43. Wilhelm, C., A. Cebers, J.C. Bacri, and F. Gazeau, *Deformation of intracellular endosomes under a magnetic field*. European Biophysics Journal, 2003. **32**(7): p. 655-660.
 44. Calatayud, M.P., E. Soler, T.E. Torres, E. Campos-Gonzalez, C. Junquera, M.R. Ibarra, and G.F. Goya, *Cell damage produced by magnetic fluid hyperthermia on microglial BV2 cells*. Scientific Reports, 2017. **7**(1): p. 8627.
 45. Fortin, J.-P., F. Gazeau, and C. Wilhelm, *Intracellular heating of living cells through Néel relaxation of magnetic nanoparticles*. European Biophysics Journal, 2008. **37**(2): p. 223-228.
 46. Rome, C., H. Loiseau, J. Arsaut, V. Roullot, and F. Couillaud, *Diversity of Contactin mRNA in Human Brain Tumors*. Molecular Carcinogenesis, 2006. **45**: p. 774-785.
 47. Walter, A., A. Garofalo, A. Parat, J. Jouhannaud, G. Pourroy, E. Voirin, S. Laurent, P. Bonazza, J. Taleb, C. Billotey, L. Vander Elst, R.N. Muller, S. Begin-Colin, and D. Felder-Flesch, *Validation of a dendron concept to tune colloidal stability, MRI relaxivity and bioelimination of functional nanoparticles*. Journal of Materials Chemistry B, 2015. **3**(8): p. 1484-1494.
 48. Rodrigues, H.F., G. Capistrano, F.M. Mello, N. Zufelato, E. Silveira-Lacerda, and A.F. Bakuzis, *Precise determination of the heat delivery during in vivo magnetic nanoparticle hyperthermia with infrared thermography*. Physics in Medicine & Biology, 2017. **62**(10): p. 4062.
 49. Kolosnjaj-Tabi, J., R. Di Corato, L. Lartigue, I. Marangon, P. Guardia, A.K.A. Silva, N. Luciani, O. Clément, P. Flaud, J.V. Singh, P. Decuzzi, T. Pellegrino, C. Wilhelm, and F. Gazeau, *Heat-Generating Iron Oxide Nanocubes: Subtle "Destructurators" of the Tumoral Microenvironment*. ACS Nano, 2014. **8**(5): p. 4268-4283.
 50. Wilhelm, S., A.J. Tavares, Q. Dai, S. Ohta, J. Audet, H.F. Dvorak, and W.C.W. Chan, *Analysis of nanoparticle delivery to tumours*. 2016. **1**: p. 16014.
 51. Levy, A., A. Dayan, M. Ben-David, and I. Gannot, *A new thermography-based approach to early detection of cancer utilizing magnetic nanoparticles theory simulation and in vitro validation*. Nanomedicine: Nanotechnology, Biology and Medicine, 2010. **6**(6): p. 786-796.
 52. Sandre, O., C. Genevois, E. Garaio, L. Adumeau, S. Mornet, and F. Couillaud, *In Vivo Imaging of Local Gene Expression Induced by Magnetic Hyperthermia*. Genes, 2017. **8**(2): p. 61.

CONCLUSION AND PROSPECTS

The aim of this PhD research project was to develop hybrid magnetic iron oxide nanoparticles biofunctionalized with polymers. Selecting thermosensitive polymers and thermosensitive elastin-like polypeptides allowed producing nanoparticles with potential medical applications as magnetic hyperthermia agents, drug delivery systems, or even MRI contrast agents. Because of the project scope, different domains of science were involved, from physics, chemistry to biology. Here are reported major advancements to obtain such systems.

At first, iron oxide nanoparticles were produced by the classical co-precipitation of iron precursors in alkaline conditions. Such strategy allowed yielding large quantities of material at the gram scale. However, the co-precipitation synthesis suffered from a major drawback, which was the lack of control over the morphology of the nanocrystals, and therefore over their magnetic properties. For these reasons, we selected the polyol route to produce iron oxide nanoparticles. This versatile method allowed producing batches of iron oxide nanocrystals with well-defined structures and magnetic properties. Importance of parameters such as temperature and reaction time, heating profile, nature of polyol solvent or of organometallic precursors on nanostructure and properties had already been described in the literature. Yet, the crucial role of water in the forced hydrolysis pathway had never been reported despite its mandatory presence for nanoparticle production. We investigated the influence of the water amount, and temperature at which it was injected in the reflux system for either a pure polyol solvent system or a mixture with poly(hydroxy)amine. Distinct morphologies of nanoparticles were thereby obtained and characterized by TEM. Ultra-ultra-small smooth spheres down to 4 nm in diameter to larger ones up to 37 nm were produced. Well-defined multicore assemblies with narrow grain size dispersity termed nanoflowers were also synthesized. A diverse and large library of samples was obtained by playing with the nature of solvents and amount of added water while keeping all other parameters constant. The properties of the IONPs were extensively studied. DLS measurements allowed estimating the hydrodynamic diameters of the IONPs as well as their aggregation state in solution, most samples being stable. Their magnetization was measured, evidencing superparamagnetic properties and magnetization saturations similar to that of the bulk material. Their SAR was evaluated using calorimetric measurements while applying a radiofrequency magnetic field. We reported SAR values of $296 \text{ W}\cdot\text{g}^{-1}$ in medically translatable conditions (frequency of 755 kHz, at $10.2 \text{ kA}\cdot\text{m}^{-1}$ of amplitude). SAR values as high as $2,000 \text{ W}\cdot\text{g}^{-1}$ were even obtained by AC magnetometry (frequency of 1023 kHz, at $20 \text{ kA}\cdot\text{m}^{-1}$ of amplitude). IONPs were also tested for MRI applications, by measuring their relaxivity properties. Transverse relaxivity r_2 exhibits also

quadratic variation with diameter for smooth nanospheres, in line with the “motional averaging regime” of the “outer sphere” model of MRI contrast agents. In the case of the smallest diameter IONPs synthesized (UUSPIOs), their longitudinal relaxivity r_1 at 1.41 T associated with moderate r_2/r_1 ratio make them alternatives to gadolinium chelates as positive MRI contrast agents, with lower risk of side effects on patients. The different morphologies led to bare magnetic nanoparticles suitable for medical applications such as magnetic hyperthermia, MRI contrast agent, or both.

The second milestone of the project was the biofunctionalization of the bare IONPs. The main objective was to bring stability to the IONPs in solution and potentially in biological conditions. At first, molecules of interest were attached by successively grafting an aminosilane, followed by a heterofunctional linker, before final attachment of a polymer or polypeptide. The aminosilane was used to bridge the gap between the inorganic core and the organic shell. Selecting an appropriate heterofunctional linker allowed bonding the polymer/polypeptide of interest with the surface of the IONPs decorated with amines. The commercially available aminosilane AEAPTMS and hetero crosslinker GMBS were used to graft the single block (VPGIG)₂₀ ELP. AEAPTMS and a synthesized azidoacetic acid molecule were used to graft a thermosensitive PDMAEMA polymer. These surface modifications had to be performed in three steps, with intermediates that were not stable in solution. Moreover, characterizing the reaction steps by NMR or TLC was rendered impossible because of the attachment of the chains onto the nanoparticles. Switching to a phosphonate anchor group allowed producing a fully chemically modified polymer or polypeptide beforehand. PEG was grafted onto the nanoparticles in a single final step, using a phosphonic acid-terminated PEG* synthesized separately, a strategy named “convergent”. We also reported the grafting onto IONPs of recombinant polypeptides made of di-block elastin-like peptide (VPGVG)₄₀-(VPG(A/G)G)₆₀ and CPP Tat sequence using this strategy. The (VPGVG)₄₀ block was thermosensitive and underwent a water de-swelling transition at a critical temperature around 35 °C in solution, the (VPG(A/G)G)₆₀ block was hydrophilic and provided colloidal stability to the resulting γ -Fe₂O₃@ELP*₄₀₋₆₀-Tat core-shell IONPs. The bio-functionalization of these IONPs with the di-block ELP*₄₀₋₆₀-Tat was achieved by a convergent strategy through strong coordination bonding of a phosphonate group introduced near the N-terminus of the polypeptide. To the best of our knowledge, this was the first report on a thermosensitive ELP layer grafted onto magnetic IONPs. A large attention was given to the grafting density of the tethered PEG* and ELP*₄₀₋₆₀-Tat. Different regimes of stretching and elongation of chains (from mushroom to brush) were obtained by varying the number of polymers and polypeptides per nanoparticle. The reduced tethered density was widely used as an indicator of the state of the brush, and helped predict the stability of the core-shell nanoparticles in solution. Additionally, a DY700* fluorescent probe functionalized with a phosphonate anchor group was synthesized and grafted at the surface of IONPs to track the nanoparticles *in vitro* and *in vivo*.

Another major challenge of this project was probing few nanometers of variations of brush thicknesses while simultaneously applying magnetic hyperthermia. A new fibre-based backscattering set-up enabled positioning a DLS remote-head as close as possible to the coil of a magnetic heating inductor to afford *in situ* probing of the backscattered light intensity, hydrodynamic diameter, and temperature. This approach provided a promising platform for estimating the response of magnetic and thermosensitive NPs to the application of a radiofrequency magnetic field. Hybrid magnetic and thermosensitive IONPs@PDMAEMA* nanoparticles were studied using this set-up, evidencing a reversible aggregation effect under magnetic hyperthermia. Other magnetic and thermosensitive systems were measured, as micelles, hollow spheres, and microgels. They proved to be responsive toward the application of magnetic hyperthermia, as they exhibited fast changes of hydrodynamic diameters. Hybrid magnetic and thermosensitive IONPs@ELP*_{40-60-Tat} were studied using this set-up. High temperature variations of the sample (up to 30 °C) could be obtained in few minutes by applying an AMF. Fast size changes of the magnetic core-thermosensitive shell nanoparticles were measured by dynamic light-scattering *in situ* while applying magnetic hyperthermia. Variations of the hydrodynamic size were compared to the classical polymer brush model revised for the highly curved surface of nanoparticles. We demonstrated that the ELP*_{40-60-Tat} chains were extended at high grafting densities, leading to an increase of hydrodynamic diameters. Moreover, larger variations of amplitude of diameters were obtained under magnetic hyperthermia. IONPs@ELP*_{40-60-Tat} nanoparticles exhibited a diminution of diameter under magnetic hyperthermia, contrary to IONPs@PDMAEMA*. This was attributed to the stabilizing effect of the hydrophilic (VPG(A/G)G)₆₀ block.

In vitro studies were performed on hybrid IONPs@PEG* nanoparticles. What started as preliminary and control tests for IONPs@ELP*_{40-60-Tat} ended up as a full study of the monocore vs. multicore effect on cell internalization and cytotoxicity. The interaction of IONPs@PEG* with a human glioblastoma cell line was studied, from the internalization pathway of the nanoparticles inside cells to the remotely magnetically induced cytotoxicity. Cellular internalization of IONPs@PEG* was observed by confocal, bright field and transmission electron microscopy, flow cytometry, and fluorescence imaging. We evidenced the influence of the dose of IONPs@PEG* during incubation over the internalization. We showed that IONPs@PEG* were most certainly internalized by micropinocytosis and ended-up in lysosomes. Few tens of millions of nanoparticles entered the cells without major impacts over cells viability. We also demonstrated a large cytotoxic effect of magnetic hyperthermia. This investigation highlighted the superior efficiency of multicore vs monocore IONPs, leading up to 90 % cancer cells death.

In vitro and *in vivo* experiments were carried on IONPs@PEG* and IONPs@ELP*_{40-60-Tat} nanoparticles. Using identical iron oxide monocore nanoparticles allowed comparing the surface

modification effect in biological conditions. Cellular internalization and toxicity assays were performed on a human glioblastoma cell line in view of applications for drug delivery activated magnetically. Superior cellular uptake of IONPs@ELP*_{40-60-Tat} was evidenced compared to IONPs@PEG* control nanoparticles. The internalization pathway in lysosomes was monitored by electron microscopy on microtomes and confocal optical microscopy on live cells. Cellular toxicity after AMF application with these core-shell IONPs was ascribed to lysosomal membrane rupture and leakage into the cytosol. The intracellular fate of such IONPs, from their internalization to the effect of an AMF application, validated the use of thermosensitive peptide brushes on IONPs as drug delivery systems, addressing lysosomal compartments and triggering leakage of their content by external AMF application. Long term fate (after 48 h) was discussed in view of the cell division with equal sharing of the magnetically loaded lysosomes among daughter cells, possibly envisioning the successive application of magnetic hyperthermia on time scales superior to the cellular life cycle. Preliminary *in vivo* experiments evidenced the positive effect of the Tat peptide end-sequence compared to the PEG brush control on the bio-distribution, with nanoparticles being present both in the liver and in U87 model tumor in mice.

To conclude, a thermosensitive, cell-penetrating, and magnetic IONPs@ELP*_{40-60-Tat} nanocarrier was developed during this project. Other systems were designed and studied, but all served as prototypes to acquire enough background knowledge for the synthesis, characterization, and experiments in biological conditions of IONPs@ELP*_{40-60-Tat} nanoparticles. IONPs obtained by polyol synthesis presenting the best morphologies and magnetic properties were selected for the core. The convergent phosphonate strategy reached maturity after testing on PEG*, and could be used to graft ELP*_{40-60-Tat} and DY700*. Understanding the theory of brushes by studying monolayers of PEG* allowed estimating correctly the number of ELP*_{40-60-Tat} to be grafted. This way, hybrid core-shell IONPs@ELP*_{40-60-Tat} nanoparticles were designed, with suitable properties for MRI and magnetic hyperthermia applications, as shown by preliminary experiments *in vitro* and *in vivo*. Drug delivery properties have yet to be tested in biological conditions.

Titre de la thèse: Synthèse de nanoparticules magnétiques et thermosensibles à base d'oxyde de fer pour des applications médicales.

Résumé : Cette thèse présente le développement de nanoparticules hybrides avec un cœur inorganique et une couronne organique pour des applications médicales. Des nanoparticules d'oxyde de fer ont été obtenues par synthèse polyol, en contrôlant leurs cristallinités, leurs morphologies (monocœur ou multicœur) et leurs tailles (de 4 à 37 nm). Leurs propriétés ont été évaluées et comparées pour de possibles applications théranostiques : en thérapie pour le traitement du cancer par hyperthermie magnétique, pour le diagnostic en tant qu'agents de contraste pour l'IRM. Les surfaces des nanoparticules ont été modifiées par greffage de polymères/polypeptides pour apporter de la stabilité en milieux biologiques et de nouvelles fonctionnalités. Le poly(éthylène glycol) (PEG) a été greffé pour ses propriétés de furtivité, le poly(2-diméthylaminoéthyl méthacrylate) (PDMAEMA) et des polypeptides dérivés de l'élastine (ELPs) pour leurs propriétés thermosensibles, et la sonde fluorescente DY700 pour permettre le suivi des nanoparticules *in vitro* et *in vivo*. Les propriétés magnétiques et thermosensibles de ces nanoparticules cœur-couronne ont été étudiées avec un instrument unique combinant l'hyperthermie magnétique et un système de diffusion dynamique de la lumière. Ainsi, les variations de température, de diamètre et d'intensité diffusée ont pu être mesurées simultanément. Les propriétés de nanoparticules monocœur et multicœur greffées avec du PEG, et des nanoparticules monocœur greffées avec un ELP contenant un peptide pénétrant ont d'abord été évaluées *in vitro*. Leurs internalisations dans des cellules de tumeur cérébrale humaine (glioblastome) ont permis d'étudier leurs cytotoxicités après traitement par hyperthermie magnétique, et ont montré une baisse de viabilité cellulaire jusqu'à 90 %. *In vivo*, l'injection intraveineuse de ces nanoparticules dans des souris a abouti à une accumulation dans les tumeurs. L'injection intratumorale suivie du traitement par hyperthermie magnétique a conduit à des élévations de température locales d'environ 10 °C, avec un effet significatif sur l'activité des tumeurs.

Title of the thesis: Synthesis of magnetic and thermosensitive iron oxide based nanoparticles for biomedical applications.

Abstract: This thesis reports the development of hybrid nanoparticles made of an inorganic iron oxide core and an organic shell for medical applications. Iron oxide nanoparticles (IONPs) were produced by the polyol pathway, leading to a good control over their crystallinity and morphology (monocore or multicore). IONPs with diameters in the range of 4 to 37 nm were produced. Their properties as MRI contrast agents were assessed and compared, for possible theranostic applications. They can be used for treating cancer by magnetic hyperthermia, and as contrast agents for MR imaging. The surface of the IONPs was modified to bring stability in biological conditions, as well as new functionalities. Poly(ethylene glycol) was grafted for its stealth property, poly(2-dimethylaminoethyl methacrylate) (PDMAEMA) and elastin-like polypeptides (ELPs) for their thermosensitive capabilities, and a DY700 fluorescent probe was grafted for tracking nanoparticles *in vitro* and *in vivo*. The magnetic and thermosensitive properties of the nanoparticles were studied using a unique set-up combining magnetic hyperthermia with dynamic-light scattering. This set-up allowed measuring the elevations of temperature of the samples as well as variations in diameter and backscattered intensity. Monocore and multicore IONPs grafted with PEG, and monore IONPs grafted with a diblock ELP were tested *in vitro*. Their interactions with glioblastoma cells were studied, from the internalization pathway inside the cells to their cytotoxic effect (up to 90 %) under magnetic hyperthermia. *In vivo*, nanoparticles intravenously injected in mice accumulated in the tumors. Intratumoral administration followed by magnetic hyperthermia treatment led to elevations of temperature of up to 10 °C, with a significant effect on the tumor activity.